Contribution to the study of the piezoelectric properties of ZnO nanowires and associated nanocomposites for application to mechanical-electrical energy transduction

Andres Jenaro Lopez Garcia

THÈSE

Pour obtenir le grade de

DOCTEUR DE L'UNIVERSITÉ GRENOBLE ALPES

Spécialité : NANO ELECTRONIQUE ET NANO TECHNOLOGIES

Arrêté ministériel : 25 mai 2016

Présentée par

Andres Jenaro LOPEZ GARCIA

Thèse dirigée par **Mireille MOUIS**,Directeur de Recherche, Université Grenoble Alpes
et codirigée par **Gustavo ARDILA RODRIGUEZ**

préparée au sein du **Laboratoire Institut de Microélectronique, Electromagnétisme et Photonique - Laboratoire d'hyperfréquences et de caractérisation**
dans **l'École Doctorale Electronique, Electrotechnique, Automatique, Traitement du Signal (EEATS)**

Contribution à l'étude des propriétés piézoélectriques de nanofils de ZnO et de nanocomposites associés en vue d'une application à la conversion d'énergie mécanique à électrique

Contribution to the study of the piezoelectric properties of ZnO nanowires and associated nanocomposites for application to mechanical-electrical energy transduction

Thèse soutenue publiquement le **3 juin 2022**,
devant le jury composé de :

Madame Mireille MOUIS
DIRECTEUR DE RECHERCHE, CNRS DELEGATION ALPES, Directrice de thèse
Monsieur Olivier THOMAS
PROFESSEUR DES UNIVERSITES, Aix-Marseille Université, Rapporteur
Madame Noëlle GOGNEAU
DIRECTEUR DE RECHERCHE, CNRS DELEGATION ILE-DE-FRANCE SUD, Rapporteure
Madame Guylaine POULIN-VITTRANT
DIRECTEUR DE RECHERCHE, CNRS CENTRE LIMOUSIN POITOU-CHARENTES, Examinatrice
Monsieur Alain SYLVESTRE
PROFESSEUR DES UNIVERSITES, GRENOBLE INP, Examinateur et Président du jury

Ackowledgments

First and foremost, I would like to express my sincere gratitude to my supervisors Dr. Mireille MOUIS and Dr. Gustavo ARDILA for their guidance and continuous support throughout these three and a half years. I want to highlight their patience, motivation, enthusiasm and enormous expertise. I will never forget all their advice which has been useful to make me grow professionally.

This project would not have been possible without the help of Xavier, Aude, Martine, and all staff at IMEP-LaHC, who also received me very kindly. In addition, I am grateful to all those people as master's students and postdoctoral researchers, who also participated and helped me during this experience in scientific research.

I would like to express my deepest thanks to my fellow labmate Chieu from LMGP, Angeliki, Miltiadis, Balraj, Namanu, Olfa, Fatoumata, all of them who shared with me the stimulating discussions and for all the fun we had in the last three years at IMEP-LaHC.

I am very grateful to my French friends, Alexandre, Thomas, Marc R., Marc P., and Hélène with whom I shared many experiences in the mountains of Grenoble, as well as French food and Latin dance. I would like to extend my deepest gratitude to all Colombia friends, especially to Monica, Ivonne and Danna which I met here in Grenoble and who were a key part of our family. I would like to recognize the invaluable friendship of Santiago, who helped me at the beginning of this project and adventure. I would also like to thank all my friends and family which I left in Colombia, who contributed with their part in my personal and professional life.

Estos dos párrafo quiero dedicarlo especialmente a mi familia, quiero agradecer a mi madre, mis hermanos y sobrinos, Zoraida, Diana, César, Alejandra, Felipe, Dayanna y Sebastián por haberme brindado su apoyo incondicional. Doy infinitas palabras de agradecimiento a mi madre por creer en mi y en mi proyecto desde el comienzo de esta historia, además de todo lo que soy. Esto es sin ninguna duda una obra construida por ti. Los amo muchísimos a todos.

A mi esposa Marcela quiero expresarte toda mi gratitud, quiero decirte que eres una persona muy importante en mi vida y que eres una actriz primordial de esta novela romántica desarrollada aquí en Francia. Te amo mi vida. Amélie mi pequeño retoño, quiero agradecerte por permitirme ser parte de tu historia y de aprender de ti a cada momento. Te amamos muchísimo de aquí hasta el infinito mi pequeña.

Abstract

With the increasing development of wireless networks of low-power sensors for the so-called internet-of-things, there is a need for efficient ways to ensure the energetic autonomy of sensing nodes. Among the various energy harvesting solutions, converting the abundant mechanical energy present in the environment into electrical energy is very promising. In this emerging field of research, ZnO nanowires (NWs) have been strongly studied during these last two decades, both as such, and integrated into nanocomposite materials. At the nanoscale, they feature improved electromechanical properties compared to bulk, as well as easy integration and manufacturing, on both rigid and flexible substrates. However, some intriguing discrepancies between the experimental and simulation results available at the beginning of this PhD highlighted the need for a better understanding of the piezoelectric operation of NW-based composites, especially for what concerns two important aspects which had been poorly addressed so far: the coupling between piezoelectric and semiconducting properties in simulations, and the dependence of electromechanical properties with ZnO NW growth method or with NW surrounding environment in experiments.

From the theoretical point of view, this Ph.D. thesis studies the coupling of piezoelectric and semiconducting properties in ZnO NWs and related nanocomposites and provides optimization guidelines for mechanical to electrical transducing applications. It investigates the influence of doping level, free carrier density, interface traps and geometrical parameters on electromechanical parameters. Simulations of ZnO NW-based nanocomposites under mechanical compression were performed using the Finite Element Method (FEM). Experimentally, several atomic force microscopy (AFM) modes, such as piezoelectric force microscopy (PFM), Kelvin probe force microscopy (KPFM), and conducting atomic force microscopy (C-AFM) were used, in order to probe locally electrical and electromechanical parameters which play a key role in the efficiency of the piezoelectric response of ZnO NWs. Our results showed that doping level, free carriers and surface traps, as well as trap dynamics, must be considered in order to explain the amplitude and the potential asymmetry of the electromechanical response, or the influence that geometry has on it. They demonstrate that semiconducting properties should be taken into account for the analysis of experimental results and for the correct design of electromechanical self-powered devices based on ZnO NWs and nanocomposites.

Keywords: surface traps, traps dynamics, finite element model, piezoelectric sensor, mechanical energy harvesting

Résumé

Avec le développement croissant de réseaux sans fil de capteurs de faible puissance pour ce que l'on appelle l'Internet des objets, il est nécessaire de trouver des moyens efficaces d'assurer l'autonomie énergétique des nœuds de détection. Parmi les différentes solutions de récupération d'énergie, la conversion en énergie électrique de l'abondante énergie mécanique présente dans l'environnement est très prometteuse. Dans ce domaine de recherche émergent, les nanofils (NFs) de ZnO ont été fortement étudiés au cours de ces deux dernières décennies, à la fois en tant que tels, et intégrés dans des nanocomposites. À l'échelle nanométrique, ils présentent des propriétés électromécaniques meilleures que le matériau massif, ainsi qu'une intégration facile sur des substrats rigides ou flexibles. Néanmoins, des divergences intrigantes entre les résultats expérimentaux et les simulations numériques disponibles au début de cette thèse ont mis en évidence la nécessité d'une meilleure compréhension du fonctionnement piézoélectrique des composites à base de NF, en particulier pour ce qui concerne deux aspects importants qui avaient été peu traités jusqu'alors: le couplage entre les propriétés piézoélectriques et semi-conductrices dans les simulations numériques et la dépendance des propriétés électromécaniques avec la méthode de croissance des NFs de ZnO ou avec l'influence de l'environnement des NFs dans les expériences.

Du point de vue théorique, cette thèse de doctorat étudie le couplage des propriétés piézoélectriques et semi-conductrices des NFs de ZnO et de leur nanocomposites et fournit des lignes directrices d'optimisation pour les applications de transduction électromécanique**.** Cette étude prend en compte l'influence du niveau de dopage, de la densité de porteurs libres, des pièges d'interface et des paramètres géométriques sur les paramètres électromécaniques. Des simulations numériques de nanocomposites à base de NF de ZnO sous compression mécanique ont été effectuées à l'aide de la méthode des éléments finis (FEM). Expérimentalement, plusieurs modes de microscopie à force atomique (AFM), tels que la microscopie à force piézoélectrique (PFM), la microscopie à force de sonde Kelvin (KPFM) et la microscopie à force atomique conductrice (C-AFM) ont été utilisés, afin de sonder localement les paramètres électriques et électromécaniques qui jouent un rôle clé dans l'efficacité de la réponse piézoélectrique des NFs de ZnO. Nos résultats ont montré que le niveau de dopage, les porteurs libres et les pièges d'interface, ainsi que la dynamique des pièges, doivent être pris en compte pour expliquer l'amplitude et l'asymétrie potentielle de la réponse électromécanique ou l'influence que la géométrie a sur elle. Ils montrent que les propriétés semi-conductrices doivent être prises en compte pour l'analyse des résultats expérimentaux et la conception correcte de dispositifs électromécaniques autonomes basés sur des NFs de ZnO et leurs nanocomposites.

Mots-clés: pièges de surface, dynamique des pièges, modélisation par éléments finis, capteur piézoélectrique, récupération d'énergie mécanique.

Table of Contents

List of Abbreviations

AC	**A**lternating **C**urrent
AFM	**A**tomic **F**orce **M**icrsocopy
AGR	**A**nnual **G**rowth **R**ate
ALD	**A**tomic **L**ayer **D**eposition
AlN	**A**luminium **N**itride
AM	**A**mplitude **M**odulation
AZO	**A**luminium-doped **Z**inc **O**xide
BC	**B**oundary **C**ondition
BTO	**B**arium **T**itanate
C-AFM	**C**onducting **A**tomic **F**orce **M**icroscopy
CBD	**C**hemical **B**ath **D**eposition
CdS	**C**aldium **S**ulfide
CVD	**C**hemical **V**apor **D**eposition
DC	**D**irect **C**urrent
EHs	**E**nergy **H**aversters
EIS	**E**lectrical **I**mpedance **S**pectroscopy
FEM	**F**inite element Method
FM	**F**requency **M**odulation
GaN	**G**allium **N**itride
IoT	**I**nternet **o**f **T**hings
ITO	**I**ndium **T**in **O**xide
KNN	**P**tassium **S**odium **N**iobate
KPFM	**K**elvin **P**robe **F**orce **M**icroscopy
MOCVD	**M**etal-**O**rganic **C**hemical **V**apor **D**eposition
NWs	**N**anowires

PDMS	**P**oly(**D**i-**M**ethyl-**S**iloxane)
PET	**P**oly(**E**thylene **T**erephthalate)
PFM	**P**iezoresponse **F**orce **M**icroscopy
PMMA	**P**oly**M**ethyl**M**eth**A**crylate
PPLN	**P**eriodically **P**oled **L**ithium **N**iobate
PVDF	**P**oly(**V**inyli**D**ene **F**luoride)
PZT	**L**ead **Z**irconate **T**itanate
SEM	**S**canning **E**lectron **M**icroscopy
SFL	**S**urface **F**ermi **L**evel
SHM	**S**tructural **H**ealth **M**onitoring
TE	**T**hermal **E**vaporation
TF	**T**hin **F**ilm
VING	**V**ertical **I**ntegrated **N**anogenerator
ZnO	**Z**inc **O**xide

Introduction

The market for wireless networks of low-power sensors for the so-called internet-of-things has been expanding rapidly during this last decade. It is targeting applications such as structure health, medical and environmental monitoring, which require small sensors for providing continuous observation. Some technologies and structures need a large number of sensors or must be permanently installed in hard-to-reach places for civil, military, and aerospace applications. Self-powered devices could be an appropriate technology to reduce battery management costs. The collection of small amounts of environmental energy to power wireless devices is a smart solution for building this kind of self-powered device.

Among the different energy harvesting technologies, piezoelectric energy harvesters have been proposed for collecting the wasted mechanical energy in the form of vibration or deformations. This mechanical energy can be provided by human motion, ocean waves and airflow among many others which are abundant in the ambient. The performance of such harvesters depends, among many parameters, on the quality of the piezoelectric material (considering properties such as the piezoelectric coefficient, dielectric permittivity, and compliance). Most piezoelectric materials are synthetics, i.e., their piezoelectric nature depends on additional processes. As for mechanical energy applications, inorganics piezoelectric, organics piezoelectric, and composite piezoelectric materials are the most used [1]. Piezoelectric nanowires (NWs) have recently exhibited a promising improvement to withstand enormous mechanical deformation [2], a reduction in the dielectric constant [3], and an increase on the piezoelectric coefficient [4]. One interesting structure based on NWs is the nanocomposite, being a mixture of NWs into a dielectric matrix. Nanocomposites based on ZnO NWs, being piezoelectric and semiconductors, have been explored because this material affords large areas, low temperature, easy manufacturing and processing. More recently, our team has theoretically shown that nanocomposites based on ZnO NWs can outperform the performance of ZnO thin films [5,6].

However, the development of these applications is currently hampered by a lack of understanding, particularly regarding the coupling, at the nanoscale, between the polarizability of the material (piezoelectric aspect), doping level and interface traps (semiconductor aspects). This thesis aims at going further in the understanding of electromechanical phenomena at the nanoscale. In particular, we are interested in the influence of size on the piezoelectric properties of NWs, with account for their possible screening by ionized dopants, free carriers, and

interface traps. To achieve this goal, the influence of several parameters will be studied, in particular doping level, surface traps density and NWs dimensions.

During the first year of my Ph.D and based on the expertise developed in the team, I performed multi-physics simulations (analytical models and numerical simulations based on the finite element method) to acquire an understanding of the nanocomposite based on ZnO NWs under compressive axial force, taking into account the coupled electromechanical properties. This was useful to reach one of the objectives related to the identification of the optimization tracks and the realization of research demonstrators, based on recent experiences developed at IMEP-LaHC. Simultaneously, I was trained in Atomic Layer Deposition (ALD) and Chemical Bath Deposition (CBD) techniques for growing ZnO NWs on Si rigid substrates. These samples were used as a reference, in particular to characterize the piezoelectric response of individual NWs using AFM techniques. For the next two years, I focused on the AFM characterization of ZnO NWs grown by CBD on flexibles substrates (in the context of the European project PULSE-COM), implementing Piezoelectric Force Microscopy (PFM), Kelvin-Probe Force Microscopy (KPFM), and current vs. voltage measurements (TUNA or C-AFM). All these measurements were correlated shedding light on the electromechanical phenomena at the nanoscale and on coupled properties by developing original measurement methodologies.

The manuscript is organized in four chapters:

i) Chapter I describes, the present research background on energy harvesting devices, piezoelectric materials, and semiconducting piezoelectric NWs for energy harvesting and sensing applications. Additionally, it explores the experimental and numerical state-of-the-art of nanocomposite transducers based on ZnO NWs.

ii) Chapter II shows, the results of our numerical simulation using the Finite element method (FEM) of nanocomposite unit cells under compressive force. The simulations considered a self-consistent set of coupled equations including piezoelectric and semiconducting properties. The dynamics of the mechanical input and the impact of ZnO NW growth method were investigated, with account for the role of surface trap charge. Finally, in order to provide better performance indications, for easier comparisons between different devices, we considered the electromechanical optimizations of a VING loaded with a resistance load. The influence of geometrical parameters (e.g. NW radius and length) on the overall performance was also studied and compared with the range of experimental values, published in the literature for comparables structures.

iii) Chapter III displays, AFM experimental results about the piezoelectric response (piezoelectric amplitude and phase) of individual ZnO NWs grown by CBD technique over rigid and flexible substrates. The development of original measurement methodologies allowed us to demonstrate the size and border effects in the piezoelectric signals, which would be attributed to the coupled piezoelectric and semiconductor properties.

iv) Chapter IV reports on complementary electrical characterizations (PFM, KPFM, and TUNA) that were carried out on ZnO NWs grown on flexible substrates using ambient atmosphere as a means to potentially modify ZnO surface properties. We showed the influence of the surrounding gas on the piezoelectric signal and on the metal-semiconductor properties of the contact between the AFM probe and the ZnO NWs. We correlated these findings with theoretical results.

Chapter I. Piezoelectric ceramics and nanocomposites: state-of-the-art

I.1 The problem of energy supply for the Internet of Things (IoT)

Technological advance has allowed revolutionizing the idea based on a new paradigm called the Internet of Things (IoT), which consists of a tremendous technology in today's world. It can connect several objects to networks (clouds) for achieving a specific task. Among some IoT devices, we can find public displays, payment terminals, wearables devices, etc.

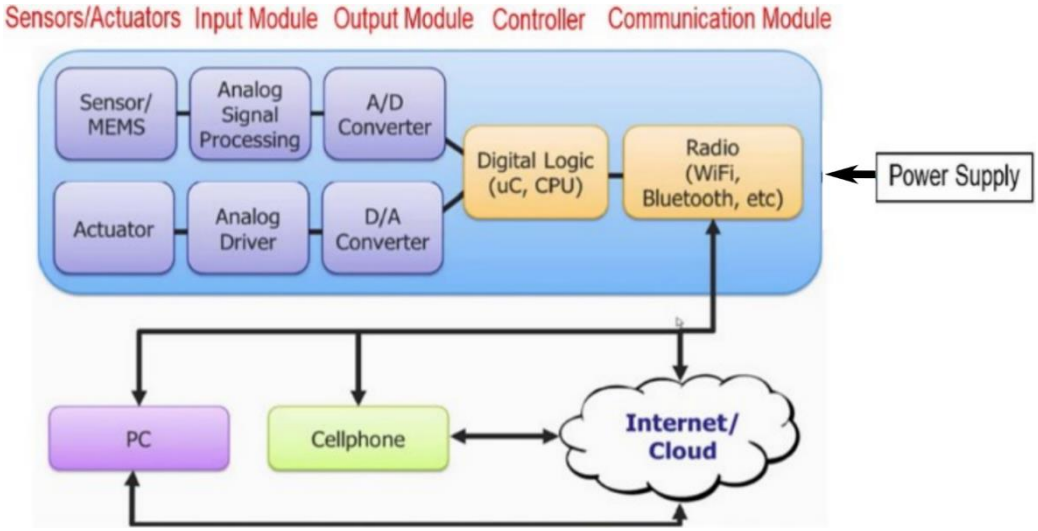

Figure I-1 Schematic of an IoT device. The figure was adapted from [7].

An IoT system comprises five fundamental components, starting with a sensor or an actuator that interacts with a wired or wireless internet section, as shown in Figure I-1. Sensors/actuators are electromechanical devices that transform the mechanical input from the external physical environment into an electrical signal and vice versa. Subsequently, the signal is transferred to the input/output (I/O) components. I/O component works as a mediator of the digital component, called processors (programmable automation controller). I/O devices treat the signal input as analogy or digital. Then, a radio component receives these processed signals using a communication protocol, such as WiFi, ZigBee, Bluetooth, etc. Finally, the radio component drives data to the Cloud, the smartphones, or PC, also known as the human-machine interface. Until now, power outlet or batteries provide energy to these devices.

Thinking a little more long-term, it is evident some energy issues because IoT devices have been exponentially increasing in recent decades and will be increasingly abundant in the years to come. According to data analysis studies, IoT devices went from 3.6 to 11.3 Billion (Bn) from 2015 to 2020 with an Annual Growth Rate (AGR) of 26%, as shown in Figure I-2. In 2021, the forecast study expected that the IoT-connected device would grow by 9% (equivalent to 12.3 Bn) from the last active point (11.3 Bn). For the next 5 years, AGR could reach an increasing percentage of 22%. It means that IoT devices would increase from 12.3 Bn to 27.1 Bn during this period. Nonetheless, self-powered devices will be required to provide future energy demand, forecasting dependence on batteries in the long term. It should be added that the standard batteries have a short lifetime, and they need to be substituted every time that the energy supply is exhausted [8]. In this regard, new technologies based on self-powered systems have been widely explored to replace obsolete battery-dependent systems. So, the main motivation of this project lies in generating self-powered systems to energy supply the next generation of low-power IoT devices.

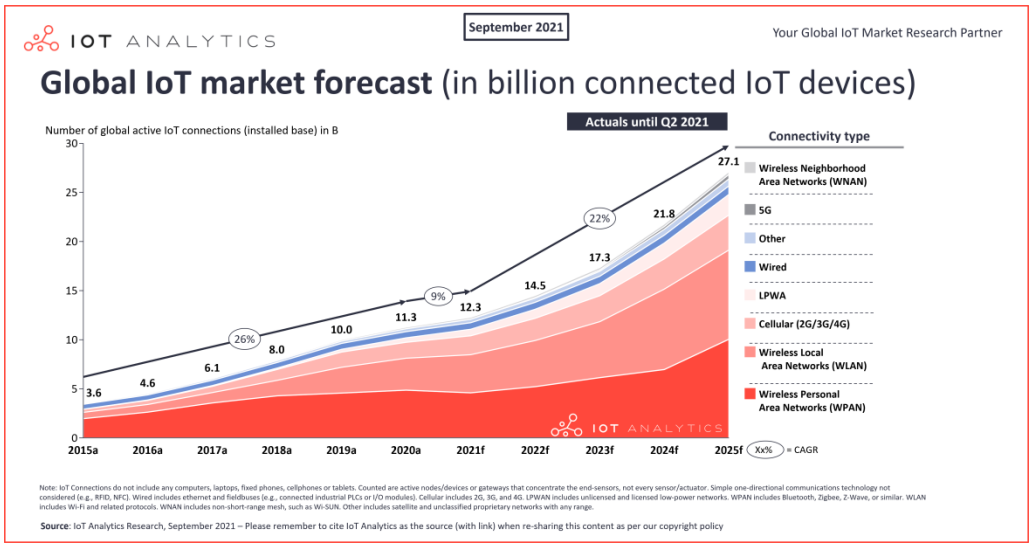

Figure I-2 Forecast of the number of connected devices as a function of years, edited in Septembre 2021 [9].

It can be highlighted that IoT is emerging as an essential technology for Structural Health Monitoring (SHM) [10]. SHM application has been used to assess and monitor the state of structures, for instance, bridges, buildings, aircraft, and so on. In real-life, these devices are occasionally put on different points of the structure (specifically in difficult access areas) when using a considerable number of sensors. After the data processing and analysis, SHM may prognosticate the structure's life or when the damage has occurred. Overall, SHM is composed of the same IoT components, which have a goal of collecting structural information, either temperature, stress, strain, vibration, or others, through the piezoelectric and

microelectromechanical system. However, this application also requires power supplies for its functionality, so batteries are not practical since their replacement would be difficult and expensive.

Some emergent technologies are ongoing to develop autonomous IoT devices by considering energy harvesting applications [11]. Energy harvesting is defined as the transformation of energy available in the ambient environment (such as photovoltaics, air, temperature, heat, and vibration, etc.) to electric energy through a particular material or transduction mechanism.

As for energy harvesting, the most common techniques that have been employed are: i) photovoltaics that converts the solar energy into electric energy (e.g., solar panels) [12,13], ii) thermoelectrics which converts a gradient of temperature to electric energy (e.g., thermoelectric generators) [14,15] and iii) electromechanical transducer that converts mechanical vibration into electric energy (e.g., piezoelectrics and electrostatic generators) [16–18].

Some of the advantages of electromechanical transducers have to do with their broad coverage in many environments in both outdoor and indoor conditions. Besides, this type of energy is focused on low-level harvesting energy (i.e., between milliwatts (mW) and microwatts (μW) to low-powered power electronics in comparison with thermal and solar energy, which can provide hundreds of watts. In this context, certain power consumption will be required for supplying the battery-powered systems, as shown in Figure I-3(a). So, the applicability of any electromechanical transducers could become an autonomous system. Mechanical energy could be helpful in many applications, such as a hearing aid, a wireless sensor node, a cardiac pacemaker, among others. This kind of application can take a harvested power from a human motion or an industrial motion source, as depicted in Figure I-3(b).

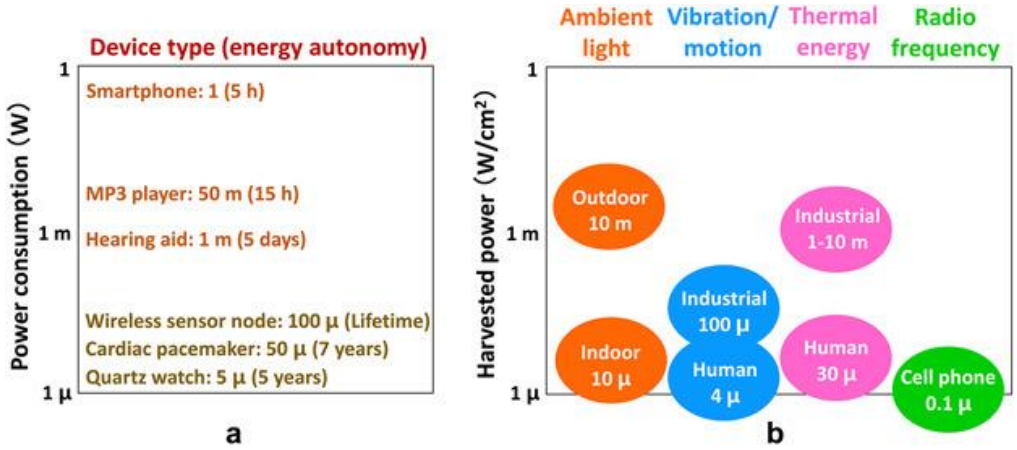

Figure I-3 (a) Representation of battery-powered devices and their power consumption. b) Power value generated by energy-harvesting technologies in different environmental conditions [17].

I.2 Mechanical energy harvesting transducers

Among the mechanical technologies, piezoelectric energy harvesters (EHs), electromagnetic EHs, and electrostatic EHs are the most commonly used. They have attracted much attention from researchers specialized in energy harvesting applications. Piezoelectric EHs work based on the principle of piezoelectric properties after applying an external strain in a material, i.e., small mechanical displacements of piezoelectric material are induced at the surface of the material, creating an electric charge on it due to a polarization field. Piezoelectric EHs techniques can vary according to their applications. For instance, the piezoelectric vibration technique consists of cantilever-based resonators to convert the mechanical energy into electricity for high-frequency vibration (between 60–100 Hz and above) [19]. It has been considerably investigated in the literature [20]. It should be added that they are not appropriate for human sources since the human body joints need a low-frequency range of about 4 Hz and large deformations values. In this respect, other techniques, such as frequency up-conversion [21–23] and piezoelectric nanocomposites [24] could solve these issues.

The mechanical frequency up-conversion system has recently been designed as a low-frequency alternative. It consists of inducing a high-frequency response from a low-frequency excitation using the magnet systems. The system can collect energy from environmental vibrations at low frequencies (< 5 Hz) [21–23]. Another alternative is the piezoelectric nanocomposites. They are generally formed by inorganic piezoelectric nanostructures, such as lead zirconate titanate (PZT), barium titanate ($BaTiO_3$), sodium niobite ($NaNbO_3$), potassium niobite ($KNbO_3$), and zinc oxide (ZnO), as well as the organic piezoelectric nanostructures as poly(vinylidene fluoride) (PVDF) [25]. These nanocomposites are generally integrated within flexible matrices and flexible substrates, making them compatible with wearable applications. Some of them have barely been manufactured at low temperatures, obtaining versatility for wearable electronics compared to thin films counterpart. Additionally, they can operate at large deformations and low frequencies (< 10 Hz) [26].

Electromagnetic EH works using electromagnetic induction. The principle of operation falls on the employability of magnets and coils of wire. These magnets or coils are moved due to an applied mechanical stimulus to produce an electric signal. Based on the types of movement, electromagnetic EH can be classified into three categories: rotational converter, oscillatory converter, and hybrid converter [27]. The rotational converters are suitable devices for applications such as turbines and low-power mobile. They need a constant rotational motion source and a rotational speed range of 1000 rpm until a maximum value of 400 krpm [27].

Scavenging energy at low frequency (i.e., for human motion application) has been a challenge for electromagnetic EH, providing a maximum power of 10.4 mW from a handshaking frequency of 8 Hz [28]. As for oscillatory converters, they are the most common devices since they are based on mass-spring-damper systems (MSD-systems). The magnets act as mobile mass oscillating, which is stimulated by mechanical input to generate a maximum power consumption at a resonant frequency value. It means that the oscillatory converters have a dependency on the resonant frequency. Finally, the hybrid converters use an eccentric rotor that converts the linear motion from the environment into a rotational. After combining the electromagnetic energy harvester, the rotational motion is transduced into electric energy. This device can generate a maximum power (approximately 5mW) at 8 Hz in the external excitation frequency [29]. The main challenge is to reduce the resonant frequency of the harvester, which until today is greater than 5 Hz, without affecting the structural parameters. This is required to collect low-frequency vibration energy from the environment [30].

Electrostatic harvesters EHs work like a variable capacitors that can be modulated by changing the spacing between two materials when applying mechanical forces [31]. Some advantages are related to easier integration with electronics, especially micro-systems, and the output voltage generated (between 2-12 volts). Some of the disadvantages are that some technologies need an additional voltage source and mechanical stops [32,33]. The most recent electrostatic EHs are triboelectric EHs. Triboelectric EHs rely on the contact electrification mechanism between two materials, referring here to non-rubbing contact between them. Its principle of operation is based on inducing an electric charge on the surface of electrodes when modifying the contact distance in both materials. This contact distance is modulated by mechanical energy to generate a potential difference. At the same time, the transferred electric charge could come from electrons [34], ions [35], and material transfer [36]. Triboelectric EHs exhibit stable performance thanks to a high power density and regardless of the operating frequency. High-efficiency energy harvesting can be reached by improving the surface electric charge density parameter of triboelectric EH. In experiment works, a triboelectric nanocomposite has recently reached a record-high charge density of 2.38 mC/m^2 by implementing a special circuitry [37].

According to a comparative study between piezoelectric and triboelectric nanocomposites, triboelectric nanocomposites demonstrate high voltage values with minimal operating frequency (i.e., below 1 Hz) at low output current. However, the lower values of current in piezoelectric nanocomposites allow for designing an easy power management circuit compared to triboelectric nanocomposites. Table I-1 summarises some advantages, disadvantages, and challenges for each type of mechanical EH.

Table I-1: Comparison of different mechanical technologies of the viewpoint of advantages, disadvantages, and challenges (adapted from [38]*).*

Type of mechanical EH	Advantages	Disadvantages	Challenges
Piezoelectric	-Constructing in the rigid and flexible substrate [24] -High output potential [39] -High energy density [40] -Structural simplicity [41]	-High impedance and low current [42] -Low-efficiency value [42]	-Ultraslow operating frequency range -Low cost in its fabrication -Biocompatibility -Enhancement of efficiency value
Electromagnetic	-Robustness and durable [43] -High current -Low output impedance [44]	-Low voltage [45] -Low efficiency at low frequency [45]	-Difficulties in miniaturizing [45] -Difficulties to integrate to MEMS [46]
Triboelectric	-High output power [42] - Structural flexibility [42] - No material constraints [42] -High-efficiency value [42]	-High impedance [42] -High frictional damage [42] -Difficult to design power management circuit	- Difficulties in miniaturizing [42] -Improving durability and reliability [38]

I.2.1 Piezoelectric materials

The piezoelectric effect was initially discovered in 1880 by Pierre and Jacques Curie under the name of “pyroelectricity”. One year later, Hankel proposed the term “piezoelectricity”. This piezoelectricity arises due to the induced effective piezoelectric charges in different parts of the crystal surfaces, generating the electric potential difference after applying mechanical stress along the polar axis. After that, Lippmann suggested that the converse piezoelectric effect existed, whose phenomenon was corroborated in 1881 by Curie brothers. The converse piezoelectric effect refers to the generation of mechanical deformation inside the material due to an applied electric field [47]. Figure I-4(a) shows the family classification of twenty-one piezoelectric crystals without and with pyroelectric and ferroelectric properties. According to the literature, twenty-one of thirty-two crystal classes are non-centrosymmetric (i.e., materials without a symmetry center in the crystal structure). Of these twenty-one, twenty classes are piezoelectric materials. Among piezoelectric materials, ten of them require an electric field or mechanical stress in order to generate a piezoelectric response inside of the material (such as happens in dielectric and paraelectric materials, as shown in Figure I-4(b)). Other tens have pyroelectric (change in polarization due to the temperature change, as shown in Figure I-4(c))

and ferroelectric properties (spontaneous polarization without any electric field, as shown in Figure I-4(d)) [48]. The materials with only pyroelectric properties are Zinc oxide (ZnO) [49], cadmium sulfide (CdS) [50] among others, while the ferroelectric materials are lithium niobate ($LiNbO_3$) [51], barium titanate ($BaTiO_3$) [52], among others.

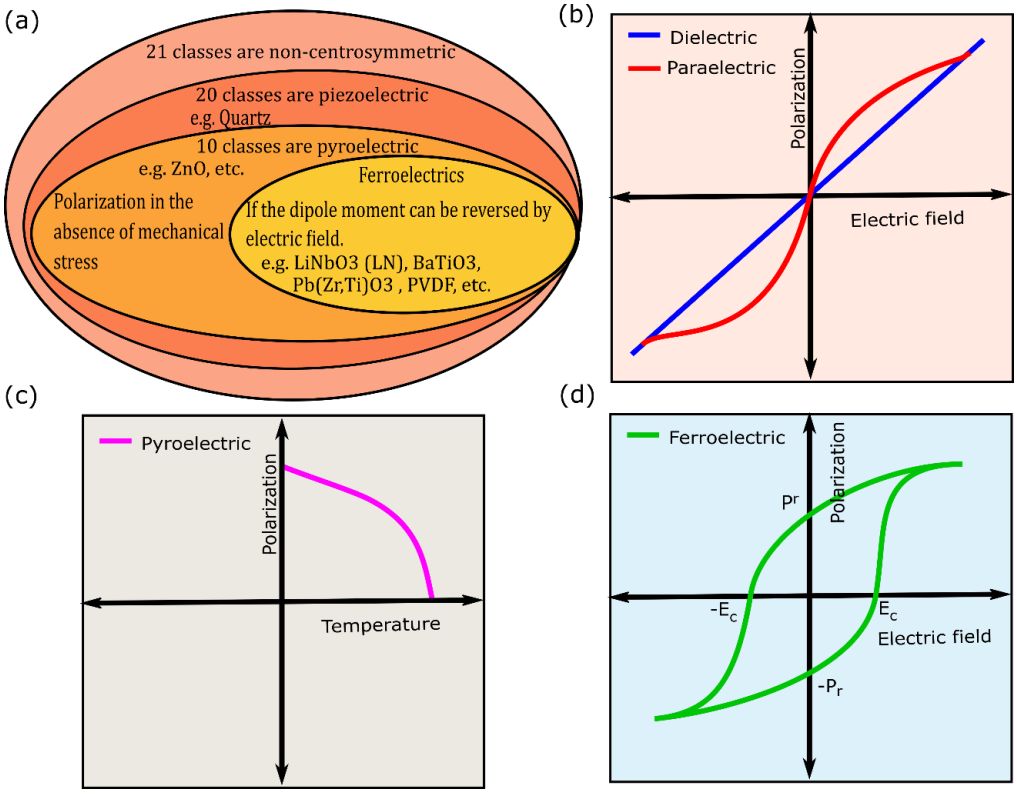

Figure I-4 (a) Clarification of piezoelectric, pyroelectric and ferroelectric materials. Figure adapted from [53]. *Schematic of polarization curves for (b) dielectric-paraelectric, (c) pyroelectric and ferroelectric materials. Figures adapted from* [54].

The piezoelectric properties of some materials are usually defined by the piezoelectric coefficient components such as e_{ki} and d_{ki}. For example, a generated piezoelectric polarization (P) is produced after applying mechanical stress (T) or strain (S). This effect is called the direct piezoelectric effect and is given by:

$$P_i = d_{ki}T_k = e_{ki}S_k \qquad \text{I-1}$$

The converse piezoelectric effect is produced after applying an external electric field (E) to the piezoelectric system, generating the mechanical deformation into the material to expand or contract it (i.e., strain (S)). Its relation is written as:

$$S_i = d_{ki}E_k \qquad \text{I-2}$$

Here d_{ki} is associated with the direction of stress relative to the poling direction (such as d_{33}, d_{15}, or d_{31}) for the wurtzite crystal structure, and its subscripts k and j follow conventional piezoelectric matrix notation given by:

$$[e],[d] = \begin{bmatrix} 0 & 0 & 0 & 0 & e_{15} & 0 \\ 0 & 0 & 0 & e_{15} & 0 & 0 \\ e_{31} & e_{31} & e_{33} & 0 & 0 & 0 \end{bmatrix}, \quad \begin{bmatrix} 0 & 0 & 0 & 0 & d_{15} & 0 \\ 0 & 0 & 0 & d_{15} & 0 & 0 \\ d_{31} & d_{31} & d_{33} & 0 & 0 & 0 \end{bmatrix} \qquad \text{I-3}$$

Effective piezoelectric conversion in a material can be assessed either by an energy harvesting figure of merit (FOMs) or the electromechanical coupling coefficient (k^2) [55]. For a piezoelectric material that is exposed to an external mechanical vibration far away from electromechanical resonance and at a low frequency, FOM and k^2 are given by:

$$FOM_{ij} = \frac{{d_{ij}}^2}{\varepsilon_r} \quad \text{and} \quad k^2 = \frac{{d_{ij}}^2}{(\varepsilon_r \cdot s_{ij}^E)} \qquad \text{I-4}$$

where ε_r and s_{ij}^E are the relative permittivity and the mechanical compliance at a constant electric field, respectively. An optimal material under mechanical stimulus (i.e., a high value of FOM or k^2) should have a high value of d_{ij} or ε_r should be low as well as s_{ij}^E (see FOM or k^2).

I.2.1.1 Types of piezoelectric materials

In nature, only the quartz and the berlinite piezoelectric materials present the piezoelectricity thanks to their specific crystalline structure. Most piezoelectric materials are synthetic, of which the inorganic piezoelectric, organic piezoelectric, and composite piezoelectric materials are the most commonly investigated in energy harvesting applications [1].

a. Inorganic piezoelectric materials

The first inorganic piezoelectric materials used in energy harvesting applications, especially piezoelectric generators, were piezoelectric perovskite ceramics such as PZT and barium titanate ($BaTiO_3$). Unlike the natural piezoelectric materials, these synthetic materials previously required a poling process to induce and improve their piezoelectricity, i.e., the crystal structure is subjected to an electric field to change the orientation of all the dipoles in the direction of the electric field permanently. Some outstanding piezoelectric efficiency

parameters are their high piezoelectric coefficients (d_{33}) and dielectric constants (ε_r) with values between 300-1000 pC/N and 1000-8000 for PZT [56] and 260- 454 pC/N and 1600-4000 for doped $BaTiO_3$ [57–62].

Recently, a thin film PZT-based MEMS was fabricated by Yi. *Et al.* [63]. Two layers of a thin film of PZT were deposited on both sides of a flexible substrate of beryllium bronze thin film (around 50 μm in thickness) using the bonding and thinning technologies. A rectangle tungsten proof-mass was put at the end of the cantilever beam, forming a volume of 30.6 mm^3 for the complete device. The peak-to-peak output voltage, the output power, and the output power density of 53.1 V, 0.98 mW, and 32 mW/cm^3 were reached, respectively. These measurements were performed at an applied acceleration amplitude of 3.5 g and a frequency value of 77.2 Hz. This device also demonstrated good stability during 1h and lighted up to twenty-one serial LEDs.

As is well-known, PZT is a harmful material because it contains the lead component, making it unfriendly to the environment and the human body. Whereas $BaTiO_3$ is a lead-free material, but it requires a high value of sintering temperature (around 1300 °C) to achieve a d_{33} value of about 350 pC/N and ε_r value of 4200 [64]. Additionally, the operating temperature or Curie temperature (T_C) range of $BaTiO_3$ is another difficulty because it is below 120 °C. Over this T_C, piezoelectric materials with ferroelectric properties transform their crystal structure from a non-centrosymmetric state to a centrosymmetric state. It means that both piezoelectricity and ferroelectricity properties disappear into the material [65]. On the other hand, lead-free ferroelectric ceramics have been recently manufactured, such as potassium sodium niobate [$(K_xNa_{(x-1)})NbO_3$, abbreviated as KNN] and sodium bismuth titanate [$(Bi_{0.5}Na_{0.5})TiO_3$, abbreviated as BNT], thereby enhancing both d_{33} and T_C. Among KNN-modified materials, we can find KNN-$LiTaO_3$ and KNN-$LiTaO_3$-$LiSbO_3$, which can have significant d_{33} values of 373 pC/N and 416 pC/N, and T_C values of 323 °C and 256 °C [66], respectively. A few works about MEMS energy harvester based on KNN thin films have been lately reported. Won *et al.* [67] performed a MEMS using an Mn-doped KNN thin film (with 1 μm in thickness) as a cantilever and Si-proof mass. The total effective volume of this device was around 0.002 cm^3. By using a small concentration of Mn addition in KNN, some good piezoelectric coefficient values were achieved of about 90 pm V^{-1} and -8.5 C m^{-2} for d_{33} and e_{31}, respectively. At the resonance frequency of 132 Hz, the device exhibited a maximum power output, a power density, and the corresponding peak voltage of 3.62 μW, 1800 $\mu W/cm^3$, and 520 mV, respectively.

As for a BNT-based piezoelectric ceramic, a pure BNT ceramic exhibits a lower d_{33} value of 58pC/N [68] and a high T_C value of 340 °C [69]. In order to increase its d_{33} for BNT ceramic,

Kang *et al.* [70] added an inorganic compound, such as barium titanate [($BaTiO_3$), abbreviated as BTO], in BNT. The (1-x)BNT-xBTO presented a maximum d_{33} value of 164 pC/N at x=0.06 and a sintering temperature of 1175 °C. In the literature, there are also very few works based on vibrational energy harvesters related to BNT-BTO-based lead-free. Cho *et al.* [71] proposed an innovative compound with a variable thick $0.94(Bi_{0.5}Na_{0.5})TiO_3{-}0.06BaTiO_3$ thin film. Both ε_r and e_{31} values exhibited an increase as BNT-BT thickness increased. In addition, a dependence on the poling process was evidenced since ε_r decreased as the poling field increased, whereas e_{31} increased. The electrical parameters in this thin-film-cantilever device, such as the optimal power density, output voltage, and output power, were 21.2 μW/cm^2/g^2/Hz, 537.7 mV, and 2.22 μW, respectively. Everything was done at a resonant frequency of 42 Hz and a BNT-BTO thickness of 2 μm, as well as under poling conditions because in the unpoled case, its maximum power was 7.6 times lower.

Even having high piezoelectric coefficient values the above-mentioned materials, all these lead-free ferroelectric materials require high-temperature processing and poling methods to improve their piezoelectric properties. More recently, other well-known materials are being investigated for energy harvester application, such as aluminum nitride (AlN) and ZnO. Both materials have a wurtzite crystal structure, an intrinsic piezoelectric property, and an easy manufacturing process. Their electrical parameters, as d_{33}, ε_r, and e_{33}, are around 3-5 pm/V [72], 10.5, and -1.05 C m^{-2} for AlN [73], and around 2-12 pm/V [74–76], 10.9, and -1.0 C m^{-2} for ZnO [73], respectively. The above indicates that their electric properties are still much less than PZT-based and lead-free ferroelectric materials, although their values of the figure of merit are promising [73]. According to MEMS applications, He *et al.* [77] designed an AlN MEMS cantilever-based vibration energy harvester for a low frequency and an acceleration vibration environment. The performed device essentially consists of a piezoelectric cantilever beam made of AlN thin film and a proof mass. The proof mass is integrated at the free end and is made of silicon material. The desired piezoelectricity of AlN thin film can be achieved by depositing highly c-axis oriented crystallites using pulsed direct-current (pulsed-DC) magnetron sputtering at a low temperature (around 260 °C). Their experimental results show that this harvester device produced about 4.66 V in maximum output RMS voltage, 56.4 μW in maximum output average power, and 854 μW cm^{-3}g^{-2} in maximum output power density. All of them under an excitation acceleration of 1g and a frequency of 210.85 Hz. As for ZnO material, Wang *et al.* [78] proposed two designs for ZnO MEMS cantilever-based vibration energy harvesters. These piezoelectric devices consist of a ZnO thin layer deposited over a silicon substrate cantilever as well as the Si-proof mass. The first design, also called design I, has a complete ZnO layer deposited over a silicon substrate. In contrast, the second design, called design II, has two ZnO

layers in parallel position deposited on the silicon substrate with an equal ZnO size area compared to design I. In a parallel connection, design II reached a higher output potential of 2.06 V at a load resistance of 1 MΩ and a maximal power value of 1.25 μW at a load resistance of 0.6 MΩ. Regarding design I, the highest output potential of 1.77 V at a load resistance of 1 MΩ and maximal output power of 0.38 MΩ were measured using the same excitation frequency of 1.3 kHz and the same acceleration value of 1g used in design II.

b. Organic piezoelectric materials

Despite the extraordinary piezoelectric performance of mentioned harvester ceramics, their fragility in flexible electronic applications is a problem, especially in human body applications. So, new organic materials have been currently implemented to reach large deformations at low-frequency applications. Among these organic materials, PVDF and its copolymer PVDF-TrFE are frequently used since these polymer materials are eco-friendly and flexible for different tasks. This type of material can offer excellent structural flexibility, high piezoelectric coefficient, ability to couple mechanical and electric properties, and high elastic compliances. PVDF is a semi-crystalline polymer and is polymerized from its monomer. Three typical crystalline phases of PVDF are indexed as the α, β, and γ phases [79], of which β shows higher dipole moment as well as higher piezoelectric, pyroelectric and ferroelectric properties [80]. For a pure PVDF, its d_{33} is between -25 pC/N to -30 pC/N [81] and ε_r is around 12, depending on the fabrication and the poling process. As for its copolymer, it is formed by introducing the TrFE units into the PVDF to be named as poly(vinylidenefluoride-co-trifluoroethylene) (abbreviated as PVDF-TrFE). PVDF-TrFE has a β phase with high crystallinity and a more significant piezoelectric response than the pure PVDF. For instance, its d_{33} is between -30 pC/N to -40 pC/N [82] and ε_r increases up to values between 13.7 and 18 due to the improvement of β-crystal in the film [83,84].

The efforts of researchers have been lately implemented in PVDF-based nanocomposites. Khadtare *et al.* [85] prepared piezoelectric nanocomposites with 80-μm-thick PVDF piezo thin film as an active layer, sandwiching it between two hybrid electrodes as the pristine silver nanowires (AgNWs). Then a conducting polymer poly(2-hexyl-2,3-dihydrothieno[3,4-b][1,4]dioxine:dodecyl sulfate (PEDOT-C_6:DS) was deposited. An output potential of 7.02 V, an electric current of 1.11 μA, and an instantaneous power density of 0.81 μW are obtained by optimizing device frequency at 18 Hz. The piezoelectric nanocomposite stability was maintained after 20,000 repeating operation cycles. However, the efficient conversion of mechanical energy into electricity can be outstandingly enhanced when considering the

electromechanical coupling properties and using a new device geometry of piezoelectric nanocomposite. Jung *et al.* [86] designed a new geometry of PVDF-based piezoelectric nanocomposite for improving the stress/strain distribution upon curving the new flexible piezoelectric generator. All the above was possible thanks to connecting two piezoelectric nanocomposites back-to-back, with gold electrodes on both sides. The output potential of 155 V, the electric current of 700 μA, and the power density of 3.9 mW cm^{-2} were obtained using finger tapping and at a low-frequency vibration below 50 Hz.

As for PVDF copolymers, Pi *et al.* [87] developed a PVDF-TrFE-based energy harvester utilizing a simple spin-coating method. They used the gold material over the PVDF-TrFE as bottom and top electrodes. In order to enhance the piezoelectric properties of copolymer film, they performed the poling process to give a virtually permanent polarization inside of the copolymer. The piezoelectric nanocomposite yielded an open-circuit voltage of 7 V, a short-circuit current of 58 nA, and a current density of 0.56 μA cm^{-2}. In order to increase the piezoelectric response in the nanocomposites, researchers have also created new geometry strategies to take advantage of mechanical input. Yuan *et al.* [88] created a multilayer β-phase PVDF-TrFE copolymer using a low-cost 3D printing process. A multilayer around six-layer PVDF-TrFE polymer sample exhibited a high piezoelectric coefficient of 130 pC/N to be 6 times greater than a single PVDF-TrFE film. In addition, PVDF-TrFE multilayer composite is wrapped around the PDMS rugby ball to analyze vibration energy harvesting using a dynamic compression platform. The output potential of 44.3 V, the electric current of 353 μA, and the power density of 16.4 mW cm^{-2} are measured after applying an input pressure of 0.046 MPa at a low frequency of 10 Hz. Owing to the miniaturization of electronic wearable devices and ongoing technology like smart textile sensors, much experimental work has been commonly performed at a low scale in both organic piezoelectric and piezo polymers. Among these, fiber-based nanocomposites have been elaborated with PVDF material, but their output energy density values in vibrational energy application are still low [89]. Thereby, Abolhasani *et al.* [89] developed a revolutionary process to tailor the porosity in PVDF-TrFE nanofibers and thus enhance the output power. A 50-μm-thick PVDF-TrFE layer with an area of 4 cm^2 was tested after impacting a compressive mechanical value of about 0.2 MPa at a range of frequency excitation of 1 Hz to 10 Hz. The nanofibers with 45% porosity yielded an output potential of 21 V, an electric current of 211 μA, and a power density of 5.7 mW cm^{-3}. This device was benchmarked against a PVDF-TrFE device without porosity, thus achieving almost 10 times the output potential and a 500-fold increase in power density.

c. Composite piezoelectric materials

The fabrication of nanocomposites has recently been growing in popularity due to some of their features when employing micro and nano-scale materials. Among these characteristics, it can be found the piezoelectric coefficient, dielectric coefficient, electromechanical coupling factor, integrate-ability, and stretch-ability. It should be added that its efficiency is influenced by either its piezoelectric material or its structure. Nanocomposite devices are typically fabricated by combining a flexible polymer and the prepared piezoelectric material. The type of structure is constructed by sandwiching among elastomechanical conductive substrates. This flexible polymer merely serves to protect the piezoelectric material from humidity and gives robustness to the device when applying a mechanical load.

As discussed above, the traditional piezoelectric ceramic-based energy harvesters have some hurdles associated with their brittleness in applications with large deformations, thereby limiting their functionality. Therefore, the recent advancement of polymer-based piezoelectric composites [90] and piezoelectric nanocomposites [91] have been carried out with high efficiency, easy process, and low cost (see shown in Figure I-5). Among nanostructured piezoelectrics, it can be found the perovskite nanostructure-based nanocomposites, PZT nanostructure-based nanocomposites, ZnO nanostructure-based nanocomposites [92], and hybrids-based nanocomposites [93]. They have been widely investigated during the last decade for fabricating the flexible self-powered energy system. These devices have essentially included nanofibers, nanocubes, nanowires, and nanosheets because it has experimentally demonstrated enhancement of mechanical and electrical properties. In addition, the nanostructures allow obtaining a high aspect ratio and large surface-area-to-volume ratio. For instance, a common strategy consists of dispersing piezoelectric nanoparticles into a dielectric matrix for building flexible nanocomposites. However, some drawbacks can be occasionally presented as poorly dispersed nanoparticles within the matrix that do not readily form percolating networks in the dielectric matrix [94,95].

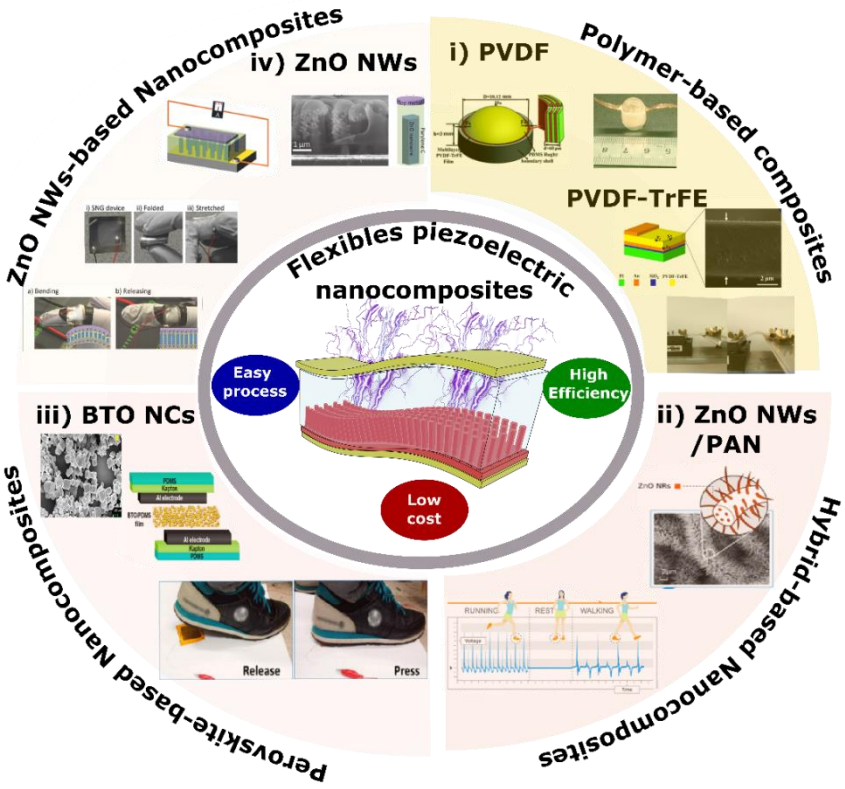

Figure I-5 Illustrative image of recent developments of flexibles composites nanogenerators such as i) polymers [87,88]*, ii) hybrids* [93]*, iii) perovskites* [96]*, and iv) ZnO NWs* [97] *materials.*

In this context, most experimental works prefer to build the ordered nanometric piezoelectric structure in order to take advantage of mechanical distribution within the dielectric matrix. Lee *et al.* [98] created a PZT nanofibres-based nanocomposite by modifying the fiber orientation. Then, they analysed the piezoelectric power response after deforming the material. The orientated nanofibers were encapsulated into a poly(dimethylsiloxane) PDMS matrix and sandwiched between two flexible indium-doped tin oxide (ITO)–PEN films. A device of 80-μm-thick PZT with 8 cm^2 in area produced an output potential of 1.1 V and an electric current of 211 μA under periodically bending and unbending motions. However, the main disadvantage is that PZT is a lead component, making it environmentally unfriendly as well as harmful to human health. Hence, its application in the field of microelectronics is limited.

In contrast, the first eco-friendly lead-free $BaTiO_3$-based nanocomposite was developed by Park *et al.* [99]. They fabricated a nanocomposite generator based on $BaTiO_3$ nanoparticles, which has been synthesized via a hydrothermal reaction and subsequently dispersed into the PDMS matrix. Afterward, they mixed it with a kind of carbon nanomaterials, such as SW/MW-CNTs and RGO, eventually reaching piezoelectric nanocomposite (p-NC). To characterise the nanocomposite of 250-µm-thick p-NC electrically, top and bottom metal-coated plastic

substrates are connected at the end side, generating piezoelectric response by a bending stage. The NCG device generated an output voltage of 3.2 V and an electric current of 350 nA under an applied strain of 0.33%. Several years later, Alluri *et al.* [96] recently produced a new piezoelectric nanocomposite that is formed by nanocubes of $BaTiO_3$ (BTO NCs). BTO NCs were synthesized using the low-temperature molten salt method and encapsulated within the PDMS matrix. Then, they used a poling process at 8 kV for 24 h at room temperature as well as two flexible electrodes of Al/Kapton. The dimensions of this piezoelectric nanocomposite device were around 16 cm^2 with a thickness of about 790 μm. Under a compressive pressure of about 988.2 Pa, the device yielded an output potential of 126.3 V, a current density of 77.6 μA cm^{-2}, and a power density of 7.6 mW cm^{-2} by employing an optimal load resistance of 100MΩ.

Despite the high efficiency of BTO nanocubes-based nanocomposite, its fabrication process requires substantially more work, such as poling process and high temperatures, to optimize its piezoelectric properties. Gallium nitride (GaN) and ZnO material are likely promising materials to fabricate the new generation of piezoelectric nanocomposites. These nanocomposites reveal a great potential in many fields thanks to a vast range of operating temperatures because its piezoelectricity does not have a phase transition, as it is occurs in ferroelectric materials. Lin et al. [100] demonstrated that GaN NWs grown at high temperature (about 900 °C) using a vapor-liquid-solid (VLS) process generated output voltage up to 1.2 V, a current and current density of 40 nA and 0.16 nA cm^{-2} under bending mode. This device was mainly composed of 5 layers of GaN NWs, and randomly dispersed horizontally, intercalated with 5 thin PMMA layers over a substrate Au-coated Kapton film. The active size of the nanocomposite was 5 mm × 5 mm. Another piezoelectric nanocomposite based on vertically GaN NW was proposed by Jamond et al. [101]. The growth process of GaN NWs was carried out by plasma-assisted molecular beam epitaxy (PA-MBE) at high temperatures between 400-760 °C. They obtained a maximum output voltage of 200 mV and an average output power density of about 6.35 mW cm^{-3} after applying lateral bending to a device of 2 cm x 1 cm with a volume of about $3.14 \cdot 10^{-6}\ cm^{-3}$. Another experimental work about GaN wires was carried out by Kacimi et al. [102]. They investigated the piezoelectric response on vertically ultralong GaN wires encapsulated within a PDMS matrix and sandwiched by two metallics electrodes. The wires were grown by employing the metalorganic vapor phase epitaxy (MOVPE) technique at high temperatures, with temperatures that can vary between 850 °C and 1000 °C [103]. Under applied pressure in compressive mode, the device with an area of 4 cm^2 delivered output potentials of about 0.4 V and 2.0 V for devices with 70 μm and 190 μm long wires, respectively. This device has shown excellent reliability and reproducibility over 1000 cycles at 1.11 Hz frequency.

As for ZnO nanowires (NWs), this nanostructured material has been commonly investigated in energy harvesters applications [104]. Its application in flexible substrates, as wearables technologies, has attracted the attention of researchers in the last year since this material has considerable potential due to its resistance to large strain. Choi *et al.* [105] proposed the first ZnO nanowire-based flexible nanocomposite using the aqueous solution method, which offers some advantages of simplicity, low growth temperature, and large-scale growth. NWs were grown on ITO-coated polyethersulfone (PES) substrate, while at the top side a palladium gold (PdAu) layer was deposited. Under a compressive force of 0.9 kgf (equivalent to 8.8 N) over an active area of 3 cm^2, an output current density of 10 μA cm^{-2} was measured. It should be noted that the ZnO NWs were not flexed to explore the NW deformation. Another experiment proposed by Hu *et al.* [106] was made by growing the ZnO NWs in both the top and bottom surfaces of a flexible polyester (PS) substrate. Then, a thin layer of polymethyl methacrylate (PMMA) was deposited on both surfaces of the PS substrate. A Cr/Au layer deposition was performed on the surface of 1 cm^2 in the area. The device produced an output potential of 10 V, a current of 0.6 μA, and a power density of 10 mW cm^{-3} under an applied strain of 0.12%. Recently, a new flexible ZnO NWs-based piezoelectric nanocomposite was developed by Dahiya *et al.* [97], encapsulating ZnO NWs into an organic material matrix, such as a parylene C. They grew ZnO NWs using a low-temperature hydrothermal growth process over an Au-coated PDMS substrate of 8 cm^2 in area. The piezoelectric nanocomposite device yielded an open-circuit voltage of 10 V, short-circuit current density of 0.11 μA cm^{-2}, and peak power of 3 μW after applying a compressive pressure of 16 kPa and using an optimal load resistance of 10 MΩ at an excitation frequency of 5 Hz. This kind of structure showed to be highly sensitive to human finger movements achieving a peak of voltage in an open circuit of 3V in finger bending. A more extensive literature review about ZnO NWs based on nanocomposite will be further assessed in section I.2.3.

As for the dimension of ZnO nanostructure, Wang *et al.* [107] demonstrated that the piezoelectric response increases significantly from a ZnO structure from 1-D NWs to 2-D nanosheets (NS) on flexible application. These 2-D ZnO nanostructures were grown on flexible ITO-PET substrates using a multi-step hydrothermal process to carry out 2-D ZnO NSs. After subjecting the device to a compressive pressure of 1 kgf over an area of 1 cm^2, ZnO NSs device generated an output current of 0.15 μA to be greater than the current value produced for 1-D NWs device (around 40 nA). Although it should be noticed that the thickness of the NSs had values between 60 nm to 80 nm to be lower than the radius values of the NWs between 50 nm to 170 nm. The mechanical input was the same for both samples.

With respect to recent progress in piezoelectric harvesters, researchers have been creating flexible hybrid piezoelectric energy harvesters by combining an inorganic nanocomposite (e.g., ZnO, BTO, PZT, etc.) and polymeric piezoelectric materials. Among polymeric piezoelectric materials are PVDF and polyacrylonitrile (PAN). In recent studies established by Choi *et al.* [108], flexible hybrid structures, such as PVDF-ZnO have shown higher electric power outputs in comparison with the flexible structures composed only of pristine PVDF. However, promising investigation work on PAN nanofiber [109] showed that their electric outputs are higher than PVDF nanofiber by subjecting to a compressive impact. So, Sun *et al.* [93] proposed a new hybrid nanocomposite using ZnO and PAN materials. ZnO/PAN flexible piezoelectric nanocomposite was carried out using electrospinning method to fabricate PAN nanofiber and a low-temperature hydrothermal growth process to create ZnO nanowires on PAN nanofiber surface. Two thin copper tapes were used as electrodes on both the top and bottom surfaces for a device with an active area of 16 cm^2. By applying an impact force of 8N at a frequency of 2Hz, ZnO/PAN-based piezoelectric nanocomposite generated an output voltage of 6.5 V, a current value of 2.3 μA, and a maximum power density value of 10.8 mW cm^{-2}. Upon comparing with a simple PAN-based piezoelectric nanocomposite, the output potential was 2.7 times higher, while its maximum power output was 6 times higher.

I.2.1.2 Summary of efficiency and performance of piezoelectric materials

A comparison of piezoelectric coefficients d_{ij} and e_{ij}, relative permittivity, and figure of merit FOM_{33} (see equation at start of section I.2.1) for a number of materials commonly used in piezoelectric harvester applications is given in Table I-2. This assessment holds for PZT, $BaTiO_3$, PVDF and its copolymer, as well as the piezo-semiconducting materials as the group-III nitrides, i.e., aluminum nitride (GaN), aluminum nitride (AIN), indium nitride (InN), and ZnO. Table I-2 shows that PZT has the best effective piezoelectric conversion compared to the other materials, and then followed by the PVDF-TrFE, PVDF, and $BaTiO_3$. An extra process as poling is particularly noteworthy because these materials require to induce and improve their piezoelectricity. The materials with intrinsic piezoelectricity as the group-III nitrides and ZnO have FOM_{33} value between 8 to 140 times lower than the PZT value, highlighting the ZnO as the best option among these piezo-semiconducting materials. However, nanostructuration opens the possibility of enhancing the electrical parameters of these materials as well as FOM_{33}. For instance, some experiments on NWs show that the dielectric constant (ε_r) is reduced as the NW diameter decreases [3].

Table I-2*: Piezoelectric properties values for different materials and piezo-semiconducting materials*

Bulk materials	Piezoelectric coefficients $d_{ij}(pC\ N^{-1}\ or\ pm\ V^{-1})$	Piezoelectric coefficients $e_{ij}(C\ m^{-2})$	Relative permittivity ε_r	FOM_{33} $(pC\ N^{-1})^2$
PZT	$d_{33} \approx$ 300 to 1000 [56]	N/A	1000 to 8000 [56]	90 to 125
$BaTiO_3$	$d_{33} \approx$ 260 to 454 [57–62]	N/A	1600 to 4000 [57–62]	42.2 to 51.5
PVDF	$d_{33} \approx$ -25 to -30 [81]	N/A	12 [81]	52 to 75
PVDF-TrFE	$d_{33} \approx$ -30 to -40 [82]	N/A	13.7 to 18 [83,84]	65.7 to 88.8
GaN	$d_{33} \approx 2.4$, $d_{31} \approx -1.2$ $d_{15} \approx -3.3$	$e_{33} \approx 0.65$, $e_{31} \approx -0.33$ $e_{15} \approx -0.3$ [110]	8.9 [111]	0.64
AIN	$d_{33} \approx 5.5$, $d_{31} \approx -2.7$ $d_{15} \approx -4.1$	$e_{33} \approx 1.55$, $e_{31} \approx -0.58$ $e_{15} \approx -0.48$ [112]	8.5 [111,113]	3.55
InN	$d_{33} \approx 8$, $d_{31} \approx -3.4$	$e_{33} \approx 0.97$, $e_{31} \approx -0.57$ [113]	8.1 to 15 [114,115]	4.3 to 7.9
ZnO	$d_{33} \approx 9.93$, $d_{31} \approx -1.34$	$e_{33} \approx 1.22$, $e_{31} \approx -0.51$ $e_{15} \approx -0.45$ [116]	8.91 [117]	11.1

Analyzing the data resulting from the explored literature in section I.2.1.1 about the different piezoelectric materials in energy harvester applications (see Table I-3), it can be seen that the inorganic PZT material reaches one of the best power densities of about 16 mW cm^{-2} in cantilever structure. Similarly, the organic material as PVDF-TrFE obtained an excellent value of power density of about 16.4 mW cm^{-2} for a multilayer generator. As for the best material with intrinsic piezoelectricity, the hybrid piezoelectric nanocomposite based on ZnO/PAN material reached a value of 10.8 mW cm^{-2} in power density. The above-mentioned power densities are coherent with the high piezoelectric coefficient for each material (see Table I-2). Note however that those precise comparisons are difficult as not all experimental works were made under the same conditions and not all data (such as dimensions and power density) are available.

Table I-3: Summary of output performances based on different piezoelectric materials

Author	Material	Dimensions	Input excitation	OPNL[1] frequency	Electrical output performance
Inorganics					
Yi *et al.* [63]	PZT thin film cantilever	0.0306 cm^3 and 6.12 cm^2.	3.5g in acceleration	77.2 Hz	The peak output voltage of 53.1 V, power is 0.98 mW, and power density are 32 mW cm^{-3} and 0.16 mWcm^{-2}.
Won *et al.* [67]	Mn-doped KNN thin-film cantilever	0. 002 cm^3 and 20 cm^2.	N/A	132 Hz	The peak output voltage of 520 mV, power is 3.62 μW, and power density are 1.8 mW cm^{-3} and 0.18 μWcm^{-2}.
Cho *et al.* [71]	BNT-BT thin-film cantilever	2 μm in Thickness	1g	42 Hz	The peak output voltage of 537.7 mV, power is 2.22 μW, and power density is 21.2 μW/cm^2/ g^2/Hz.
He *et al.* [77]	AlN thin film cantilever	50 μm in Thickness	1g	210.85 Hz	The maximum output RMS voltage is 4.66 V, the maximum output value of the average power is 56.4 μW, and maximum output power density are 854 μW $cm^{-3}g^{-2}$ and 4.27 μW $cm^{-2}g^{-2}$.
Wang *et al.* [78]	Two ZnO thin film in parallel cantilever	N/A	1g	1.3 kHz	The maximum Output potential is 2.06 V at 1MΩ, and its maximal output power is 1.25 μW at 0.6 MΩ.
Organics					
Khadtare *et al.* [85]	PVDF thin film generator	0.0072 cm^3 and 9 cm^2	N/A	18 Hz	Output potential is 7.02 V, electric current is 1.11μA, and output power is 0.81μW. Power density are 112.5 μW cm^{-3} and 0.09 μW cm^{-2}.
Jung *et al.* [86]	PVDF curved thin-film generator	0. 28 cm^3 and 28 cm^2	Tapping fingers	< 50Hz	Output potential is 155 V, electric current is 700 μA,

[1] Acronym of operational

Author	Material	Dimensions	Input excitation	OPNL[1] frequency	Electrical output performance
					and power density are 39 μW cm^{-3} and 3.9 mW cm^{-2}.
Pi *et al.* [87]	PVDF-TrFE thick film generator	0. 00058 cm^3 and 0.09 cm^2	0.943 % in stretch and release process	0.5 Hz	Open-circuit voltage is 7 V, short-circuit current 58 nA, and current density are 0.56 μA cm^2.
Yuang *et al.* [88]	A multilayer PVDF-TrFE generator	10 μm in thickness	0.046 MPa in compressive pressure	10 Hz	Output potential is 44.3 V, electric current is 353 μA, and power density are 1.64 W cm^{-3} and 16.4 mW cm^{-2}.
Abolhasani *et al.* [89]	Porosity PVDF-TrFE nanofibers thin-film generator	0.02 cm^3 and 4 cm^2	0.2 MPa in compression mode	1 to 10 Hz	Output potential is 21 V, electric current is 211 μA, and power density are 5.7 mW cm^{-3} and 28.5 μW cm^{-2}.
<u>Nanocomposites</u>					
Lee *et al.* [98]	PZT nanofibers-based piezoelectric nanocomposite	0.064 cm^3 and 8 cm^2	0.18 % of strain under periodically bending and unbending motion.	N/A	Output potential is 1.1 V, and current density is 211 μA.
Park *et al.* [99]	BaTiO3 nanoparticles-based piezoelectric nanocomposite	169 cm^2 in active area	0.33 % of strain in bending mode	2.5 Hz	The output voltage is 3.2 V, and the electric current is 350 nA.
Alluri *et al.* [96]	BaTiO3 nanocubes-based piezoelectric nanocomposite	13.3 cm^3 and 16 cm^2	988.2 Pa under a compressive pressure	10 Hz	Output potential is 126.3 V, current density is 77.6 μA cm^{-2}, and power density are 93.2 mW cm^{-3} and 7.6 mW cm^{-2}.
Jamond et al. [101]**.**	GaN nanowire-based piezoelectric generator	0.0314 cm^2	1.5 N under bending mode	1-6 Hz	Output voltage of 200 mV and an average output power density are 6.35 mW cm^{-3} and 0.6 μW cm^{-2}.
Choi *et al.* [105]	ZnO nanowires-based piezoelectric nanocomposite	3 cm^2	0.9 kgf in compressive mode	N/A	Output current density 10 μA cm^{-2}.

Author	Material	Dimensions	Input excitation	OPNL[1] frequency	Electrical output performance
Hu *et al.* [106]	ZnO nanowires with double layers	1 cm^2	0.12 % of strain in bending mode.	N/A	Output potential is 10 V, electric current is 0.6 μA, and power density are 10 mW cm^{-3} and 2 μW cm^{-2}.
Dahiya *et al.* [97]	ZnO nanowires-based piezoelectric nanocomposite	8 cm^2	16kPa in compressive mode	5 Hz	Open-circuit voltage is 10 V, short-circuit current is 0.11 μA cm^{-2}, and power peak is 3 μW and power density is 0.37 μW cm^{-2}.
Wang *et al.* [107]	ZnO nanosheets-based piezoelectric nanocomposite	1 cm^2	1kgf in compressive mode	N/A	Output current is 0.15 μA.
Sun *et al.* [93]	ZnO/PAN hybrid piezoelectric nanocomposite	16 cm^2	8 N under an impact force	2Hz	The output voltage is 6.5 V, the output current is 2.3 μA, and power density is 10.8 mW cm^{-2}.

It can be noted that polymer and composites materials provide a breakthrough solution to scavenge the mechanical energy produced by the human body because of their low operating frequency values compared to ceramics harvesters with cantilever architecture (see Table I-3). They can also operate under large displacement and produce high piezoelectric responses due to their flexibility, which is essential to recover energy from human joints, wearable electronic textiles, wearable sensors, and smart skin, as well as light sources through a new concept consisting of photo-piezo-actuators developed in the project PULSE-COM [118].

I.2.2 General properties of ZnO material

I.2.2.1 Crystal structure, polarity and growth process of ZnO

ZnO is a piezoelectric and semiconducting material that has different crystal forms as wurtzite, zinc blende and rocksalt structure [119]. Depending on the pressure conditions at ambient temperature during the formation of ZnO crystal, the wurtzite crystal structure is the most common thanks to its high thermodynamics stability [120]. Wurtzite crystal structure has a hexagonal structure (see Figure I-6(a)) that is formed by high-speed crystal growth. In addition, it belongs to the space group of C_{6v}^4 [121]. This structure consists of alternating planes of Zn2+ and O2-, tetrahedrally coordinated and stacked to each other along the c-axis. Furthermore, the

hexagonal structure exhibits six nonpolar m-plane sidewalls along $(10\bar{1}0)$ planes. It is worth mentioning that the wurtzite structure lacks the center of inversion symmetry since the crystal configuration of ZnO material is not the same after rotating the tetrahedral coordination along the y-axis by 180°, as shown in Figure I-6(b). Owing to this lack of center inversion symmetry, this kind of material presents a spontaneous polarization. It also possesses two possible polarities: the Zn-terminated (0001) polarity and the O-terminated $(000\bar{1})$ polarity [122] (see Figure I-6(b)). The polarity direction goes from the O atom toward the Zn atom for O-polar, while direction for polarity Zn-polar goes from the Zn atom toward the O atom [123]. Many properties of ZnO materials can be affected by its polarity effect, such as photoluminescence (PL) [124], the barrier height of a Schottky contact [125], the piezoelectric properties [126,127] and surface energy [128,129].

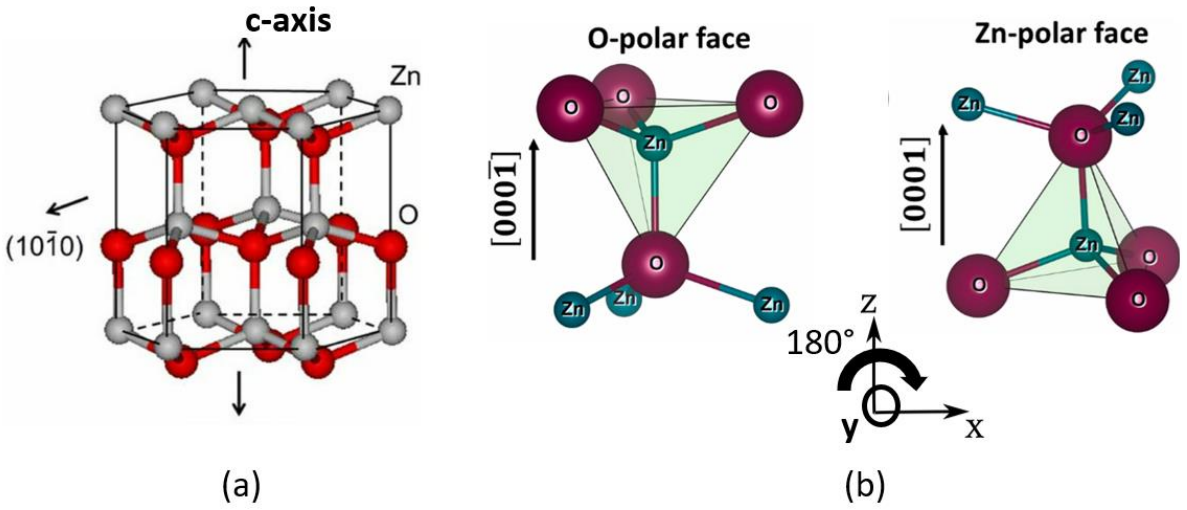

Figure I-6(a) Schematic model of the wurtzite structure for a bulk ZnO taken from [130] *and (b) schematic of the different kinds of polarity in the c-plane crystal structure taken from* [123].

As for the ZnO NWs growth process, there are still challenges for growing NWs on flexible substrates (such as PET and textiles materials) in order to fabricate the new generation of electronic devices. The aqueous solution method (also known as Chemical Bath Deposition or CBD) has been frequently used to grow ZnO NW since this method has several advantages (such as low temperature, low cost, and easy process [139–141]) in comparison with other methods such as catalyst-free physical and chemical deposition techniques. Among these techniques, we can find thermal evaporation [142], pulsed-laser deposition [143], chemical vapor deposition [144], spray pyrolysis [145], and metal-organic chemical vapor deposition [146]. Recently, few investigations have obtained experimentally polar surfaces for ZnO NWs using the CBD technique. Conssoni *et al.* [131] achieved switching from O-terminated $(000\bar{1})$

surface to Zn-terminated (0001) surface of ZnO NWs, depending on the polarity of patterned c-plane ZnO single crystals.

There are not many experimental reports which investigate the role of polarity on the piezoelectric response in ZnO materials. Although recently, Bui *et al.* [127] analysed the piezoelectric response of ZnO in the form of thin films and nanostructures grown Si substrates using pulsed-liquid injection metal-organic chemical vapor deposition (PLI-MOCVD). By increasing the growth temperature from 400 °C to 750 °C, they demonstrated that the morphology of ZnO changes from a stacked thin film to a columnar thin film. For instance, dense arrays of isolated nanowires were reached at higher growth temperatures of 700 °C and 750 °C. Using the piezoelectric force atomic (PFM) technique, they found two piezoelectric domains along with the ZnO thin film that is related to O-polarity and Zn-polarity. Their values of piezoelectric amplitude were -10 pm (in domains with O-polarity) and 12.4 pm (in domains with Zn-polarity). As for ZnO nanowires, they found only a single domain concerning the domain of Zn-polarity with a value of the piezoelectric amplitude of 21.8 pm. They concluded that the polarity issue in ZnO material is mainly attributed to the change of morphology of ZnO from thin film to nanostructure when increasing the growth temperature. Regarding their piezoelectric phase responses, which correspond to the direction of polarization of the sample, O-polar and Zn-polar domains exhibited values of -90° and 70°, respectively. It is worth noticing that the Zn-polar domain presents a more significant piezoelectric response than the O-polar domain, and also both polarities exhibit opposite polarization directions, thereby corroborating the importance of the polarity effect into ZnO materials as mentioned above.

Regarding the advantages of ZnO NWs compared with its thin-film and bulk counterparts, we can mention the ability to resist high deformation values without any fracture [132–134], the high values of Young's modulus [135,136], the high values of piezoelectric coefficient [4], and high surface-to-volume ratio. In relation with this last aspect, our team rencently demonstrated that is of great importance since electric properties can be influenced by the surface Fermi level pinning, thus enhancing the piezoelectric response [6,137]. It may be also added that the integration of vertically ZnO NWs into a nanocomposite offers advantages to improve the electromechanical coupling [138].

I.2.2.2 Piezoelectric properties of ZnO

Piezoelectricity is related to the non-symmetry of the crystal lattice and polarity effect, as was discussed above. For instance, if an external value of stress or electric field is applied over ZnO crystal, the anions (O^{2-}) and cations (Zn^{2+}) change their positions, creating a crystal dipole and a piezoelectric polarization ($\boldsymbol{P}_{pz}$), imultaneously. This polarization depends on the piezoelectric coefficient components, as e_{ki} and d_{ki} (see section I.2.1), as well as the direction of applied stress and applied electric field. As for the polarity effect, it generates an inherent polarization or spontaneous polarization ($\boldsymbol{P}_{sp}$) along the c-axis (i.e., a nonzero dipole moment per unit volume), whose value can be approximately -0.057 C m^{-2} according to ab initio calculation [139]. Therefore, the total polarization ($\boldsymbol{P}_{Tot}$) corresponds to the sum of the piezoelectric and spontaneous polarizations [140].

According to the orientation of ZnO crystal structure (i.e., Zn-polarity or O-polarity) along the z-axis, $\boldsymbol{P}_{sp}$ is positive (for Zn-polarity) or negative (for O-polarity) and $\boldsymbol{P}_{pz}$ is negative (for Zn-polarity) or positive (for O-polarity) for compressive stress. Consequently, $\boldsymbol{P}_{Tot}$ is globally affected as well as the piezoelectric response, taking into account the polarity effects.

Experimental determination of the piezoelectric coefficients for piezo-semiconducting materials is difficult due to their small value. In the literature, ZnO shows superiority in piezoelectric properties over the III-nitride group materials, as shown in Table-2 in the previous section. It should also be noted that ZnO and GaN materials have revealed theoretically giant e_{33} values when modifying their structure, as has been demonstrated in some DFT calculations [4]. Since the 2000's, piezoelectric coefficients and the crystal polarity have been further investigated using different experimental techniques, such as piezoelectric force microscopy (PFM) [76,141–145], nanoindentation [146], piezoelectric impedance measurement [75], and direct piezoelectric method [147].

The effective piezoelectric coefficient (noted here as d_{33}^{eff}) includes all possible contributions from longitudinal and transversal coefficients. It can be deduced when an electric field in the longitudinal direction (E_3) is applied to the piezoelectric material, the piezo-material extends easily for a constant value of stress. On the other hand, when a value of stress is applied to the piezoelectric material in the longitudinal direction, many charges are measured at the electrodes for a value of electric field equal to zero. Therefore, d_{33}^{eff} represents the mechanical to electrical conversion using the converse or direct piezoelectric effect. Among these techniques, the most of them utilise the direct piezoelectric method (e.g. nanoindentation and piezoelectric impedance), while PFM technique uses the converse piezoelectric method. Table I-4 shows that the converse piezoelectric coefficients $\boldsymbol{d_{33}^{eff}}$ can vary from 1.8 pC N^{-1} to 12 pC N^{-1} (or pm V^{-1})

for bulk, thin-films, and NWs of ZnO. PFM technique uses the converse piezoelectric method to carry out the measurement of $\boldsymbol{d_{33}^{eff}}$ values. According to the result, their values oscillate between 2.3 pm V^{-1} up to 11.8 pm V^{-1} at a low-frequency range of 15kHz - 40kHz for ZnO NWs. Whereas for ZnO thin films, their d_{33} values vary from 1.8 to 2.6 pm V^{-1} [76]. However, the measured d_{33} can be affected by some parasitic interactions between the AFM tip/cantilever and the sample surface, thus amplifying the piezoelectric signal as a result of the electrostatic effect [148].

Table I-4 Comparison of $\boldsymbol{d_{33}^{eff}}$ obtained from different ZnO structures and experimental methods.

Structure	Diameter (nm), length (µm), thickness (nm)	Substrate	Stiffness tip (N/m)/Frequency (HZ)	$\left\|\boldsymbol{d_{33}^{eff}}\right\|$ (pm/V) ou (pC/N)	Polarity (The sign of $\boldsymbol{d_{33}^{eff}}$)	Type of method
ZnO bulk [141]	-, -, -	-	40 / 30k to 300k	9.93	Positive	PFM
ZnO NW [142]	300, 2, -	GaN	3 / 33k	7.5	Positive	PFM
ZnO NW [143]	150, 0.6, -	Ag	40 / 15k	4.41	Positive	PFM
ZnO NW [146]	150, 2.3, -	paper/PEDOT:PSS	- / -	9.2	-	Nanoindentation
ZnO NW [144]	150, 1.5, -	Si/Au	8.8 / 40 k	11.8	Positive	PFM
ZnO NW [145]	30, -, -	Glass/ITO, PET/ITO	5 / 15k	2.13 and 5.2	Positive	PFM
ZnO single crystal [75]	5 × 5 × 5 mm³	ITO, Ag	- / -	0, 11	Positive	Impedance and direct piezoelectric measurements
ZnO Thin film [76]	-, -, 1100	Si	45 / 7k	1.8 to 2.6	Positive/Negative	PFM

The direct piezoelectric method is another alternative to explore the piezoelectricity of ZnO NWs. For instance, nanoindentation performed using the AFM instrument has provided a $\boldsymbol{d_{33}^{eff}}$ value of 9.2 pC N^{-1} for ZnO NWs[146]. It should be noted that although the experiments found

in the literature do not use the same technique, it can be said that $\boldsymbol{d_{33}^{eff}}$ is an intrinsic property either calculated by converse (pm/V) or direct (pC/N) piezoelectric techniques.

I.2.2.3 Electronic properties of ZnO

ZnO is a semiconducting material with a direct and wide bandgap of 3.34 eV at low temperature and 3.37 eV at room temperature. This conducting material also has a significant exciton binding energy of about 60 meV, making the ZnO an active material for optical devices [149]. As-fabricated ZnO nanostructure, whatever the growth technique, regularly exhibits high levels of non intentional n-type doping [121]. As ZnO material reduces its dimension, the surface-area-to-volume ratio increases, becoming more sensitive to adsorb a large amount and variety of gas molecules from the environment. Therefore, a high density of surface defects or trap density appears over ZnO surfaces, modifying the overall energy level and the electric properties [150]. Both electric properties are a technological advantage for gas sensors application [151], but they also can be a disadvantage for piezoelectric applications [152].

a. Doping of ZnO

As said above, ZnO tends to be non-intentionally n-type doped, with a concentration of donor atom N_d much larger than the concentration of acceptor atom N_a, and with an electron density $n \approx N_d^+$ (under the full ionization assumption) much larger than the intrinsic carrier density n_i ($3 \cdot 10^{-10} cm^{-3}$ in ZnO). The concentration of donors is an essential parameter to be considered for ZnO NWs-based piezoelectric applications because the range of N_d^+ in these NWs strongly depends on the growth method. Different experimental methods have been explored in the literature, which deduce some measurement values of the above mentioned semiconductor parameters. Among them, we have the field-effect (FET) measurements [153–159], I-V measurements four-terminal contacted ZnO NWs [160–165], terahertz spectroscopy [166], conductive AFM, and electrochemical impedance spectroscopy [167–169]. Figure I-7 recaps experimental data of N_d for different growth methods such as thermal evaporation (TE), chemical vapor deposition (CVD), metal-organic CVD (MOCVD), chemical bath deposition CBD with either O- or Zn-polarity, and electrodeposition. According to vapor phase deposition techniques, the ranges of N_d is between 10^{17} cm^{-3} to 5 x 10^{17} cm^{-3}, 10^{17} cm^{-3} to 10^{18} cm^{-3}, and 10^{18} cm^{-3} to 5 x 10^{18} cm^{-3} for TE, CVD, and MOCVD, respectively. On the other hand, the wet chemistry techniques lead to a higher mean N_d ranging from 5 x 10^{17} cm^{-3} to 5 x 10^{18} cm^{-3}, 5 x

10^{18} cm^{-3} to 10^{19} cm^{-3} and 5 x 10^{19} cm^{-3} to 10^{20} cm^{-3} for CBD(O), CBD(Zn) and electrodeposition, respectively.

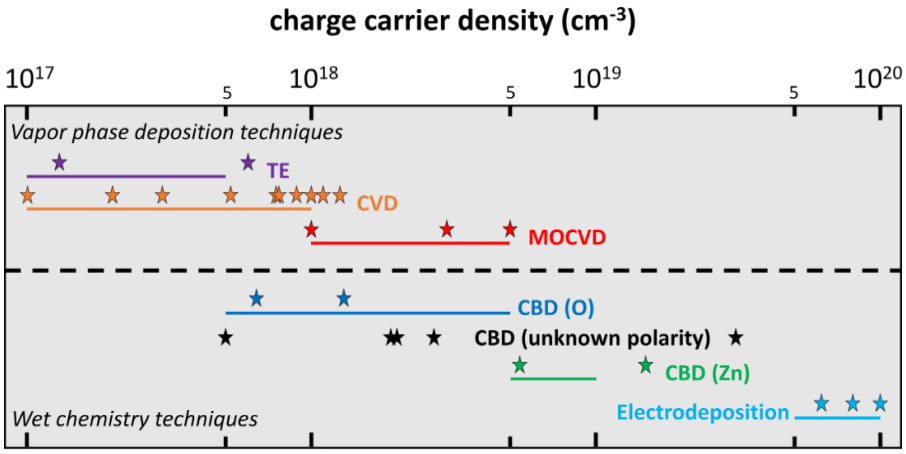

Figure I-7 Schematic diagram summarizing experimental data for charge carrier density in ZnO NWs grown by TE, CVD, MOCVD, CBD (O), CBD (unknown polarity), CBD (Zn), and electrodeposition (Figure was taken from [137]*).*

b. Surface states of ZnO

Unintentionally-doped ZnO NWs can present several atomic imperfections, also known as native defects, involving essential elements such as zinc and oxygen. Among these native defects, we found that the oxygen vacancies (V_O) and Zinc vacancies (V_{Zn}) are the most common native defects in ZnO. They correspond to host atoms (oxygen and zinc), that are missing from the crystal structure. We can find other defects such as the zinc interstitial Zn_i, oxygen interstitial O_i, the zinc antisite Zn_O, and oxygen antisite O_{Zn}, as shown in Figure I-8.

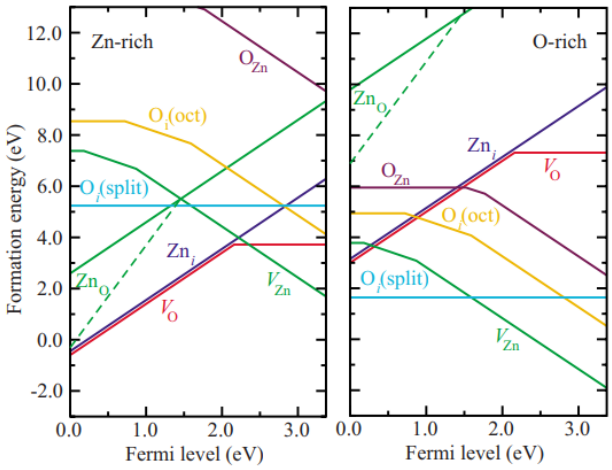

Figure I-8 Formation energy of different native point defects as a function of Fermi-level values for a ZnO with Zn-rich and O-rich conditions. Figure was taken from [170].

Janotti *et al.* [170] provide for more information concerning the native defect energetics in ZnO employing ab initio calculations. The formation energy of native points defects were calculated as a function of Fermi level corresponding to ZnO with extreme Zn-rich and O-rich conditions (see Figure I-8). It is likely that these defects are incorporated in the bulk and on the surface of ZnO NWs, modifying the electronic and optical properties. It should be mentioned that the concentration of a point defect has low values when the value of the formation energy is high at the thermodynamic equilibrium and *vice versa*. As can be seen in Figure I-8, the formation energy of V_O is quite high for n-type material (3.72 eV for the extreme Zn-rich condition). It means that the concentration of V_O is low under equilibrium condition. In addition, the author concluded that these defects act as a deep donor. As for V_{Zn}, these defects act as shallow donor with high formation energy (even is much higher than n-type material), making them unlikely to be stable under equilibrium conditions.

Overall, these vacancies or defects are experimentally expected on the surfaces of ZnO NWs. Some ab initio calculations [171] demonstrated that defects in ZnO nanowires, as V_O and V_{Zn}, strongly contribute to the optical absorption in the visible range. Many experimental efforts have been carried out to detect the presence of these kinds of defects on ZnO nanostructure. For instance, photo-/cathodoluminescence spectra have been the most used technique to evaluate these defects on ZnO nanostructure, associating the green emission in the visible spectral to transitions of V_O [172,173] and V_{Zn} [174,175]. As for ZnO nanowires, some experimental works have demonstrated more surface disorder defects compared to nanogrenades and nanoislands because of their high surface-volume ratio [176]. Other reports ascribed the green emission on PL experiment to the presence of V_{Zn} on the surface of ZnO NWs [177].

In a semiconducting material, the surface states or surface trap density plays a vital role in assessing the surface electronic properties. These surface states are formed due to the breaking of crystal periodicity with surface dangling bond generation, surface relaxation, and surface reconstruction. Additionally, these states are localized within the electronic bandgap state with a different electron density concerning the bulk part. Typically, space-charge regions can appear near the surface due to differences between the Fermi levels within the semiconducting bulk material and its surface before a thermodynamic equilibrium. In the scenario of an n-type ZnO NW (see Figure I-9), the bulk Fermi level is close to the conduction band.

In the presence of a density of traps in the band gap of ZnO, at the surface of the nanowire, a band bending occurs in order to ensure charge neutrality, with the positively charged depleted region compensating the negatively charged traps, as shown in Figure I-9. These negatively charged traps (Q_s) can be determined as:

$$Q_s = -q \cdot N_{it} \cdot (\varphi_s - \varphi_F) \qquad \text{I-5}$$

where q is the electron charge, N_{it} is surface traps density, φ_s is the surface potential and φ_F is the difference between the Fermi level and intrinsic level, as shown in Figure I-9. N_{it} parameter as well as its dependence on each growth method has not been widely investigated by experimental works. In the literature, some N_{it} values have been estimated for ZnO NWs growth by the physical vapor deposition technique to be between $2 - 3 \cdot 10^{12}\ cm^{-2}$ [178,179]. As for NWs grown by CBD method, N_{it} value has been roughly deduced from the time-resolved optical spectroscopy through the determination of the surface recombination velocity to be between $1 - 4 \cdot 10^{13}\ cm^{-2}$ [180], namely one order of magnitude compared to physical vapor deposition.

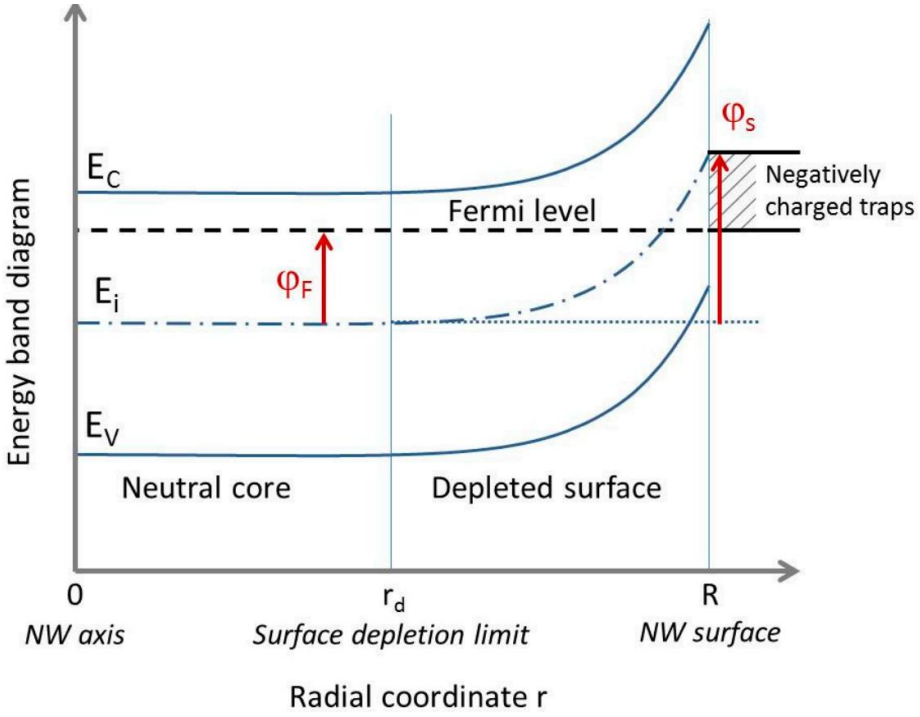

Figure I-9 Energy band diagram after thermodynamic equilibrium along half cross-section of an n-type ZnO NW. Figure was taken from [137].

I.2.2.4 Mechanical properties of ZnO

Investigation and understanding of the mechanical properties of ZnO nanostructure are significant for their applications. The most common application consists of bending ZnO nanotubes in order to rub against each other for mechanical energy harvesting [181,182]. It is also important to mention that ZnO crystal exhibits anisotropic mechanical properties since its mechanical properties differ in different directions. The mechanical response of a material is

described by elastic constants or elastic stiffness coefficients (c_{ki}) which measure the proportionality between strain (S) and stress (T) in a crystal, as long as the strain is not so large as to violate Hook's law (i.e., the linear region between stress (T) and strain (S) curve). The stress T is defined as the force per unit area, normally expressed in pascals (Pa). As for the strain S, it is a dimensionless constant that normally describes the relative displacement of the crystal (deformation).

As ZnO material is anisotropic, we have to employ the generalized Hooke's Law for a linear elastic material, where each of the stress tensor components (T_i) is defined as linear functions of the strain tensor (S_k) components as

$$T_i = \mathrm{c}_{ki} S_k \qquad \text{I-6}$$

where c_{ki} is the elastic stiffness coefficients. The matrix of stiffnesses [c] is called the stiffness matrix. The inverse of this elastic stiffness matrix ($i.e.,\ [c]^{-1}$) represents compliance matrix [s] with unit of area per newton [$m^2\ N^{-1}$]. Hence, the inverse relationship may be written as

$$S_i = s_{ki} T_k \qquad \text{I-7}$$

Generally, these equations of anisotropic elasticity are written in matrix form with 36 elements of c_{ki} and s_{ki}, respectively. It is not easy to model fully anisotropic material due to the great number of elastic constants. Since the crystal structure is symmetric, the stiffness matrix is thus reduced, obtaining only five independent elastic constants such as c_{11}, c_{12}, c_{13}, c_{33} and c_{44}. Therefore, the stiffness matrix has the following form:

$$[c] = \begin{pmatrix} c_{11} & c_{12} & c_{13} & 0 & 0 & 0 \\ c_{12} & c_{11} & c_{13} & 0 & 0 & 0 \\ c_{13} & c_{13} & c_{33} & 0 & 0 & 0 \\ 0 & 0 & 0 & c_{44} & 0 & 0 \\ 0 & 0 & 0 & 0 & c_{44} & 0 \\ 0 & 0 & 0 & 0 & 0 & \dfrac{c_{11} - c_{12}}{2} \end{pmatrix} \qquad \textit{I-8}$$

Here, the coefficients c_{11} and c_{33} represent the elastic stiffness coefficients of the crystal under normal stress, along the axis of the crystal respectively (i.e., longitudinal compression mode). As for the coefficients c_{13} and c_{12}, they correspond to the elastic stiffness coefficients of the crystal faces due to shear stresses (i.e., transverse mode). Finally, the coefficients c_{44} and c_{66} represent the torsional behavior of the crystal (i.e., shear mode). c_{66} is equivalent to $(c_{11} - c_{12})/2$.

According to the literature, the values of elastic stiffness coefficients for ZnO material are listed in Table I-5.

Table I-5. Piezoelectric and semiconducting properties of ZnO material.

ZnO properties	Symbol	Value	References
Elastic constants	c_{11}	209.7 GPa	[183]
	c_{12}	121.1 GPa	
	c_{13}	105.1 GPa	
	c_{33}	210.9 GPa	
	c_{44}	42.47 GPa	

Recent investigations have demonstrated that ZnO NWs have mechanical advantages compared to their thin film and bulk counterparts, such as the capability to withstand enormous mechanical deformation up to 6% of fracture strain without breaking the NW into two-part [2]. For example, Roy *et al.* calculated the elastic modulus of several ZnO NWs, showing a slight variation concerning the diameter of the NWs, i.e., they obtained values of 123 GPa to 154 GPa in the elastic modulus for NW diameters of 78 nm to 310 nm, respectively. Additionally, they determined the strain (S) and Young's modulus (E) in a single ZnO NW by pushing it with a tip towards the direction of the substrate surface (as pointed at the black arrow in Figure I-10(a,b)). This S value can be easily calculated knowing previously the diameter of ZnO as well as the minimum value of the radius formed by the arc of the curvature (R_{min}) after applying strength (T) over ZnO NW, as shown in Figure I-10(b). Corresponding transmission electron microscopy (TEM) analysis revealed that S was around 4.1 % ± 0.4 % for a T value of 5.8 ± 0.6 GPa prior to fracture for a 165 nm wide NW. Thus, E was about 140 GPa. They also showed that the strain fracture increases from 2.1% to 6.0% as the diameter decreases from 316 nm to 114 nm. The above glitters the idea of the durability and robustness of nanowires and how they can be enhanced via fabricating smaller-sized nanowires to maintain their fatigue-free nature.

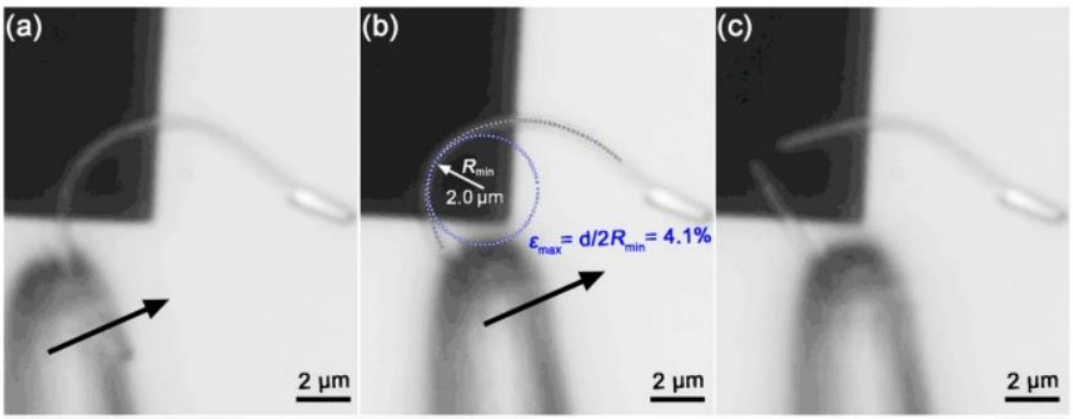

Figure I-10 Optical images of a ZnO NW's subjected to bending strain force. The black arrows in (a,b) point out the direction of the push. The dotted line circle indicates the curvature of the most bending shape of the ZnO NW right before fracture. Figure was taken from [2].

I.2.3 ZnO NWs-based on energy transducer nanocomposites

In 2006, Wang *et al.* [184] were the first to propose a mechanism to convert mechanical deformation into electric potential using ZnO NWs, i.e., harvest energy from the surrounding environment. They measured a generated voltage of around 8 mV and output power of 0.5 pW deforming a single ZnO NW using an Atomic Force Microscopy (AFM) tip probe. During the following 4 years, a hybrid nanocomposite consisting of zinc oxide nanowires grown radially around textile fibers was elaborated by Qin et al. [185], thus opening the possibility of fabricating the new generation of textile technologies. However, this kind of structure has been less explored currently. The most common nanocomposite structures have been the laterally integrated nanogenerators (LINGs) (see Figure I-11(a,b)) and the vertically integrated nanogenerators (VINGs), as shown in Figure I-11(e,f). Xu *et al.* [186] built LINGs composed of lateral ZnO NWs and sandwiched by two Au electrodes, as depicted in Figure I-11(a,b). Simultaneously, they developed VINGs by growing NWs on Au-coated Si using a low-temperature hydrothermal growth method (i.e., CBD method). Consequently, a layer of PMMA is deposited over the vertically NWs through the spin-coating technique to give mechanical robustness to the structure and avoid possible short-circuiting between the bottom and top electrodes. An oxygen etching process was made to remove the PMMA material over the tip of the NWs, as shown in Figure I-11(e). Finally, a deposition process was carried out to contact a platinum electrode with the NWs to former a Schottky barrier, as depicted in Figure I-11(f).

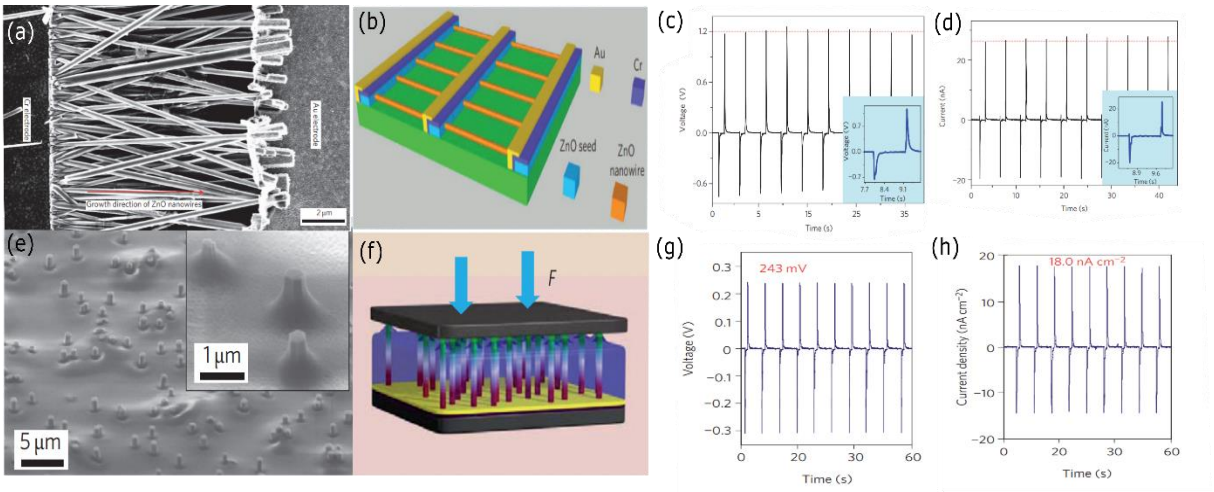

Figure I-11 SEM, schematics, and electrical output images of the (a-d) LING and (e-h) VING. Figures were adapted from [186].

In the case of LING, the substrate was bent producing a tensile strain in the NWs and, in turn, some electrical signals, as displayed in Figure I-11(c,d). They applied a cyclic external force to the flexible substrate producing a strain value of 0.19% over the sample. The LING produced a maximum peak of output potential of 1.2 V and a current pulse of 26 nA. As for VING, the force of 6.25 MPa was applied uniaxially to compress the NWs along the c-axis (see Figure I-11(f)). Three VINGs devices exhibited output potentials of 80 mV, 90 mV, and 96 mV, and current density values of 6.0, 3.9, and 8.9 $nA\ cm^{-2}$. A maximum output potential value of 0.243 V and a current density value of 18 $nA\ cm^{-2}$ were also reached for a serial connection between those three VINGs, as illustrated in Figure I-11(g,h). At first glance, LING demonstrated a better performance than VING devices, perhaps because the LING structure takes better advantage of mechanical energy to convert it into electricity. However, its significant disadvantage is related to its complex manufacturing process and high-tech equipment used to deposit and contact all NWs lying laterally on the substrate. Consequently, the VING structure became the better option thanks to its easier fabrication at a large scale and low cost.

I.2.3.1 Experimental works about VINGs based on ZnO NWs

During the last two decades, scientists have extensively explored the VINGs structures for harvesting bending (see Figure I-12(a,b)) and compressive (see Figure I-12(c,d)) mechanical energy. The design of the VING device has become a crucial aspect of increasing its efficiency. Efficiency assessments have been carried out by measuring the output potential in open-circuit condition or with a load resistance. The current density is usually measured in short-circuit conditions. In order to develop useful power value when the device is compressed or bent, these devices are fabricated with Schottky junction, insulator junction, or p-n junction at least on one side of the nanowire.

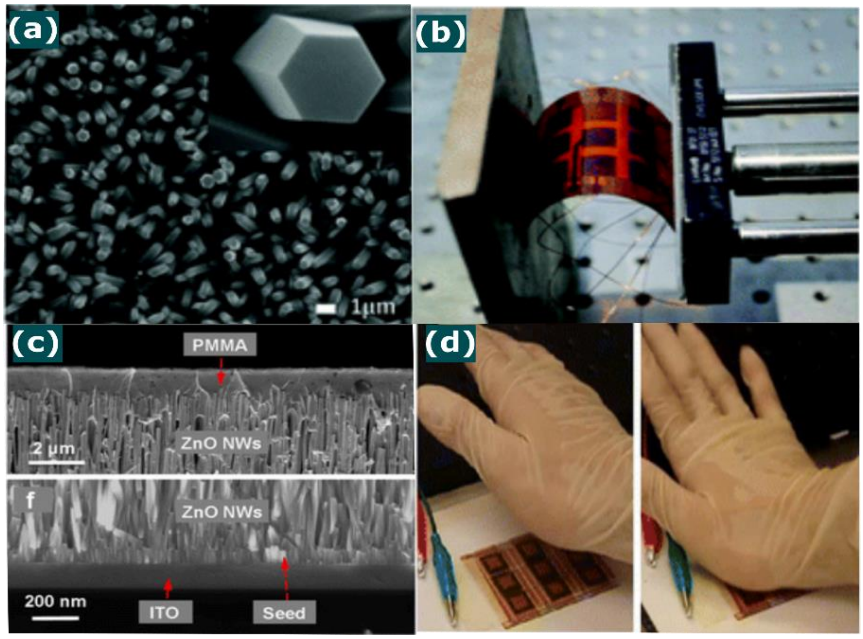

Figure I-12 SEM images of vertical ZnO NWs and mechanical mechanism for (a,b) bending (Figures were taken from [187] *and (c,d) compressive mode (Figures were taken from* [188]*).*

a. VINGs with Shottky junction

In the literature, there have been many experimental works to harvest the mechanical energy on VINGs. For instance, Yu *et al.* [189] developed a single VING and another with nine individuals NGs connected mixing parallel and serial ways. Each VING was contacted to a piece of polyethylene terephthalate (PET) coated with titanium (Ti) and gold (Au) layer electrode with the top tip of NWs to create a Schottky barrier. VING device integrating 4µm long and 400nm wide ZnO NWs in a polymer matrix (PMMA) produced about 64 mV in output potential, 2.5 nA in output electric current, and 0.31 nW cm^{-2} in output power density by subjecting an unmentioned compressive force. While the optimized VINGs of nine individuals ZnO NGs generated an output potential of 150 mV, a current value of 7.2 nA (i.e., three times that of single VING), and output power density around 2.8 nW cm^{-2} (i.e., nine times that of single VING). Subsequently, a flexible VING was built by growing the ZnO NW over a Phynox[2] metal alloy substrate coated with Chromium (Cr) and Au layer. By removing the PMMA material over the top surface of ZnO NWs and putting a Kapton film coated with Cr and Au layers, an output potential of 930 mV was achieved for ZnO NWs with 170 nm wide and 3µm long by applying fingertip impacts [190].

[2] This is a material composed by Cobalt-Chrome-Nickel alloy.

b. VINGs with insulator junction

Afterwards, another type of VING flexible structure was constructed with five-layer structures. ZnO NWs were grown on both sides of a polyester film substrate coated with Cr layers. Then a 2-μm thick PMMA layer was deposited over the ZnO NWs and then followed a Cr/Au layer on the top surface as the electrode of the nanocomposite. The Schottky contact was replaced by the dielectric material layer between the NWs and the top electrode by what researchers called a sandwich structure or insulator junction. Under an applied strain of 0.12% over nanocomposite, an output potential and electric current were generated of about 5V and 300 nA, respectively [191]. Another sandwich structure used a photolithography process to order ZnO NWs array into squares with narrow spacing between them. Their NWs were grown over silicon substrate coated with an ITO electrode. Following that, an aluminum (Al) film was deposited as a top electrode and packaged in another layer of PMMA. After applying a compressive force of around 1 MPa, the device generated peaks of potential and current of about 37 V and 12 μA, respectively [188]. In order to reproduce the high efficient value obtained in this kind of sandwich structure, our group fabricated the same VING structure reported by the previous experimental work. This VING device generated an output potential of about 290 mV and an output power density of 85 μW cm^{-3} under a compressive force of 1.5 N (equivalent to 15 kPa) for NWs with 3 μm long and 300 nm wide [192].

To take better advantage of mechanical energy on this VING device, Lin *et al.* constructed [193] the first transparent and flexible piezoelectric nanogenerator, growing the ZnO NWs over a PDMS thin film and then encapsulating them into a PMMA matrix. Two ITO electrodes were used on the top and bottom sides to contact it. Thanks to the PDMS thickness of around 200 μm, it was possible to bend the VING device using a linear motor, with strain values up to 0.12%, thus producing output potential values of 8 V, current values of 0.6 μA, and a power density of 5.3 mW cm^{-3}. Recently, Deng *et al.* fabricated a flexible tactile sensor based on ZnO NWs. They used a Kapton substrate coated with a copper (Cu) layer to grow NWs and encapsulated the NWs with PMMA. Next, they deposited another Cu layer on the top surface of PMMA and packaged the whole device with PDMS to provide mechanical support. All electrical outputs were evaluated under a compressive and bending test bench. The piezoelectric sensor exhibited a output potential of 350 mV and a current value of 1.2 nA under a uniaxial mechanical load of about 1MPa. As for the bending test bench, the sensor produced 270 mV in output potential and 0.3 nA in current for a squeezing distance of 15 mm [187].

Other works have fabricated flexible VING devices by changing the dielectric material or insulating layer (i.e., PMMA layer) on the top surface of ZnO NWs [97,194–196]. For instance,

Opoku *et al.* [194] built a VING device with ZnO NWs grown on seedless Polyethylene Naphtholate (PEN) substrate. Next, they deposited a 7μm thick PDMS polymer matrix over the ZnO NWs. One end side of the VING device was fixed onto an aluminium block and the opposite side was left free to be deflected. A constant distance of deflection value between 3 mm to 4mm was maintained at the unclamped part of the flexible nanocomposites to produce a piezoelectric voltage pulse of 22 mV, a density current of 5.5 μA cm^{-2}, and an output power density of 288 nW cm^{-3}. Later, Dahiya *et al.* [97] built a VING device with PDMS as a substrate (with around 250 μm in thickness) coated with Pt electrode. They grew ZnO NWs using a seed layer and immerged them into an organic matrix called parylene C. For devices with NWs of 50 nm in diameter and 0.5 μm in length yielded a peak voltage of 10 V, a current density of 0.11 μA $cm^{-2,}$ and a power value of 3μW after subjecting it a compressive force of about 100 kPa. Recently, the same group cited above also analysed the effect of the electrode deposited on the PDMS in the VING (i.e., the bottom electrode). They maintained the same structure except for the electrode below the ZnO seed layer, replacing it with Au and ITO electrodes. They obtained voltage peaks of 6.8 V, electric current values of 28 nA in short-circuit conditions, and power values of 64 nW for ITO electrode, and 3.9 V, 15 nA, 29 nW for Au electrode at a high load resistance (around 100 MΩ), respectively. Everything was obtained under a compression force of 3 N for VING devices with 70 nm wide and 700 nm long NWs [195].

c. VINGs with p-n junction

Smart textiles have recently attracted interest in the scientific community for exploring the piezoelectric energy harvesting device which can harvest mechanical energy from human motion. A new revolutionary textile nanogenerator device based on ZnO NWs has been developed by He *et al.* [196]. Using CBD method, they grew ZnO nanorods (NRs) on a rectangular Cu/Ni coated polyester textile, as shown in Figure I-13(a-c). They used the copper thiocyanate (CuSCN) to cover all NRs and passivate them, thus suppressing the surface-induced free mobile carriers [197]. Next, a conductive polymer called PEDOT:PSS is deposited on the top surface of NRs to create a p-n junction, as depicted in Figure I-13(d). This textile nanogenerator yielded a voltage peak of about 5 V and an output power density of 0.7 μW cm-2 under impacting force on the device. They also demonstrated that output potential values increase as the ZnO length increases. For instance, three samples with different NRs length values of 2.3 μm, 3.9 μm, and 5.9 μm obtained output potential of about 0.43 V, 0.66 V, and 1.32 V, respectively.

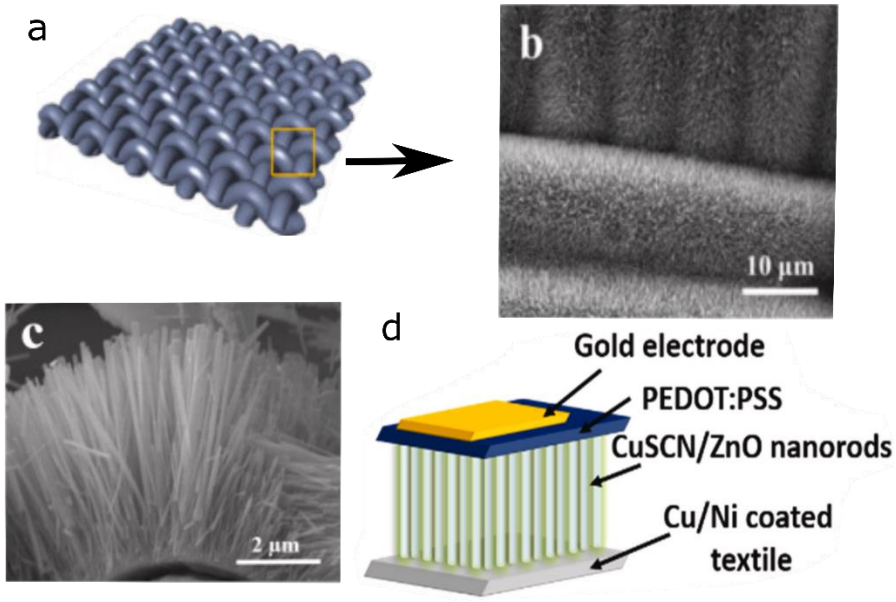

Figure I-13 (a) Schematic image of textile nanogenerator based on ZnO NWs, SEM images of NWs over Cu/Ni coated textile (b) low-magnification and (c) high-magnification of the cross-section and (d) representation of the complete textile nanogenerator. Imagen adapted from [196].

To sum up, all previously explored electrical parameters shown two different groups, corresponding to the VINGs with high output voltage values (about a few volts) and others with lower voltage values (about a few millivolts), as listed in Table I-6. It must be that they do not have the same geometry (i.e., the exact size of ZnO NWs), the same force (either bending or compressive), and neither the same structure, although then differences are not too huge. Therefore, we can intuit that more parameters could play an essential role in explaining the high and low efficiencies of VING devices, such as the semiconducting properties related to the doping level (N_d) and free carriers inside ZnO NWs.

Table I-6 Summary of the electrical output of VING devices based on ZnO NWs for different structures.

Dielectric matrix	NW diameter	NW length	Applied pressure	Output voltage	Output current	Power	Ref.
PMMA	150nm	4µm	6.25MPa (compression)	90mV	3.9nAcm^{-2}	N/A	[186]
PMMA	400nm	4µm	Compressive force	45mV	2.5nA	0.31nWcm^{-2}	[189]
PMMA	170nm	3µm	Fingertip impacts	930mV	N/A	N/A	[190]
PMMA	75nm	2µm	0.12% strain	5 V	300nA	N/A	[191]
PMMA	N/A	N/A	1 MPa (compression)	37V	12 µA	N/A	[188]
PMMA	250nm	6µm	0.12% strain (bending)	8V	0.6µA	5.3mWcm^{-3}	[193]

Dielectric matrix	NW diameter	NW length	Applied pressure	Output voltage	Output current	Power	Ref.
PDMS	115nm	0.97µm	Deflection of 3-4mm (Bending)	22mV	5.5µAcm^{-2}	288nWcm^{-3}	[194]
PMMA	50nm	600nm	1 MPa	350mV	1.2nA	N/A	[187]
PMMA	100nm	3µm	5 kPa (Compression)	290mV	N/A	85µWcm^{-3}	[192]
Parylene C	50nm	500nm	110 kPa (compression)	10V	0.11µA cm^{-2}	3µW	[97]
Parylene C	70nm	700nm	3N compression	6.8 V	28 nA	64nW	[195]
PEDOT: PSS	150nm	2µm	Impacting force	5V	N/A	0.7µWcm^{-2}	[196]

I.2.3.2 Sensor based on ZnO NWs

The electromechanical transducer can be used as a sensing system or mechanical energy harvester, as shown in Figure I-14. An electric sensor involves recollecting and exchanging information between the physical device and the energy source through sensor networks or energy-harvesting technology with specific functionalities. The revolutionary idea of the new generation of sensors is to collect information and operate in an independent manner. Namely, the sensor must serve as a sustainable power source itself or at least recharge a battery when the sensor is connected to it.

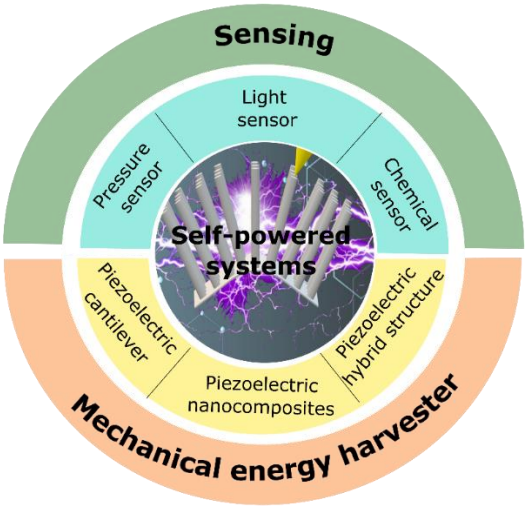

Figure I-14 Diagram of different types of self-powered systems based on the mechanical transducer which will be considered in this section.

There are many studies about self-powered portable sensing platforms of which piezoelectric transducers have been widely investigated in the last years for developing strain, light, and chemical sensors.

a. Strain sensor

Novel sensing technologies are being currently thought of as a system with multi-functionality. In collaboration with Georgia Tech, our group has successfully fabricated an ultrathin flexible VING as self-powered sensor device for detecting localized deformation (i.e., strain) on a human skin [198]. ZnO NWs were grown over a ultrathin Al-foil coated anodic aluminium oxide (AAO) layer, which works like blocking layer for electron transport among ZnO seed layer and Al electrode, as illustrated in Figure I-15(a) and 15(b). Under compressive and tensile strain (see Figure I-15(c)), the sensor device is capable of generating the piezoelectric potential, demonstrating its capability to work as an active strain sensor.

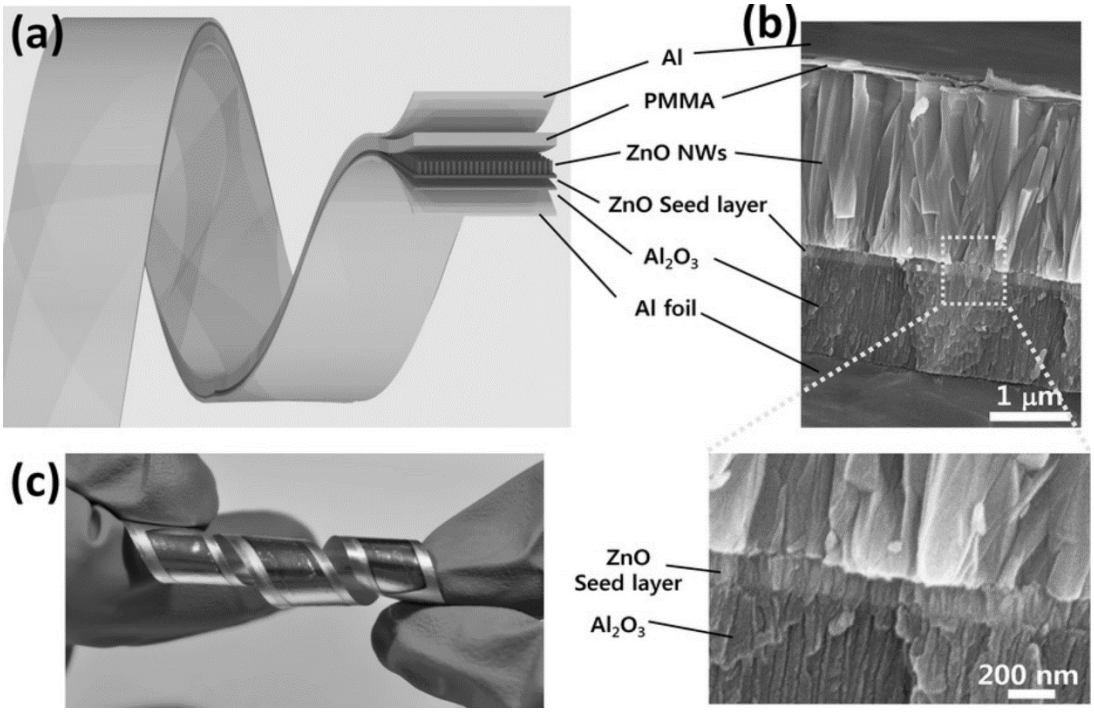

Figure I-15 (a) Schematic of flexible VING device based on ZnO NWs array for skin sensor applications. (b) A cross-section SEM image of flexible VING device. (c) Optical image of VING device after subjecting to twist deformation. These figures were taken from [198].

With this in mind, piezoelectric semiconducting materials have been extensively considered as candidates for fabricating the innovating sensing device thanks to their piezotronic effect. This effect was first proposed by Wang's group [199] in 2008. They discovered that electric current flowing across the metal-ZnO nanowires (NWs) -metal structure is controlled through input mechanical strain or piezoelectricity of NWs [200]. In other words, the piezoelectric properties work like a gate component making the analogy with the transistors mechanism. They also observed that the current decreases as the bending force increases for a sweep of voltage from

−5 to 5 V [200], as shown in top plots in Figure I-16. Additionally, they developed a force sensor in the nanonewton range for all measurement results.

Zhou *et al.* [201] reported a fully packaged strain sensor based on a single ZnO piezoelectric wire placed over polystyrene (PS) substrate and connected two silver contacts at the end sides, as depicted in the bottom plots in Figure I-16. The strain sensor showed Schottky contacts with different barrier heights, and I-V electric characteristic exhibited high sensitivity under strain action. One of the end sides was constrained to move, while the free end one was subjected to lateral force to compress or stretch one lateral face of the wire. Depending on the type of force, the current decreases and increases, as happens for compressive and tensile, respectively. They found a linear relationship between the barrier height and the applied strain and associated it with the combination of the piezoelectricity and strain-induced changes in the band structure.

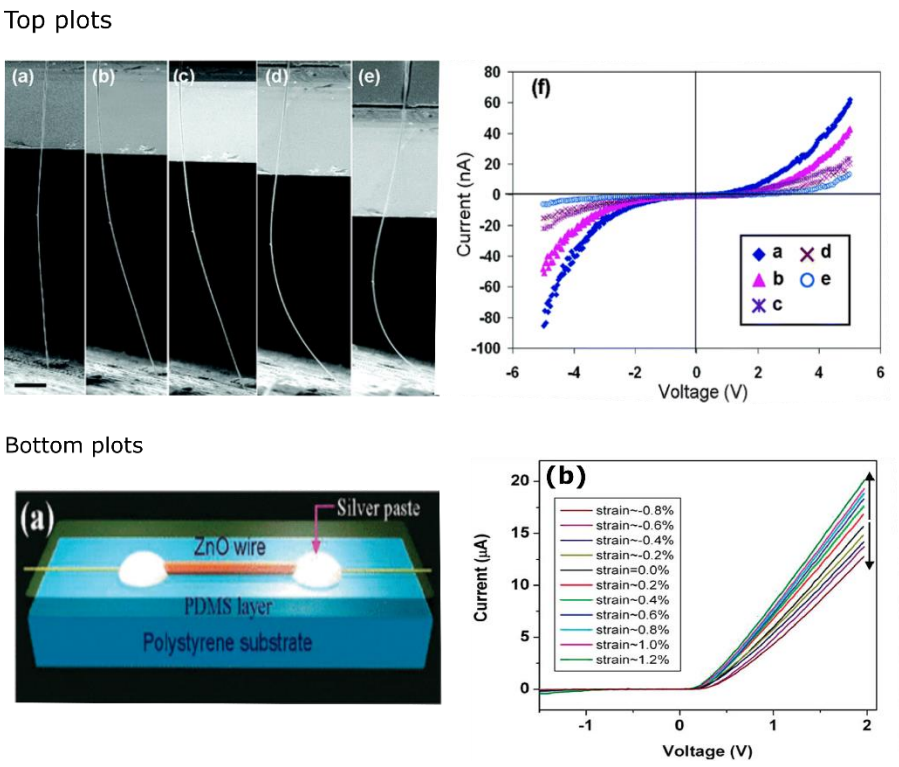

Figure I-16 Piezotronics effect on (top plots) a single piezoelectric ZnO NWs under a compressive force [200] *and (bottom plots) a flexible sensor device under compressive and tensile force* [201].

b. Light sensor

Another piezoelectric sensing system consisting of the piezo-phototronic effect combines piezotronics with the photon excitation mechanism. Mainly, the generated polarization charge formed at an n-p junction after a mechanical stimulus may modify the photo-induced

mechanism without taking into account other optical processes, such as electron-hole pair generation, separation, and recombination. Pan *et al.* [202] fabricated a light-emitting sensor using vertically aligned ZnO nanowires (NWs) arrays, as shown in Figure I-17 (a-c). Basically, the ordered NWs were grown over p-GaN film to form a p-n junction, which is responsible for the photo emission mechanism. Subsequently, the NWs were encapsulated into a polymethyl methacrylate (PMMA) matrix exposing the tips of the NWs. Next, a thick layer of indium-doped tin oxide (ITO) was deposited at the top surface of NWs to contact the sensor device with the external circuit. The light-emitting device was tested applying pressure over the top surface with an engraving mold of the word "PIEZO", while a bias voltage of 5 V is used to obtain an emission spectrum (see Figure I-17(d)). A charge-coupled device (CCD) was used to analyse the image pixel by pixel. First, a background signal was recorded at zero applied strain, as depicted Figure I-17 (f). Then, this was compared with the light-emitting image at the applied strain of -0.15%, showing an enhancement of the emission intensity of 300% for each pixel (see the bottom image in Figure I-17(f)). In conclusion, this work demonstrated the piezo-phototronic effect for the development of the next generation of touchpad equipment, electronic skin, and wearable electronic devices.

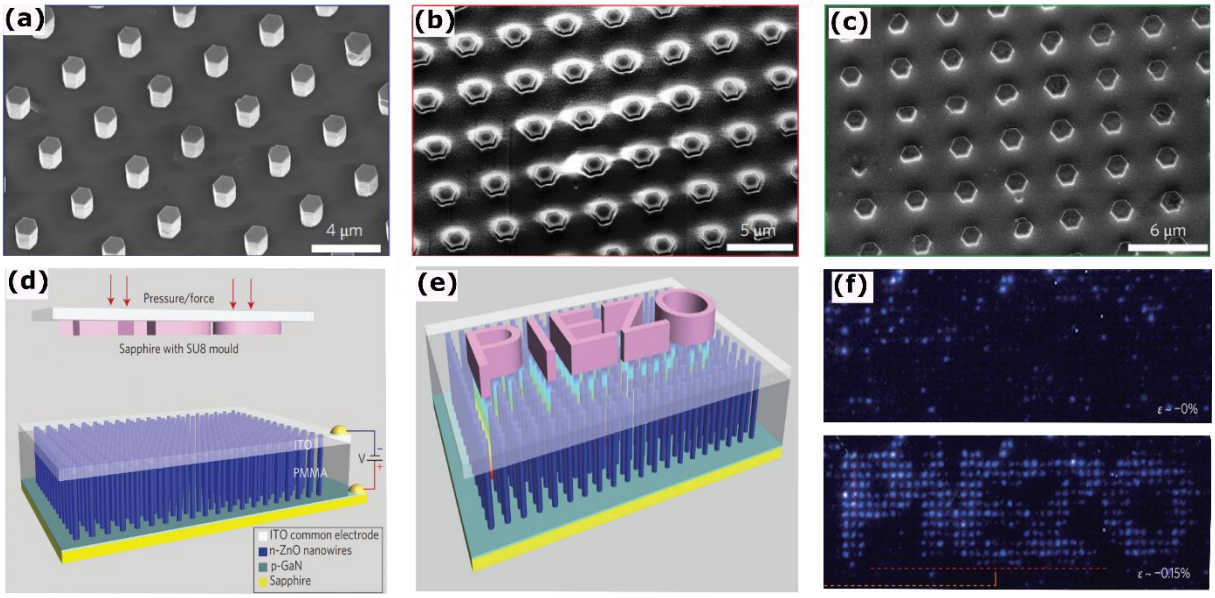

Figure I-17 SEM cross-section images of ZnO nanowire arrays grown (a) on p-GaN film; (b) encapsulated into PMMA with exposed tips after etching and (c) after ITO deposition. (d) Schematic of the device during test procedure after (e) applying a pressure using a mold with the word "PIEZO". (f) Experimental electroluminescence images of the device at the strain of 0% and 0.15 % [202].

c. Chemical sensor

In addition to the two above-mentioned sensors, Hu *et al.*[203] developed a humidity sensor based on a single ZnO microwire (see Figure I-18(a)), forming Schottky contacts by contacting the tips ends with metal as shown in Figure I-18(b, c). They bent the sensor device inside a humidity chamber to control the humid air when applying compressive strain (see Figure I-18(d, e)). They measured the I-V curves by sweeping the bias voltage from -3 to 3 V, evaluating the humidity and piezotronic effects. Without any strain value (see Figure I-18(f)), they observed that the current decreases as the relative humidity (RH) value increases, associating this effect to the intrinsic defects into the ZnO material. These defects play an essential role in its conductivity. Additionally, they observed that the current increases as the compressive strain values increase for a fixed value of RH, as depicted in Figure I-18(g), thereby demonstrating the piezotronic effect. This work supplied valuable information about enhancing sensor sensitivity to increase from 300% to 1240 % in responsivity when rising from 0 to -0.2 % the strain value at the low humidity values.

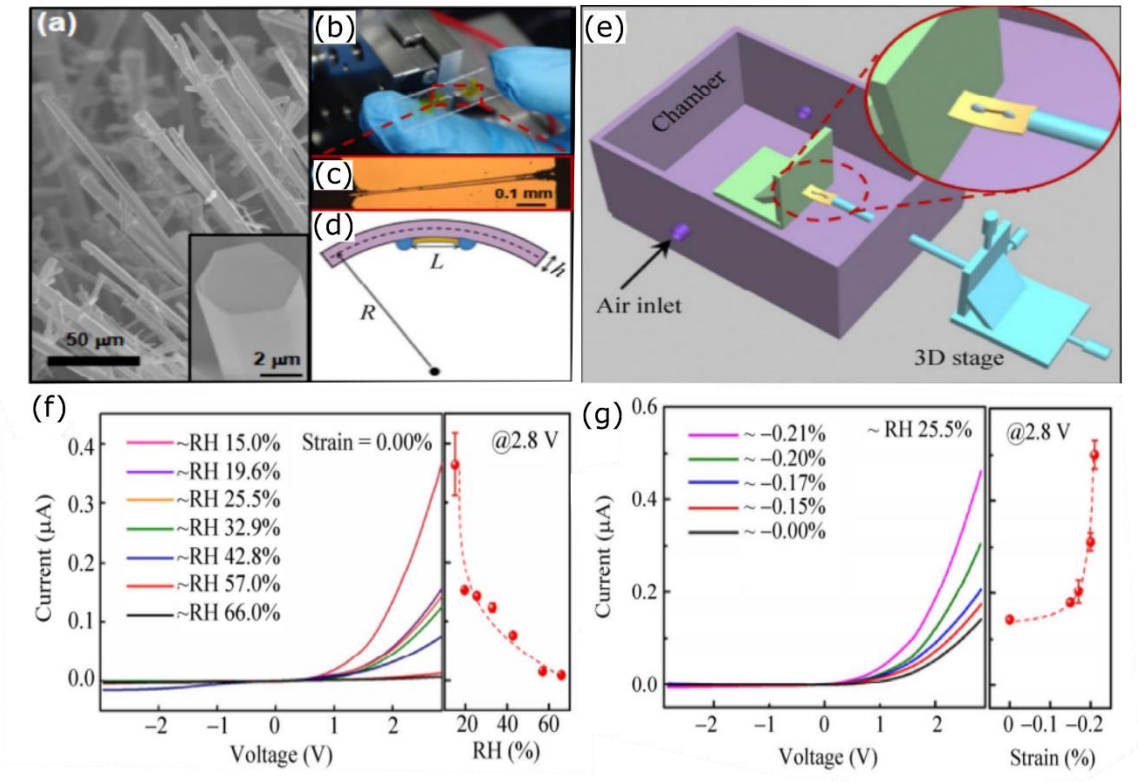

Figure I-18 SEM image of ZnO microwires grown by the vapor-liquid-solid method. b) Visual view of the humidity sensor device. c) Microscopy picture of the sensor with a single ZnO microwire. d) Schematic of the bending sensor and e) measurement set-up under a compressive strain. f) I-V curves of the humidity sensor for different relative humidity (RH) values with a constant strain value of 0% and g) for different strain values with a constant RH value of 25.5%. Figures were taken from [203].

These demonstrations evidence that apart from piezoelectric properties (as was discussed in the previous sections), there are more effects as piezotronic and piezo-phototronic, which can be taken into account in the next generation of electromechanical transducers dedicated to sensors devices. In addition, these promising properties enhance the sensing resolution and provide an alternative way to build self-powered device systems.

I.2.4 Numerical simulation of piezo-semiconducting ZnO NWs

Most of the numerical simulation works have considered the ZnO NWs as a piezoelectric and insulating material, namely, the semiconducting properties, as the free carriers and trap density, have been not taken into account in their studies [102,204–211]. On the other hand, there are some works of which have added the semiconducting properties, at least the free carriers, on the ZnO NWs to study the piezoelectric response [6,211–214].

Since 2007, analytical and numerical simulations have been proposed to study the piezoelectric response (i.e., the output potential and electric charge distribution) after applying any deformation on ZnO NWs. Two investigated scenarios, such as NW under the lateral bending force and vertical compressive force, have been the most investigated.

I.2.4.1 Lateral bending force on a single ZnO NW model

The first theoretical work consisted of an analytical model using the perturbation theory to calculate the piezopotential when bending a ZnO NW at the top [215] (see Figure I-19(a)). This analytical model considers the mechanical conditions (see equation I-9) and without free charge inside the charge density term (ρ_e) (see equation I-10):

$$\nabla \cdot \mathrm{T} = 0 \qquad \text{I-9}$$

$$\nabla \cdot D = \rho_e = 0 \qquad \text{I-10}$$

where D, T are the stress and the electric displacement vector, respectively. The fully coupled constitutive equations are expressed in terms of elastic coefficient (c_{pq}), strain (S_q), electric field (E_k), piezoelectric coefficient (e_{kp}), and dielectric constant ε_{ik}. They are defined as

$$\begin{cases} \mathrm{T_p} = \mathrm{c_{pq}S_q} - \mathrm{e_{kp}E_k} \\ \mathrm{D_i} = \mathrm{e_{iq}S_q} + \varepsilon_{\mathrm{ik}}\mathrm{E_k} \end{cases} \qquad \text{I-11}$$

By comparing the same order of perturbation and solving until the first order, Gao *et al.* [215] obtained the decoupling and coupling between the electric field and mechanical deformation given by

$$\begin{cases} T_p^{(0)} = c_{pq} S_q^{(0)} \\ D_i^{(1)} = e_{iq} S_q^{(1)} + \varepsilon_{ik} E_k^{(1)} \end{cases} \quad \text{I-12}$$

Here superscripts represent the orders of perturbation, and the zeroth-order corresponds to the physical scenario of entirely mechanical deformation (see equation I-12).

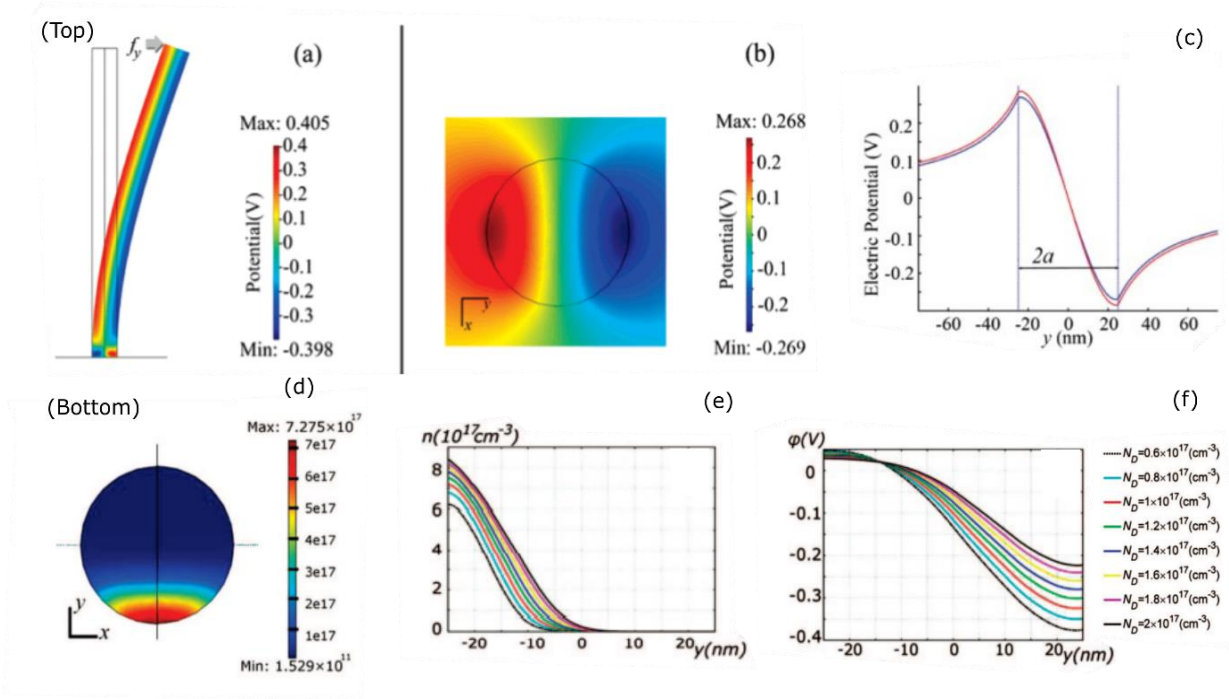

Figure I-19 Piezopotential distribution of (a) whole lateral side of NW, (b) cross-section, and (d) along the y-axis at the top surface of a single ZnO NW with 50nm in diameter and 2μm in length after applying a lateral force on the tip. All the Top figures correspond to the model without the free carrier [215]. *Free carrier distribution of the (e) cross-section of a single ZnO NW with 50nm in diameter and 600nm in length after applying a force of 80nN. (e) Free carrier values and (f) piezopotenital values along the y-axis for different doping level values at the top surface* [212].

In contrast, the first order involves the direct piezoelectricity, where the strain-stress generates the electric field in the NW. In order to calculate the potential at the surface of NW, they used equation I-10, assuming a cylindrical shape with a uniform cross-section of diameter 2a and length l, as shown in Figure I-19(b). For a lateral force of about 80 nN (i.e., a lateral deflection of 145 nm), the NW generated a potential distribution of $\pm 0.28\, V$ along the top surface, as illustrated in Figure I-19(c). Additionally, they demonstrated that the analytical solution under the first-order approximation (red curve in Figure I-19(c)) has a good match with the results obtained from the full numerical simulation using the finite element method (FEM) (curve blue in Figure I-19(c)).

However, the ZnO semiconducting material has a significant amount of free electrons and, even more importantly, the unintentionally doped ZnO NWs are generally n-type due to the growing

process. The Lippman theory in which the conductivity can be negligible for piezoelectric NW is not enough to describe the generated potential on n-type ZnO NWs. Two years later, Gao *et al.* [212] introduced the free carrier into the ZnO by considering the doping level N_d parameter into the ZnO material. They included this parameter modifying the Gauss'law and remaining the same constitutive piezoelectric equations. The new Gauss'law is defined as

$$\nabla \cdot D = \rho_e = e\, N_d^+ - e\, n(r) \qquad \text{I-13}$$

Where $n(r)$ is the electron concentration in the conduction as a function of space coordinates and N_d^+ is the ionized donor concentration. They assumed that n-type ZnO NWs have a range of N_d^+ around of $10^{17} cm^{-3}$ and solved the nonlinear partial differential equations using FEM simulation. Figure I-19(d-f) show that the free carrier distribution and piezopotential (φ) are unequally distributed at the surface of NW. They concluded that the compressed side of the NW is largely depleted (i.e., with lower n values as shown in Figure I-19(d,e)) and maintains the same negative piezopotential value at the lowest N_d, as shown in Figure I-19(f). In contrast the stretched side of NW accumulated the electron charge, reducing the positive potential as a consequence of the partially screened effect by free charge. In this simulation work, the authors concluded that piezopotential value is completely neutralized for $N_d > 10^{18}\ cm^{-3}$.

I.2.4.2 Compressed uniaxial force on a single ZnO NW model

Romano *et al.* [214] were the first to develop a numerical simulation model for a single ZnO NW under compressive mode including as well semiconducting properties. This simulation consisted of a seedless ZnO NW with a radius of 150 nm and a length of 4 μm surrounded by air, as shown in Figure I-20 on the right.

They used the Poisson equation to calculate the piezoelectric potential (φ), considering the free carriers n and doping level N_d. This equation is given as

$$\frac{\partial}{\partial x_i}\left(\varepsilon_{ij}\frac{\partial \varphi}{\partial x_j}\right) = e\, N_d^+ - e\, n + \frac{\partial}{\partial x_i} P_i \qquad \text{I-14}$$

By applying a compressive force of about 6.25 MPa (corresponding to 442 nN), the NW generated a negative piezoelectric potential in the order of magnitude mV at the top surface, varying from -5 mV to - 42 mV (see Figure I-20(a-d)) for N_d from $5 \cdot 10^{17}$ to $\cdot\, 10^{16}\ cm^{-3}$, respectively. They found that the output potential comes from the potential difference near the NW tip and that most of the length of the NW does not contribute to the final output potential.

They also found that the depletion width decreases when increasing N_d as well as the influence of dielectric properties of the material around the NW for low donor concentration (e.g. $N_d = 10^{16}\ cm^{-3}$). Regarding the dielectric properties, they considered that the piezopotential value could be affected by surrounding the NW with materials that have a relative permittivity value close to the intrinsic NW value.

In order to overcome the screening effect on piezoelectric-semiconducting materials such as AIN, ZnO, and GaN, few numerical simulations have proposed the idea of including an electric charge at the piezo-semiconducting interface. Some works have developed the idea based on surface functionalization on these NWs, understood here as an extrinsic property that creates a depletion region due to the addition of negative surface charges [213,216].

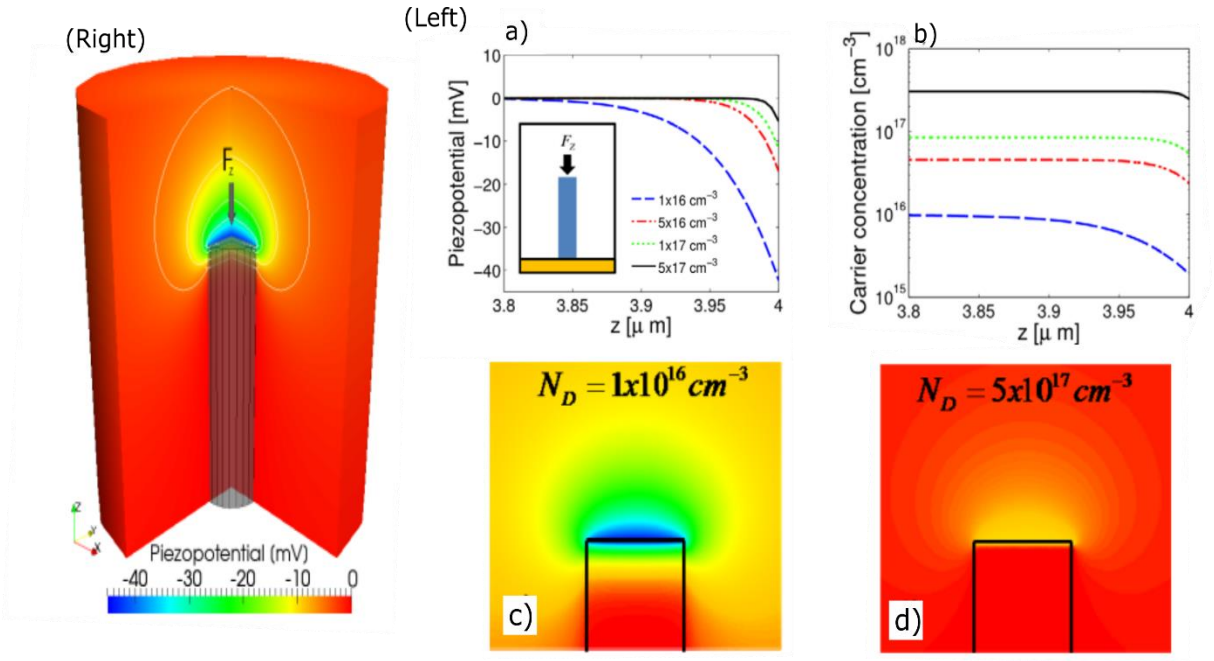

Figure I-20 (Right) Piezopotential distribution of complete ZnO structure. (Left) Variation of (a) piezopotential value and (b)carrier concentration along the z-axis for different values of N_d *. Piezopotential distribution at the top surface of NW at (c) low and (d) high values of* N_d*. It was adapted from* [214].

Kim. *et al.* [216] studied the effect of external surface charge on piezoelectric potential in two kinds of structures: NW and nanotubes (NTs) for ZnO and AlN. The first model consisted of putting the external charge on the top surface, while in the second model, the external electric charge surrounded the NW and NTs, as shown in Figure I-21(a). They used the Poisson equation I-14 to determine the electric potential and assumed a doped value of $10^{17}\ cm^{-3}$ for both materials. As for the external electric charge (σ_s), this parameter was included in the

boundary conditions according to each model described above. They calculated the piezoelectric potential on the top surface before ($\varphi(T_z = 0Pa, \sigma_s)$) and after ($\varphi(T_z = 10MPa, \sigma_s)$) applying a compressive force of 10 MPa. The appropriate piezoelectric potential was estimated by subtracting the potential after and before for the NW or NTs with 100nm wide and 600nm long. They observed that piezoelectric potential linearly increased when the amount of σ_s increase on the top surface (see Figure I-21(b)). But after σ_s value of –0.01 C $m^{-2,}$ the piezoelectric potential presented saturation values of –0.65 V and –0.35 V for ZnO and AlN, respectively. These saturation values correspond to the same piezoelectric potential reached in intrinsic NWs (i.e., without N_d and σ_s) since the NW is fully depleted inside. For the second model, all NWs and NTs achieved the same saturation values after σ_s values of $-4.1 \cdot 10^{-4}$ C (see Figure I-21(c)) m^{-2} and $-1.6 \cdot 10^{-4}$ C m^{-2} (see Figure I-21(d)), respectively. Finally, they concluded that NTs reach the saturation value of piezoelectric potential, requiring a relatively smaller range of σ_s in comparison with NW. They also highlighted that this model enables providing important guidelines to construct functional high-power semiconducting piezoelectric nanogenerators.

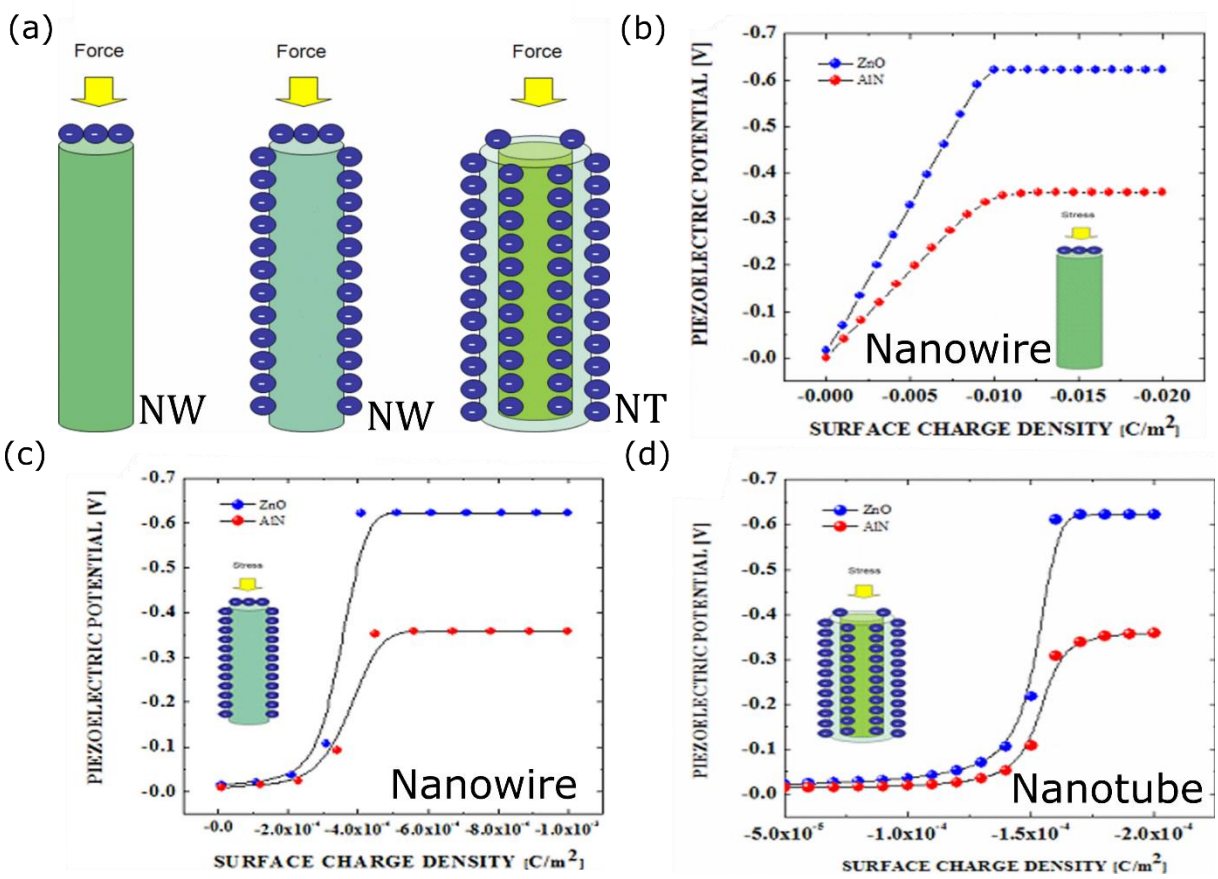

Figure I-21 (a) Schematic models to improve the piezoelectric potential on NW and NTs varying the surface charge density distribution on the top surface of NWs, the whole surface of NWs, and NTs.

Piezoelectric potential as a function of surface charge density with the surface charge on the top (b) and (c) complete surface of one NW as well as (d) the entire surface of NTs. They were taken from [216].

Later, Fathi *et al.* [213] simulated a 50nm wide and 600nm long ZnO NW under a compressive force of 80nN (corresponding to a pressure of 41 MPa), as shown in Figure I-22(a). The authors initially considered high doping concentrations ranging from 10^{15} cm^{-3} up to 10^{18} cm^{-3}. They also concluded that the application of the force produced a depletion region only at the top of the nanowire, and that an increase of doping concentration reduced the piezoelectric response. The second set of simulations included an external surface charge density (see Figure I-22(b)), ranging from -0.002 $C.m^{-2}$ to -0.08 $C.m^{-2}$, at the top of the NW to extend the depleted region. Then they also defined the final piezoelectric potential as the subtraction between the total potential model (with applied force) and the electrostatic potential model (without applied force), as depicted in Figure I-22(b). The piezoelectric potential was increased, until an eventual saturation, as in Kim *et al.* work [216]. For a doping concentration of 10^{17} cm^{-3}, the potential was found to saturate at -250mV for external surface charge values beyond -0.03 $C.m^{-2}$, as depicted in Figure I-22(c).

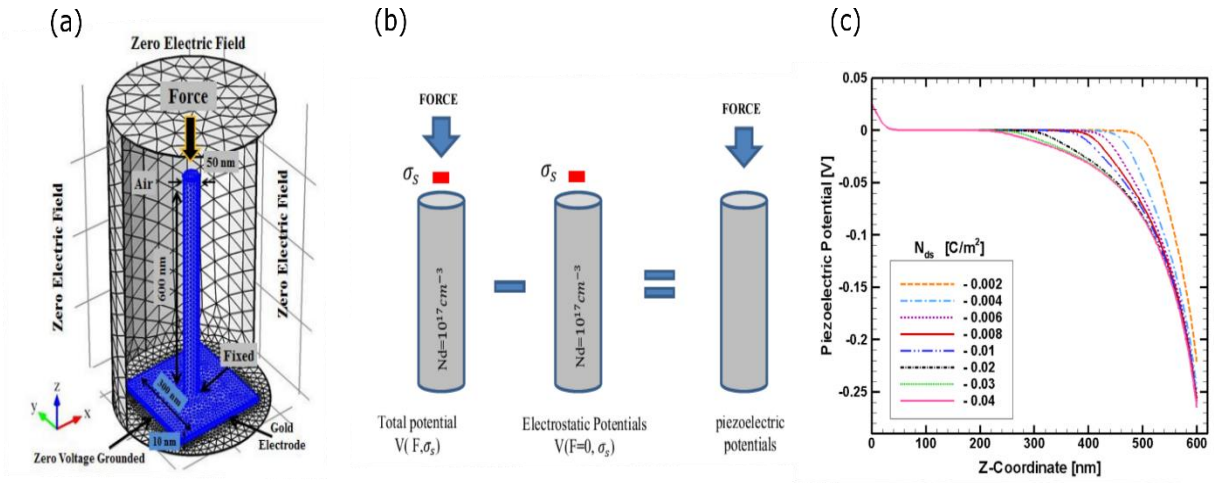

Figure I-22 (a) Schematic nanogenerator model based on a single ZnO NW within air environment. (b) Electrical and mechanical boundary conditions are used on NW to extract the piezoelectric potential. (c) Piezoelectric potential values along the z-coordinate in the middle of NW for different values of external surface charge. Figures were adapted from [213].

The theoretical results mentioned so far concerned only single NWs. Extremely few theoretical works can be found of piezo nanocomposites based on NWs. Most of them are from French groups and consider the NWs as insulators [102,204–211]. In recent work, Tao *et al.* [6] proposed a numerical simulation of VING using PMMA as the dielectric matrix (see Figure I-23(a)). This structure was inspired from Hintchet *et al.* [211] work who studied the efficiency of a complete VING structure by including the effect of the matrix polymer, several NWs,

diameter and length effect, as well as the screening effect. That work established for the first time the idea of the surface defects or trap density present on ZnO NWs as electric charge density (Q_s), such as it was discussed in section I.2.2.3. Q_s was set as a function of the electric potential at the surface of NW to solve the coupling of piezoelectric and semiconducting equations as a self-consistent problem. Overall, these kinds of defect levels within the bandgap commonly exist at the surface of semiconducting III-V and II-VI compounds. Namely, these surface defects are considered as intrinsic properties (see section I.2.2.3 in Electronic properties of ZnO). They can accumulate negative charges on the semiconducting surface, generating a depleted region due to band bending formed at the surface.

Tao's work included the surface charge density using the equation I-5 at the interface between ZnO and PMMA for two models: i) surface charges on the top surface of NW (see schematic on the left in Figure I-23(a)) and ii) surface charge everywhere of NW surface (see schematic on the right in Figure I-23(a)). The piezopotential values were obtained by calculating the average value from the top surface of VING, corresponding to the contribution of piezoelectric terms in the coupled systems equations after applying a constant compressive force of 1 MPa. For a doping value around $10^{17}\ cm^{-3}$, they observed that the model with top surface charge was depleted near the top surface of NW. Whereas, the model with surface charge everywhere of NW surface exhibited almost full depletion at the core of NW. As a result, the piezopotential value with the second model was 8 times greater than with the first model since the polarization values in the depleted zone which are important in generating the output potential (see Figure I-23(b)). They also examined that the piezopotential value decreases as N_d value increases until reaching a neutral core (i.e., the piezopotential drops to zero) in both models for $N_d > 2 \cdot 10^{17}\ cm^{-3}$, as shown in Figure I-23(c). In addition, the size effect was also studied in this work, obtaining some important conclusions as independence of ZnO length on piezopotential for the first model and strong length-dependence for the second model. The slight dependence of piezopotential values with respect to ZnO radius was found for both models.

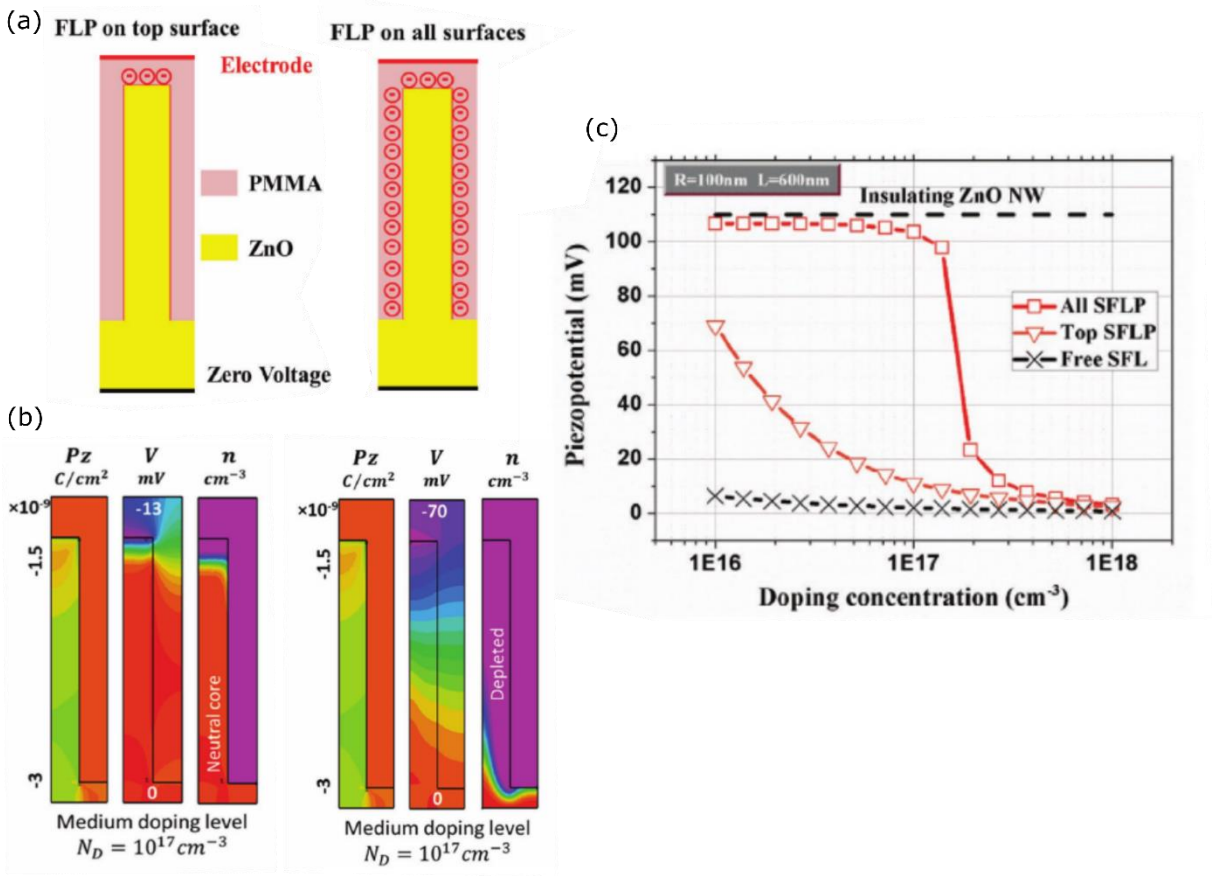

Figure I-23 (a) Schematic of a 2D VING with different configurations for surface charges. (b) Polarization, potential, and carrier concentration distribution for the models with only surface charges on the top surface of NW (figures on the left) and surface charges on the whole NW surface (figures on the right). (c) Effect of doping level Nd on the piezopotential values in both configurations maintaining a fixed trap density parameter N_{it} equal to $5 \cdot 10^{11} eV^{-1} cm^{-2}$. Reference geometry (NW with a radius of 100nm and a length of 600 nm). Figures were adapted from [6].

I.3 Conclusions

As a complement to our experimental work, we also explored the numerical simulation of VING devices based on ZnO NWs. Most numerical simulations presented in the literature assumed the ZnO NWs as insulating material without considering its semiconducting properties. Other simulations have included only doping levels, but their results contradict experimental results due to their values of piezoelectric potential being strongly affected by the screening effect. Until now, there is only one work that has included doping level N_d and surface trap density N_{it} in their simulations, in order to solve that contradiction. This work demonstrated higher piezoelectric potential and a geometry dependency when the surface traps were assumed on the whole ZnO NW surface. However, it is noteworthy that in these simulations, surface traps have been considered as an ultra-slow dynamic. It means that they did not have the time

to charge or discharge within the time frame of the piezoelectric response induced by a change in the mechanical load. Throughout this PhD thesis, the analysis of trap dynamics will be evaluated by comparing two extreme cases, such as ultra-slow and ultra-fast traps. On the other hand and as said in the literature, both N_d and N_{it} strongly depend on the growth method for ZnO NWs. Therefore, a complete study of numerical simulation will be deeply investigated to correlate experiment data and theoretical models. In addition, the most important electrical parameters related to electromechanical optimization have not been explored yet using this complete model. We will also explore the role of growth methods on the performance of nanocomposites based on ZnO NWs when tuning the values of N_d and N_{it}. Finally, we will investigate more piezoelectrical parameters under optimized conditions.

This first chapter highlighted the importance of promoting emergent technologies using lead-free piezoelectric materials for mechanical applications, such as self-powered systems, in order to replace the batteries. We have shown many alternative technologies to collect the mechanical energy present in the environment, such as mechanical vibrations, displacements, among others. We also analysed that the type of piezoelectric material plays an essential role in the piezoelectric device performance, which can be evaluated and enhanced through their electrical components (i.e., piezoelectric coefficient and dielectric constant) as well as the mechanical component (i.e., mechanical compliance). For instance, most inorganic and organic piezoelectric materials require an extra poling process or even higher values of temperature in the manufacturing process to improve their piezoelectric nature. Other materials add some inorganic compound to achieve the same objective. However, the fabrication process is often complex and make it challenging to build a piezoelectric device at low cost and low temperature. In this context, this PhD thesis intends to build a piezoelectric device based on ZnO NWs arrays on flexible substrates with easy manufacturing, low cost and low temperature.

Lead-free piezoelectric material as ZnO, at least in terms of bulk material, has exhibited better piezoelectric qualities (e.g., the piezoelectric coefficient) than other materials with the semiconducting property. The piezoelectric coefficient is an essential parameter, which paves the way for boosting the performance of energy harvesters based on ZnO NWs. A few studies to date have reported the effective value of longitudinal piezoelectric coefficient d_{33}^{eff} of ZnO NWs while such studies have not been conducted for our samples that have used the CBD growth method. In addition, the coexistence of two polarities (as Zn- and O-polarity) in ZnO

nanostructure have been recently controlled via the growth process of ZnO nanowires using CBD method. This polarity has been associated with the sign of the piezoelectric coefficient or the piezoelectric field domain revealed by the phase signal in the PFM technique. However, the coexistence of these domains has not been investigated for ZnO nanowire using the CBD method. In this context, we will propose a statistical method to study the piezoelectric response of an array of n-type ZnO NWs grown by the CBD method, using the PFM mapping at the scale of a few NWs to probe the piezoelectric coefficient as well as the polarity on their top surfaces.

As observed on the novel sensing application of piezoelectric ZnO NWs, the piezotronics effect is a very promising mechanism for enhancing the performance of chemical sensors. This effect provides a novel approach for controlling junction contact properties through mechanical input. In collaboration with Georgia Tech, our group demonstrated the piezotronics effect on vertically aligned GaN NWs by applying transverse force with an AFM probe [217]. In order to extend the same study in the future in our laboratory when employing ZnO NWs, we need to study the role of surface trap density and other semiconducting properties in locally piezoelectric response, electrical and electromechanical parameters of individual ZnO NW grown on flexible substrates by modifying the atmospheric conditions. In this regards, several atomic force microscopy (AFM) modes, such as piezoelectric force microscopy (PFM), Kelvin probe force microscopy (KPFM), and conducting atomic force microscopy (C-AFM) will be used experimentally, in order to probe locally electrical and electromechanical parameters which play a key role in the efficiency of the piezoelectric response of ZnO NWs.

Chapter II. Numerical simulation of VING devices based on ZnO NWs

Computational modeling studies based on the finite element method (FEM) are well-established tools that provide the numerical prediction of electromechanical behavior of VING devices integrating ZnO NW, contributing to the development of a roadmap in order to enhance the performance of VING devices experimentally by tuning structural or intrinsic parameters. These tools also offer a better understanding of the underlying aspects of the semiconducting and piezoelectric properties involved in ZnO NW-based material. In this chapter, we first introduce the FEM model as well as the full piezoelectric and semiconducting equations, which are used for the VING devices under uniaxial compression mode. Secondly, the dynamics of trap density are studied following the mechanical transient whereby the Press and Release action is analyzed by calculating the piezoresponse and the effective piezoelectric coefficient d_{33}^{eff}*. Two extreme cases of traps dynamic were investigated considering either ultra-slow or ultra-fast trap. We have compared the VING model with the thin-film structure since this structure is theoretically well-known. Thirdly, the impact of the growth method used for ZnO NWs on VING devices was explored in order to find out the optimal piezoresponse value by taking into account the affordable range of radius and length. Finally, many electric characteristics related to the efficiency of the VING devices were investigated considering the Chemical Bath Deposition (CBD) growth method and an external resistance load for finding the optimal output parameters.*

As presented in chapter I, the VING structure integrating ZnO NWs has been widely investigated for self-powered nanosystems and sensor applications in the last two decades. Experiments and theoretical works (using the FEM approach) have been effectively developed for VING device under compressive mechanical input to determine the piezo potential and the electrical energy. However many factors, such as the applied force, NW dimensions, dielectric matrix, and NW growth method, play an essential role in the mechanical into electric energy conversion. This could explain the variability of output potential that has been observed in

different experimental reports with results that can range from a few millivolts to a few hundred millivolts and volts, as was discussed in Chapter I.

Based on the literature overview presented in Chapter I, we identified several points which deserve to be analysed in details based on simulation:

a) Most numerical simulation works based on the FEM method have considered ZnO materials an insulator (i.e., a full depleted NW), obtaining the maximum performance results for specific NW dimensions and mechanical input. But the question here is whether this assumption could be valid for any NW dimension value. On the other hand, other numerical simulations in which the doping level N_d has been taken into account (as a realistic case) have reached output potential values of a few millivolts, at maximum, due to the strong screening effect generated by free carriers inside NWs. In this regard, surface Femi level (SFL) incorporated in the VING simulation model has been used by our group to solve the screening effect issue, obtaining a complete model with semiconducting and piezoelectric properties for ZnO material when including the experimental values as doping level N_d and trap density N_{it}. Besides, this new model can generate output potential values in the order of magnitude achieved in the experimental reports. Until now, this new SFL model has been explored under the assumption that traps were ultra-slow only while the opposite assumption of ultra-fast traps would deserve to be studied in order to evaluate their influence on VING performance.

b) Moreover, like the output potential, the effective piezoelectric coefficient d_{33}^{eff} is very important for evaluating the piezoelectric properties of any material. This d_{33}^{eff} value has not been theoretically estimated yet with account for the full coupling between piezoelectric and semiconducting properties for VING devices based on ZnO NW.

c) Depending on the ZnO NW growth method, the doping level N_d and trap density N_{it} can vary in a specific, although rather broad, range of N_d and N_{it} values. A theoretical study of VING performance for different values of N_d and N_{it} has not been performed yet, although it would help in choosing between all growth methods. According to some experimental evidence, the VING device has shown an enhancement in its performance as the ZnO NWs diameter decreases and length increases. Radius and length dependence has not been numerically demonstrated for a wide range of N_d values.

d) The evaluation of the harvested energy of nanocomposites based on ZnO NWs in a practical application requires an external resistive load (between 100 Ω and 10 MΩ) to be added in order to extract the maximum power output generated through impedance matching. Therefore, a complete numerical study about all the electric characteristics parameters, which impact the

VING performance, such as power density, current density, charge density, and electric energy, has not been done yet at least with full account of N_d and N_{it} parameters.

In this chapter, we will address then different points using FEM simulations of VING devices based on ZnO NWs. We concentrated on the VING operated in compression. All our simulations accounted for the full coupling between piezoelectric and semiconducting properties.

In view of all those mentioned considerations, the numerical simulations are employed to investigate the output electric parameters under compression mode for VING device integrating ZnO NW. All these simulations utilized the full coupling piezoelectric and semiconducting equation for the ZnO material and FEM, as will be introduced below.

II.1 Numerical simulation framework

II.1.1 Mechanical/electrical coupled system of equations

As mentioned in chapter I (section I.2.1), piezoelectricity is an electro-mechanical phenomenon arising in some materials under the application of an external pressure or voltage. This phenomenon couples the elastic and dielectric behaviors, which are described by a mechanical equation and an electrical equation, respectively. The mechanical equation can be modeled in both dynamic and static cases while the propagation effect will be neglected in the electrical equations. This approximation is valid when the electric field temporal variations are slow (below a few tens of kilohertz). Thus, the general mechanical and electrical equations used in this numerical simulation work write:

$$(\boldsymbol{\nabla} \cdot \mathbf{T}(t)) = \varrho \frac{d^2 \boldsymbol{u}}{dt^2} \qquad \textit{II- 1}$$

and

$$\boldsymbol{\nabla} \cdot \boldsymbol{D}(t) = \rho(t) \qquad \text{II- 2}$$

where T, D, ϱ, $\boldsymbol{u}$, and t are the stress, displacement field, mass density (per unit of volume), the mechanical displacement vector, and the time, respectively. Depending on the assumptions done, ZnO can be considered as a non-charged insulating material ($\rho = 0$) [209,211] or as a semi conduction [6,213,214]. In the latter, the charge density can account for the free concentration of electrons (n), holes (p), and ionized donor atoms (N_d^+), as described in equation II- 3

Here, the electric charge density (ρ) can go to zero for an insulating ZnO material or ρ can include the electron (n), hole (p) and donor N_d^+ concentrations for an semiconducting ZnO, as described in equation II- 3

$$\begin{cases} \rho = 0, & \text{Insulating ZnO} \\ \rho(t) = q(p(t) - n(t) + N_d^+), & \text{Semiconducting ZnO} \end{cases} \quad \textit{II- 3}$$

here, free electron (n) and hole (p) concentrations are functions of the local electric potential (φ). Additionally, we used the symmetric part of the displacement ($\boldsymbol{u}(t)$) gradient (see equation II- 4), and electric field that is defined as the opposite of electric potential gradient (see equation II- 5).

$$\boldsymbol{S}(t) = \frac{1}{2}(\nabla \boldsymbol{u}(t) + \nabla \boldsymbol{u}^t(t)) \quad \textit{II- 4}$$

$$\mathbf{E}(t) = -\nabla \varphi(t) \quad \textit{II- 5}$$

As mentioned in the section I.3.3.2 of Chapter I, the linear electro-mechanical coupling appears in the constitutive relations, which we can rewrite as:

$$\boldsymbol{T}(t) = \mathrm{c}\,\mathbf{S}(t) - e^t \mathbf{E}(t) \quad \textit{II- 6}$$

$$\boldsymbol{D}(t) = \mathrm{e}\mathbf{S}(t) - \varepsilon \mathbf{E}(t) \quad \textit{II- 7}$$

where the piezoelectric coupling coefficient (e), is the coupling term for the equations II- 6 and II- 7. By replacing the equation II- 6 and II- 7 into the equations II- 1 and II- 2, we can express the general mechanical and electrical equations in terms of φ and $\boldsymbol{S}(t)$ as follows:

$$\boldsymbol{\nabla} \cdot [\mathrm{c}\,\boldsymbol{S}(t)] + \boldsymbol{\nabla} \cdot [e^t \nabla \varphi(t)] = \varrho \frac{d^2 \boldsymbol{u}}{dt^2} \quad \textit{II- 8}$$

$$\boldsymbol{\nabla} \cdot (\mathrm{e}\boldsymbol{S}(t)) - \boldsymbol{\nabla} \cdot \varepsilon \nabla \varphi(t) = \rho(t) \quad \textit{II- 9}$$

These last equations represent the complete piezo-semiconducting coupling model to study the ZnO nanocomposites. All the piezoelectric and elasticity coefficients used in the numerical simulations correspond to literature values for ZnO material (see Table I-2 and Table I-5 in Chapter I).

II.1.2 Simulated structure of VING

All the simulations presented in this PhD document are based on a VING single cell to model the nanocomposite devices based on ZnO NWs, as illustrated in Figure II-1. A 2D axisymmetric cylindrical model was proposed for the unit cell, as shown in Figure II-1(a). This simulation strategy has been developed in our group [4] to reduce the computational cost since a nanocomposite is made of millions of NWs. This cylindrical model usually consists in a single ZnO NW over a seed layer surrounded by an insulating (PMMA) matrix. The 3D geometry is obtained by the rotation of the 2D profile around the NW axis, as shown in Figure II-1(b). The VING dimensions, namely seed layer thickness (L_{seed}), top PMMA thickness (L_{PMMA}), ZnO radius (R_{NW}), ZnO length (L_{NW}) and nanocomposite width (W) correspond to the dimensions of the devices fabricated experimentally investigated in this PhD work (see Chapter III) and the last numerical simulation performed by our group [6] .These dimensions are recalled for each specific simulation.

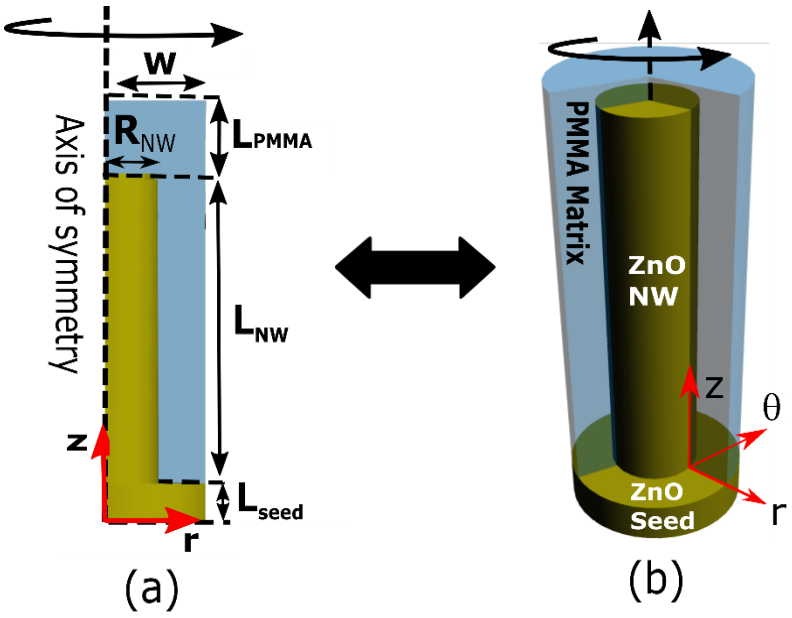

Figure II-1 Schematic of a single unit cell of : (a) 2D axisymmetric VING model considered in the simulation and (b) a 3D cylindrical geometry of the VING device.

II.1.3 Mechanical and electrical boundary conditions

Mechanical and electrical boundary conditions (BC) are uncoupled parameters. They are applied separately to the electrical and mechanical equations. There are two groups of boundary conditions which deal with the values or the derivative of φ (for electrical BC) and u (for mechanical BC.

Mechanical boundary conditions are specified in Figure II-2(a): i) a vertical pressure of P_1 along the NW axis (*z*-axis) on the top surface of the cell, with free vertical (v) and radial (u) displacement, ii) free lateral displacement with forbidden vertical displacement on the bottom side, iii) free lateral and vertical displacement on the lateral side and iv) free vertical displacement and forbidden lateral displacement on the axis of symmetry.

Electrical boundary conditions are specified in Figure II-2(b): i) the bottom electrode was grounded. ii)The top surface was connected to the external resistive load by including a surface charge density Q_0, which is deduced by a discontinuity of the normal component of $\vec{D}$ at the top surface of the device. iii) a local surface charge Q_s was included at the interface between ZnO and PMMA. Q_s introduced the discontinuity in the normal component of $\vec{D}$ at ZnO/PMMA interfaces:

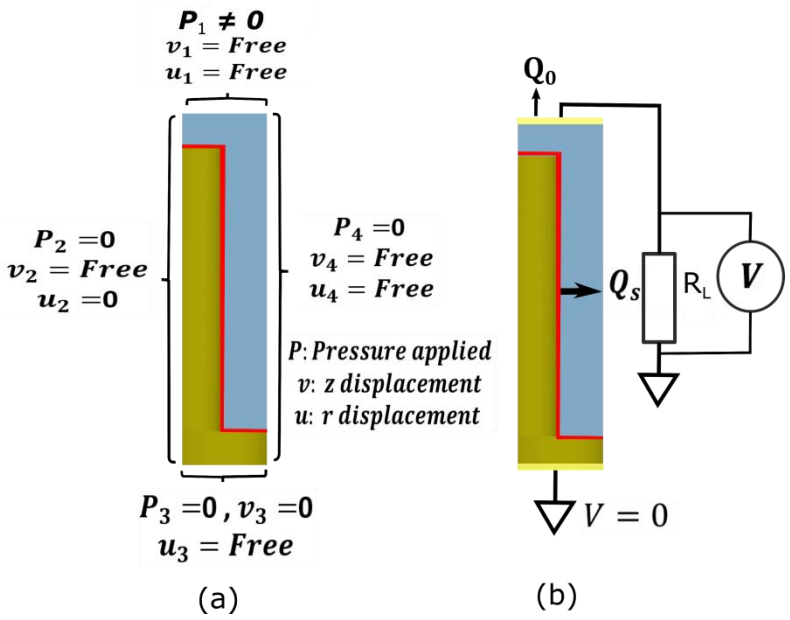

Figure II-2 (a) Mechanical boundary conditions and (b) Electrical boundary conditions for VING single cell. The red color interface represents the region where a surface charge (Q_s) is considered.

The external circuit will be employed for exploring more electric parameters, as current, current density, capacitance, piezoelectric coefficient, and electric energy density, when utilizing the Terminal node in COMSOL Multiphysics environment. Depending on the type ZnO NW properties, either insulating or semiconducting material, the electrical BC are modified as follows.

II.1.3.1 Insulating ZnO NW case

Most numerical simulations found in the literature concerning nanocomposites under compression consider the ZnO NW as an intrinsic semiconductor with initially no free-carrier concentration ($n_i = 10^{-10} cm^{-3}$ in ZnO) [177–180], and with no surface traps.

II.1.3.2 Semiconducting ZnO NW case

As discussed concerning the electrical properties of ZnO in section I.3.2.3 of Chapter I, some intrinsic surface defects can be originated during the growth process of the ZnO nanostructure..

At the surface of ZnO NWs, oxygen molecules can act as acceptor-like surface states, and electrons from n-type ZnO occupy them, forming a low-conductivity depletion region near the ZnO surface and upward surface band bending [154] (see Figure I-9 in Chapter I). These negatively charged traps or surface states are considered within the simulation model modifying the electrical BC by including Q_s everywhere at the interface between ZnO and matrix material. Q_s is defined using equation I-5 in section I.2.2.3 of Chapter I.

II.2 Role of surface trap dynamics on VING device

VING simulations in this section used COMSOL Multiphysics environment to evaluate the piezoelectric response generated over a load resistance (R_L), as really happens in experiments, following a modification of the input uniaxial compressive force. All simulations have employed the coupling of the piezoelectric and semiconducting properties by solving the equations II- 8 and II- 9. This mechanical transient is assumed to be instantaneous. It is obtained manually by modifying the mechanical BC. For instance, simulations in "Press action", the initial state corresponds to system 1 without input pressure, while the final state corresponds to the system 2 with input pressure. Piezoelectric and semiconducting properties are considererd in both systems. A negative piezoresponse is obtained as expected because the c-axis in the NW is oriented along the [0001] direction (i.e. Zn polarity).

II.2.1 Piezopotential versus Piezoresponse

It is very important to introduce some precisions about the evaluation of the device response to an input pressure. Most of simulation works used the definition of the piezopotential to the output potential calculated on the top surface of the VING device. The piezopotential was

calculated as the difference between the potential distribution with and without the direct and converse piezoelectric term (e) of the equations II- 8 and II- 9 for obtaining the piezoelectric contribution under a constant compressive force. In contrast, the variation in output potential resulting of "Press action", called here as piezoresponse, should be calculated as the difference of the average value of electric potential at top electrode with and without a pressure applied on the cell. The system without pressure was called here #1 (with a corresponding top electrode potential V_{top1}(t)), while the system under applied pressure was called here #2 (with a corresponding top electrode potential V_{top2}(t)). The piezoresponse was defined as the peak value of V_{top2}(t)-V_{top1}(t). As can be seen in Figure II-3, we found that the two notions may widely differ for large values of the interface traps density and they reach values greater than the simulation with no surface traps.

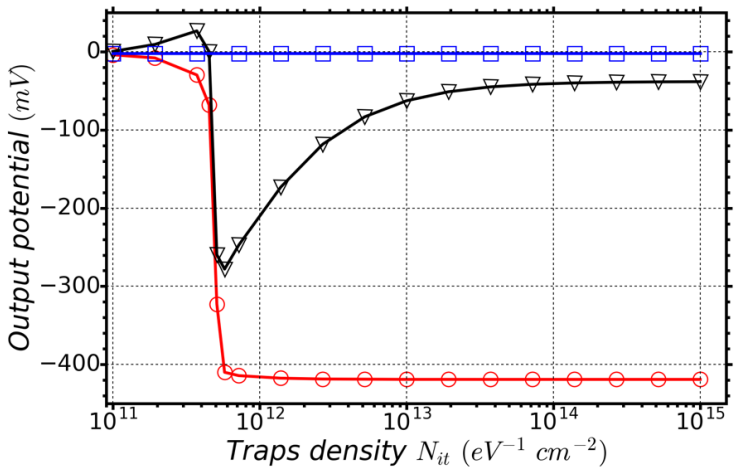

Figure II-3 Variation of the output potential as a function of traps density extracted from static simulations using two different methods to calculate the output potential: piezoresponse under pressure (⊙) and piezopotential in "Press action" mode (▽). The output potential of a system with free SFL (⊡) was also calculated as a reference. Ultra-slow traps. Doping concentration $N_D = 1x10^{17}\ cm^{-3}$.

II.2.2 Time-dependence

In order to simulate the VING device with a load resistance (R_L) or for time-dependent studies a circuit terminal is required for calculating the current (I_0) flowing in R_L, given by:

$$I_0 = \frac{\partial Q_0(t)}{\partial t} \qquad \text{II- 10}$$

The electrostatic equations may also be solved in time-dependent, assuming the charge density, and electric potential as a function of time. Therefore, the electric charge defines the coupled VING equation at the terminal node and is given by

$$\iint_{\Omega} \boldsymbol{D}(t) \cdot \hat{n} = Q_0(t) \qquad \text{II- 11}$$

Despite the applied pressure being constant during the whole range of time in each system, both the V_{top2}(t) and V_{top1}(t) vary exponentially as a function of time due to the electrostatic equilibrium between the VING device and the external circuit.

II.2.3 Piezoelectric coefficient d_{33}^{eff} calculation

Effective piezoelectric coefficient (d_{33}^{eff}) represents the mechanical to electrical conversion using the direct piezoelectric effect. d_{33}^{eff} of VING and thin-film structures was calculated using the following equation.

$$d_{33}^{eff} = \frac{\mathrm{C}\, V_{top}(t_{0+})}{F(t_{0+})} \qquad \textit{II- 12}$$

The capacitance C, F, V_{top}, t_{0+} refer to the capacitance, force applied, electric potential at the top surface, and origin of time, immediately after mechanical loading by force F at t_0, respectively.

The capacitance (C) of the test structure (VING or thin film) was determined by analyzing the output potential pulse as a function of time (as will be addressed following).

II.2.4 Output potential and piezoresponse pulses against time

In section II.2, the simulated VING model has similar dimensions to what has been obtained in the experimental work of this Ph.D., with L_{NW} of 3µm, R_{NW} of 100 nm, L_{seed} of 40nm, and L_{PMMA} of 100 nm. The geometry ratio (R_{NW}/W) was fixed at 0.5.

Upon including the trap density or surface traps on ZnO NW, system 1 yields an output potential V_{top1}(t) pulse even without mechanical input (see blue curve in Figure II-4(a)). It happens due to an intrinsic strain generated by the presence of the surface trap on NW, thus creating an electrostatic output potential throught converse piezoelectric effect. Without traps V_{top1}(t) would be equal to zero. Once the mechanical input is applied to system 2, the VING model produces an output potential V_{top2}(t) greater than V_{top1}(t) (see the red curve in Figure II-4(a)),

corresponding to the electrostatic and piezoelectric output potential. In order to obtain the appropriate piezoelectric contribution in the output potential, we have calculated V_{top2}(t)-V_{top1}(t), obtaining the piezoresponse value under the "Press action", as illustrated Figure II-4(b). We verified that, by doing so, the amplitude of the pulse calculated with a large density of traps (depleted ZnO NW) was equal to them calculated in the simple case of an intrinsic NW with no traps.

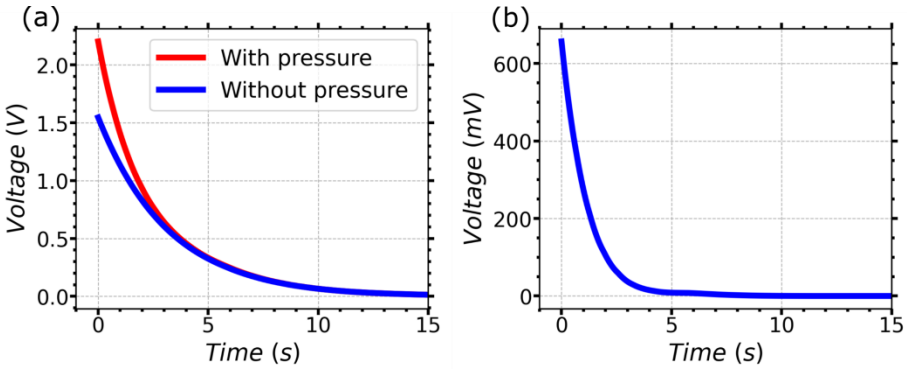

Figure II-4 Absolutes values of (a) the output potential without and with (1 MPa) pressures and (b) piezoresponse as a function of time calculated through the load resistance (R_L) of $10^{18}\Omega$ *for ZnO NWs of 3µm long and 100nm wide. The semiconducting parameters were* $N_d = 10^{17}\ cm^{-3}$ *and* $N_{it} = 10^{13}\ eV^{-1}\ cm^{-2}$.

II.2.5 Validation of the capacitance method and substraction of the voltage pulse

A simple piezoelectric VING model (without N_d and N_{it}) only generates a single pulse as a function of time. So, thanks to their easy equations in comparison to the semiconducting model is possible to get a complete pulse during the mechanical transient (pressing and releasing), as shown in Figure II-5(a). In this study, we have used a compressive mechanical force ($F = P_1 \cdot \pi \cdot {R_{VING}}^2$) equal to 31.4 nN (equivalent to 1 MPa for VING device with radius values of 100 nm), which is then released, as shown the top plot in Figure II-5 (a)). As expected, the VING device does not generate any output potential without a mechanical pressure during the first 0.4 seconds (see the bottom plot in Figure II-5 (a). Once the pressure is applied, a negative peak of output potential appears due to the piezoelectric field generated inside of ZnO NW. Subsequently, the output potential exponentially decreases to zero in the following few seconds due to electric equilibrium reached in the external circuit. When the mechanical load is removed, the opposite phenomenon occurs producing an inverted output potential, as depicted in Figure II-5 (a). This mechanical transient is in agreement with experimental works performed by our group and many others in the literature. The output potential pulse as a function of time has

important electric information associated with the VING capacitance, electric charge density, and piezoelectric coefficient [218].

Assuming that these models are like a capacitor discharging over a load resistance R_L, the capacitance value can be calculated by employing the equation II- 13 from the exponential curve of one of two peaks.

$$Log\frac{V_{top}(t)}{V_{top}(t_{0+})} = -\frac{t}{R_L \cdot C} \qquad \textit{II- 13}$$

Hence, the exponential curve is plotted in a logarithmic scale as a function of time (see inset image in Figure II-5(b)) to calculate the slope of the linear fit (decay time constant τ^{-1}), and in turn the capacitance value.

Similarly, the capacitance value is extracted for VING model with piezoelectric and semiconducting properties (with $N_{it} = 10^{13} eV^{-1}cm^{-2}$ and $N_d = 5 \cdot 10^{17} cm^{-3}$) after substracting the output potentials of the system 2 and 1 ($V_{top2}(t)$-$V_{top1}(t)$) and assuming ultra-slow dynamic (see Figure II-5(c)). Both models were simulated by connecting an external load resistance (R_L) of $1 \cdot 10^{18}\ \Omega$ and ZnO NW with 50nm wide and 3µm long. These parameters were used to get a full depleted state inside of NW.

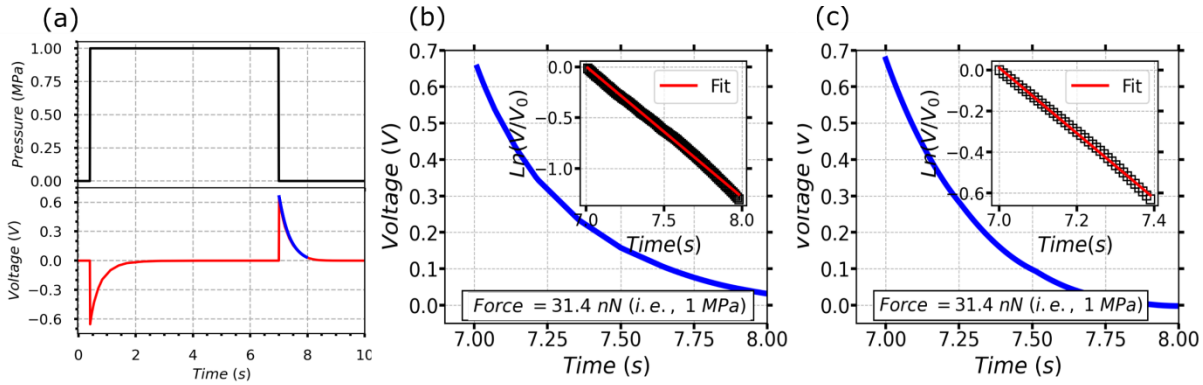

Figure II-5 (a) The complete pulse after a compressive and release force applied on the top surface of the VING model based on insulating ZnO NW (top graph) is synchronous to the output potential pulse (bottom graph) as a function of the time. The absolute value of the generated voltage signal as a function of time after applying a compressive force on the top surface of (b) insulating and (c) semiconducting ZnO NW. Everything was made for ZnO NW with 50nm wide and 3µm long, connecting to R_L of $10^{18}\Omega$.

Table II-1 summarizes the maximum output potential and the capacitance values for both models. When comparing the electrical results, it can be mentioned that the insulating and

piezo-semiconducting models exhibit the same electrical values, thus validating the capacitance method and the subtraction process of the output potential.

Table II-1 Comparison of capacitance values for VING with an insulating and piezo-semiconducting ZnO NW.

Model	**Max. Piezoelectric potential (V)**	**Capacitance value (F)**
Insulating ZnO NW	0.65	$7.77 \cdot 10^{-19}$
Piezo-semiconductor ZnO NW (in full depletion)	0.67	$6.27 \cdot 10^{-19}$

II.2.6 Effect of trap density on piezoresponse

First of all, we have carried out the numerical simulation on a thin film since it is a practical system of which we can analytically obtain the electrical parameters as the capacitance and the piezoelectric coefficient. These models work as reference model to compare with the VING and thin-film devices with SFL approach.

References cases: Insulating and free SFL thin film models

We have simulated a thin-film cell with almost the same size parameters as the VING device. This cell is a rectangular piece of 200nm in wide and 3μm in long (without PMMA dielectric matrix and with relative permittivity ε_r of 8.3). We considered two assumptions, one where the semi-conductor was considered as free of doping atoms and free carriers (thus equivalent to a non-charged insulating film) and one where free carriers and doping atoms were accounted, but without surface traps (referred to as "Free SFL thin film"). Table II-2 provides the calculated values of output potential (taken on top electrode), film capacitance and effective piezoelectric coefficient d_{33}^{eff} that were calculated using the equations II- 12 and *II- 13* for the simulation models. In order to compare the values with an analytical expression, the capacitance and d_{33}^{eff} were determined by employing the following equations

$$C = \frac{\varepsilon_0 \varepsilon_r A}{\mathrm{d}} \quad \text{and} \quad d_{33}^{eff} = \frac{e_{33}}{c_{33}} \qquad \textit{II- 14}$$

Where A and d are the top area and the thickness of the thin film. The piezoelectric coefficient e_{33} and the elasticity coefficient c_{33} used in the simulation are equal to 1.22 C/m^2 [116] and 211 GPa [219], respectively. So, the theoretical value of capacitance and d_{33}^{eff} that are then

expected for an insulating thin film are $3.07\ x\ 10^{-18}$ and 5.8 pC/N, respectively. As shown in Table II-2, both the capacitance of $2.28\ x\ 10^{-18}\ F$ and d_{33}^{eff} values of 6 pC/N calculated by FEM amounted are in fair agreement with the expected theoretical value. This validates our extraction method of d_{33}^{eff} from FEM simulations. It can be said that d_{33}^{eff} value remains unchanged and that their values are in good agreement with those reported in the literature with a range of 2.5 to 8 pm/V (units equivalent to pC/N) [127,220–222] .

Table II-2 Absolute value of the maximum generated piezoresponse at t=0, capacitance and effective piezoelectric coefficient (d_{33}^{eff}) for two thin film models: Insulating (without semiconducting properties) and Free SFL (only with N_d). The simulations were made under a compressive force.

Electric Parameters	**Insulating thin film (TF)**	**Free SFL TF**	**Theoretical value TF**
Abs. Piezoresponse (mV)	331	1.36	NA
Capacitance (F)	$2.28\ x\ 10^{-18}$	$5.6\ x\ 10^{-16}$	$3.07\ x\ 10^{-18}$
Piezoelectric coefficient d_{33}^{eff} (pC/N)	6	6	5.8

As for the thin films with SFL at top surface, the screening effect is rather strong at high values of N_{it}, so that a maximum value of piezoresponse of 15 mV was reached. Comparing the piezoresponse values, the semiconducting thin-film exhibits a value 22 times smaller than its insulating counterpart (see value in Table II-2).

Comparation of piezoelectric and semiconducting VING with thin-film devices

Once the capacitance method is validated, the electrical parameters as the piezoresponse and the effective piezoelectric coefficient were explored by varying the N_{it} parameter under a "Press action" for the VING model. In this study, we have used a compressive mechanical force ($F = P_1 \cdot \pi \cdot {R_{VING}}^2$) equal to 126 nN (equivalent to 1 MPa for VING device with radius values of 200 nm). As expected, the negative values of the piezoresponse appear under the compressive pressure, which is consistent with the negative values of the polarization field inside of the NW, as illustrated in Figure II-6(a). At low values of N_{it}, the piezoresponse decreases considerably

until a few units of mV due to the screening effect that affects the polarization field by the free carrier (see Figure II-6(b) and II-6(c)). It means that the free carriers are distributed into the core of NW, producing only the piezoresponse on the top surface of VING. In contrast, the high values of piezoresponse (around the hundreds of mV) are generated at high values of N_{it}, as a consequence of a full depletion into the core of NW.

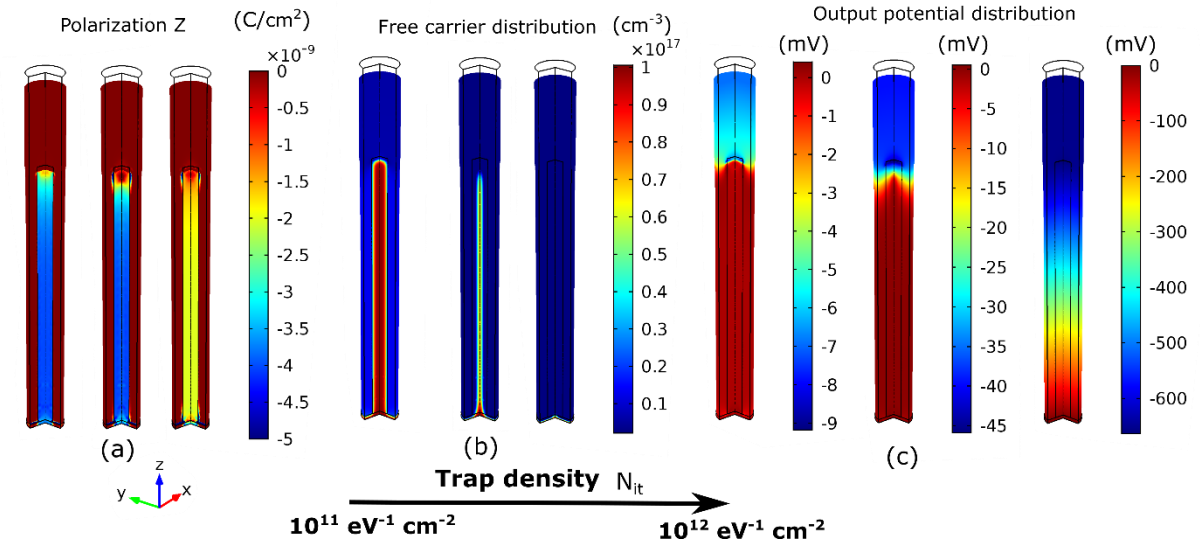

Figure II-6 Distribution maps of (a) polarization component along c-axis (Z direction), (b) free carrier, and (c) output potential for three different values of N_{it} equivalents to $10^{11}, 4 \cdot 10^{11}$, and $10^{12}\ eV^{-1}cm^{-2}$, respectively. Everything was made under a doping level of $10^{17}\ cm^{-3}$, and an applied pressure of 1MPa in ultra-slow dynamic.

After analysing the exponential curves for different values of N_{it}, the piezoresponse, the capacitance and the d_{33}^{eff} (using the equation II- 12) were calculated (see Figure II-7) and compared to the thin film with SLFP imposed only on the top surface. As can be seen in Figure II-7(a), the piezoresponse begins to increase after a N_{it} value of $4 \cdot 10^{11}\ eV^{-1}cm^{-2}$, reaching the full depletion state for the VING device. In this depletion state, the VING model reaches the same piezoresponse value (650 mV) as its insulating counterpart (see Figure II-7(a)). At high N_{it}, the piezoresponse of the VING device is thus 40 times larger than that of the semiconducting thin film.

As has been noted, the simulated models without traps (as the insulating case) always generated the highest piezoresponse values under axial compression, achieving the same piezoresponse value as the model with SFL on all surfaces at high N_{it}. Instead, it did not happen for the thin film with SFL only on the top surface since the system could not reach the full depletion state

for the same range of N_{it}. To sum up, the SFL approach suppresses the screening effect if is imposed everywhere on the NW surface, as was previously investigated by Tao *et al.* [6].

As for capacitance value, Figure II-7(b) shows that the thin-film and VING devices have values between $10^{-16}\,F$ and $10^{-17}\,F$, respectively. Comparing these structures, they have a difference of about one order of magnitude, which can be associated with the dielectric permittivity (ε) of the PMMA matrix involved in the VING model and its geometry. Additionally, the capacitance values decrease as N_{it} increases as a result of the reduction of the free carrier by suppressing the screening effect inside the ZnO material.

Figure II-7(c) shows the trap density-dependent piezoelectric coefficient d_{33}^{eff}. Because of the high area surface-to-volume ratio of NW-based VINGs. The d_{33}^{eff} value for a VING goes from 0.5 pC/N to 12 pC/N at low and high N_{it}, showing consistency with experimental values for ZnO NWs [142–146], as discussed in section I.2.2.1 of Chapter I (Table I-4).

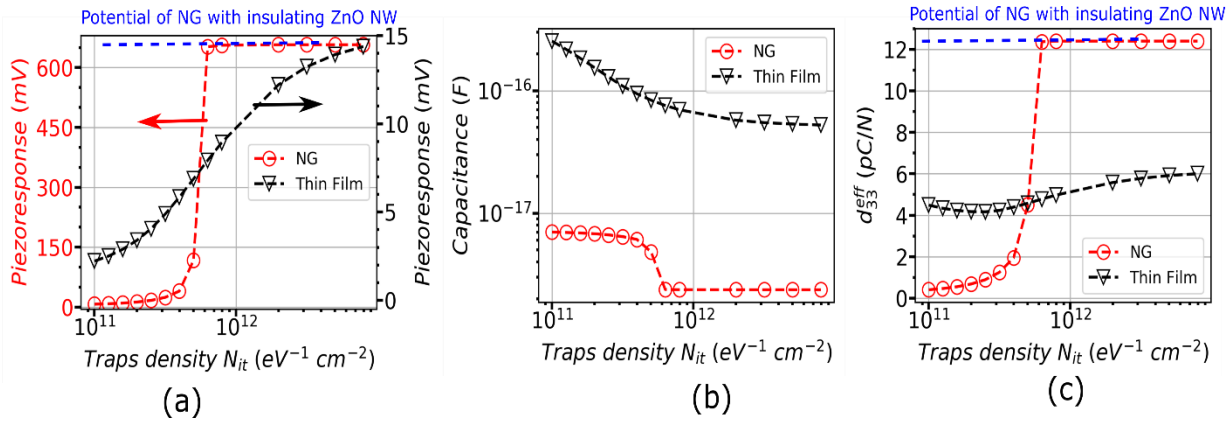

Figure II-7 (a) Absolute value of the piezoresponse evaluated at t=0 (b) capacitance and (c) effective piezoelectric coefficient as a function of N_{it} under ultra-slow trap density for a VING single cell (⊙) and a thin film (∇) in "Press action" mode. A doping concentration $N_d = 10^{17}\ cm^{-3}$ was considered in the simulations. The dashed blue line corresponds to the VING model with an insulating ZnO NW.

Based on the results, it is concluded that the presence of interface traps at the surface of ZnO provides a very strong advantage to composite material based on NW, by strongly improving their performance compared to that of a thin film of equivalent thickness.

II.2.7 Symmetry and asymmetry of piezoresponse

This section explores the mechanism of "Press" and "Release" actions on the VING structure employing the ultra-slow trap dynamic. The "Release action" was defined as the subtraction of

the output potential between system 1 (V_{top1}(t)) and system 2 (V_{top2}(t)) given by V_{top1}(t)-V_{top2}(t), that is the inverse case of the "press action". Additionally, the surface trap charge Q_s was redefined and fixed like a constant for the systems #1 and #2 as a function of the local potential of the initial state (i.e., the system #2), such as $Q_s(V_{top2}(t))$.

Figure II-8 (a-c) shows that the absolute piezoresponse, capacitance, and d_{33}^{eff} values are similar at the highest and lowest N_{it} values for the pressing and releasing pulses. It can be expected indeed at low N_{it}, independently of its exact value, the piezoelectric field is thoroughly screened by the free carrier generating negligible values for both mechanisms. On the other hand, the device is fully depleted at high Nit leading to the maximum values that can generate a VING device, namely the same value generated under insulating conditions for ZnO material. Consequently, "Press" and "Release" mechanisms provide the same values both for low and high values of N_{it}.

However, as observed in Figure II-8 (a-b), there is an interesting range of N_{it} (between $5 \cdot 10^{11}$ and 10^{12} $eV^{-1}cm^{-2}$) that could explain the asymmetry in the electric pulses reported in some experimental measurements for VING devices [6,192,223]. In the range of the trap density values, the absolute values of piezoresponse for "Press" and "Release" mechanisms exhibit a difference of a few tens or even hundreds of millivolts, as depicted in Figure II-8(a). Still further it should be noted that d_{33}^{eff} values mechanisms are exactly the same for "Press" or "Release" actions (see Figure II-8(c)).

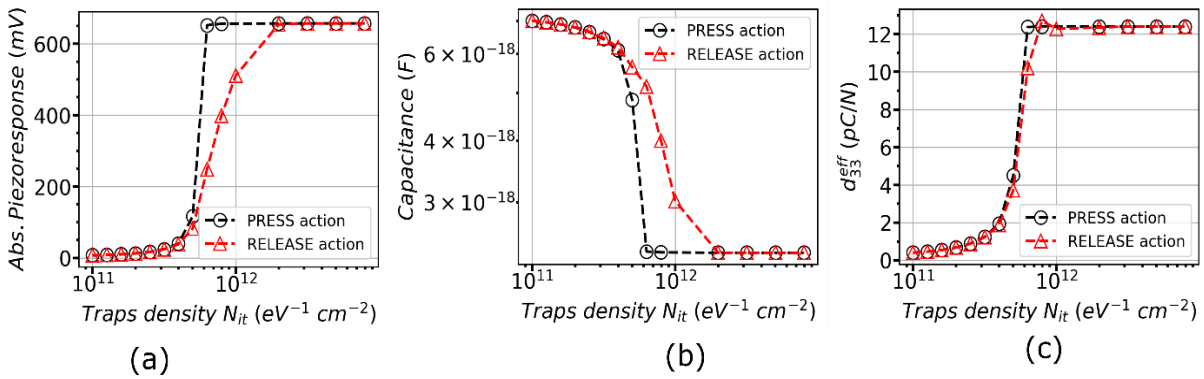

Figure II-8 Comparison between the "Press" and "Release" action modes as a function of N_{it} under ultra-slow trap density for a VING single cell. (a) The absolute value of the piezoresponse, (b) capacitance, and (c) the effective piezoelectric coefficient d_{33} for doping concentration $N_d = 10^{17}$ cm^{-3} and force applied of 126 nN (equivalent to 1 MPa).

In order to give a reasonable explanation of the asymmetry of piezoresponse in 'press' and 'Release' actions, we analyzed the free carrier n along the two lines of the NW for system #1

(without pressure) and system #2 (with pressure), one along the axisymmetric axis (blue line) and the other along the radial axis (purple line), as displayed in Figure II-9(a) for the piezoresponse points at $N_{it} = 10^{12}\ eV^{-1}\ cm^{-2}$. It is clear that the NW is fully depleted into the NW core for 'Press' action since their n values 10^{10} times lower than the N_d value. The screening effect is only present on the ZnO seed layer, as exhibited in the upper images of Figure II-9(b). Regarding the 'Release' action, the bottom images in Figure II-9(b) display that a considerable quantity of n ($10^{14} cm^{-3}$) occurs in the vicinity of the top surface of the NW for system #1. It suggests that the NW is partially screened by the free carrier after releasing the compressive force (final state). While under the mechanical action (initial state), the NW is completely depleted (see Figure II-9(c)).

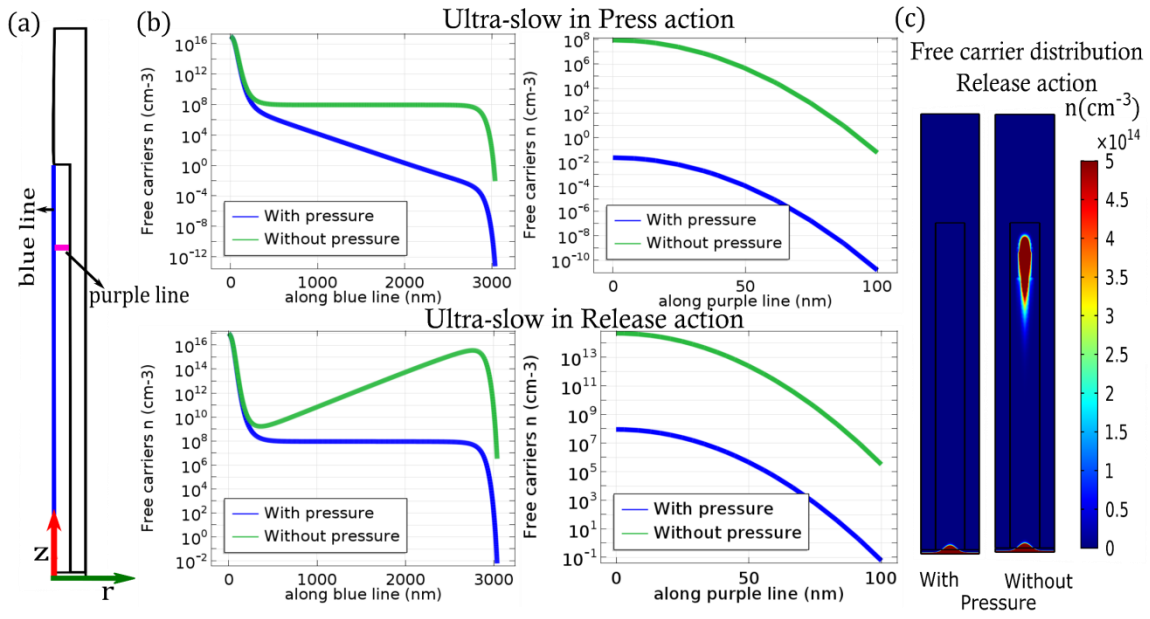

Figure II-9 (a) The vertical *(blue line) and horizontal (purple line) lines selected to evaluate the free carriers at* $N_d = 10^{17}\ cm^{-3}$ *and* $N_{it} = 10^{12}\ eV^{-1}\ cm^{-2}$. *(b) Free carriers along the blue and purple lines for the cases 1ps (green curve) and 2ps (blue curve) in 'Press' (upper images) and 'Release' (bottom images) action employing the ultra-slow dynamic. (c) Maps of the free carrier distributions into the nanocomposite for the cases 2ps (with pressure) and 1ps (without pressure) in 'Release' action. Everything was simulated for a ZnO NW of 3µm in long and 100 nm in wide. The scale bar was appropriately selected for detecting the contrast of the free carrier on the top surface.*

In conclusion, in this specific range of N_{it} values, the difference observed in the simulations between "Press" and "Release" actions would explain the asymmetry of the piezoresponse. It would mean that slow traps are involved.

II.2.8 Dynamics of trap density

Until now, we have assumed that the surface charge or surface traps on NW were frozen during the mechanical load, as was defined in the ultra-slow trap dynamics. However, it is important to explore the opposite assumption where the trap response time would be much faster than the mechanical load transient. It means that the traps would achieve the thermodynamic equilibrium at any time and that Q_s for system 1 must be defined as a function of the local potential V_{top1}(t) while Q_s for system 2 must be defined as a function of local potential V_{top2}(t). This kind of dynamics is called ultra-fast traps in this work. Under the "Press action", the numerical simulations were carried out for ultra-fast and ultra-slow traps. In addition, the modeling with free SFL was evaluated by calculating the absolute piezoresponse and d_{33}^{eff}, as shown in Figure II-10.

Figure II-10 shows that the results of modeling with free SFL are fully screened by free carriers, getting the lowest values of piezoresponse and d_{33}^{eff} (a few units of mV and pC/N respectively) as have been demonstrated in refs. [211,214] for similar mechanical and N_d conditions. With ultra-fast dynamics, the piezoresponse values are very close to those values obtained for a system without surface traps (i.e., free SFL) for a large density of N_{it}. It can be added that the piezoresponse values for ultra-fast and ultra-slow dynamics are 2 and 130 times greater than with free SFL. However, most experimental works [186–190,192], based on VING structures with more or less the same dimensions, mechanical input, and materials (see Table I-6 in Chapter I), reported piezoresponse values of few hundred mV and volts, which are in better agreement with the numerical results obtained with ultra-slow dynamics.

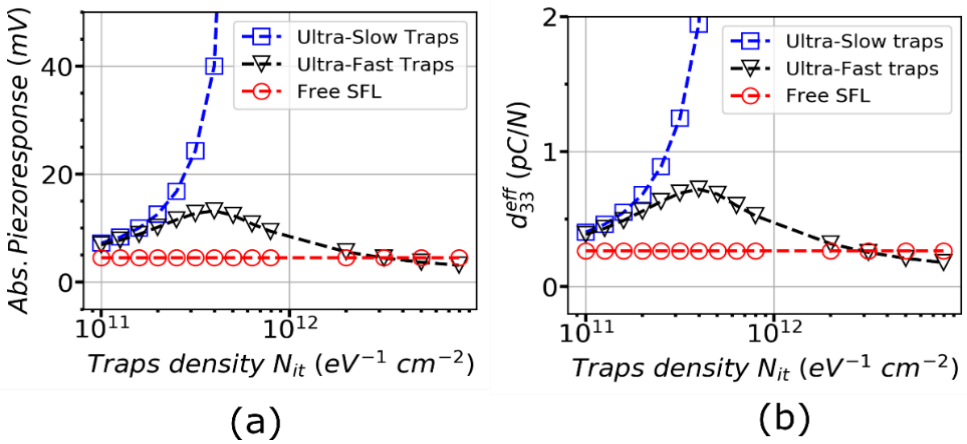

Figure II-10 (a) Piezoresponse in "Press action" mode obtained under three different assumptions at ZnO surface. (b) Comparison of the d_{33}^{eff} piezoelectric coefficient considering ultra-slow traps and ultra-fast traps as a function of trap density in "Press" action mode. In these graphs we considered: ultra-slow traps (⊡) and ultra-fast traps (△). The free SFL (no traps) is plotted for reference (⊙). Everything was made for doping concentration $N_d = 10^{17}$ cm^{-3} and force applied of 126 nN (1 MPa).

In reality, we can expect that both slow and fast traps are present at the surface of NWs. These two ultra-fast and ultra-slow dynamics should be considered as the extreme cases between which the real performance of the nanocomposite should be found. Finally, the numerical finding is therefore clear evidence of the important role of surface traps and their dynamics in the study of piezoelectric phenomena in devices based on piezoelectric semiconducting nanostructures.

II.3 Impact of the growth method

As shown in the state-of-the-art (see Chapter I) and the numerical finding in the last section, it is not straightforward to predict the piezoresponse of NW-based piezoelectric transducers since several key parameters are involved, such as geometrical dimensions (i.e. radius and length), doping level (N_d), and surface trap density (N_{it}). In practice, these key parameters depend on the growth method used to form ZnO NWs. ZnO is an exceptional material which can be formed in the shape of NWs by a considerable number of growth methods. According to the literature, ZnO NWs can be grown by vapor deposition [224,225], whose methods include thermal evaporation (TE), chemical vapor deposition (CVD), metal-organic CVD (MOCVD), and wet chemical techniques [226,227] with chemical bath deposition (CBD) method. N_d and N_{it} can be experimentally affected by the growth method due to significant incorporation of residual impurities (i.e., Al, Ga, In, …) which play a role as shallow donors for the vapor phase deposition technique [162], and hydrogen molecules for wet chemistry techniques [164]. Up to now, the growth method has not been strictly taken into consideration in the design and optimization of numerical simulation works based on ZnO NWs piezoelectric transducers from the point of view of its effect on doping level and surface trap density. Additionally, the optimal NW radius has not been deeply explored for each growth method, nor has the variation of NW length, which would serve as a roadmap for the design of new devices along with their optimization.

The numerical simulation for VING cell model used in this section is similar to what has been used in the previous section using the ultra-slow trap under compression mode. In geometry, the aspect ratio was fixed at 0.5. The thickness of the ZnO seed layer was also fixed to 100 nm and the thick insulating cap layer (PMMA) to 100 nm, as in previous works of Tao *et al.* [6]. As for ZnO NW dimensions, the radius was varied and the length was fixed to 5µm, chosen as an average length for the different growth methods. The piezoresponse was calculated by modifying the values of N_d and N_{it} depending on what is known for each NW growth method.

a) Parameters used for vapor deposition technique: As discussed in section I.2.2.3 of Chapter I, TE method experimentally has a broad N_d range from $10^{17}cm^{-3}$ to $5 \cdot 10^{17}cm^{-3}$, while CVD and MOCVD methods have ranged from $10^{17}cm^{-3}$ to $1 \cdot 10^{18}cm^{-3}$ and 1 to $5 \cdot 10^{18}cm^{-3}$, respectively. All methods were performed by fixing the crystal structure along the [0001] direction (i.e., along the positive z-axis). The mentioned methods have the same N_{it} of $10^{12}eV^{-1}cm^{-2}$.

b) Parameters used for wet chemical technique: As for CBD method, we have found that this has a large range of N_d so that we have defined two specific ranges that go from $5 \cdot 10^{17}cm^{-3}$ to $5 \cdot 10^{18}cm^{-3}$ and $5 \cdot 10^{18}cm^{-3}$ to $10^{19}cm^{-3}$ for O- and Zn-polar NWs, respectively. In order to change the polarity, the c-axis for Zn-polar in the numerical simulation was fixed along the [0001] direction (i.e., along the positive z-axis), while O-polar was fixed along the [000-1] direction (i.e., along the negative z-axis). For both polarities, the N_{it} was fixed to $10^{13}eV^{-1}cm^{-2}$.

In addition, we have explored the piezoresponse evaluating the effect of length-dependent piezoresponse for the CBD method which is one of the most used in the elaboration of ZnO NWs for piezo applications. We have taken the O-polar orientation as an example, fixing the NW radius to 50 nm.

II.3.1 Vapor deposition techniques

As shown in Figure II-11, we calculated the piezoresponse while varying the ZnO radius parameters for the lowest (blue curve) and highest (red curve) values of doping level expected for TE, CVD and MOCVD methods. The range of interest is on the left-hand side of each curve: NW radius must be smaller than the threshold values at which screening effects are reduced inside the NW core. The threshold radius increases as N_d decreases. For instance, a significant piezoresponse can be obtained whenever NW radius remains smaller than 40 nm (upper limit of N_d) or 140 nm (lower limit of N_d), as is the case of thermal evaporation (TE) (see Figure II-11(b)). Safely a good optimization would require 40 nm at maximum, but there is an optimization window of 80 nm where adequate control of the doping level is in principle under reach with the growth method and could allow NW radius to be relaxed to large values.

Figure II-11(c) shows the simulation results of VING devices integrating ZnO NWs grown by CVD. It reveals the poor piezoresponse obtained with NWs exhibiting radii larger than about 140 nm for low doping levels (blue curve) and 25 nm for high doping levels (red curve). On the

contrary, higher performance is obtained for NW radii below 120 and 20 nm for low and high doping levels, respectively. In this regard, the optimization window for CVD is 100 nm.

Regarding the MOCVD method, the piezoresponse can be effectively improved if ZnO NWs radius is smaller than 22 nm for minimum N_d (blue curve) and smaller than 5 nm for maximum N_d (red curve), as shown in Figure II-11(c). In contrast, poor performance is obtained for NWs with radii larger than 30 nm and 7 nm for minimum and maximum N_d values, respectively. As expected, the optimization window for this growth method (about 20 nm) is lower than TE and CVD ones since it has the highest doping levels.

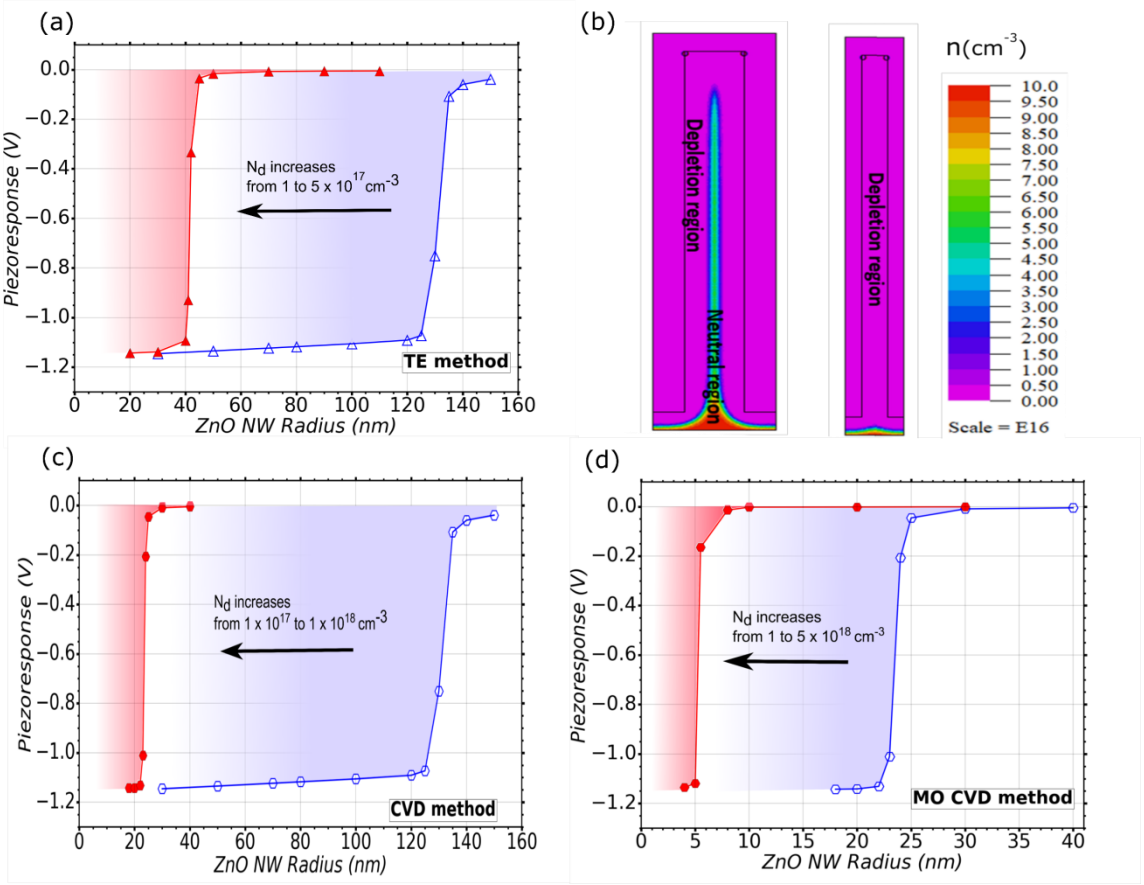

Figure II-11 Variation of the piezoresponse of a VING as a function of the ZnO NW radius for the lowest (blue curve) and highest (red curve) doping level range corresponding to (a) TE method. (b) Free carrier distribution of an NW with N_d=1 x 10^{17} cm^{-3} and a radius of 140 nm (left) and 80 nm (right). The piezoresponse values versus ZnO radius for (c) CVD and (d) MOCVD method. A trap density N_{it}=1 x 10^{12} eV^{-1} cm^{-2}, a constant pressure of 1 MPa and NW length of 5µm were considered in the simulation.

When comparing these last three growth methods, different ranges of radii are required to attain optimal performance, namely 120 nm, 120 nm, and 22 nm at a low doping level and 40 nm, 20 nm, and 5 nm at a high doping level for TE, CVD and MOCVD, respectively, In addition, it is

should be highlighted that MOCVD method requires NWs with the smaller radii in order to get the full depletion of free charge carriers and thus to reduce the screening effect.

II.3.2 Wet chemistry techniques

As discussed above, this technique has been widely used to grow the ZnO NWs on piezoelectric applications because is relatively easy, low-cost, and low temperature in the manufacturing process. Figure II-12(a,b) shows that NWs with c-axis oriented along the [0001] direction (i.e. Zn polarity) present negative values of piezoresponse (see Figure II-12(a)), while those orientated along the [000-1] direction (i.e. O polarity) have positive piezoresponse (see Figure II-12(b)). Another difference is that the transition from poor to high performance for maximum and minimum N_d, is less steep for O-polar ZnO NWs. VING devices integrating Zn-polar NWs yield the optimal performance using NWs with radii values below about 18 nm and 12 nm for low and high doping levels (see Figure II-12(a)), respectively.

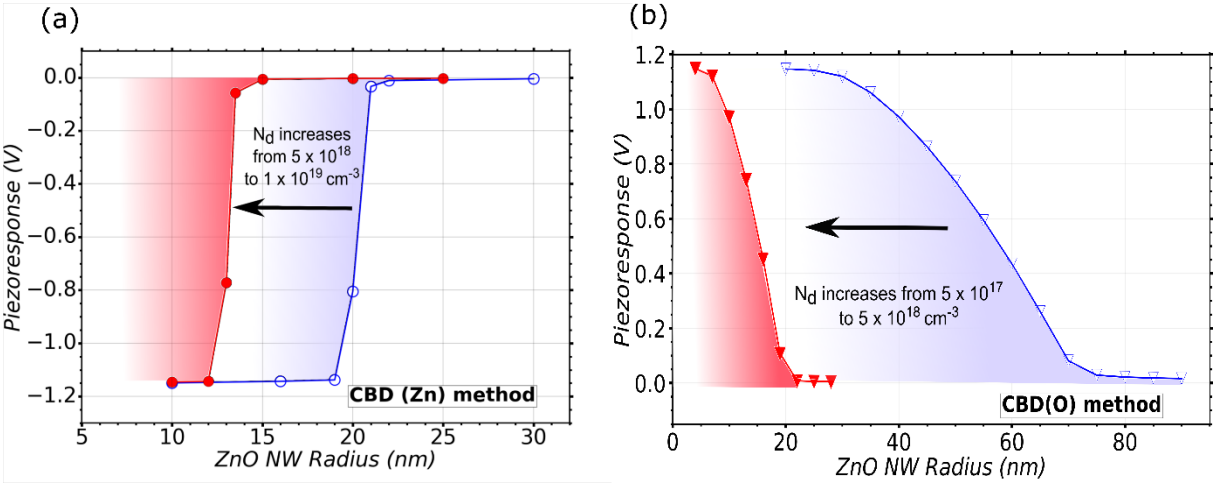

Figure II-12 Variation of the piezoresponse of a VING as a function of the ZnO NW radius for the lowest (blue curve) and highest (red curve) doping level range corresponding to CBD method for (a) Zn- *and (b) O-polar NWs. A trap density N_{it}=1 x 10^{13} eV^{-1} cm^{-2}, a constant pressure of 1 MPa and NW length of 5µm were considered in the simulation.*

Figure II-12(b) shows that O-polar ZnO NWs can provide high performance for NWs with radii values below 20 nm and 5 nm for low and high doping levels, respectively. Whereas NW with radii values larger than 70 nm (low doping level) and 22 nm (high doping level), weak performance is obtained, as illustrated in Figure II-12(b). Despite NWs grown on CBD and MOCVD being similarly doped, CBD shows better performance because of the higher surface trap density. For instance, half the optimal piezoresponse (~0.6V in absolute value) can be obtained for an NW grown by CBD (O) with a radius of ~55 nm, while NW grown on MOCVD

needs a radius of ~23 nm, resulting in a factor of 3 of difference. Finally, it should be added that the optimization window for VING devices integrating Zn-polar NWs grown in CBD (Zn) method is 9 times lower (estimated to be 6nm) as compared to the CBD (O) method (estimated to be 52nm). Up to this point, the CBD (Zn) method seems to be the most limited one in comparison with the other techniques considered in this study based on the optimization window and the very low radius that is needed to obtain optimal devices.

We classified and summarised the range of NW radius, below the NW critical value which the performance of VING transducers can be largely improved, for every growth method, as shown in Table II-3.

Table II-3 Summary of NW radius values to achieve full depletion or optimal performance for the different growth methods (NW critical radius) taken from the numerical results made in the previous section.

Growth method	***ZnO NW radius for full depletion***	
	Min. N_d (nm)	***Max. N_d (nm)***
TE	*< 120*	*< 40*
CVD	*< 120*	*< 20*
MOCVD	*< 22*	*< 5*
CBD (O)	*< 25*	*< 5*
CBD (Zn)	*< 18*	*< 12*
Electrodeposition	*Not simulated (estimated <4)*	*Not simulated (estimated <4)*

II.3.3 Analytical model of critical radius for full depletion

At the threshold value of radius corresponding to the value for which the core of NW reaches neutrality, it is possible to obtain an analytical expression by solving Poisson's equation. In order to obtain values of amplitude, we solved Poisson's equation in 1D dimension and cylindrical coordinates using the parameters given in Figure I-9 of section 1.2.2.3 of Chapter I. Assuming doping n-type material for the ZnO (i.e. $n, p \ll N_d$), the electric charge density ρ can be given by

$$\rho = \begin{cases} 0 & 0 \le r < r_d \\ qN_d & r_d \le r \le a \end{cases} \qquad \textit{II- 15}$$

Subsequently, the electric potential function at the NW surface $\varphi_s(a_{crit})$ can be expressed following the boundary conditions as

$$\varphi_s = \frac{\mathrm{qN}_d}{4\varepsilon} \cdot {a_{crit}}^2 \qquad \textit{II- 16}$$

and applying the charge neutrality condition at the surface between Q_s and the definition of depletion charge Q_{dep} given by

$$Q_{dep} = \mathrm{qN}_d \cdot \pi {a_{crit}}^2 \qquad \textit{II- 17}$$

Finally, we can find the analytical equation for a_{crit} as a function of N_{it} and N_d at a fully-depleted NW core, expressed as

$$a_{crit} = \frac{\varepsilon}{qN_{it}} \left[-1 + \sqrt{1 + \frac{4kT}{\varepsilon} \frac{{N_{it}}^2}{N_d} \cdot ln \frac{N_d}{n_i}} \right] \qquad \textit{II- 18}$$

Figure II-13 shows the a_{crit} values calculated with equation II- 18 (red and green curves) and the values reported in the previous sub-sections for the different growth methods (symbols). The resulting a_{crit} extracted from the numerical simulation results are within the range of the theoretical values for each value of N_{it} and N_d, according to each growth method. In the case of CBD (O), the analytical value a_{crit} is larger compared to the values extracted from our simulations, namely theoretical values of ~70 nm and ~25 nm were calculated for low and high doping concentrations, while the simulations were of ~20 nm and ~5nm respectively. The analytical model also allowed us to estimate the possible critical radius of NWs grown by the electro-deposition method (~3 nm). The electrodeposition method has also been used to grow ZnO NWs, but it was not considered in the numerical simulation study due to its high N_d (~10^{20} cm^{-3}). Such a high doping level is above the degeneracy limit in ZnO (a few $10^{18} cm^{-3}$) and information about the amount of ionization of doping atoms is missing. However, the critical radii which would result from such a high doping level are below 5 nm. Beyond the fact that obtaining free-standing NWs of the diameter with several μm length would be challenging, it has been shown in the literature that surface reconstructions effects worked to be visible, leading to modification in mechanical and piezoelectrical properties [228].

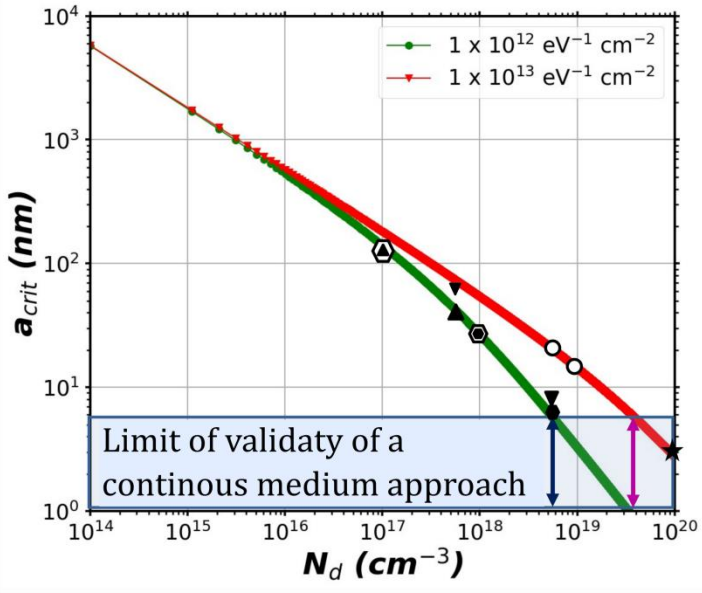

Figure II-13 Critical radius a_{crit} as a function of N_d for two ZnO NWs with values of N_{it} from 10^{12} (green curve) and 10^{13} eV^{-1} cm^{-2} (red curve). The black marks on the curves indicate the radius values for which full depletion was obtained from the numerical results in the previous section. The mark (▲) corresponds to the TE method, (○) to the CBD(Zn) method, (▼) to the CBD(O) method, (⬡) to the CVD method and (⬢) to the MOCVD method. The blue and magenta arrows indicate the limiting value of N_d for N_{it} =10^{12} $eV^{-1}cm^{-2}$ and 10^{13} $eV^{-1}cm^{-2}$. Beyond this doping value, the critical radius goes below 5nm and we consider that surface effects could modify piezoelectric coefficients. The mark (★) corresponds to the conditions of NWs grown by the electron-deposition method, which was not simulated.

II.3.4 Effect of the variation of NW length

In the experimental works, the VING device integrating NWs grown by CBD method has demonstrated a length-dependent piezoresponse under compressive forces, increasing the piezoresponse value [196] or the electric energy [229] as the NW length parameter increases. Initial simulation works, which assumed insulating ZnO NWs demonstrated that the performance parameters (mechanical and electrical energies) depend only on the piezopotential values [205], the NW length and the ratio value of the VING device. The latter is calculated by the diameter of the NW and the width of the VING unit cell [211]. In contrast, a more recent simulation work which included the influence of doping level and free carriers in order to evaluate the output potential in more realistic conditions, concluded that the output potential was very small and independent of nanowire length [214]. With this in mind, we studied the effect of the variation of the length in three particular cases in order to compare and have a complete model with ZnO NW length-dependent output potential and semiconducting properties. The main difference from which previous simulations were that we included also

surface traps. The three cases considered here were the simplest model (insulating ZnO NW), the free SFL model (ZnO NW with only N_d), and the SFL model (ZnO NW with N_d and N_{it}), as illustrated in Figure II-14. For this study, we used the same geometry for all VING models with an NW radius of 50 nm under a compressive force of 31 nN (equivalent to 1 MPa for a VING device with radius values of 100 nm). While the parameters used for semiconducting ZnO were $N_d = 5 \cdot 10^{17}\ cm^{-3}$ and $N_{it} = 10^{13}\ eV^{-1}cm^{-2}$ which correspond to CBD(O) growth method.

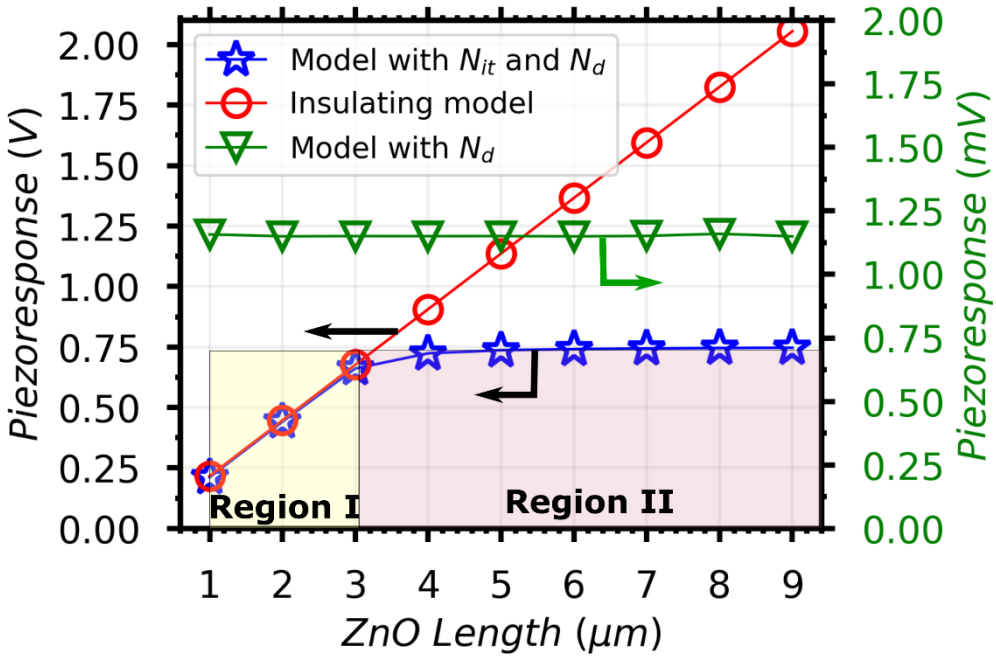

Figure II-14 Variation of the piezoresponse of a VING device as a function of the NW length for three different models: Model with ZnO as insulating material (red line), Model with ZnO including only N_d, and Model with ZnO including N_d and N_{it} (with SFL). The parameters of the NW with semiconducting properties correspond to ZnO NWs grown by the CBD (O) method. Applied force of 31nN (equivalent to 1MPa) on the top surface of NW diameter 50nm with $N_d = 5 \cdot 10^{17}\ cm^{-3}$ and $N_{it} = 10^{13}\ eV^{-1}cm^{-2}$.

Figure II-14 shows that piezoresponse increases linearly as the NW length increases for a simple model (red curve), showing a variation of piezoresponse of 400% between the longest and shortest NWs. The same ratio result was obtained by Zhang *et al.* [205] for a constant NW radius of 42 nm and the same mechanical input. The doped model (green curve) reveals that piezoresponse values are limited to a few units of mV and are independent of ZnO NW length. This is in agreement with simulation results of Romano *et al.* [214] and is linked to the screening effect in the whole core of ZnO NW whereby the low piezoresponse is obtained only from the tip of NW. However, this model is in contradiction with the experimental result [196]. The blue curve represents the SFL model including both N_d and N_{it}. For short NWs, the piezoresponse

increases linearly up to $3\mu m$, obtaining the same values compared to the simple model (between 0.25V to 0.65V), and the same variation of piezoresponse (160%) between the shortest and longest NWs. The similar values of piezoresponse for the simple and SFL models have much to do with the depleted state on the core of the NW (with n value 10^{10} times smaller than N_d), as depicted in Figure II-15(a, b). As NW length increases, the piezoresponse asymptotically approaches 0.75 V in absolute value since the potential reaches the value at which the core of the NW starts to be populated with electrons (see Figure II-15(a)). Therefore, the contribution of the piezoresponse comes only from the bottom part of the NW since, as discussed before, the local potential at the interface ZnO/PMMA is different in each configuration, and in turn, Q_s is also different leading to modification of the free carrier distribution into the core of ZnO NW.

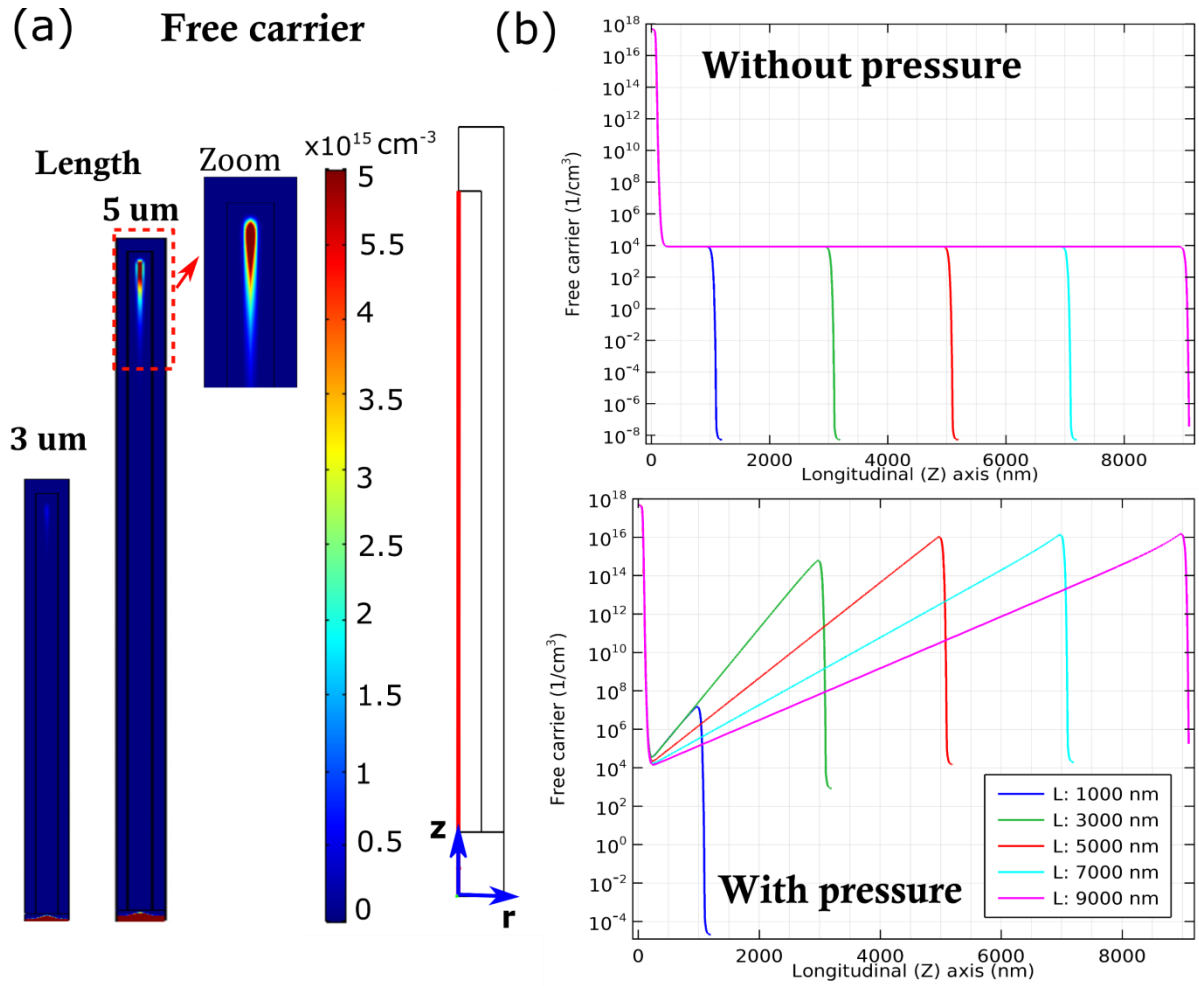

Figure II-15 (a) Free carrier distribution of VING device integrating on NWs grown by CBD(O) method under a force of 31nN (equivalent to 1MPa) on the top surface and an NW with 50nm wide. (b) Free carrier values along the red line in the c-axis (Z axis) varying the NW length for VING without (top plot) and with (bottom plot) applied force at $N_d = 5 \cdot 10^{17}\ cm^{-3}$ *and* $N_{it} = 10^{13}\ eV^{-1}cm^{-2}$.

Upon considering all the facts in the VING model (as N_d and N_{it}), the numerical results showed the length-dependent piezoresponse in the region I and length-independent piezoresponse in region II (see Figure II-14). As observed above, there is no advantage in further increasing NW length. We expect that the length at which this saturation occurs is probably smaller for NWs of a larger radius.

II.4 Electromechanical optimization of the VING device

For VING simulations, we investigate several electrical parameters such as the electrical current density, the capacitance, the electrical charge density, the electrical energy density, the piezoelectric coefficient, and the power density, as a function of the NWs radii. The simulation solves the piezoelectrics and semiconducting coupled equations II- 8 and II- 9 using the Finite Element Method (FEM) and BC (equations in equations II- 8 and II- 9). The initial cell size consists of a 3µm long ZnO NW, the geometry ratio of 0.5 calculated as the ZnO radius R_{NW} divided by the wide of the nanocomposite W (R_{NW}/W), 40nm thick seed layer, and 1 μm thick insulating capping layer of PMMA. The mechanical input parameter of 100 kPa (in the range of what was used in experiments) was fixed in all studies. The VING was connected to a resistive load (R_L) and the electrical parameters were computed. In all our studies, we consider a semiconducting ZnO model, together with simulations of an insulating ZnO model as a reference. In this section, we have oriented the c-axis along the [0001] direction (i.e. Zn polarity).

II.4.1 Electric parameters as a function of load resistance on VING device

The load resistance connected to the VING device allows for the extraction of the electrical energy generated by the mechanical stimuli applied to the device. All the $N°$ unit cells of the whole 1 cm^2 VING device have the same dimensions and spacing between them, as depicted in Figure II-16(a). Finally, all the unit cells are electrically connected in parallel under the same compression. Thus, the load resistance can be extrapolated using the relation:

$$R_{VING} = \frac{R_L}{n} \qquad \textit{II- 19}$$

For instance, a VING device of $1cm^2$, with 200nm width and ZnO NW of 50 nm radius, can contain up to $3.18 \cdot 10^9$ NWs per cm^2, which corresponds to an extrapolating R_L value of one unit cell from $10^{16}\Omega$ to a R_{VING} value of VING device of 3.1 $M\Omega$. It should be noted that R_L

values of one cell are consistent with existing numerical values obtained by FEM simulation in COMSOL environment and a 1D analytical model of ZnO VING with a value of $6.33 \cdot 10^{16}\Omega$ [204,209]. These works consider similar NWs dimensions ($2\mu m$ long and 50nm radius, 0.5 in geometry ratio) and mechanical input (5 N cm^{-2}). Moreover, the extrapolated R_{VING} value is of the same order of magnitude as the one experimentally measured previously by our group (1 $M\Omega$) [192].

When the VING device is subjected to deformation, the generated current flows in the load resistance. The transferred power depends on the load resistance and the internal impedance of the VING. The electric current is computed from equation II- 10, and the instantaneous power is given by

$$P_{NW} = \frac{\Delta\varphi(t)^2}{R_L} = I_0(t) \cdot \Delta\varphi(t) \qquad \textit{II- 20}$$

Where $\Delta\varphi(t)$ is the piezoelectric output potential as defined in Appendix I. We have demonstrated that the power density in this time-dependent FEM model can be obtained either using R_L or I_0 as a variable (see App. I.1 in Appendix I). This complete study of electric parameters on VING devices takes into account also the generated charge (Q_0 (t)) on the top surface (equation II- 11), and piezoelectric coefficient (d_{33}^{eff}) (equation II- 12).

The capacitance value is obtained by analyzing the exponential decay of voltage against time upon considering the VING device as a capacitor discharging element (see section II.2.5).

The energy delivered during a "Press" or "Release" action can also be calculated by integrating the power over R_L between t_1 (actuator) and t_2 (end of charging or discharging process) [230], following equations

$$E_{elec} = \int_{t_1}^{t_2} \frac{\Delta\varphi(t)^2}{R_L}\, dt \qquad \textit{II- 21}$$

Figure II-16 (b-d) shows electrical output characteristics as a function of resistance load. It is worth noticing that both the voltage and current vary as the R_{VING} parameter increases (see Figure II-16 (b, c)), increasing until an asymptotic value (for absolute value of voltage) and reducing to zero (for current), such as experimentally happened in some reports As a consequence, the output power density as a function of R_{VING} is bell-shaped and reaches a maximum value of 0.452 nWcm^{-2} at an optimal load value (R_{opt}) of 3.14 $M\Omega$. According to

previous works [209,231], this R_{opt} is associated with the impedance value of the VING device. It is also worth mentioning that the order of magnitude of this power density is 30 times lower than the one measured in our group (13 nWcm^{-2}) for R_{opt} of $1M\Omega$ [192]. Nevertheless, this calculated power density is of the same order of magnitude as the other one measured by Yu group (0.31 nWcm^{-2}) [189] for an unknown value of R_{opt}, and without PMMA matrix on the top surface of the NWs(see Table I-6 in Chapter-I), but with the same geometrical parameters for ZnO NW. The possible reason for these deviations could be the exact measurement of mechanical input in the experimental works as well as the values of N_{it} and N_d for NW grown by CBD method and the assumption of totally homogeneous NW into the unit cells.

Further electric parameters such as electric charge density and energy density were explored because they are intimately related to the efficiency of the piezoelectric VING device [211]. Figure II-16(e) shows that the electric charge density follows the same trends of electric current, achieving a maximum value of about -60 pC cm^{-2}. So far, no theoretical references exist to compare the calculated electric charge density. However, a few recent experimental works measured the electric charge displaced per peak of mechanical stimuli for a VING device based on ZnO NW [196,205]. He et al. [196] employed ZnO NWs with dimensions comparable to our numerical model, although the mechanical input is not reported, as listed in Table I-6 in Chapter-I. For an area active of piezoelectricity of ZnO NW of 2.5 cm^2, the VING device generated some values of charge displacement between 1.2 nC and 1.9 nC, which correspond to the charge displacement density between 480 pC cm^{-2} and 760 pC cm^{-2}. The results of our simulations are between 8-12 times lower than the values reported in the literature. This discrepancy is probably due to a different mechanical input since the output potential (around 660 mV) [196] is about ten times larger than in our study (see Figure II-16(b)). More recently, Zhang et al. [205] performed electrical experiments to extract the electric charge density on VING using the same structure as our model, but with different ZnO NWs dimensions (40nm radius and $1\mu m$ long) preventing a precise quantitative comparison. For dynamic stress of 200kPa at 1Hz applied on the top surface of the device, they obtained surface density values of 50 and 75 pC cm^{-2} for two different thicknesses of PMMA of 1.5 μm and 2 μm, respectively.

Figure II-16(f) displays the instantaneous electric energy density per mechanical actuation as a function of R_{VING}. Its maximum value of about 2 pJ cm^{-2} was achieved for an R_{VING} value of 100 $M\Omega$ and its order of magnitude is 4 times lower than the value reported by Hinchet et al. [211]. This value was obtained for a single and array of ZnO NWs of the same radius (50 nm), but shorter (0.6 µm) and with a larger applied force (1 MPa). A couple of experiments works have reported energy values three orders of magnitude higher (around 1-10 nJcm^{-2}) than our

simulation results [195,229]. The disagreement can be mainly associated with mechanical input, NW density, doping level N_d, trap density N_{it} and flexible substrates, which enhance the mechanical conversion efficiency in the VING device.

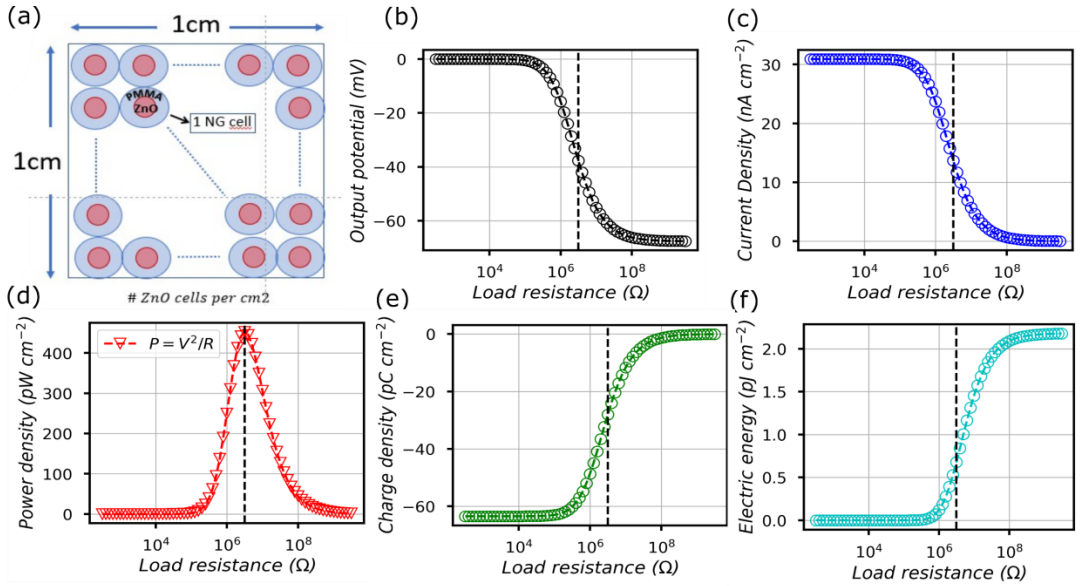

Figure II-16 (a) Schematic cross-section of the number of unit cells inside an area of 1cm x 1cm. Extrapolation of generated electric values such as (b) output potential, (c) electric current density, (d) instantaneous power density, (e) electric charge density, and (f) instantaneous electric energy density for a VING device of 1cm² as a function of load resistance (R_L) connected in parallel, an applied force of 3.14nN (equivalent to 100kPa) on the top surface, 50nm wide and 3µm long.

II.4.2 Comparation of simulated and experimental values of R_{opt} and C_{NG}

The present study aims at comparing the internal impedance, as well as the capacitance value calculated in the VING simulation with our values and values found in the literature. To do this, we extrapolated the optimal resistance R_{opt} and capacitance C_{NG} values of a single VING unit cell from the numerical results (see App. I.2 in Appendix I) by dividing R_{opt} or multiplying C_{NG} by the number of unit cells (n) into a specific area (A). These values allow quantitative comparison of results from different sources.

Figure II-17(a) illustrates the extrapolated R_{opt} of a 1 cm² VING device as a function of ZnO radius when the VING device is in the optimal conditions for the instantaneous power density. For comparison, we took the values from the literature [192,196] considering a VING device with an area of 1 cm². It can be observed from Figure II-17(a) that the reported values are within the range of simulated values. Besides, the piezo-semiconductor FEM simulation demonstrates

a ZnO radius-dependent resistance R_{opt} (corresponding to the place of power density), exhibiting two distinct values of 3.14 $M\Omega$ and 1.25 $M\Omega$ for smaller (<70 nm) and larger (>70 nm) ZnO NW, respectively. This ZnO radius-dependent resistance is associated with the values of semiconducting properties as the doping level and trap density (red dash line in Figure II-17(a)). The low and high R_{opt} values would correspond to results where the core of the nanowires is neutral (polarization screened by free carriers) and fully depleted, respectively. Note that the radius at which the transition occurs is a function of the exact doping level and traps density.

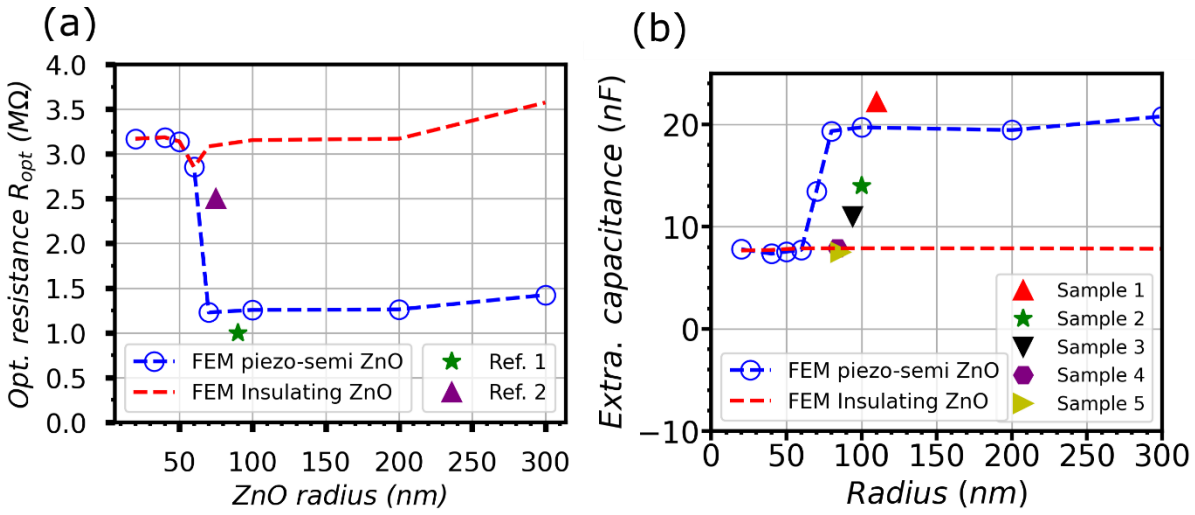

Figure II-17 FEM results of (a) the optimum load resistance values for a VING device with an area of 1cm² and (b) the capacitance values for a VING device with an area of 5.7 cm² without (red dashed line) and with piezo-semiconducting properties after applying a constant pressure of 100kPa on the top surface to NW with 3µm long at $N_d = 5 \cdot 10^{17}\ cm^{-3}$ *and* $N_{it} = 10^{13}\ eV^{-1}cm^{-2}$. *The reference works used in (a) plot correspond to Ref.1* [192] *and Ref.2* [196]. *The experimental data correspond to the Table App. I- 1 in Appendix I.*

As for the resulting capacitance value, the simulated values were compared with measurements performed on five VING devices through the electrical characterization using the Electrical Impedance Spectroscopy (EIS) technique. VING devices exhibit the same ZnO NW dimensions (length, radius, seed layer, and PMMA thickness) and an area covered with NWs of 5.7 cm^2 (more details of the EIS process in App. I.3 of Appendix I). Similar to the results obtained for the optimal resistance, the simulated capacitance exhibit a ZnO radius dependence when considering the piezo-semiconducting model (see Figure II-17(b)). The capacitance varies from 8 nF to 20 nF for small and large NWs, respectively. In contrast, in the insulating ZnO FEM simulation, no effect of the radius is observed and the capacitance has a constant value of 8 nF. The experimental values measured by EIS also exhibit an NW radius dependence, with values

in the range corresponding to the numerical simulation. The experimental results seem clear to follow a significant influence of semiconducting properties.

II.4.3 Effect of radius in generated electric parameters on VING device

To further optimize the VING devices, we investigated the effect of the NW radius on the VING electrical parameters (voltage, current, power, charge density energy density and piezoelectric coefficient) at the optimal load resistance value R_{opt}. Figure II-18(a-f) shows that each electric parameter reaches a maximum value when the ZnO NW radius is smaller than 60 nm. The values obtained for small radius are similar to the ones obtained when considering ZnO as an insulating material (red curve in Figure II-18 (a-f)). The above consists of the fact that the screening effect is reduced at low radii, so that the whole ZnO NWs contributes to the generated piezoelectric field, such as happens in the model which does not consider the semiconducting character of ZnO. In contrast, NWs with a radius value larger than 70 nm exhibit poorer performance due to the screening effect.

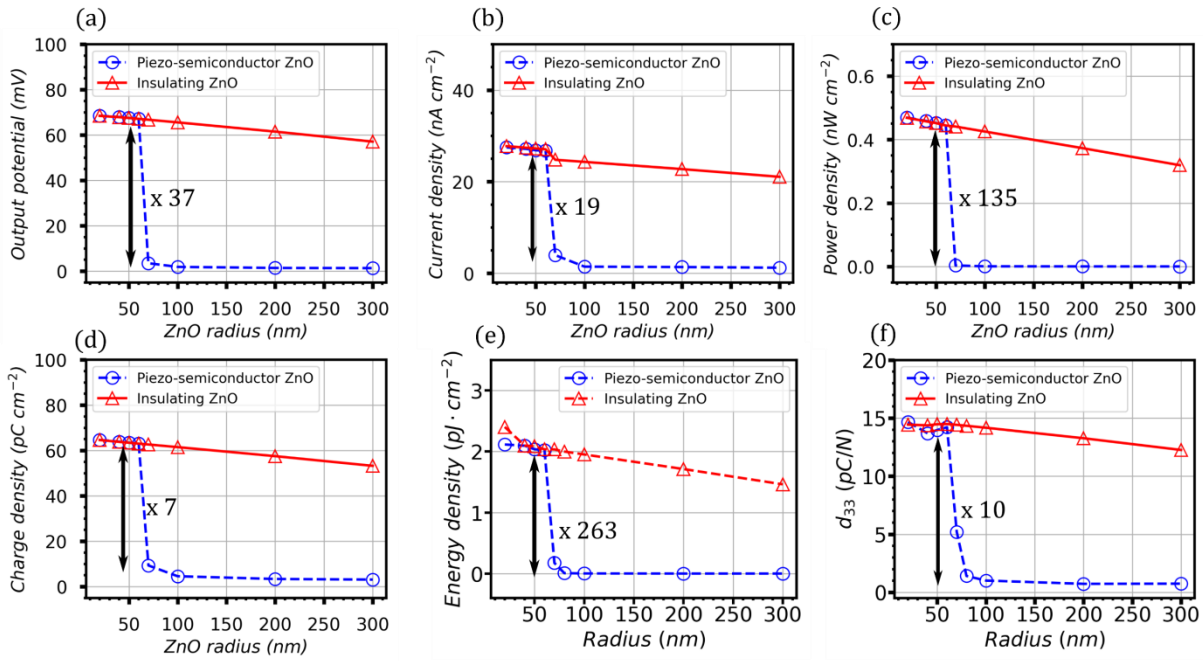

Figure II-18 The optimal value of (a) output potential, (b) current density, (c) instantaneous power density, (d) charge density, (e) electric energy density, and (f) piezoelectric coefficient generated by the VING device after applying a constant pressure of 100kPa as a function of ZnO radius for an insulating (red line) and semiconducting (blue dash line) ZnO NW with 3μm long. Everything was made at a high load resistance value except for the electric current and the electric charge density.

To compare the simulated electric parameters, Figure II-18(a-f) shows that the output potential, the current density, the optimum power density, the charge density, the electric energy density,

and piezoelectric coefficient for smaller ZnO NW radius were 37, 19, 135, 7, 263, and 10 times larger than those with large ZnO NW radius (i.e., radii values greater than 80 nm).

As evidenced in Figure II-18 (f), the calculated effective piezoelectric coefficient of the VING devices reaches its maximum value of 14 pC N^{-1} at a smaller radius (full depleted NW) and decreases down to 1 pC N^{-1} for the larger NWs (strong screening). These values are comparable to the effective piezoelectric values d_{33}^{eff} (between 2-12 pm V^{-1}) measured on ZnO NWs using the converse piezoelectric method [142–145], and higher than those of ZnO thin films (between 1.8-2.6 pm V^{-1}) [76] at the optimal conditions. Furthermore, another experimental value of 4.8 pC N^{-1} reported by Tao *et al*. [218,232] is also within this range of values for the VING device based on ZnO NW with a radius close to 70 nm and using a similar direct piezoelectric method.

II.5 Conclusions

In this chapter, we have carried out the continuation of the theoretical study of trap density or SFLP approach on VING device based on ZnO NW developed by R. Tao in our group. At that time, she calculated the piezopotential as the contribution of piezoelectric effects by comparing the results obtained with and without account for the piezoelectric coupling terms in the electro-mechanical equations. This approach is valid for rather low trap density values. However, as we discovered during her thesis, above a few 10^{12} $eV^{-1}cm^{-2}$, surface traps generate a non-negligible polarization in the nanowire, as a result of the converse piezoelectric effect. Since experimental trap density seems to be rather in the range of 10^{13} $eV^{-1}cm^{-2}$, we modified the approach to calculating the change of output potential resulting from the change of external mechanical load (comparing the results with and without external pressure on the VING or on the NW in our case), keeping the piezoelectric coupling terms in the equations. This approach is valid in a wider range of N_{it}, N_d and size (radius, length) parameters.

Using time-dependent FEM simulations, we also extracted an effective piezoelectric coefficient d_{33}^{eff}. The piezoresponse and d_{33}^{eff} values were extracted from simulation with account for doping and surface traps. Our results demonstrate that the polarization field is significantly screened by free carriers for low densities of surface traps (N_{it}), while for large densities the screening effect is suppressed, allowing much better performance to be reached. Besides, a non-symmetry between the piezoresponse pulses obtained after “Press” and “Release” actions was detected for certain values of N_{it}. This was explained by a partial screening of polarization near the top of the NW after “Release” action, when traps are considered ultra-slow. In terms of trap dynamics, we only considered the two extreme cases of ultra-slow and ultra-fast traps. A

significant impact was observed on VING performance, resulting in a much larger piezoelectric response for ultra-slow traps than for ultra-fast traps. Differences in trap density but even more in trap dynamics may explain the dispersion of experimental values found in the literature in terms of piezoresponse and effective piezoelectric coefficient.

We used simulation to evaluate what could be expected from the different classes of methods which can be used to grow ZnO materials. Through a collaboration with V. Consonni in LMGP, we characterized these methods by their affordable range of NW dimensions, range of doping level and estimated density of surface traps. Our results explicitly showed a radius-dependent and length-dependent piezoelectric response, similar to what has been exhibited in some experimental reports. Longer and narrower ZnO NW provided a much better piezoelectric response, as a result of full depletion. However, the critical radius below which the full depletion condition can be reached was different for each class of growth method. We verified that an analytical evaluation could be used in order to evaluate this critical radius based on doping level and trap density. We included in this analysis, the CBD method used for the fabrication of VING devices in our group. We found that growth orientation (Zn-polar or O-polar) should have an influence, with the possibility of using wider NWs with O-polar orientation.

We found also that the piezoresponse of thin NWs should saturate when length increases. This was explained by the fact that there is a linear increase of potential along the length of the nanowire, as a result of the polarization of the depleted NW, which stops when the potential reaches a value at which the conduction band approaches the Fermi level, so that the core of the NW starts to be populated with electrons. Increasing NW length above this point has no effect on the piezoresponse.

Our simulation results are in excellent agreement with the experimental electrical features measured on realistic VING connected to resistive loads. In particular, the extrapolated numerical results for the optimum load resistance and capacitance are in good agreement with previous studies as well as experimental results from our group. Our simulations predict an NW radius dependence of the electrical features of VING under compression, with better performances for small NWs. Using $5 \cdot 10^{17} cm^{-3}$ doping level and 10^{13} $eV^{-1}cm^{-2}$ trap density, which are in the range of values expected for CBD based on literature, the NW radius value should stay below 70 nm. Simulation results demonstrated a very similar trend compared to experimental results. Further adjustment of doping level and trap density may even allow a perfect fit to be reached.

In view of all these simulation results, it seems that accounting for surface traps, with slow dynamics, could provide a consistent representation of the piezoresponse and effective piezoelectric coefficient d_{33}^{eff} of VING devices based on ZnO.

A first step toward the direct evaluation of the radius-dependent piezoelectric response could consist in measuring the effective piezoelectric coefficient $\boldsymbol{d_{33}^{eff}}$ of an individual piezoelectric NW using the AFM-based technique and comparing the coupled simulation results, as will be presented in the next chapter. In addition, the importance of the surface charge associated with surface traps evidenced in the simulations provides a strong incentive to consider the concept of chemical sensors based on piezoelectric detection due to the influence of the environment atmosphere on band bending inside the NW. This can be done in a second step after evaluating the surface potential (KPFM measurement) and the Schottky barrier height (CAFM measurement) under a controlled atmosphere, and by comparing it with a model of the Schottky junction, which includes doping level N_d and trap density N_{it}. In this regard, the surface trap density and surface Fermi level position can be extracted from the fit with measurements, as will be shown in the last chapter.

Chapter III. Local assessment of the piezoelectricity of ZnO NWs

The piezoelectric coefficient $\boldsymbol{d_{33}^{eff}}$ is well-known as an important parameter for any piezoelectric material. We demonstrated numerically in the last chapter that nanocomposites based on ZnO NWs reach the optimal d_{33}^{eff} values for a certain combination of NW radius, doping level and trap density. These optimal values are also related to the optimal value of output potential and power density. Experimentally, the local piezoelectric properties of nanostructures are usually evaluated employing the effective piezoelectric effect under AFM. This tool offers the possibility to extract the effective piezoelectric coefficient $\boldsymbol{d_{33}^{eff}}$ as well as the polarity of the crystal structure. In this chapter, ZnO NWs were grown on flexible substrates (PET/ITO and PET/AZO) using gravure printing for depositing the ZnO seed layer, and then CBD method for growing the NWs. Both methods work at low temperatures, are low-cost, and easy manufacturing processes. The piezoelectric response of these NWs was measured using the Piezoelectric Force Microscopy (PFM) technique for different substrates, where Si/ITO was used as a reference. Moreover, the effect of sintered seed layers on the morphology of the grown ZnO NWs and their piezoelectric properties was thoroughly investigated using a sophisticated statistical method. Finally, the radius effect on the piezoelectric performance of ZnO NWs was analysed.

As was mentioned in Chapter I, energy transducers based on ZnO NWs integrated on flexible substrates are interesting but challenging as they require low-temperature processes compatible with the substrate. Within the project PULSE-COM, ZnO seed layers were deposited over flexible substrates employing an alternative method called gravure printing. These substrates were supplied by Italian partners from the Italian Agency for New Technologies, Energy and Sustainable Economic Development (ENEA). Different electrodes were used as well: Aluminium-doped Zinc Oxide (AZO) and indium-doped tin oxide (ITO). Moreover, different sintering times were applied to the seed layers in order to investigate their effect on the growth process and the morphology of the grown NWs. The analysis of the morphology of the successfully grown NWs will be presented in the first part of this chapter.

As examined in Chapter I and Chapter II, the performance of a piezoelectric material can be evaluated through the piezoelectric coefficient $\boldsymbol{d_{33}^{eff}}$. In the simulation results, optimal values of output potential and power density were obtained for thin ZnO NWs, which was also directly related to the optimal values of d_{33}^{eff}. This coefficient showed a clear dependency on the radii of NWs with a transition value around 70 nm NWs grown by the CBD method. Experimentally, the $\boldsymbol{d_{33}^{eff}}$ of ZnO NW parameter had not been previously investigated in our group, and to the best of our knowledge, its radius dependence has not been investigated by other groups. On the other hand, some experimental works have demonstrated the effect of ZnO NW radius on the generated current [233] and voltage [234] by nanocomposites structures. Therefore, the exploration of $\boldsymbol{d_{33}}$ is one of the objectives of this chapter.

Two crystal polarities were previously observed on top of ZnO NW grown by CBD technique according to the literature (see section I.2.2.1 in Chapter I). The piezoelectric response (i.e., the global $\boldsymbol{d_{33}^{eff}}$) could be affected by the type of polarity. Recently, Piezoelectric Force Microscopy (PFM) technique has been widely employed by researchers in order to study the $\boldsymbol{d_{33}^{eff}}$ and the polarity of thin films and nanostructures simultaneously. This $\boldsymbol{d_{33}^{eff}}$ coefficient represents the mechanical to electrical conversion using the converse piezoelectric effect.

In the second part of this chapter, we utilized the PFM technique and proposed a new statistical strategy to measure $\boldsymbol{d_{33}^{eff}}$ and the polarity of ZnO NWs grown on rigid (Si/ITO) and flexible (PET/ITO and PET/AZO) substrates. Finally, the effect of using different electrodes and sintering treated seed layers on the $\boldsymbol{d_{33}^{eff}}$ coefficient of ZnO NWs was explored.

III.1 ZnO Nanowires growth

III.1.1 Seed layer deposition

Following the similar work performed by Z. L. Wang at Georgia Tech, and, our group, the work of Dr. Hinchet, the CBD method has been extensively used in IMEP-LaHC as a standard recipe for growing ZnO NWs on rigid (such as Si) or flexibles (such as stainless steel foil) substrates. This recipe [192] utilizes ZnO seed layers that are deposited by the Atomic Layer Deposition (ALD) instrument available in the clean room of Upstream Technology Platform (PTA) at MINATEC. Typically, this instrument requires a high-vacuum system and a relatively high temperature (around 250°C) for depositing a high quality ZnO seed layer of about 40 nm in thickness. In this PhD work, a 166-nm-thick conductive layer of ITO was deposited over Si substrates of 375 μm in thickness and 1.5 x 1.5 cm^2 in area using sputtering technique, then the

ZnO seed layer was deposited by ALD. These rigid samples were prepared as a reference for the growth of ZnO NWs and piezoelectric characterizations.

Under the project PULSE-COM, the main objective is to develop flexible piezoelectric devices at low cost (vacuum-free) and compatible with low temperature processing (below 90 °C). The ZnO seed layer was then deposited on flexible substrates made of poly(ethylene terephthalate) (PET) with 125 μm in thickness and 2 x 1.5 cm^2 in area, employing the gravure printing technique (see more detail about this method in App. II.1) at low temperature (100 °C), as depicted in Figure III-1(a). Gravure printing has been rarely used to grow ZnO NWs and no piezoelectric characterization has been reported on NWs fabricated with this technique. This gravure printing process was carried out by Italian partners within PULSE-COM. The printing of a ZnO seed layer 55 nm thick was deposited on a 150-nm-thick ITO coated PET film or a 100-nm-thick AZO coated PET film. After printing, the samples were exposed to a vapor annealing sintering treatment at a low temperature (50 °C) to investigate its effect on NW morphology during different times as 0 hours (h), 1h, 1h and 30 min and 2h and 30 min on both ITO/PET and AZO/PET substrates. These times will be represented in the results as 0h, 1h, 1.5h and 2.5h, respectively.

III.1.2 Chemical bath deposition (CBD)

NWs were grown on seeded substrates using a precursor solution through the chemical bath deposition (CBD) process. The precursor solution was combined with an equimolar of 50 mM of Hexamethylenetetramine (HMT, $(CH_2)_6N_4$ (CH2), Sigma-Aldrich) and Zinc Nitride hexahydrate ($Zn(NO_3)_{2.6}H_2O$, Sigma-Aldrich) in 500 ml of deionized water (DI) at room temperature. This precursor solution was stirred for 20 min at 1000 rpm. and afterward, it was put to rest for 40 min before transferring the clear solution inside glass bottles (see Figure III-1(b)). Then, each seeded substrate was clamped on glass slides using Kapton tape and placed face-down into the solution, as shown in Figure III-1(c) and 1(d). Afterward, the hydrothermal growth process was executed by putting the samples into an oven at 85 °C for 16 h. Following the chemical reactions, the ZnO NWs over PET-ITO/AZO substrates were rinsed with DI water and dried with N_2 gas.

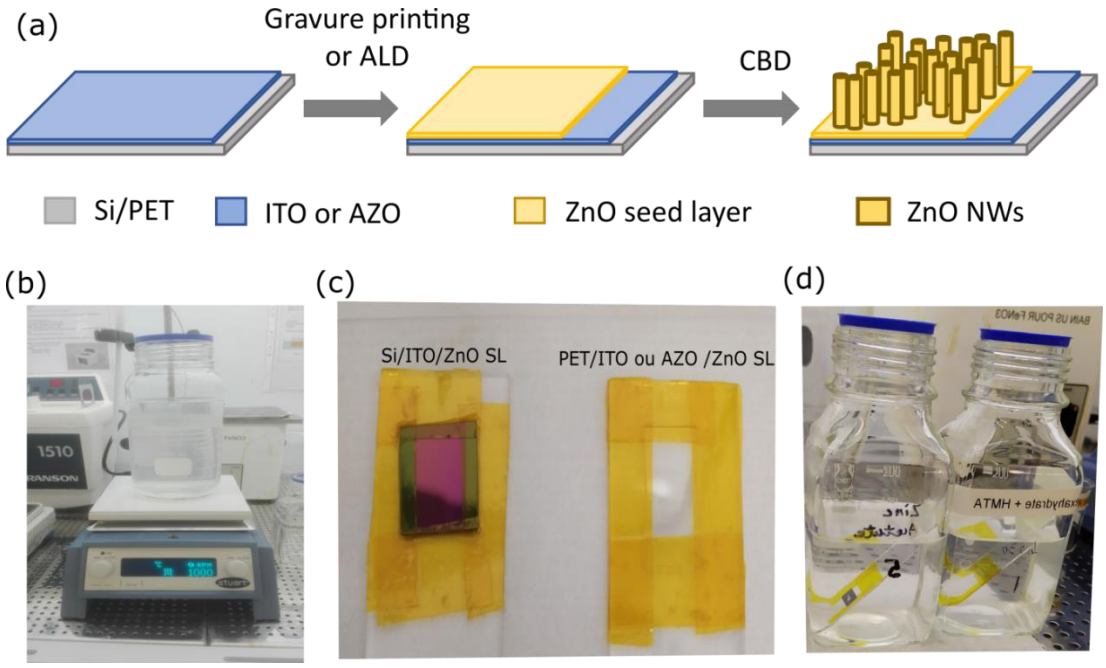

Figure III-1 (a) Schematic image of the fabrication process of ZnO NWs over rigid (Si/ITO) and flexible (AZO/PET or ITO/PET) substrates with a ZnO seed layer deposited by ALD and gravure printing techniques. (b) Optical image of the stirring process for the precursor solution (Zinc nitride and HTMA concentrations). (c) Pieces of Si/ITO/ZnO and PET/ITO or AZO/ZnO substrates are attached to a glass film using an adhesive Kapton tape on the edges. (d) Samples tilted face down in the precursor solution.

III.1.3 Vertical ZnO NWs integrated into dielectric matrix

To carry out the PFM characterization in the classical contact mode, a particular sample (called here sample #1) was developed by encapsulating the ZnO NWs that were grown on the ZnO seed layer (ALD)/Si substrate (see steps i) and ii) in Figure III-2(a)). Afterward, two types of poly(methyl methacrylate) (A2 and A6 from MicroChem 495PMMA) were deposited on the top of the NWs by employing the spin-coating technique [192]. Firstly, two layers of PMMA A2 were directly put on ZnO NWs. This type of polymer has a low viscosity which allows easy penetration between the NWs. Secondly, two additional layers of PMMA A6 (with high density) were used to completely cover the NWs surface, as shown the step iii) in Figure III-2(a). Finally, the polymer layer was etched by Reactive Ion Etching (RIE) using Ar/O_2 gas for 10 min at 60 W until the NWs tip were visible, as shown in Figure III-2(a) and Figure III-2(b).

Figure III-2(b) shows that the NWs exhibit a hexagonal shape and are vertically aligned over a Si substrate. The density of the NWs is around 10-12 NWs/μm^2. After statistical analysis, the

NWs diameter shows a Gaussian distribution between 100 nm and 400 nm, as shown in the inset image in Figure III-2(b). The distribution of NW diameter was analysed as the superposition of 2 Gaussian families, as shown in the inset of Figure III-2(b). The average NW radius of the main Gaussian distribution is about 95 nm.

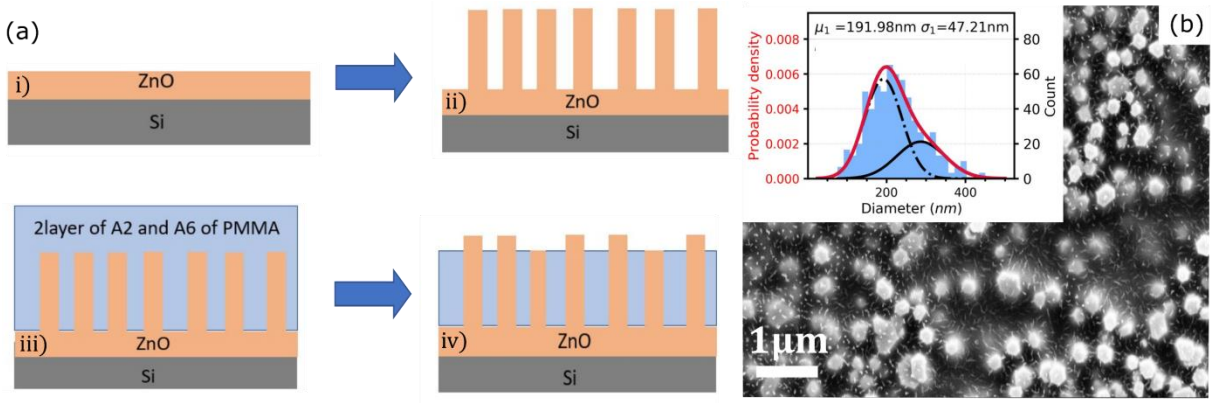

Figure III-2 (a) Fabrication process of the encapsulated ZnO NWs with PMMA dielectric matrix. These NWs were grown on Si substrate using CBD. (b) Top-view SEM images of ZnO NW after the etching process with Ar/O_2 for 10 min at 60 W. The inset image corresponds to the fit of the diameter distribution of this sample.

III.1.4 ZnO NWs growth on different substrates

Following the guidelines of the PULSE-COM project, two samples were fabricated using a rigid ZnO (ALD)/ITO/Si substrate (called here sample #2) and a flexible as-printed (not annealed) ZnO seed layer/ITO/PET substrate (called here sample #3). The structure of sample #2 has been regularly used by the last two Ph.D. works for fabricating the composite nanogenerator devices (although without ITO electrode), so it will be the reference sample. While sample #3 has been considered as a new perspective on fabricating flexible piezoelectric devices under vacuum-free conditions and low temperatures, which has not been carried out so far by our group.

All parameters of the CBD method were kept constant for both samples, as discussed at the beginning of this section. Figure III-3(a) and 3(b) show that ZnO NWs display good vertical alignment and comparable density values of about 13 NWs/µm^2 and 10 NWs/µm^2 for samples #2 and #3, respectively. By extracting the mean radius value (see the inset images in Figure III-3(a) and 3(b)), sample #2 has a value of 100 nm and sample #3 a value of 105 nm. The cross-sectional SEM images of ZnO NWs grown on samples #2 and #3 show that their length values are approximately 3.5 µm (see Figure App.II- 2) which is similar to the values achieved by Tao *et al.* [192]. Qualitatively speaking, the NWs grown on the flexible substrate were

successfully achieved. Their NWs size characteristics are comparable in terms of radius and verticality to those grown from a seed layer deposited by the ALD technique.

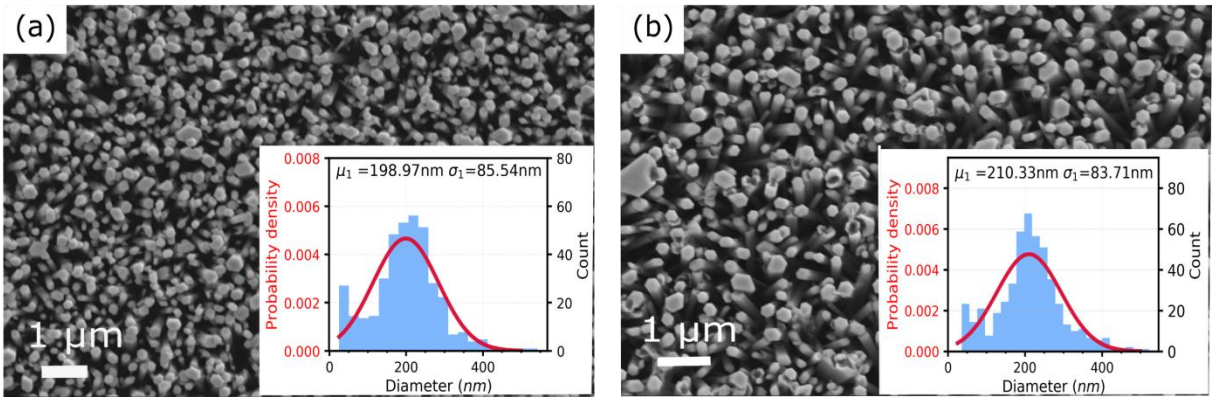

Figure III-3 SEM images of the ZnO NWs grown on (a) ZnO (ALD)/ITO/Si substrate and (b) as-printed (non-annealed, i.e., 0h) ZnO seed layer/ITO/PET substrate. The inset images correspond to the fit of the radius distribution of each sample.

III.1.5 ZnO NWs growth on different electrodes

Once the growth of ZnO NW on flexible substrates has been effectively accomplished, the assessment of piezoelectric properties on ZnO NW was proposed among the objectives of this Ph.D. work and within PULSE-COM project when employing two electrodes (ITO and AZO) and different sintering time parameter of 0h, 1h, 1.5h and 2.5h on the as-printed ZnO seed layers. The CBD method was performed while keeping constant all parameters, such as those fabricated previously.

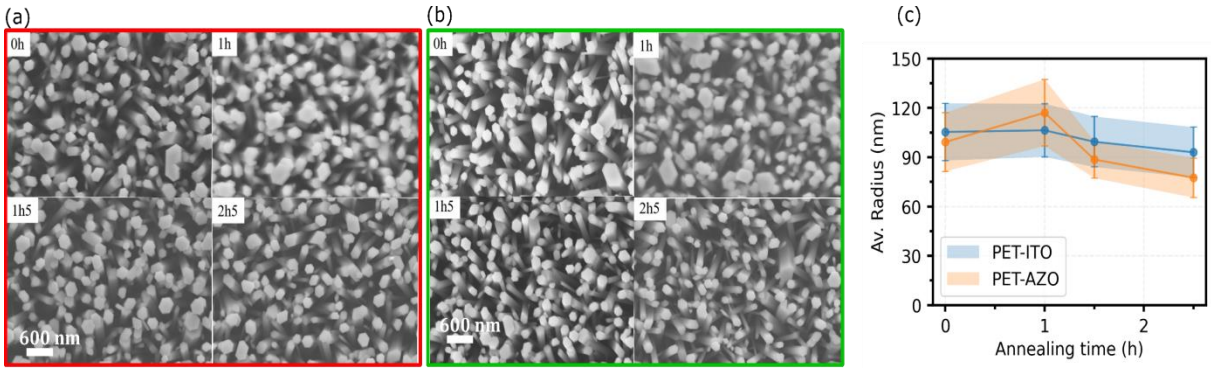

Figure III-4 SEM images of the top view of ZnO NWs grown on (a) PET-ITO and (b) PET-AZO substrates by CBD technique for different sintering treatment times in ZnO seed layer as 0h, 1h, 1.5h and 2.5h. (c) The mean value of ZnO radius of fitted Gaussian distributions extracted from the histograms in App. II.3 for each sample, as a function of the sintering treatment time in both ZnO/ITO and ZnO/AZO substrates. The limit of the colored region corresponds to the standard deviation of the radius values.

III.2 PFM measurements

Piezoelectric Force Microscopy (PFM) is commonly utilized to analyse the piezoelectricity on piezoelectric and ferroelectric nanomaterials [235]. PFM is usually a contact mode AFM method that uses the converse piezoelectric effect, i.e., the material is deformed as a consequence of an applied driving voltage between the sample bottom electrode and AFM probe. The PFM technique is being widely used as well to study the polarity and the piezo response properties on thin films and NWs [127,236]. A Bruker Dimension Icon (Santa Barbara, CA, USA) atomic force microscope instrument was used to carry out all PFM experiments, as shown in Figure III-5(a). This instrument is composed of the AFM head, the piezoelectric and photodetector systems (see Figure III-5(b)). In the head, an AFM probe is placed at the end side. The piezoelectric system moves the cantilever in three degrees of freedom and the photodetector system measures the smallest displacements made from the cantilever. In our experimental PFM setup, a periodic AC signal (see Eq. III- 1) is applied to the tip with a frequency ω and amplitude A_{AC} with the help of a lock-in system, as illustrated in Figure III-5(c) and 5(d).

$$V = A_{AC} \cdot \cos(\omega t) \qquad \textit{III- 1}$$

Local and non-local electric fields are generated between the tip and sample making the piezoelectric sample expand and contract as a result of the driving electrostatic forces. The cantilever deflection information z is retrieved by the photodiode system and treated by the lock-in system. This deflection signal is frequently measured at the first harmonic component ω of the electrostatic force F_ω (see equation App. 4 in Appendix II) and given by:

$$z = \Delta z_{piezo} + z_\omega \qquad \textit{III- 2}$$

where Δz_{piezo} is the local piezoelectric deformation ascribed to the effective piezoelectric coefficient $\boldsymbol{d_{33}^{eff}}$ of the material and z_ω is the local electrostatic deformation produced by the electrostatic effect [237]. These quantities can be calculated as

$$\Delta z_{piezo} = \boldsymbol{d_{33}}\, A_{AC} \sin(\omega t + \varphi) \qquad \textit{III- 3}$$

$$z_\omega = \frac{F_\omega(t)}{k} = -\frac{\partial C(z)}{k\,\partial z}(V_{dc} - V_s)\, V_{AC} \sin(\omega t + \varphi)$$

where k, C, V_{dc}, V_s and φ are the cantilever stiffness, capacitance of cantilever–sample structure, the external DC bias, the surface potential, and the phase shift between the driving voltage and the AC piezoresponse signal, respectively. According to Eq. III- 3, it is clear that the electrostatic contribution, in this type of technique is inevitable since z_ω depends on the characteristics of AC signal as well as ω, C and k. Many experimental reports have implemented different strategies for reducing the electrostatic effect (i.e., reducing $z_\omega$value) to obtain an appropriate value of piezoresponse (i.e., a value 100 % of Δz_{piezo}). Among these strategies, recent experimental works have modified either the capacitance between sample and tip [238] or tip stiffness [239] values to enhance the piezoelectric response.

It should be added that PFM technique can simultaneously provide the lateral and vertical amplitude values, as shown in Figure III-5(e) and 5(f). In the case of lateral amplitude, the sample can generate expansion and contraction along the surface plane, twisting the probe to an angle in the direction either clockwise or anticlockwise. As a consequence, the laser point on the photodiode will be moved to the right or left (see Figure III-5(e)). As for vertical motion, Figure III-5(f) shows that an expansion along the z-axis of the material will be moved up the laser point on the quadrant photodiode, while in the opposite case (contraction), the laser will be moved down.

The local polarization orientation of the sample is extracted from phase images. When a positive voltage is applied to the substrate, an electric field appears pointing toward the positive z-axis. If the crystal polarization is antiparallel to the electric field, the piezoresponse exhibits a phase shift value of 180° (also called out of phase), as illustrated by the bottom-right image in Figure III-5(f). In this situation, the sample is axially compressed. On the contrary, when the crystal polarization is parallel to the electric field (see the top-left image in Figure III-5(f)) both voltage signals will be in-phase, producing a stretching of the material.

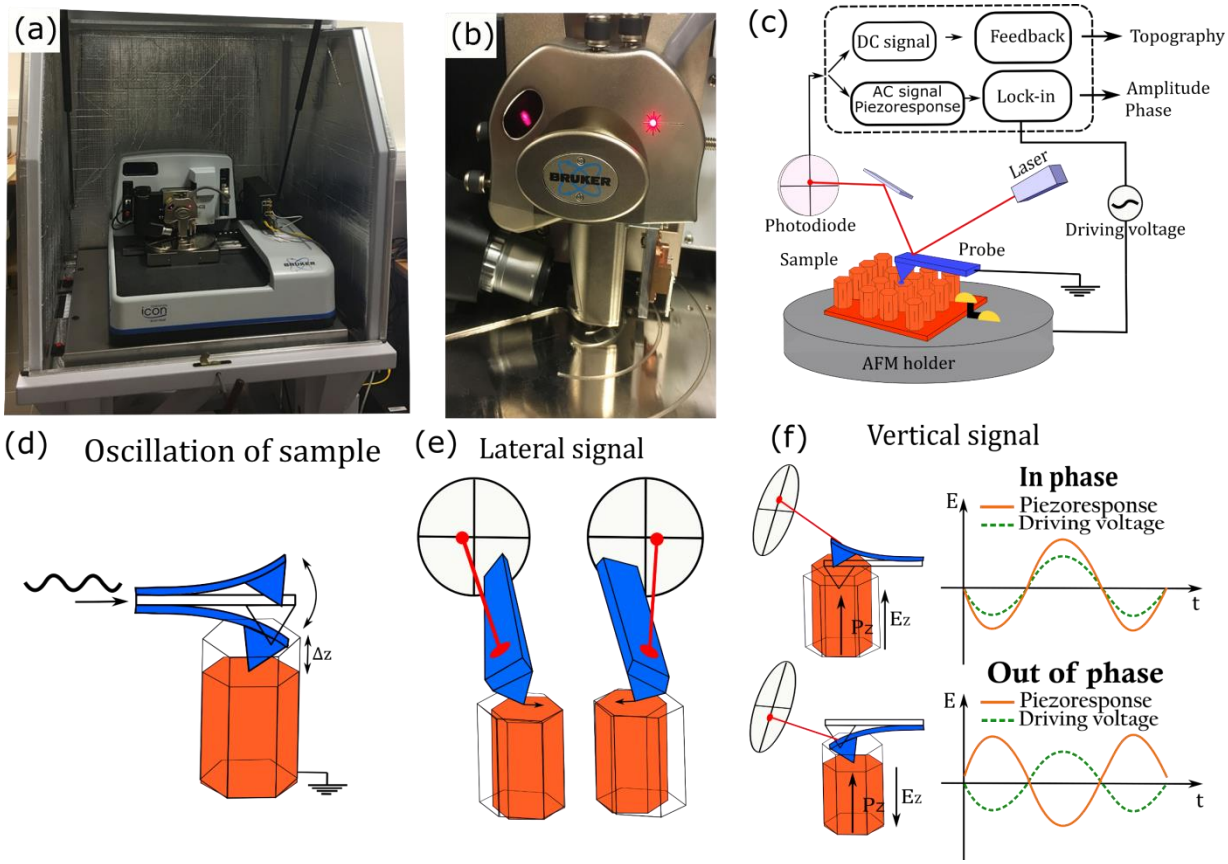

Figure III-5 Optical images of (a) AFM instrument and (b) its head used for calculating the piezoelectric parameters of ZnO NWs. Schematic images of (c) the working principle of AFM instrument in PFM mode, (d) the vibration of the sample after applying an AC signal, (e) the lateral and (f) vertical PFM signal.

III.2.1 Minimizing the electrostatic effect on PFM

The measurement of piezoelectric properties of semiconducting and piezoelectric materials with a relatively small piezoelectric response (i.e., $d_{33} < 10\ pm/V$) may be affected by the influence of a frequency-dependent background that is inherent to the experimental system [240,241]. To avoid a misunderstanding of the PFM signal in our samples, different strategies will be explored in this section to minimize the electrostatic background.

III.2.1.1 Contact resonance frequency of the cantilever

The scanning probe characteristics are the most important element of PFM measurements since they determine the electromechanical coupling with the surface and provide information to the system about the probe displacement. Most research suggests that a frequency-dependent PFM signal is especially important for exploring weakly piezoelectric materials at a contact

resonance frequency of the cantilever [242]. However, recent studies about piezoelectric and semiconducting materials have directly measured and ensured an appropriated value of frequency (about 17 kHz) that is far away from the contact resonance frequency [236]. The latter was done with the aim of avoiding any amplification of the PFM signal. This PhD project used two types of scanning conductive cantilever, such as SCM-PIT and Pt/Si-coated probes. Both probes have their own free resonance frequency of about 62 kHz and 277 kHz, respectively. Their typically contact resonance frequencies on a Periodically Poled Lithium Niobate (PPLN) are about 260 kHz for SCM-PIT probe and 450 kHz and 750 kHz for Pt/Si-coated probe, as shown in Figure III-6(a) and 6(b).

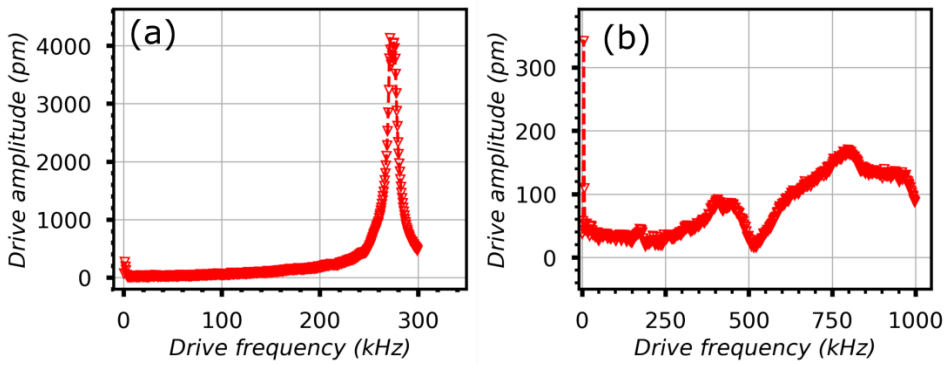

Figure III-6 PFM amplitude response as a function of drive frequency for a scanning probe with (a) 3 N/m (SCM-PIT) and (b) 40 N/m (Pt-Si) in stiffness after contacting the PPLN reference sample at $V_{AC} = 5\ V$.

As shown in Figure III-6(a), the PFM amplitude for SCM-PIT tip is considerably reduced far away from the resonance frequency, reaching up to a value of 30 pm for frequency values less than 50 kHz. As for the Pt-Si tip, the amplitude values are also reduced up to a value of 35 pm for a wider frequency range below 250 kHz. So that, the stiff cantilevers ($k > 20\ N/m$) are preferably selected to keep away the amplification of PFM amplitude near the resonance frequency for PFM measurements. For this reason and as shown later, the Pt-Si probe with a stiffness value of 42 N/m is better in comparison to SCM-PIT probe with the stiffness value of 3 N/m. In addition, the local electrostatic deformation (see equation III- 3) can be reduced by using a stiff cantilever (i.e., $k^{-1} << 1$) since this expression is inversely proportional to the spring constant of the AFM probe. Therefore, the results are better with high k values.

III.2.1.2 Background signal on PFM measurement

The choice of the scanning probe must be carefully revised through the Periodically Poled Lithium Niobate (PPLN) reference sample since its piezoelectric coefficient value is

experimentally well known between 8-8.4 pm/V [243,244]. In addition, PPLN sample is a ferroelectric material with positive (up) and negative (down) domains, making it suitable to put in evidence the electrostatic effect as well as the quantification of the background signal inherent in the PFM technique. As the sample based on ZnO has an unexplored polarization domain, the generated background signal for soft and stiff probes will be explored using the PPLN sample to minimize possible contributions to the PFM amplitude.

PFM measurements were made in the PPLN sample using SCM-PIT and Pt-Si tips before measuring the study sample, as depicted in Figure III-7(a-d). The amplitude distributions on the frontier of polarization domains were evaluated for each tip at 14kHz in frequency and 5V in AC drive voltage (see Figure III-7(a) and 7(b)), revealing that the SCM-PIT tip has a greater contrast among each domain than the Pt-Si tip. This difference is related to the background contribution generated by the tip characteristics (see more detail in [241]). Regarding the phase distributions (see Figure III-7(c) and 7(d)), both scanning probes show an ideal phase contrast with the phase values between -100° (for down domain) to 75° (for up domain) that differ by approximately 180°. To quantify the background signal, Jungk's method [240,241] was employed for each tip. But first must be understood the phase demodulation by the digital lock-in system.

Figure III-7(e) illustrates the vector diagram of the digital lock-in implementation where the phase angle varies between 180° to -180° degrees without any drive phase rotation. Most PFM instruments break down the phase signal into two values: i) in-phase (denoted as X-signal) and ii) quadrant (denoted as Y-signal). The positive domain +z and negative domain -z of the PPLN sample is represented by **P** and **N** vectors, respectively.

In this configuration, it is not possible to obtain an optimal contrast of the phase signal. Hence the drive phase signal is rotated 90° in the initial parameters of PFM measurement, turning the drive phase vector of electric field $\boldsymbol{D_E}$, **N**, **P**, and the background **B** vectors. In this scenario, the vectors **N** and **P** lie in the third and fourth quadrant with the measured phase value being very close to the -90° (corresponding to vector **N**) and 90° (corresponding to vector **P**), obtaining the optimal contrast of the phase signal, as illustrated in Figure III-7(c) and 7(d). According to Jungk's method and the vector in Figure III-7(e), the values measured of PFM amplitude **P** and **N** are equivalent to **B**-**d** and **B**+**d** where ±**d** represents the piezoelectric signal from the up and down domain generated by the sample. The background signal is calculated as the average of the PFM signal generated on the up and down domain, i.e., $\boldsymbol{B} = \frac{1}{2}(\boldsymbol{N} + \boldsymbol{P})$ and its magnitude is expressed as $\boldsymbol{B} = ((B_x)^2 + (B_y)^2)^{1/2}$.

These last mathematical expressions were used to calculate the background contributions for four different probes of SCM-PIT and Pt-Si materials. Figure III-7(f) shows that the SCM-PIT tip's background signal is twice as large as that of the Pt-Si tip. These results indicate that the cantilever stiffness effect is not negligible for piezoelectric materials with $d_{33} < 10\ pm/V$ since the background signal generated by the soft probe can be as high as 3.5 pm/V. In comparison, the rigid probe reaches a maximum value of about 1.5 pm/V. Consequently, the Pt-Si probe was chosen to carry out all the PFM experiments on ZnO NWs.

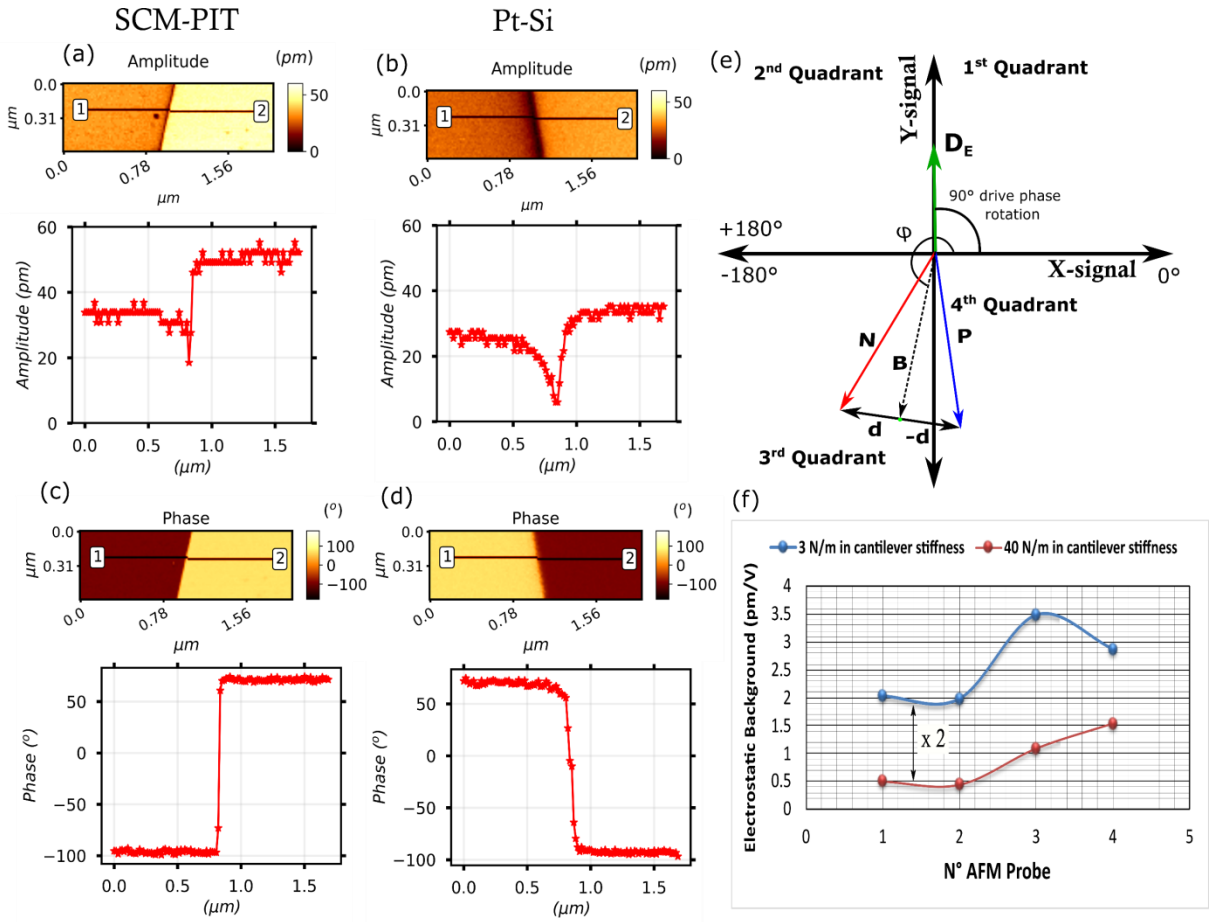

Figure III-7 Images of PFM amplitude and phase distributions of the PPLN sample using the (a), (c) SCM-PIT and (b), (d) Pt-Si tips at 14kHz in frequency and 5V in AC drive voltage for both experiments. (e) Schematic vector diagram of the digital lock-in amplifier. This figure was adapted from [240,241]. *(f) Background values were measured from the PPLN sample using four different probes of SCM-PIT (blue curve) and Pt-Si (red curve).*

III.2.2 DataCube technique for PFM measurement on NWs

PFM measurements on ZnO NWs are currently a challenge because this technique requires constant contact between the tip and the sample, preventing a clear PFM image due to collisions

during the scanning process when the NWs are separated by voids. For this reason, most experiments based on NWs materials have used PMMA matrix material in order to ensure the complete immersion of NW into the polymer and to planarize the substrate. Then, an etching process is performed to remove the PMMA layer that covers the top surface of the NW [127,236]. There is a promising technique called "DataCube mode" in AFM microscopy to explore the electrical properties of materials at the nanoscale. In this section, classical PFM and "DataCube mode" will be compared to show the reproducibility, advantages and drawbacks upon extracting the PFM signal on NWs.

DataCube mode uses the force-volume method to get highly accurate Force-Distance measurements or the deflection of the cantilever at any point (or pixel) in a two-dimensional array over the sample surface. Each measurement is made during a dwell time (hold segment) defined in the input parameters of this mode, as shown in Figure III-8(a) and 8(b). In PFM mode, the electrical parameters as amplitude and phase are simultaneously measured, recording this information while the tip is in contact with the sample (see Figure III-8(d)). After each pixel measurement, the scanning probe is withdrawn and moved to a new location in order to avoid continuous contact (as it happens in the classic PFM contact mode). This makes this technique more advantageous for exploring the PFM parameters on NWs without any matrix materials. The data acquisition is divided into three essential steps: i) Firstly, the tip approaches the surface until coming into contact (see Figure III-8(c)). During this step (around 50 ms), there is no deflection of the cantilever or piezoresponse signal (see Figure III-8(d)). ii) Once the cantilever achieves a given deflection setpoint (20 nm for all of our experiments), the tip height is fixed (for a dwell time of 80 ms) and the piezoresponse amplitude and phase are recorded with hold segments of 204 values (i.e., number of repetitions of the measurement). iii) Subsequently, the tip is withdrawn from the surface reducing both the cantilever deflection and the piezoresponse signals, as shown in Figure III-8(d). Finally, the probe is moved to the next pixel repeating the process again.

After scanning the selected surface, DataCube file has 204 frames (fixed in this experiment) of the amplitude and phase distributions corresponding to the hold segment. The data is treated using Python programming language to calculate the average of about 20 frames of the amplitude and phase values, which were chosen randomly among all the frames. This forms the new distribution images (see Figure III-8(e) and 8(f)). This number of frames is enough to improve the measurement accuracy and image quality.

In order to compare both PFM methods, samples #1 and #2 were used to measure the PFM response using the classical PFM contact mode and PFM DataCube mode. In this experiment,

the parameters related to the substrate, seed layer, and growth process remained unchanged throughout the manufacturing process of the samples based on ZnO NWs (see details in section III.1). Sample #1 of ZnO NWs has the PMMA matrix with the NWs tip exposed to air (see more details of this sample in section III.1.3).

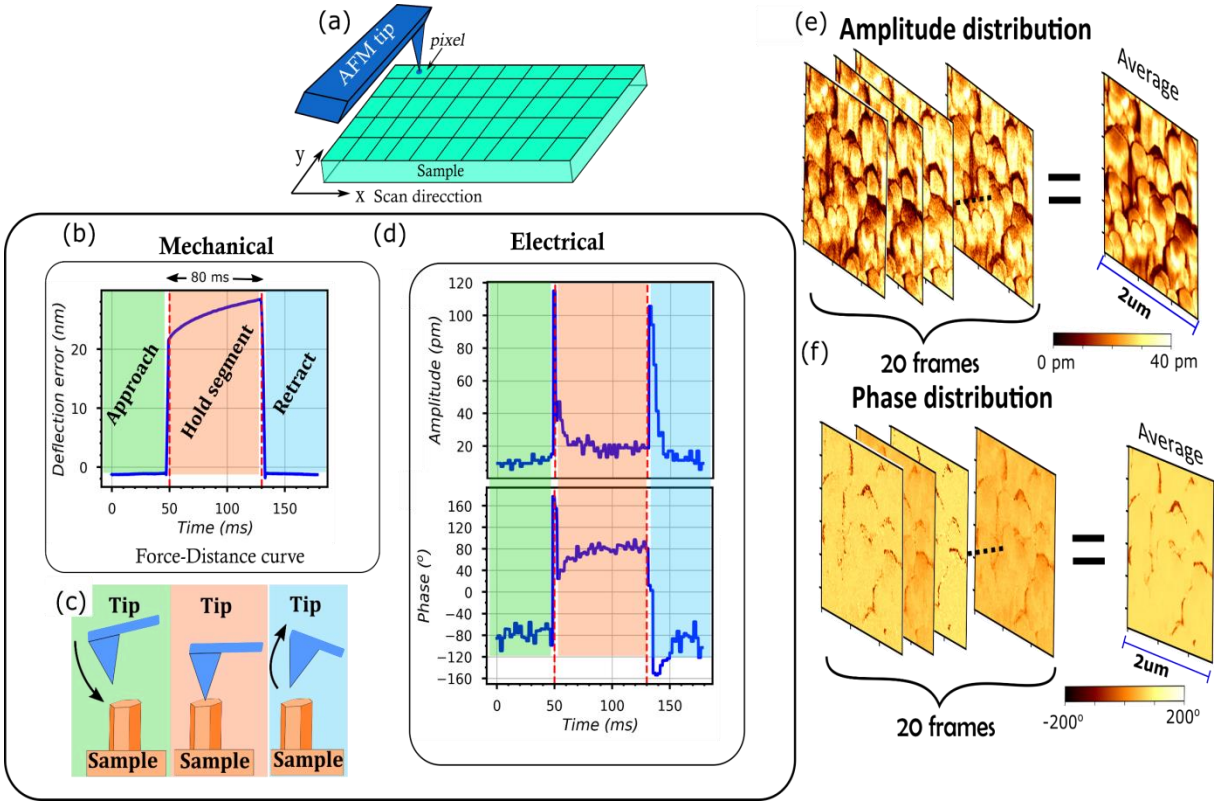

Figure III-8 (a) Schematic image of 2D scanning technique of DataCube mode in a single pixel. (b) Deflection curve of the cantilever as a function of time. (c) Schematics image of PFM DataCube procedure describing the position of the tip when it approaches the sample surface, held at a fixed height and then retracted. (d) Piezoelectric amplitude and phase values during data acquisition in one pixel as a function of time. (e) Averaged amplitude and (f) averaged phase maps after data treatment of 20 frames.

PFM measurement was performed at 14 kHz and 5 V in AC drive amplitude using the classical contact mode, obtaining topography, piezoelectric amplitude, and phase images of the top surface of ZnO NW, as depicted in Figure III-9(a-c). The AC signal frequency was chosen after evaluating the PFM response for both amplitude and phase as a function of frequency on ZnO NWs, with the aim of avoiding any PFM amplification due to the contact resonance between the tip and the sample (see the results in App. II.4 of Appendix II). As for sample #2, PFM measurement was carried out on ZnO NWs using PFM DataCube mode, acquiring the same experimental quantities as above (see Figure III-9(d-f)) using the same parameters for the AC input signal.

Figure III-9(a) and 9(d) show that the surface of the sample with PMMA (with height variation in nm) is flatter than the sample without PMMA (height variation in μm), making it safer to measure the PFM in contact mode. The DataCube mode exhibits an excellent topography image throughout the scanning surface of the top ZnO NW, defining the hexagonal shape and position of NWs.

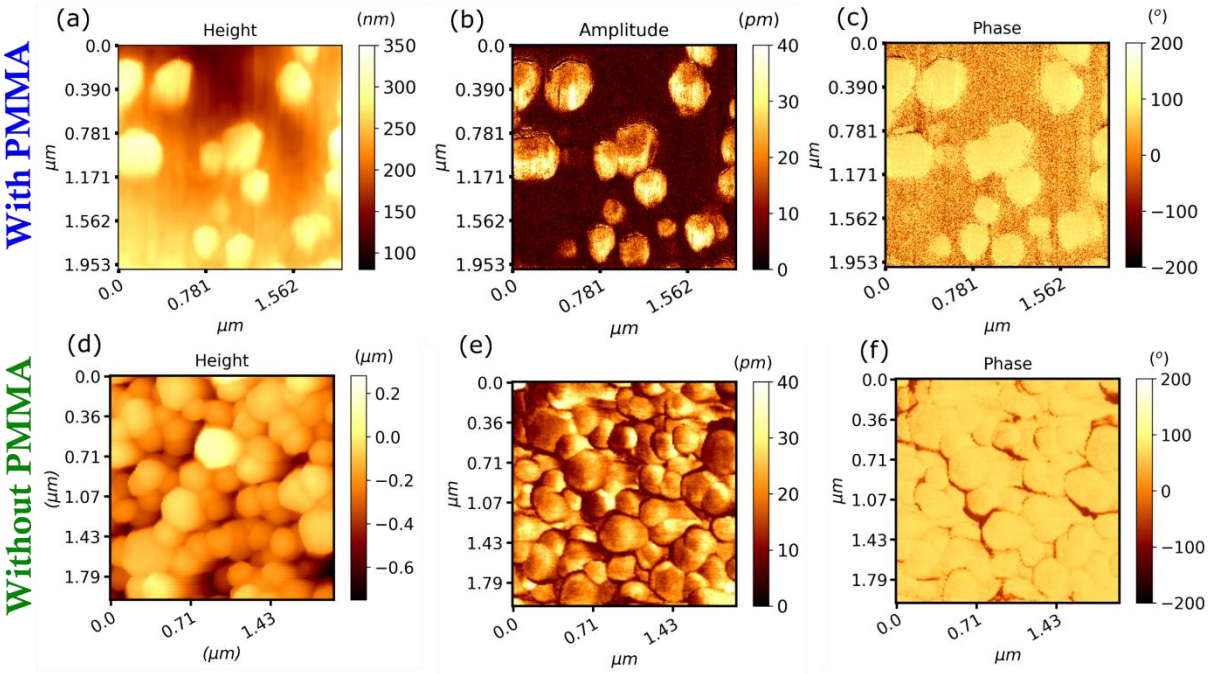

Figure III-9 Topography, piezoelectric amplitude, and phase images of the top surface of ZnO NW grown by CBD technique over Si substrate (a-c) employing the classical PFM contact mode (NWs immersed in PMMA) and (d-f) employing the PFM DataCube mode (without PMMA). Both measurements were made at 14kHz in frequency and 5V in AC drive voltage.

The piezoelectric amplitude distributions show that their values are inhomogeneous on the surface varying from 5 pm to 40 pm, as is confirmed by their amplitude histograms in Figure III-10(a) and 10(b). It should be noticed that the PMMA matrix (with NWs beneath) generated an amplitude signal with a value of about 5 pm (see the black dashed line Gaussian curve in Figure III-10(a)). Regarding the amplitude signal of the top surface of ZnO NW, both methods are in agreement with amplitude values between 10 pm to 40 pm. It can be seen in Figure III-10(b) and 10(d), that the top surface of ZnO NW displays values of piezoelectric phase of about +70° which is attributed to the nature of the ZnO crystal polarity (see section I.2.2.1 in Chapter 1). These results are confirmed in both samples by the phase histograms, showing a narrower Gaussian peak for the sample without PMMA since the dielectric matrix contributes with distributed phase values between -100° to 50 °, as shown in Figure III-10(b).

In conclusion, it can be said that the DataCube mode is an appropriate method (comparable to the classical contact mode) to extract the effective piezoelectric coefficient directly of the ZnO NW without the need for extra processes, such as encapsulating and etching. The advantages of the DataCube method are related to the saving of time and the exposure of the sample during the manufacturing process as well as its reproducibility and resolution during data collection.

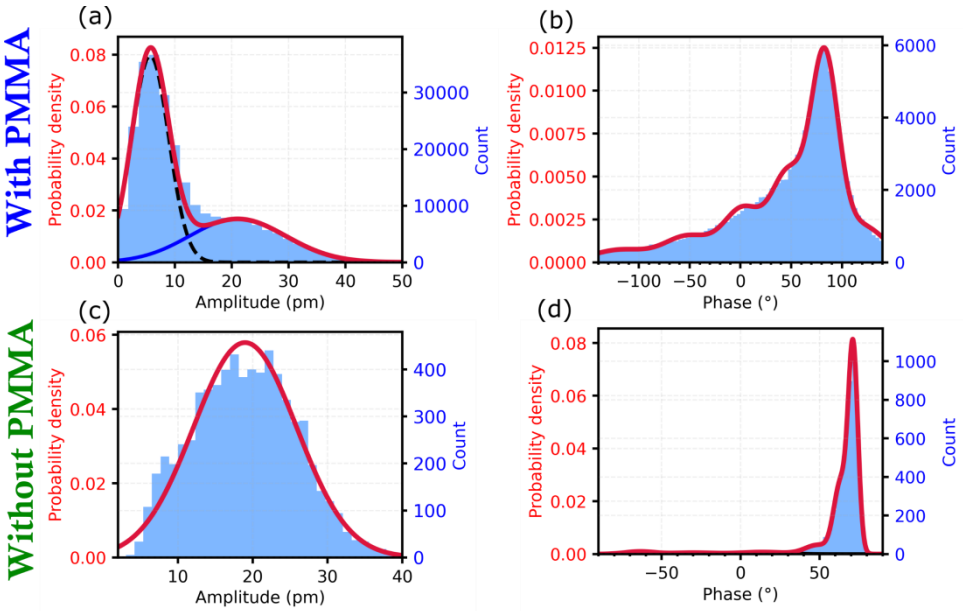

Figure III-10 Piezoelectric amplitude and phase histograms after data treatment of the top surface of the ZnO NWs grown by CBD technique over Si substrate (a, b) employing the classical PFM contact mode (NWs immersed in PMMA) and (c, d) employing the PFM DataCube mode (without PMMA). Both measurements were made at 14kHz in frequency and 5V in AC drive voltage

III.3 Experimental results and discussions

III.3.1 Measurement of d_{33}^{eff} on ZnO NWs grown on different substrates

In this section, the effectiveness of the gravure printing method (sample #3) is evaluated using PFM measurements on ZnO NWs grown on flexible substrates. The results are compared with ZnO NWs grown from a seed layer deposited by ALD on a silicon substrate (sample #2). The effective piezoelectric coefficients $\boldsymbol{d_{33}^{eff}}$ are computed by analysing the piezoelectric amplitudes, as presented in Figure III-11(a-f).

DataCube was used to perform the PFM measurements on both samples, employing the Pt-Si probe with a high spring constant (range values among 43–50 N/m). The characteristic electrical signal was fixed for a drive voltage of 5 V using a frequency of 14 kHz. Figure III-11(a, d) shows the topography distributions for ZnO NWs grown on ITO/Si and ITO/PET structures.

They displayed good uniformity and hexagonal shape. These results are consistent which is typically observed with SEM images of section III.1.4 (see Figure III-3). Figure III-11(b, e) show that the distribution of PFM amplitude is not homogenous throughout the whole surface, varying from 5 pm to 40 pm for both samples. However, the distribution of the piezoelectric phase is rather homogenous, showing a single and positive phase value.

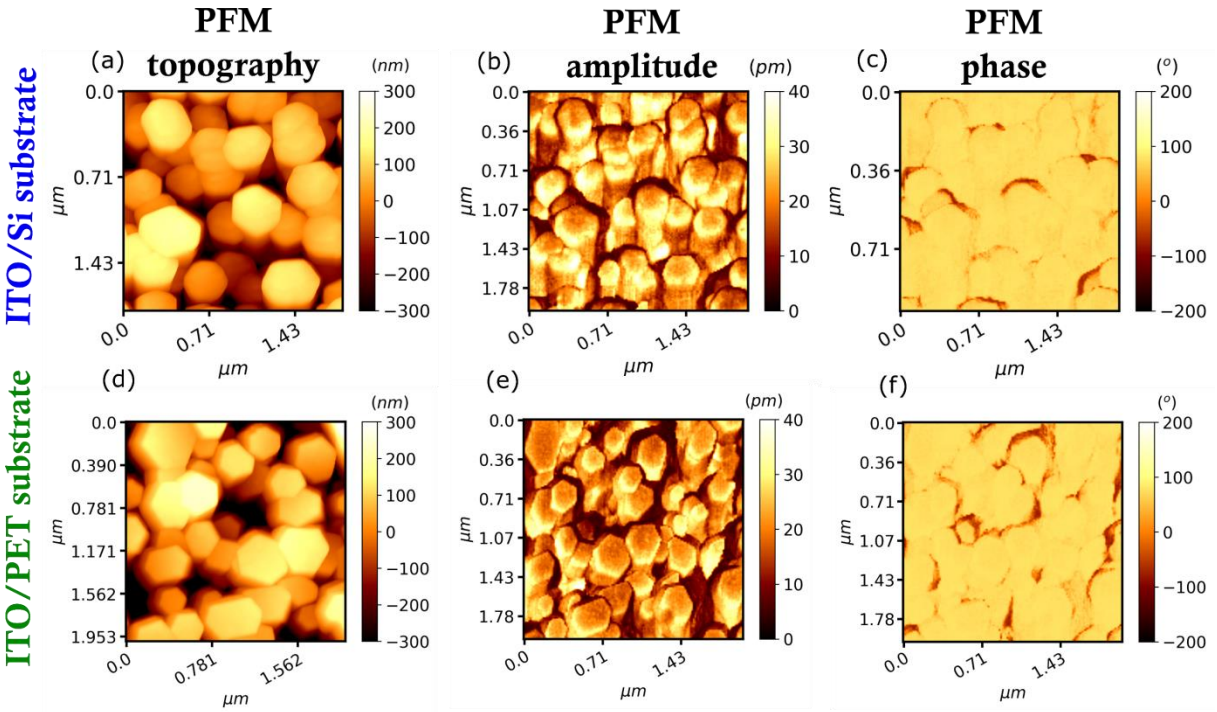

Figure III-11 Distribution images of topography, amplitude, and phase extracted from PFM measurement performed on ZnO NW grown on (a-c) ZnO (ALD)/ITO/Si (images lined up above) and (d-f) as-printed (not sintered) ZnO seed layer/ITO/PET substrates (images lined up below), employing a Pt-Si probe at 14kHz and 5V in frequency and AC voltage, respectively.

After analysing the DataCube file, we have extracted the piezoelectric amplitude and phase values from the top surface of ZnO by discriminating the amplitude values between the NWs. The above-mentioned process was possible thanks to the mechanical (i.e., the adhesion force distributions) and electrical (i.e., the piezoelectric responses) correlation obtained from the force-volume method in DataCube (see more details App. II.5 in Appendix II). Employing these additional filters, the mean values of amplitude and phase values were extracted from the corresponding amplitude and phase histograms, as illustrated in Figure III-12(a-d). According to the results, the mean amplitude values (μ) were very similar for the rigid (ITO/Si) and flexible (ITO/PET) samples with values of 22.74 ± 8.49 pm and 20.96 ± 7.21 pm (see Figure III-12(a, c)), respectively. Subsequently, $\boldsymbol{d_{33}}$ is estimated by dividing the piezoelectric amplitude by the applied drive voltage, resulting in values of 4.6 pm/V and 4.1 pm/V for the ZnO NWs grown

on ITO/Si and ITO/PET, respectively. It is worth noticing that both samples exhibited almost the same value of $\boldsymbol{d_{33}}$. so the gravure method does not seem to affect the effectiveness of the piezoelectric response of the ZnO NWs. Additionally, The values are inside the range of 2–12 pm/V, as previously reported by other experimental studies (see section I.2.2.2 of Chapter I).

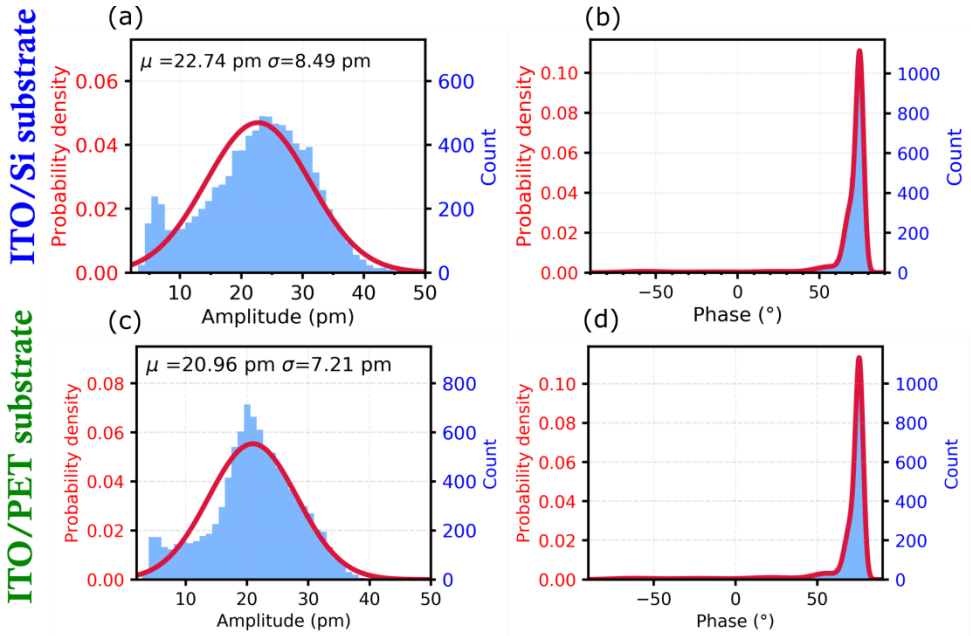

Figure III-12 Piezoelectric amplitude and phase histograms extracted from distribution images of the top of ZnO NW surface grown on (a, b) ZnO (ALD)/ITO/Si and (c, d) as-printed (not sintered) ZnO seed layer/ITO/PET substrates, employing a Pt-Si probe at 14kHz and 5V in frequency and AC voltage, respectively. The red curve corresponds to one Gaussian curve.

Regarding the crystal polarity of these NWs, the piezoelectric phase histograms showed a single-phase value of 75° for both samples, as depicted in Figure III-12(b, d). It means that the crystal structure in the top surface of NWs has a Zn-polarity, as has been observed in previous experiments [127]. It should be recalled that a single polarity throughout the whole surface is quite convenient to get better effectiveness of the piezoelectricity in an array of ZnO NWs. Otherwise, two domains with opposite polarity would affect the global piezoelectricity since the polarization in their vicinity could be canceled.

III.3.2 Measurement of d_{33}^{eff} on ZnO NWs grown over different electrodes

In this section, we present the PFM measurement on ZnO NW grown on flexible substrates but with two different bottom electrodes: ITO (samples #4 to #7) and AZO (samples #8 to #11). One of the objectives is to observe if there is any effect of the bottom electrode in the

piezoelectric response of ZnO NWs as well as its reproducibility. Another aim is to understand why the piezoelectric response on the top surface is not homogenous. To respond to this question, we have employed different statistical studies for smaller and larger scanning sizes, as well as numerical simulations using COMSOL software to investigate the generated displacement under an applied voltage at the top surface of a single ZnO NW.

III.3.2.1 PFM measurement at large scale

In this series of experiments, we employed the DataCube mode with the same Pt-Si probe for applying an AC signal with the drive voltage of 5 V in the range of 13-30 kHz in frequency, according to the stable value of amplitude response for each sample. The corresponding piezoelectric responses for a scanning area of about 2 µm x 2 µm on the ZnO NWs grown on ITO/PET substrate for different sintering treatment times are presented in Figure III-13. By comparing the topography images (top row) with the piezoelectric amplitude images (middle row), it is noted that the hexagonal-shaped nanowires presented inhomogeneous values of piezoelectric amplitude where the brighter domains indicate the regions with the higher piezoelectric coefficients (especially for the smaller NWs and its edges) and *vice versa*. As for the piezoelectric phase images (images lined up on the bottom), the top surface of NW exhibited the Zn-polar signals, as was also observed in the last experiments.

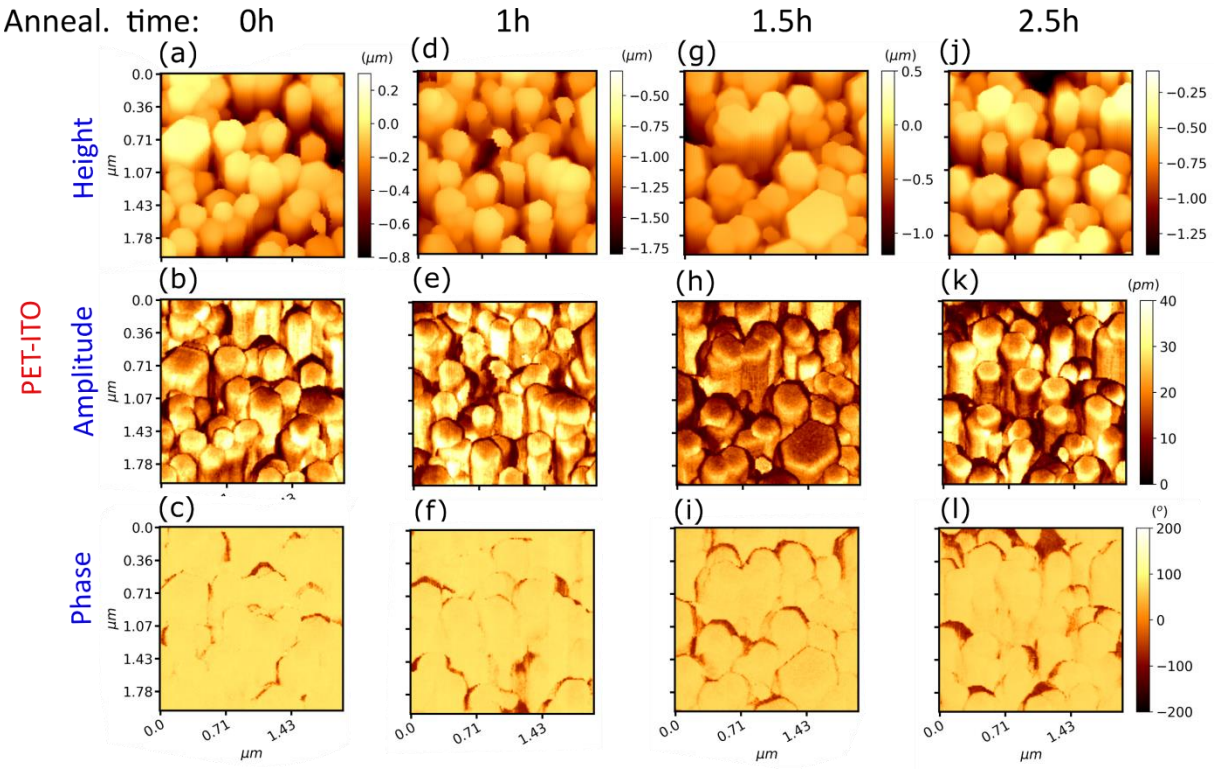

Figure III-13 Topography, piezoelectric amplitude, and piezoelectric phase of ZnO NWs grown by CBD method on PET-ITO substrate with sintering treatment times of (a–c) 0 hours (h), (d–f) 1h, (g–i) 1.5h, and (j–l) 2.5h.

To test the reproducibility of these results, PFM measurements were made in three different regions (selected randomly) in each sample, as shown in Figure App.II- 6(a). Each spot was further investigated by analysing the piezoelectric amplitude histograms and fitting with multiple Gaussian curves (see the images lined up on the top of Figure App.II- 6(c)). At large-scale scanning, we have chosen four Gaussian curves for the amplitude histograms in order to present the different piezoelectric contributions, as shown in the top histograms of Figure App.II- 6(c). Four curves were enough to fit the complete histogram since it does not obey a simple Gaussian behaviour (see Figure III-14).

Among those Gaussian curves, the peak concerning the small amplitudes (black Gaussian curve) is related to the screening effect presented in the bigger (wider) ZnO NWs (see more detail in App. II.7 of Appendix II), as was demonstrated in section II.4.3 of Chapter II. Moreover, it can be added that this screening effect can be connected to the free carriers, either due to locally smaller surface trap density or to free carrier tunnelling among adjacent ZnO NWs [245], thus reducing even more the piezoelectric amplitude. On the contrary, the peak with larger amplitudes (purple Gaussian curve) is always present at the edge of the ZnO NWs and is associated with the semiconducting character of NWs, as will be discussed later with the support of COMSOL simulations. Analysing the ZnO NWs individually (see App. II.8 in Appendix II), we can observe that the wide and thin NWs can generate an amplitude value of 20 pm and 25 pm, respectively. So that, the radius-dependent piezoelectric response must be taken into account in the statistical analysis, including the blue (for wide NWs) and green (for thin NWs) Gaussian curves.

By extracting the mean values of piezoelectric amplitude for each Gaussian curve and comparing them with each PFM measurement performed in different spots (see Figure App.II-6(b)), we can mention that the piezoelectric response is reproducible and unchangeable in each selected region. Hence, the piezoelectric amplitude histograms of the three regions are combined in a single histogram in order to compare and sum up all piezoelectric results, as shown in Figure III-14.

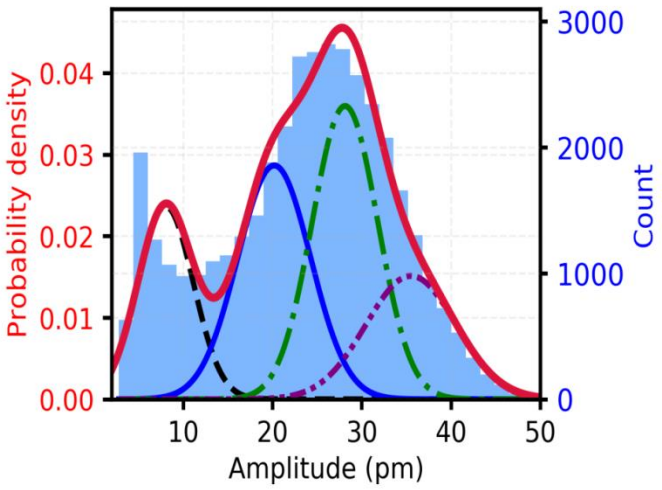

Figure III-14 Histogram of piezoresponse amplitude of three different randomly located spots. The sample is constituted of ZnO NWs grown on PET-AZO using the sintering treatment time of 2.5 h (sample #10). Measurements are recorded applying 5 V in AC drive voltage at 13 kHz.

As for AZO/PET substrates, the PFM measurements were also carried out for different sintering treatment times, as depicted in Figure III-15. Similar to ITO/PET samples, the piezoelectric amplitude values on the top surface of NW are not homogenous (see the images lined up in the middle in Figure III-15) and its polarity is Zn at the top surface of NW with the phase value of 70° (see the images lined up on the bottom in Figure III-15) for all sintering treatment times.

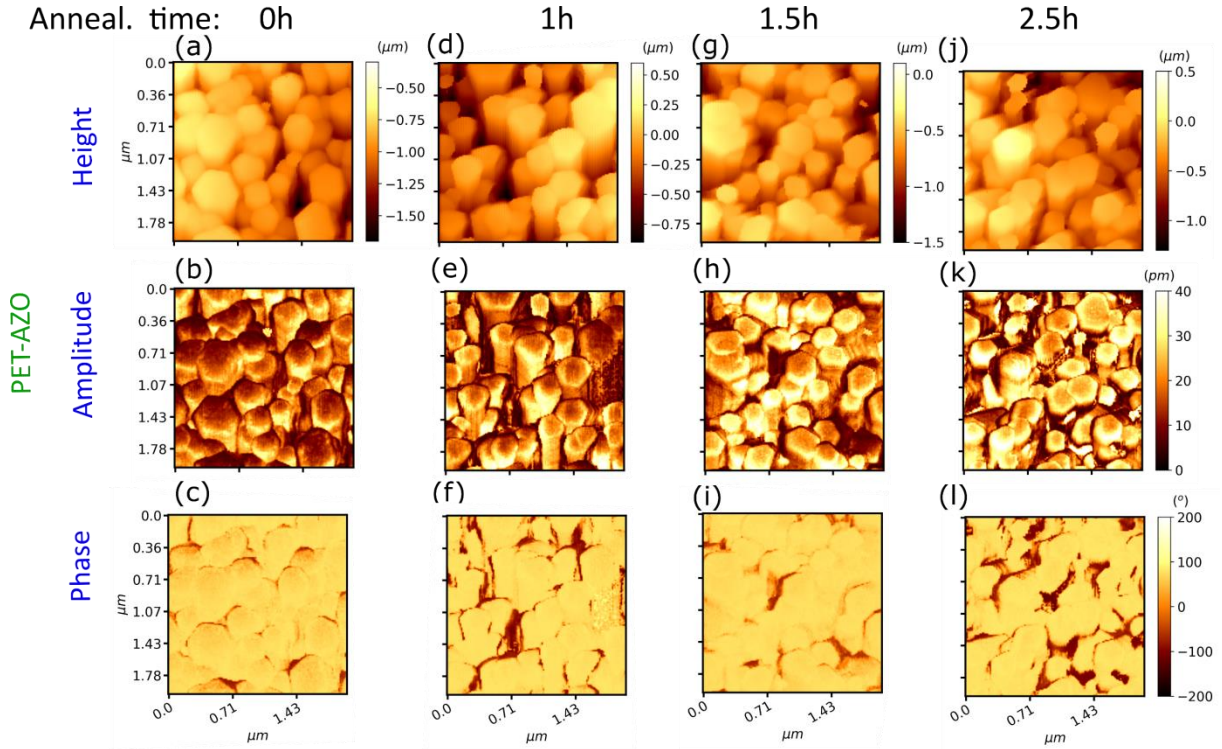

Figure III-15 Topography, piezoelectric amplitude and piezoelectric phase of ZnO NWs grown by CBD method on PET-AZO substrate with a sintering treatment time of (a–c) 0 hours (h), (d–f) 1h, (g–i) 1.5h, and (j–l) 2.5h.

To further investigate and compare the samples, the piezoelectric results were statistically treated by plotting the radius distribution, piezoelectric amplitude, and phase histograms for ITO/PET (see Figure App.II- 9) and AZO/PET (see Figure App.II- 10) substrates and for each sintering treatment time.

By extracting the mean value of each Gaussian curve in the amplitude histograms, both kinds of samples (ITO/PET and AZO/PET) showed a similar piezoelectric response, as depicted in Figure III-16(a-d). Figure III-16(a) revealed that the border contribution can reach values around 35 pm (equivalent to 7 pm/V in $\boldsymbol{d_{33}}$), while the value of wide NWs and thin NWs are around 20 pm (equivalent to 4 pm/V in $\boldsymbol{d_{33}}$) and 25 pm (equivalent to 5 pm/V in $\boldsymbol{d_{33}}$), respectively. It means that the border contribution shows is larger by 75 % and 40 % for wide NWs and thin NWs. Concerning the contributions of lower amplitude values (around 10 pm), they presented a reduction of 2 times with respect to the optimal wide and thin NWs (see Figure III-16(d)). As for the polarity of NW, the statistical method confirmed once again that both samples have a single Zn-polar crystal structure on the top surface with a phase value of around 75° regardless of the electrode and sintering treatment time on the seed layer (see Figure III-16(e)).

Using all AFM topography images from each PFM measurement, we extracted the NWs radius distributions for each sintering treatment time and substrate (see the first column of histograms in Figure App.II- 9 and II-10). The average NW radius slightly decreases with the sintering time, from 146 to 107 nm for PET-AZO and from 118 to 90 nm for PET-ITO. It is worth noticing that the average NW radius is always smaller on PET-ITO substrate than on PET-AZO, as revealed in Figure III-16(f). This radius trend did not show any effect on the piezoelectric response using the above statistical strategy. For this reason, another statistical method was employed, as will be presented in the next section.

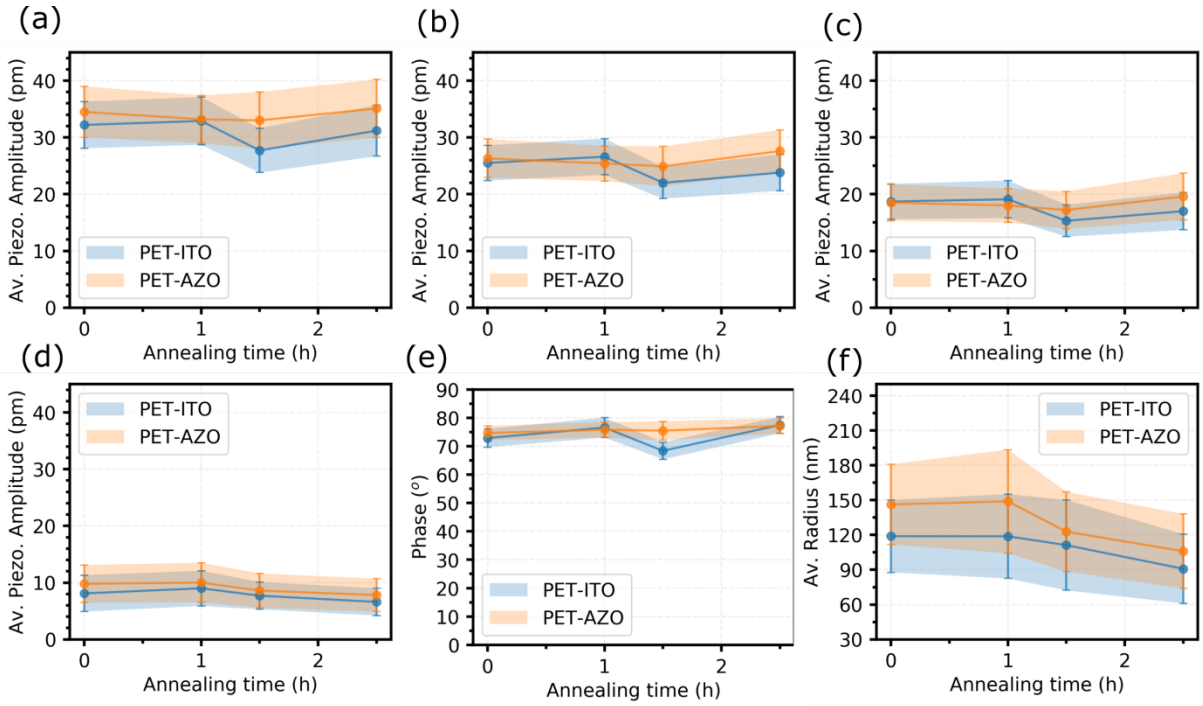

Figure III-16 The mean value of the piezoelectric amplitude as a function of the sintering treatment time, in both PET-ITO and PET-AZO substrates, for (a) the border effect, (b) the thin NWs, (c) the wide NWs, and the screened NWs contributions. (e) the mean value of the piezoelectric phase and (f) the ZnO NW radius as a function of the sintering time in both ITO and AZO seed layers. All this data was extracted from the PFM histograms of Figure App.II- 9 and II-10 of App. II.9 in Appendix II.

III.3.2.1 Radius-dependent piezoelectric response

Employing the same PFM results and in collaboration with T. Jalabert (post-doctorate in our group), we analysed the piezoelectric amplitude response individually for each ZnO NW in the three spots, as depicted in Figure III-17(a). Assuming that amplitude values are homogeneous on the top surface of each NW, we calculated the mean value of piezoelectric amplitude over the top surface for each NW. Both $\boldsymbol{d_{33}}$ and ZnO radius were simultaneously extracted by employing a python code for each NW over the scanned area. Figure III-17(b) and III-17(c) show the summary of the results of $\boldsymbol{d_{33}}$ as a function of the radii of NWs grown on PET/ITO and PET/AZO substrates at different sintering treatment times, respectively. It is noticeable that both samples demonstrate a radius-dependent piezoelectric response regardless of the kind of electrode and sintering process. As can be seen in both figures, $\boldsymbol{d_{33}}$ increases by 2.1 times (from 3 pm/V to 6.5 pm/V), as the radius of ZnO NWs decrease from 250 nm to 75 nm. Figure III-17(b) shows four clusters corresponding to 0h, 1h, 1.5h, and 2.5h sintering times (dense regions surrounded by sparse points). The clusters follow the same trend in denser regions with the highest values of $\boldsymbol{d_{33}}$. This is because PET/ITO samples demonstrated lower values of radius

changing for different sintering times (see Figure III-16(f) in the previous section). In contrast, the clusters for PET/AZO substrate at 0h and 1h spread out reaching higher values of radii (see Figure III-17(c)), exhibiting sparse regions of points with large radius and lower values of $\boldsymbol{d_{33}}$ (below 4 pm/V). As the time of sintering treatment increases, the clusters for 1.5h and 2.5h exhibited a similar trend distribution as the PET/ITO samples, reaching $\boldsymbol{d_{33}}$ values between 4 - 6.5 pm/V. Overall, larger NWs were detected at low values of sintering time with lower values of $\boldsymbol{d_{33}}$, while the smaller ZnO NWs are obtained (comparable to PET/ITO sample) by high values of the sintering time, reaching higher values of $\boldsymbol{d_{33}}$.

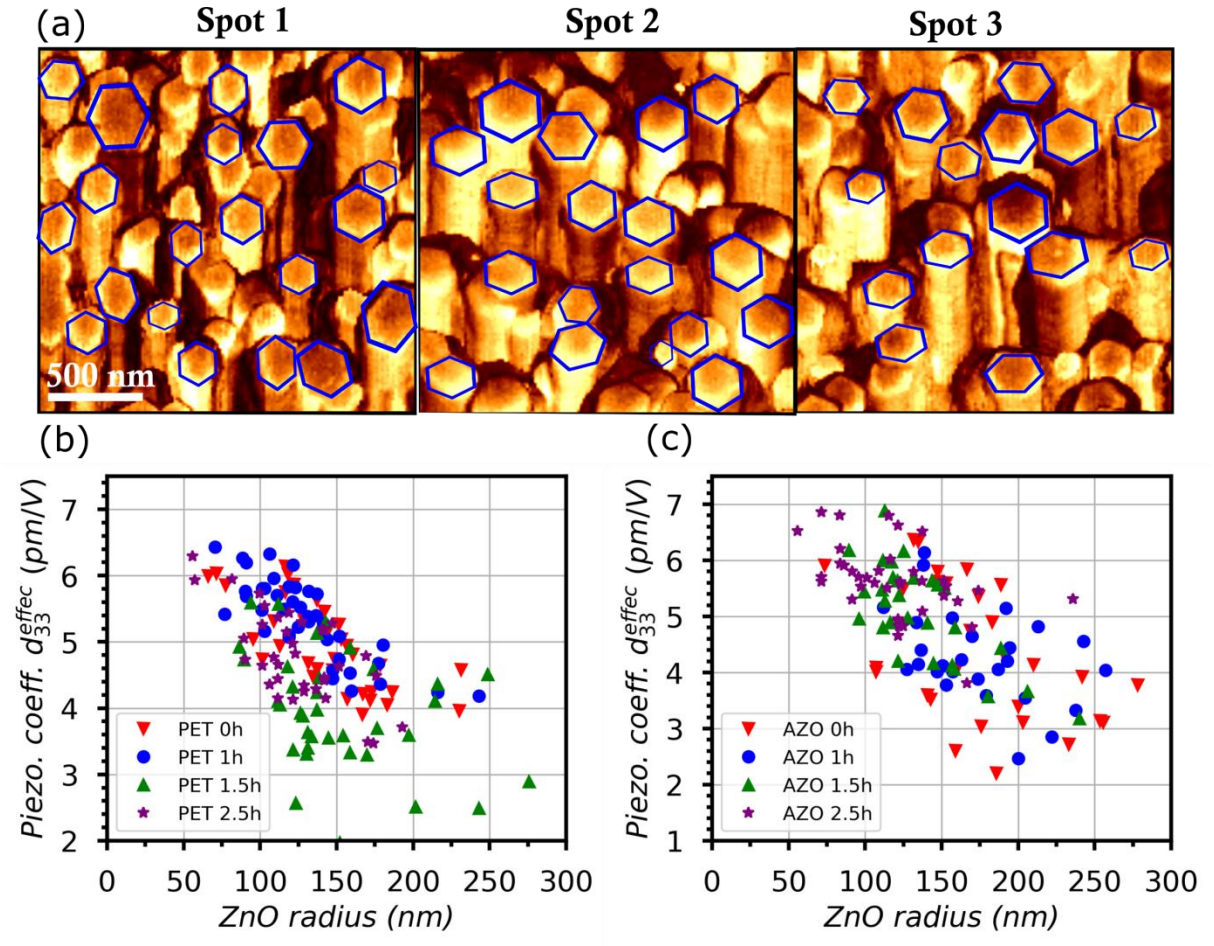

Figure III-17 (a) Distribution of the piezoelectric amplitude of each measured spot for ZnO NW grown on PET/ITO substrate at 2h and 30 minutes (2h5). The hexagonal shapes refer to the NWs statistically analyzed by the individualized method. The effective piezoelectric coefficient as a function of ZnO NW radius extracted from its top surface for different sintering treatment times on (b) PET/ITO and (c) PET/AZO substrates.

III.3.2.1 COMSOL simulation related to the PFM measurement

In order to further investigate the higher values of piezoelectric amplitude at the top surface of ZnO NWs, i.e., the purple sub-Gaussian curve discussed in the previous sections, a two-dimensional (2D) COMSOL finite element simulation of a single ZnO nanostructure with a respective seed layer of 40 nm, length of 3 μm and radius of 100 nm, was performed. On the top surface of the NW, a 25 nm wide square was added to mimic the contact area between the AFM probe and the NW. According to recent works [236], static simulations are sufficient to provide the displacement of the nanostructures since the PFM results are not experimentally frequency-dependent, at least in our selected range of 13kHz – 30kHz. The static voltage was applied at the bottom side of the seed layer and the interface of the contact area between the probe and NW was grounded (see the details of boundary conditions of section App. II.10 in Appendix II).

This model employed the coupled piezoelectric and semiconducting equations that were defined in section II.1.1 in Chapter II, without taking into consideration the surface trap density for the moment due to its complexity. The difference in screening was obtained by varying the doping level (undoped NW versus doping level typically of CBD). Figure III-18(a) shows the electric field-induced displacement distribution of the 2D nanostructure for a doping level N_d of $5 \cdot 10^{17} cm^{-3}$, which was chosen according to the growth method used in our samples (CBD). At first glance, the entire NW does not produce any displacement value, as a consequence of screening by free carriers in the core of the nanostructure. To prove this, the same model was calculated without the semiconducting properties (i.e., without free carriers), exposing some displacement values along the core of the ZnO NW, as illustrated in Figure App.II- 12(a) of section App. II.11 in Appendix II. In the semiconducting model, the positive value is observed at the interface of probe and NW contact (see zoom image in Figure III-18(a)). The sign of this displacement means that the material is being axially expanded since the c-axis of the piezo structure is oriented upwards corresponding to the Zn-polar and is parallel to the electric field direction, as observed in our measurements. When the square shape picturing the tip is positioned at the center of the 2D nanostructure, the maximum piezo-induced displacement at the tip-nanostructure interface reaches 25 pm to be almost half of the optimal value without free carriers (around 46 pm), as shown in Figure App.II- 12(b).

For the purpose of emulating the PFM technique data acquisition, we have accomplished several numerical simulations by moving the AFM probe (i.e., the squared shape) step-by-step towards the edges of the nanostructure. Subsequently, the average of the displacement values

between the interface probe and NW surface was carefully calculated in each position. As can be viewed in Figure III-18(b), the displacement or amplitude value of the piezoelectric response is constant when the AFM probe position is placed near the middle of the ZnO nanostructure (see black scattered circles). However, this amplitude value increases when the AFM probe approaches the nanostructure edge, achieving a value close to the piezoelectric amplitude of the model without semiconducting properties (red dashed line).

The increase of the piezoresponse amplitude at the edge observed by the numerical results corresponds qualitatively with the values measured by the PFM technique on our NWs (see Figure III-18(c) and III-18(d)). To conclude, we suggest that the border effect can be explained by the semiconducting nature of the ZnO NWs. Further numerical simulations are needed including 3D geometries and surface traps to fully understand this effect.

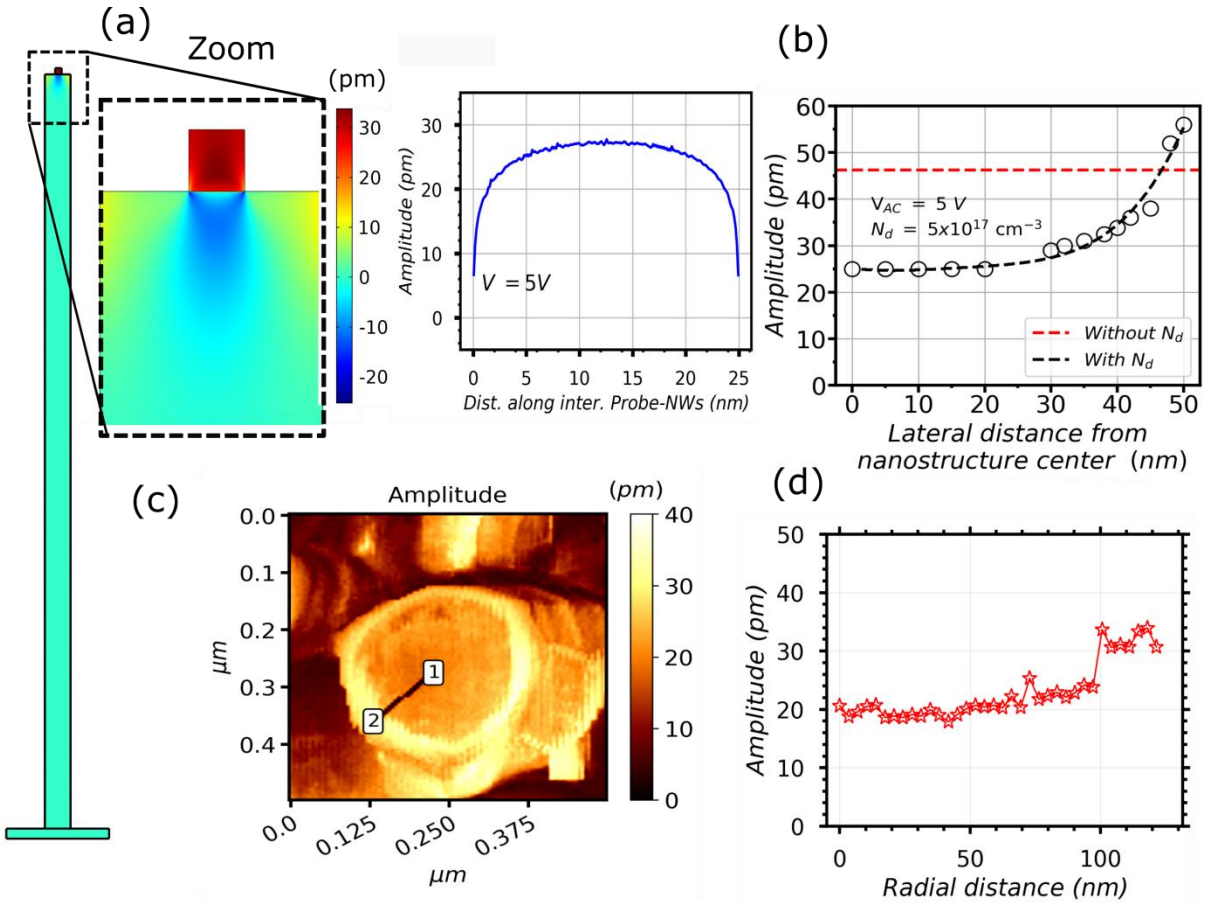

Figure III-18 (a) Electric field-induced displacement distribution and amplitude value along the interface of the tip and the 2D nanostructure. (b) Absolute amplitude value along the lateral distance from the center on the top surface of the 2D nanostructure for a system with (black circle points) and without (red dashed line) semiconducting properties (N_d). (c) Piezoelectric amplitude distribution on a single ZnO NW and (d) along the radial distance between points 1-2.

III.4 Conclusions

We successfully grew ZnO NWs on flexible substrates, such as PET/ITO and PET/AZO, utilizing gravure printing as a promising low-temperature, low-cost, and easy manufacturing method for depositing the ZnO seed layer. We found that parameters such as NW radius, vertical alignment, orientation and density were comparable to those obtained for ZnO NWs grown on Si/ITO substrates, which have been commonly used by our group when depositing the ZnO seed layer with the ALD method at 250°C. The growth process over flexible substrates was not influenced significantly by modifying the electrode (AZO and ITO), neither by the sintering treatment times on the ZnO seed layer.

We have demonstrated that the DataCube mode is a powerful AFM technique to measure directly the piezoelectric properties of ZnO NWs without needing extra processing like matrix encapsulation of the NWs. The NWs grown on flexible substrates reached the same effective piezoelectric coefficient $\boldsymbol{d_{33}^{eff}}$ (around 4-5 pm/V) as the reference samples on Si. In addition, all analysed samples revealed a single polarity (Zn-polar) on the top surface of the ZnO NW, which would be a good signal to strengthen piezoelectricity at a large scale.

We have proposed a sophisticated statistical method to analyse the piezoelectricity on ZnO NWs, employing the DataCube mode. After analysing the results, a radius-dependent piezoelectric response was detected on ZnO NW grown on the rigid and flexible substrates, obtaining higher values of $\boldsymbol{d_{33}}$ for thinner NWs and lower values for wider NWs. This is consistent with the trend deduced from the simulation in Chapter 2 when considering doping levels and surface traps in ZnO NW. Furthermore, it was noticed that the piezoelectric amplitude was not homogeneous on the top surface of the NWs, exhibiting the lowest amplitude values for a few NWs and the highest amplitude values at the edges of most NWs. This effect is supported by numerical simulations by including both the piezoelectric and semiconducting properties in the nanostructures. More complex simulations (i.e. 3D geometries, surface traps) would be required to fully understand this effect.

Chapter IV. Complementary electrical measurements on ZnO NWs under controlled ambient conditions

Our simulations have shown the role of screening by free carriers and the importance of nanowire diameter, doping level and interface trap density on the piezoelectric operation of semiconducting ZnO NWs. They have shown that proper nanostructuration made it possible to enhance the electromechanical performance of ZnO-based electromechanical energy transducers (energy harvesters or sensors) compared with what is expected from thin film material. However, there have been few experimental studies of the coupling between semiconducting and piezoelectric properties at the nanoscale, and even less for ZnO NWs grown on flexible substrates using the CBD technique. In this chapter, we start to study this point experimentally by comparing the results obtained in different ambient conditions, liable to modifying ZnO surface state. We carried out complementary electromechanical characterizations, including KPFM, PFM and I-V measurements. The results provided an estimation of doping level, interface trap density and their effects on piezoelectric properties and electrical parameters of ZnO NWs. This chapter starts with a short description of the AFM setup for I-V and KPFM measurements. Subsequently, I present PFM, KPFM, and I-V results in two different environmental conditions (air and N_2 gas) on ZnO NW grown on a flexible substrate (PET-ITO). The effective piezoelectric coefficient of the NW, as well as the work function and the Schottky barrier height at the AFM tip/NW interface, were measured in both environmental conditions. The experimental results seem to support our understanding of ZnO NWs operation, with a key role of interface trap density effects, as obtained in our previous computational studies. Finally, the theoretical and experimental developments can be used to extract the doping level and/or interface trap density from a deep study of the Schottky barrier height.

IV.1 Working principle of the AFM experimental setup

The Kelvin Probe Force Microscopy (KPFM) and current-voltage experiments were carried out at room temperature using a Bruker Dimension Icon (Santa Barbara, CA, USA) atomic force microscope (AFM) instrument, as displayed in Figure IV-1(a). This instrument is mainly composed of the AFM head, the probe holder, the stage to hold the sample, and the TUNA module (for I-V measurements). The AFM head contains the piezoelectric system to move the cantilever in x, y, and z coordinates, and the photodetector to determine the angular deflections of the cantilever. We selected the frequency modulation mode of KPFM to measure the contact potential difference (V_{CPD}) generated between tip and sample. V_{CPD} is obtained by the variation of the oscillation frequency after interaction between the AFM probe and the sample, which depends on distance variation (see more detail in App. III.1 of Appendix III). Using V_{CPD}, the work function of ZnO and the AFM tip can be deduced. TUNA Module was used for the measurement of the electrical current passing through the sample and the tip after applying a DC voltage. The I-V measurement was operated in DataCube mode (see the principle of operation in section III.2.4 of Chapter III). The operating principle of DataCube in TUNA mode consists mainly of four steps: i) The probe is first approached to get in contact with the sample surface without applying any DC bias. ii) Once the probe touches the top surface of the sample, the cantilever starts to bend until a given controlled cantilever deflection value. iii) When the cantilever reaches the selected deflection setpoint, a DC bias is applied and the TUNA module measures the corresponding current value. iv) Finally, the probe is withdrawn to continue with the next pixel. All those steps are illustrated in Figure IV-1(b) and 1(c). Figure IV-1(d) displays the current distribution as a function of DC bias during a voltage ramp from 0.5V to 1.5V. The complete scanned surface data has been extracted from the DataCube file. This DataCube technique allows to explore the evolution of the electric current distribution as DC bias changes, overcoming artifacts, sample damage and simplifying data analysis compared to the conventional Contact mode.

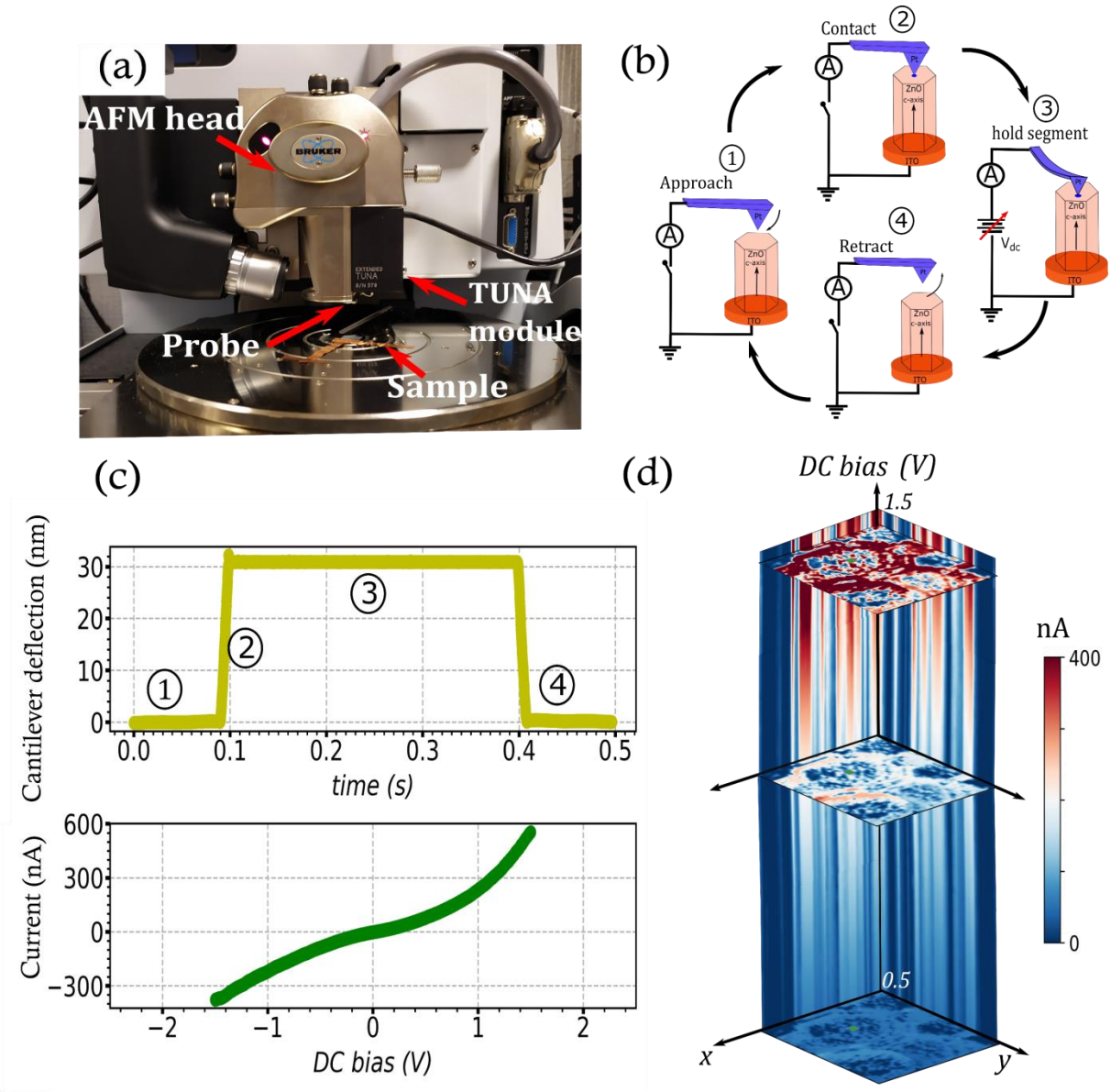

Figure IV-1 (a) Photo of the AFM measurement set-up for I-V measurements on individual ZnO NWs. (b) Illustration of the acquisition process between the probe and sample and (c) cantilever deflection and TUNA current plots during four steps: approach, contact-deflection, dwell and retract. (d) 3D TUNA current distribution along the DC bias for a ramp of 0.5 V to 1.5 V applied to a ZnO NW grown on a flexible substrate (PET-ITO).

IV.2 Characterization results on ZnO NWs

IV.2.1 AFM measurements under modified atmosphere conditions

The ZnO NWs analyzed in this section were prepared in collaboration with Italian partners from ENEA using the gravure printing technique. They prepared the ZnO seed layers over PET-ITO in the context of the European project PULSE-COM. The ZnO seed layer was subjected to an annealing sintering process for 2 hours and 30 minutes (i.e., 2.5h). The NWs were grown using the CBD method (as presented in section III-2 of Chapter III). As can be seen in Figure IV-2(a),

the NWs are well aligned and the radius values remain around $87 \pm 41\ nm$. The AFM topography (see Figure IV-2(b, c)) shows that the density of NWs is around $18 - 20\ NWs/\mu m^2$. Roughness parameters were calculated from these figures: arithmetic roughness average (R_a) and root mean square (R_q), corresponding to $88.8\ nm$ and $109\ nm$ respectively. With these values, it is possible to land the AFM tip safely to perform the electrical measurement in the AFM system.

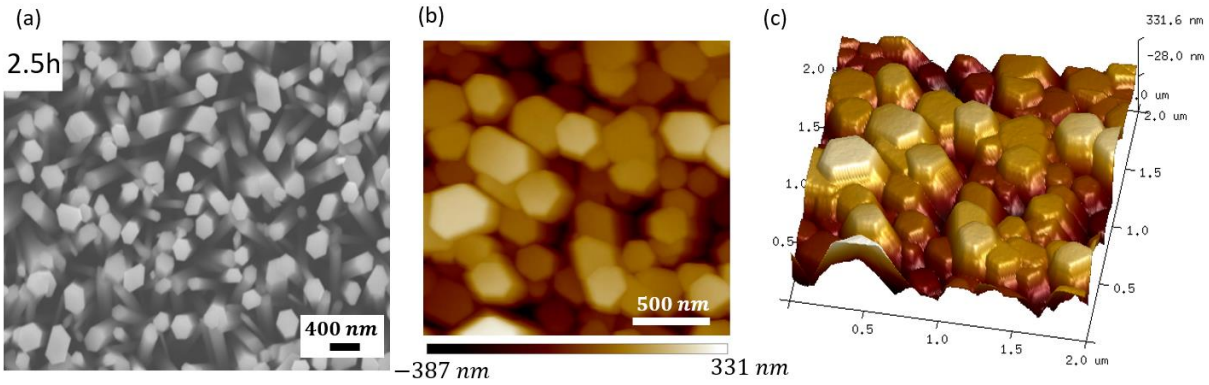

Figure IV-2 Cross-sectional (a) SEM and (b,c) AFM images of ZnO NWs grown on PET-ITO substrate using CBD technique. The ZnO seed layer was exposed to a vapor annealing sintering treatment at a very low temperature (50 °C) for 2h and 30 min (defined here as 2.5h).

IV.2.1.1 PFM over large areas under controlled ambient conditions

In this section, we present complementary PFM measurements to those presented in Chapter III. In this new series of experiments, we have changed the ambient conditions to highlight the effect of defects on the surface of NWs.

PFM measurements were performed on as-grown vertical ZnO NW over flexible substrates. The AFM cantilever used was Platinum coated silicon (Pt-Si) with a tip radius around 25 nm and stiffness in the range of 43-50 N/m. The measurements were performed under two gases (i.e. air and N_2) for large scanning areas of ZnO NW arrays (around 2 µm × 2 µm). PFM amplitude signals from these NWs were obtained by applying a drive voltage of V_{AC} = 5 V. The frequency was selected at 20 kHz to avoid parasitic piezoelectric amplitude magnification due to the electrostatic contribution (typically above 50 kHz), as was discussed in section III.2.2 in Chapter III.

Figure IV-3(a, d) shows the topography extracted from DataCube mode PFM for air and N_2 gas ambients. The topography shows approximatively the same NWs array during both experiments. Figure IV-3(b, e) shows the average PFM amplitude distribution after processing 20 frames of amplitude signal from the DataCube file, as was discussed in Chapter III. At first view, we can see that on the top surface of NWs the amplitude values in regions near the edge

(called here border effect) for air conditions have slightly higher values than for N_2 gas ambient. By plotting the outcomes in a statistical way, it is possible to observe the purple Gaussian curves in Figure IV-3(c, f) (corresponding to the PFM at the border of NW) is slightly shifted towards the left for N_2 atmosphere. This suggests a reduction of the PFM amplitude signal near the top NW edges. In order to validate this finding, PFM measurements were also carried out at a smaller scale as will be discussed below.

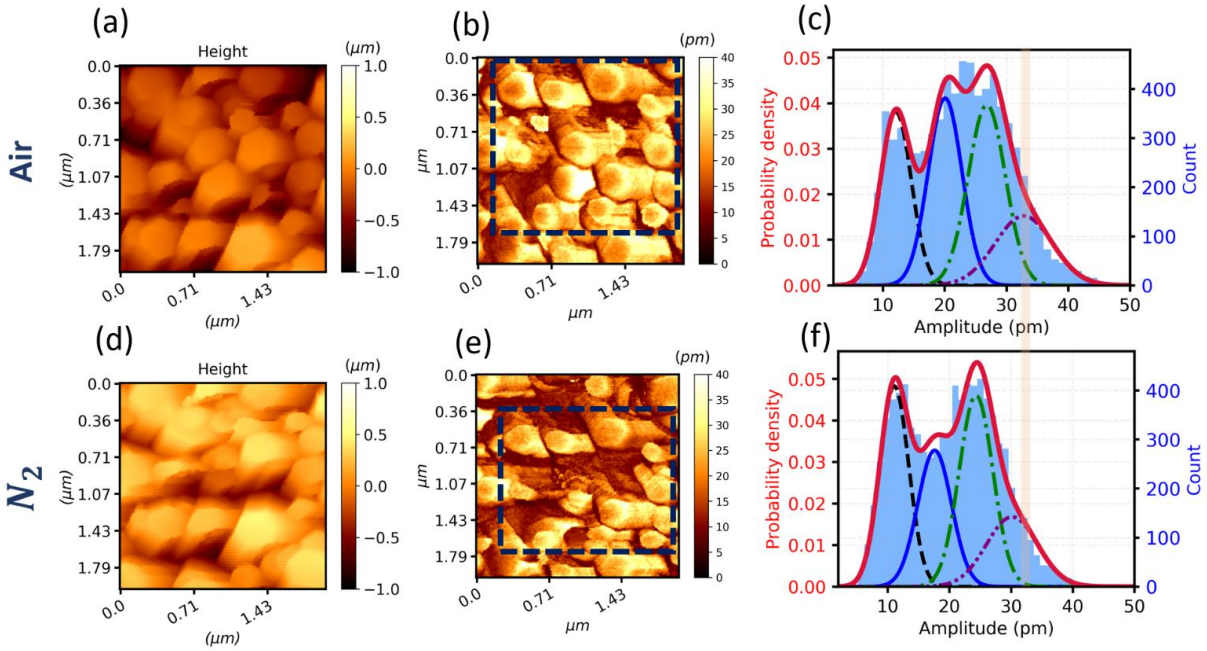

Figure IV-3 Topography, PFM amplitude images, and histograms of PFM amplitude values at the top of NWs grown on ITO/PET substrate under (a-c) atmospheric air and (d-f) N_2 gas. The measurement was done for the same sample region as illustrated by the dashed blue square in (b) and (e). The vertical line in (c) and (f) plots serves as a guideline to see the shift between both purple Gaussian curves.

IV.2.1.2 PFM overs small areas under controlled ambient conditions

In order to further analyze the effect of the ambient atmosphere on the PFM amplitude values close to NW edges, PFM measurements were performed on a single ZnO NW. In this part, we have used a Pt-Si tip with the same characteristics of stiffness and radius as in the previous experiment. The drive frequency and AC bias voltage were set to 14 kHz and 5V, respectively.

Figure IV-4(a) and IV-4(c) show the top-view topography image for a single and same ZnO NW under atmospheric air and N_2 gas. The extracted PFM amplitude values are not homogenous on the top surface of the NW, exhibiting the highest value of 30 pm close to NW

edges, and values in the center of the NW between 12 pm to 20 pm in atmospheric air, as shown in Figure IV-4(b) and IV-4(d) and Figure IV-5(a) and IV-5(c). In other words, the values of effective piezoelectric coefficient $\boldsymbol{d_{33}^{eff}}$ on the edges of the NW (around 6 pC/N) are remarkably larger than those commonly measured in the center (between 2.4 pC/N to 4 pC/N).

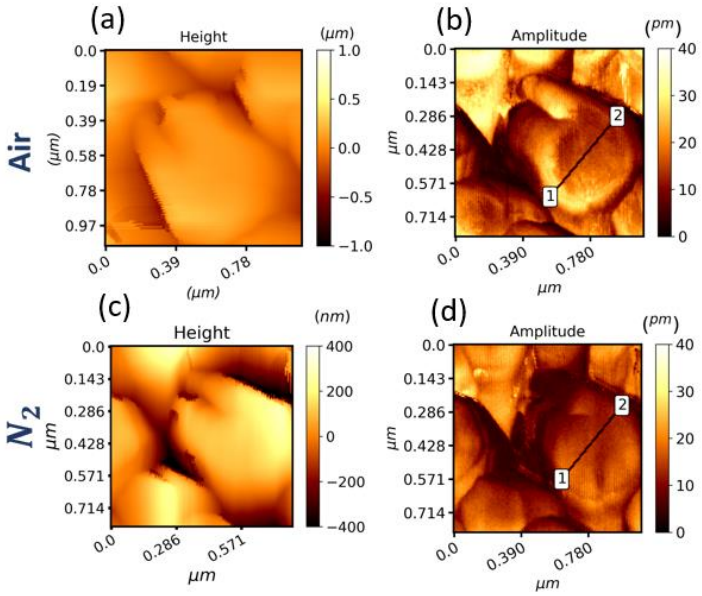

Figure IV-4 Topography and PFM amplitude distributions for a single NW grown on ITO/PET substrate under (a, b) atmospheric air and (c, d) N_2 gas ambient.

The percentage of humidity was then reduced by introducing N_2 gas. For driest conditions (around 8 % of humidity), the PFM amplitude on the top surface decreased down to a few picometers in the center of NW (see Figure IV-5 (a) and IV-5(c)). The PFM amplitude near NW borders was considerably reduced (with values of 20 pm) when compared with the measurement in atmospheric air.

After evaluating all the PFM amplitude values measured on the top surface under different environmental conditions (see Figure IV-5(b) and IV-5(d)), we can more clearly see the reduction of PFM amplitude. The amplitude values lay below 30 pm for the NW evaluated under N_2 gas, as shown by the vertical reference line in Figure IV-5(b) and IV-5(d). In comparison, the maximum PFM amplitude lies below 40 pm under atmospheric air.

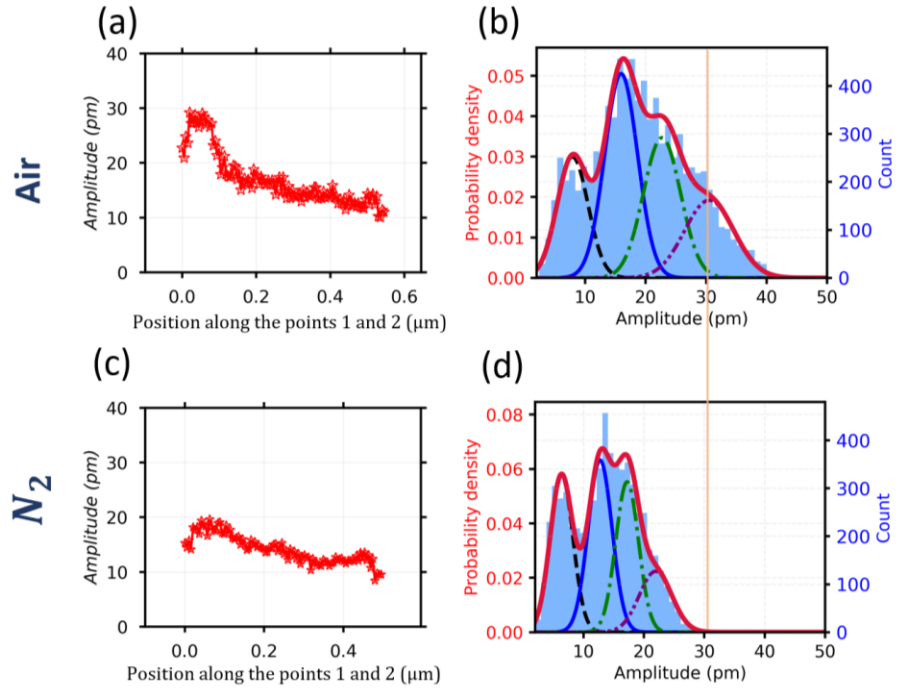

Figure IV-5 PFM amplitude values along points 1 and 2 of the black line in Figure I-4 (b, d), and histograms of amplitude values extracted from the top surface for a single NW grown on ITO/PET substrate under (a, b) atmospheric air and (c, d) N_2 gas ambient. The vertical line in (d) and (h) plots highlights the shift between both purple Gaussian curves.

The observed trends could be consistent with publications showing the effect of working in different ambient atmospheres on PFM measurements. It has been shown that oxygen molecules based on O^-, O^{2-}, or O_2^- and hydroxyl groups can be adsorbed on the NW surface, with an effect on work function and band bending [246]. These chemisorbed oxygen species or hydroxylation reactions that generally occur by exposure to air can form an insulating layer between the semiconductor and the external ambient. This has been demonstrated by the density-functional theory for the absorption of oxygen atoms on Zn-polar surface [247] and by experimental works related to the formation of H and O layers on the Zn-polar surface under ultra-high vacuum conditions [248]. These oxygen or OH coverage can trap electrons inside of n-type ZnO semiconductor, forming a depletion region width (δ) at the NW surface [249], as depicted in Figure IV-6(a). Consequently, the large piezoelectric response on the top surface of NW is ascribed to the fully depleted region (i.e., near NW borders). In contrast, a small piezoelectric response is obtained from the center of NW due to conducting region, which affects the piezoelectric properties of ZnO NW. Figure IV-6(b) represents the ZnO NW surrounded by N_2 gas. The oxygen molecules over the NW are displaced in the gas, reducing the percentage of the trapped electrons on the surface and increasing the conducting region in

the core of NW. This could reduce the piezoelectric response of NW edges since the depletion region is reduced. It is important to mention that a similar effect has recently been observed by Ahmad *et al*. [250] when measuring the output piezoelectric voltage generated by a VING structure based on ZnO NWs under different times of exposure to oxygen in a gas chamber. They achieved an increase in the peak of voltage generated after applying mechanical load when the samples were exposed initially to oxygen in the gas chamber. For instance, an increase of 425.8 % was achieved for exposure to oxygen for 1 h (464 mV) and 5 h (2.44 V).

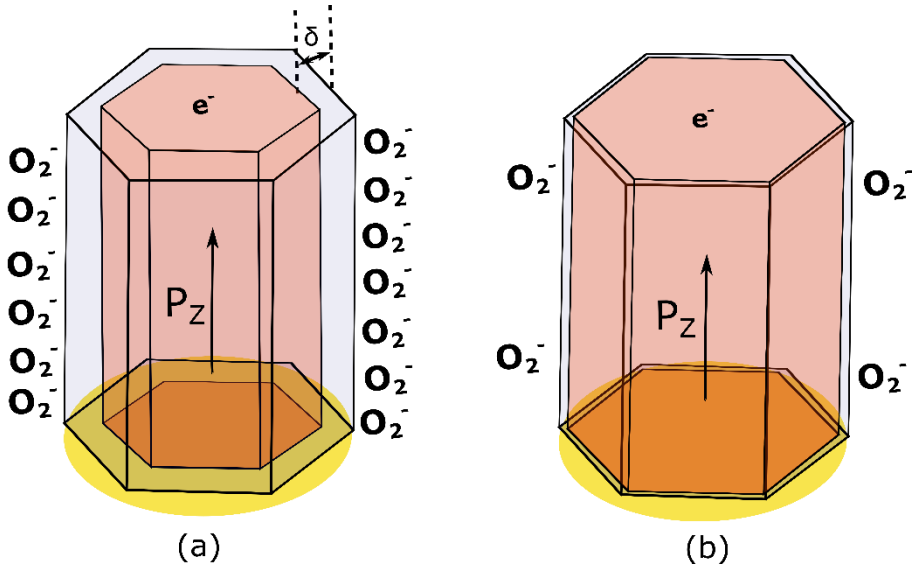

Figure IV-6 Schematics of the depleted (represented by depletion region width (δ)) and conducting (orange color) regions for a single ZnO NW under (a) atmospheric air and (b) N_2 gas.

To go further in this analysis, the efficiency of the piezoelectric response of nanocomposites based on piezoelectric NWs is intimately related to the quality and formation of a Schottky contact at least in one of the two electrical connections [251–253]. In previous studies of nanocomposites based on ZnO [251,252] and GaN [253] NWs, it has been found that an enhancement of piezoelectric response can be possible for higher values of the Shottky barrier. While an ohmic contact can affect completely the performance of the nanocomposite. This is due to the fact that a leakage current can occur through the metal-semiconductor (MS) contact, thus greatly reducing the piezoelectric potential or response [251]. Therefore, the improved piezoelectric response of ZnO NW under air ambient detected in PFM measurement could be evaluated and corroborated by analysing the electron transport at the interface of ZnO NWs/Pt-Si. With this in mind, the barrier height will be studied using KPFM and TUNA measurement for ZnO NWs under air and N_2 gas conditions in the rest of this chapter.

IV.2.2 KPFM measurement under modified atmosphere conditions

The contact potential difference V_{CPD} of the n-type ZnO NW grown on PET-ITO substrate was measured before and during the exposure to N_2 gas. We have used new Pt-Si probes to carry out all experiments. The measurements were done several times with different probes to verify the reproducibility of the FM-KPFM measurement. Figure IV-7(a) and IV-7(e) show the topography images from the top surface of NWs under atmospheric air and N_2 gas at 8% of humidity. Figure IV-7 (b) and IV-7(f) show their V_{CPD} values distributed along the whole scanning area. In order to extract the V_{CPD} values from the top surface of NW, the phase images from the tapping mode were used since they have high contrast and allow distinguishing the top surfaces from the NWs, as depicted clearly in Figure IV-7(c) and IV-7(g). Using Python programming language, V_{CPD} values were appropriately extracted from the top NW surface by plotting their histograms curve (see Figure IV-7(d) and IV-7(h)). The KPFM measurements show values that are distributed between -100 mV and -300mV in atmospheric air and between -200 mV and -400mV for NW in N_2 gas.

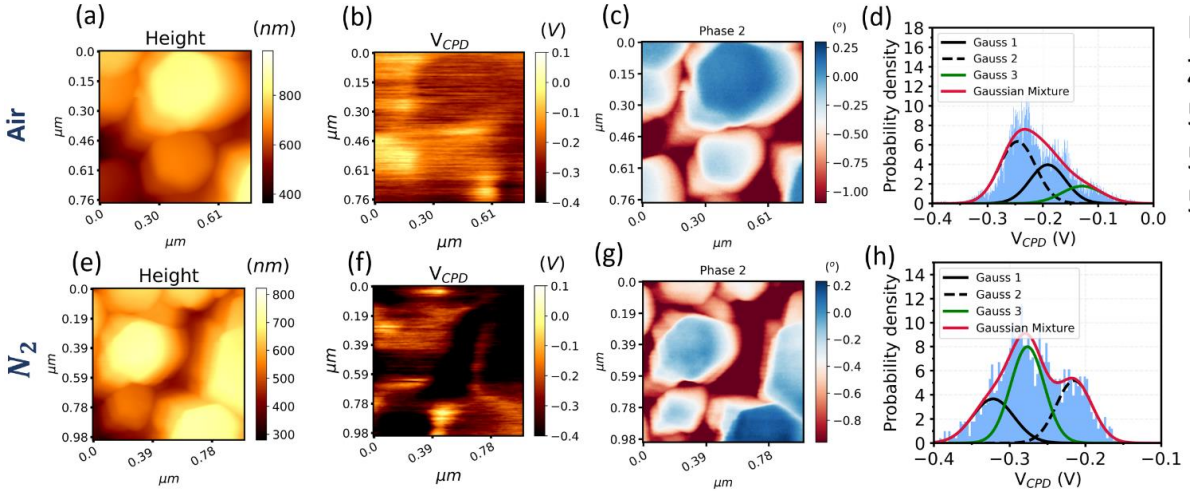

Figure IV-7 Top-view AFM images of topography (a, e), surface potential (V_{CPD}) (b, f), phase (c, g) and histograms (d, h) extracted from V_{CPD} maps using a Pt-Si tip on ZnO NW under (a-d) atmospheric air and (d-h) N_2 gas. The tapping mode phase images (c, g) helped extract the V_{CPD} values only at the top surface of the NWs.

Each probe was calibrated with a reference sample (see more details in App. III.1.2 of Appendix III). From this calibration, the work functions (ϕ) were extracted for ZnO NWs (ϕ_{ZnO}) and the Pt-Si tip (ϕ_{Pt-Si}), as summarized in Table IV-1. These results indicate that ϕ_{Pt-Si} was slightly larger than ϕ_{ZnO} under the same atmospheric condition. It means that an upward band bending was formed on the conduction band because of the transfer of electrons from ZnO to the Pt-Si probe after reaching the thermodynamic equilibrium. In addition, ϕ_{ZnO} decreased until 50 meV when the NWs are placed into N_2 gas, indicating that the Fermi level position was

shifted toward the conduction band as a consequence of changing of the trapped electrons at the surface.

Table IV-1 Work functions values of ZnO NW into atmospheric air and N_2 gas from different experiments.

Parameters / Experiment	Gas condition	ϕ_{ZnO} (eV)	ϕ_{Pt-Si} (eV)
1	Air	(5.00 - 5.12) ± 0.04	5.25 ± 0.04
2	Air	5.00 ± 0.03 eV	5.30 ± 0.03
3	Air	4.95 ± 0.04 eV	5.20 ± 0.04
4	N_2	(4.78 - 4.89) ± 0.03 eV	5.10 ± 0.03
5	N_2	4.82 ± 0.03 eV	5.10 ± 0.02
6	N_2	4.93 ± 0.01 eV	5.20 ± 0.01

IV.2.3 Modelling of the metal-semiconductor junction in the AFM configuration

In order to understand thoroughly the electrical characterization of the metal-semiconductor junction for the ZnO NW, two models are crucial for calculating Schottky barrier ϕ_B when taking into account the semiconducting and piezoelectric properties of NWs. Similarly, Cheung's model is explored in this section for extracting ϕ_B experimentally.

IV.2.3.1 The metal-semiconductor junction

An analytical equation of the Schottky barrier ϕ_B for a semiconductor-insulator-metal structure can be defined considering three different surface charges at the surface of each interface (see Figure IV-8). The space charge (Q_{sc}) formed in the depletion layer inside of the semiconductor (i.e., ZnO NW), the surface state charge density (Q_{ss}) with acceptor surface states, as was done by Bardeen and Crowell [254,255] where its density is N_{it} ($eV^{-1}cm^{-2}$), and an opposite surface charge (Q_m,) formed at the probe tip by electrostatic induction as shown in Figure IV-8. According to the Crowell's model [254], these three surface charge are given in terms of the energy level parameters as

$$Q_{sc} = \left[2q\varepsilon_s N_D \left(qV_{bi} + \Delta\phi_n - \frac{kT}{q}\right)\right]^{\frac{1}{2}} \quad \text{IV- 1}$$

$$Q_{ss} = -qN_{it}\left[E_g - \phi_{CNL} - \phi_B - \Delta\phi_n\right] \quad \text{IV- 2}$$

$$Q_m = -(Q_{sc} + Q_{ss}) \quad \text{IV- 3}$$

By solving this system of equations, a single equation of ϕ_B is determined in terms of a few known parameters:

$$\phi_B = \gamma(\phi_m - \chi) + (1 - \gamma)(E_g - \phi_{CNL}) \quad \text{IV- 4}$$

Where ϕ_m is the work function of the Pt-Si probe (ϕ_{Pt-Si}), χ is the semiconductor electron affinity of ZnO, E_g is the energy bandgap of ZnO, ϕ_{CNL} is the charge neutrality level, and $\gamma = \frac{\varepsilon_{air}}{(\varepsilon_{air}+q^2\xi N_{it})}$ is a parameter in which $\varepsilon_{air} \sim \varepsilon_0$, correspond to the dielectric permittivity in the vacuum and ξ to the thickness of the interface trap charge.

Two extreme cases can be identified: i) the surface trap density N_{it} can tend to zero, resulting in the familiar equation for a simple Schottky barrier of a metal-semiconductor contact. In this case $\gamma \to 1$ and $\phi_B \cong (\phi_m - \chi)$. This would correspond to the NW with clean surfaces and free of defects. ii) The second case is when the surface trap density N_{it} tends to infinity, in this case, the Fermi level is therefore "pinned " at the surface regardless of the metal work function [254]. In this case $\gamma \to 0$ and $\phi_B \cong (E_g - \phi_{CNL})$.

Figure IV-8 shows the energy levels after contacting the Pt-Si probe to the NW surface. Assuming surface trap charge at the NW surface, an intrinsic upward band bending (depletion) is formed near the NW surface. Using Kelvin Probe Force Microscopy (KPFM) (see section IV.2.2), the work function of ZnO NW (ϕ_{ZnO}) is lower than the work function of the Pt-Si probe (ϕ_{Pt-Si}), so that a further upward band bending along the NW-air layer- metal junction probe is formed.

In general, ϕ_B can be reduced by increasing N_{it}. Thus, it can be expected that ϕ_B of ZnO NWs in air ambient (line back in Figure IV-8) is lower than in N_2 (the red line in Figure IV-8). In order to measure ϕ_B in our experiment, we used Cheung's method [256] for the analysis of the electrical results in different ambient conditions, as will be seen below.

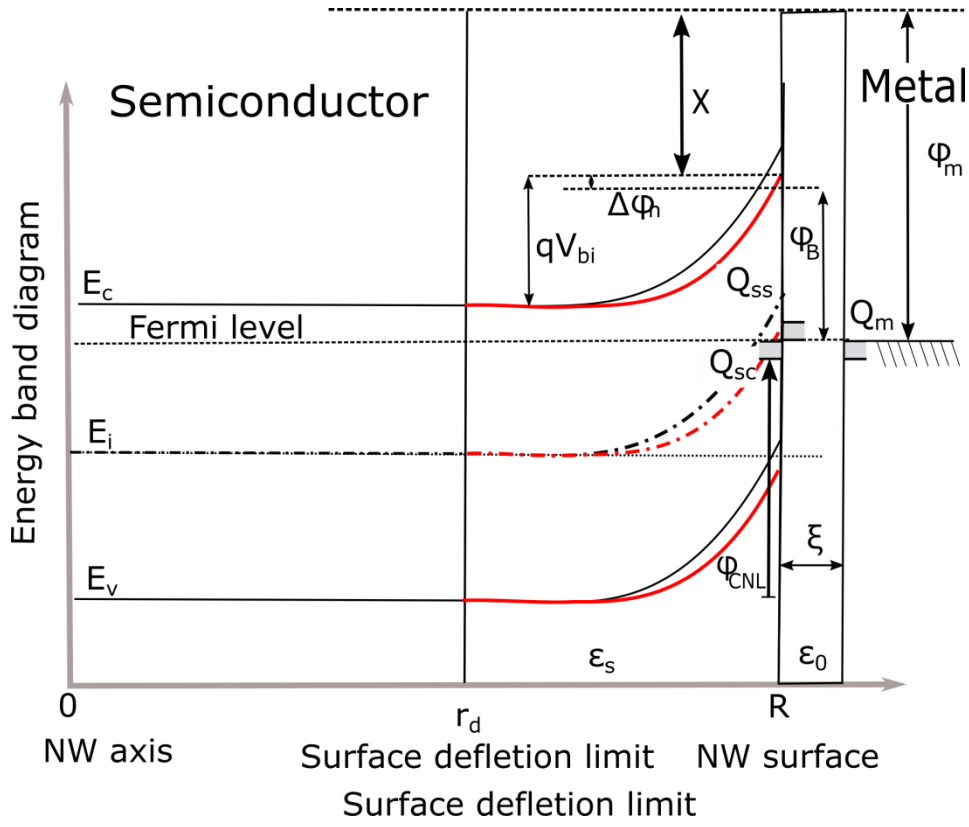

Figure IV-8 Schematic of the energy bands along ZnO/insulator/metal structure for atmospheric air (represented by the black lines) and N_2 (represented by the red lines) as gas. The figure was adapted from [254].

IV.2.3.2 The metal- piezo-semiconductor junction

As discussed before, ZnO is a piezoelectric material. It means that the piezoelectric effect must be taken into account in the electrical junction because we established contact between the probe and NW under a certain applied force. With this in mind, ϕ_B is redefined by considering the piezoelectric effect at metal/ZnO NW in the junction with the definition of a new ϕ_B' defined as [257]:

$$\phi_B' = \phi_B - \Delta\phi_B^{IFL} + \Delta\phi_B^{PZ} \qquad \textit{IV- 5}$$

Here, ϕ_B is defined in Eq. IV- 4. The second term on the right-hand side is related to the image force lowering contribution due to the induction of positive image charges at the surface of the metal and it can be written as:

$$\Delta\phi_B^{IFL} = \left(\frac{q^3 N_d |V_{bi}|}{8\pi^2 \varepsilon_{ZnO}}\right)^{\frac{1}{4}} \qquad \textit{IV- 6}$$

where N_d, V_{bi}, and ε_{ZnO} are the doping level, built-in potential, and permittivity of ZnO, respectively. Regarding the third term, it corresponds to the piezoelectric effect:

$$\Delta\phi_B^{PZ} = -\frac{\sigma^{PZ}\delta_s}{2\varepsilon_{ZnO}} \qquad \textit{IV- 7}$$

where σ^{PZ} and δ_s are the piezoelectric charge density and thickness of the piezoelectric charge. By employing Eq. I-1 defined in section I.2.1 of Chapter I, the z-component of the polarization field ($|P_3| \approx \sigma^{PZ}$) was experimentally calculated using the effective piezoelectric coefficient $\boldsymbol{d_{33}^{eff}}$ and the applied stress T_{33} on the NW. $\boldsymbol{d_{33}^{eff}}$ was measured by PFM technique in section IV.2.1.2 and T_{33} was calculated by the applied force F and the cross-sectional area A during the contact between the probe and NW during I-V experiments (TUNA module).

By taking Eq. IV- 5, we can extract the theoretical value of ϕ_B' (as will be shown below), assuming several parameters of ZnO from the literature and employing the electrical parameters calculated from PFM and KPFM experiments, as listed in Table IV-2. Additionally, the doping level N_d and the surface trap density N_{it} were assumed to take the value expected for the CBD growth technique [137]. These values vary from $5 \cdot 10^{17}$ cm^{-3} to 10^{19} cm^{-3} and from $10^{12} eV^{-1}cm^{-2}$ to $10^{13} eV^{-1}cm^{-2}$, respectively. The results of these calculations will be compared with experimental results in the last section of this chapter.

Table IV-2 Input parameters used in the complete ϕ_B' model

Parameters	Values	Taken from	Ref.
ϕ_m	5.1 eV	KPFM experiments using Pt-Si tip	Our work
χ	4.5 eV	The literature	[258]
E_g	3.37 eV	The literature	[259]
ξ	≈ 0.5 nm	The literature	[257]
ε_{ZnO}	8.9	The literature	[259]
V_{ib}	0.34 V	The literature	[257]
σ^{PZ}	-0.86 C m^{-2}	PFM experiments and I-V experiment	Our work
δ_s	≈ 0.2 nm	The literature	[257]
φ_{CLN}	2.5 eV	The literature	[260]

IV.2.3.3 Cheung's method for extracting the barrier height from measurements

Generally, the Schottky barrier model uses the thermionic emission theory to calculate the current in a metal/semiconductor contact using the following equation

$$I = A^{**}T^2 \exp\left(\frac{-q\phi_B}{kT}\right)\exp\left(\frac{q(V - IR_s)}{nkT}\right) \qquad \textit{IV- 8}$$

where A_{eff}, A^{**}, T, q, V, k, n, ϕ_B, and IR_s are the effective area of the diode, the Richardson constant, the absolute temperature, the fundamental charge constant, the applied DC bias, the Boltzmann constant, the ideality factor, the Schottky barrier, and the voltage drop across the series combination of the diode, respectively.

Implementing Cheung's method [256], two linear functions can be deduced from Eq. IV-8 (see Eq. IV-9 and IV-10). This allows the calculation of the ideal factor n, the series resistance Rs and the barrier height ϕ_B with a single I-V characteristic curve.

$$\frac{dV}{d(Ln(I))} = \frac{nkT}{q} + R_s I \qquad \textit{IV- 9}$$

$$H(I, n, R_s) = R_s I + n\phi_B \qquad \textit{IV- 10}$$

These quantities can be measured experimentally from the slope and y-axis intercepts after plotting $\frac{dV}{d(Ln(I))}$ vs I and H (V, I, n) vs I using the I-V data (see more details in App. III.2 of Appendix III), as will be seen in the next sections. It should be added that this method has been widely used for exploring the junction contact formed by metal/ZnO NW [17–19].

IV.2.4 AFM Electrical measurements under modified atmosphere conditions

To evaluate the environmental effect on electrical measurements, we measured I-V curves for the same and single ZnO NW upon exposing it to two gases, such as air and N_2. The maximum value of AFM cantilever deflection was set to 30 nm, which is equivalent to a constant applied force of 1045 nN (for a measured tip stiffness of 35 N/m) between tip and top NW surface. A DC bias voltage was applied in the range of ±3 volts. The I–V characteristics show a clear non-ohmic behavior for the NW in both ambients conditions, when forward-biased (i.e., under positive DC voltage values $+V_{dc}$) and when reverse-biased (i.e., under negative DC voltage values $-V_{dc}$), as shown in Figure IV-9(a). To further understand I-V curves, we must consider two Schottky junctions, such as Pt/ZnO NW and ZnO NW/ITO on the AFM measurement (see

Figure IV-9(b)) which can be compared to the back-to-back Schottky diode (BBSD) model. This BBSD model has been previously used for the study of the electron transport on M-S-M structures based on ZnO NW devices, considering the junction resistance (R_s) connected in series among both barriers [261–263]. In such structure, the current is limited by the current in the reverse-biased diode, which is the ITO-ZnO diode for negative DC bias and the ZnO/Pt probe diode for positive DC bias.

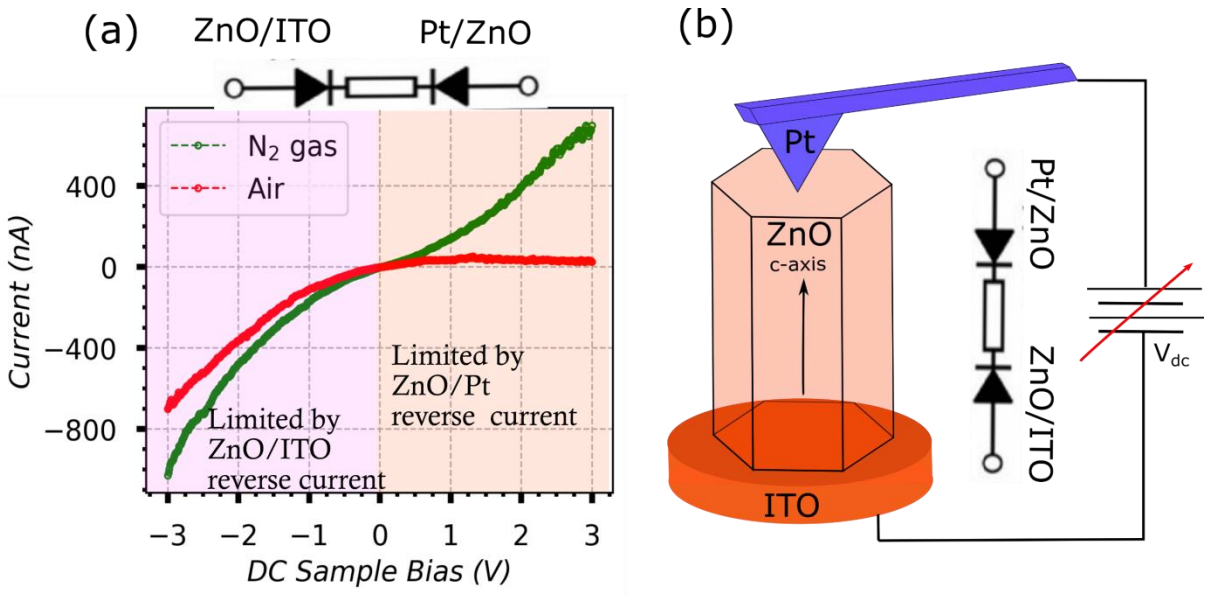

Figure IV-9 I–V characteristics of ITO/ZnO NW/Pt at high (in air ambient) and low (in N_2 gas) humidity percentage; the top schematic image represents the electrical equivalent circuit of the device with double contact junctions. (b) Diagram of the AFM measurement showing the double contact junction.

Some reports on ZnO [264] and GaN [253] NWs have demonstrated that the Shottky contact is strongly affected by the size of the contact. According to the theoretical calculations [265], if the contact size is smaller than the characteristic length l_c (see Eq. IV-11), the Schottky barrier will therefore decrease by decreasing the contact size. l_c is given by the following equation

$$l_c = \sqrt{\left(\frac{2\varepsilon_{ZnO}\varepsilon_0 V_s}{e\, N_d}\right)} \qquad \textit{IV- 11}$$

where V_s corresponds to the surface potential. In our case, this can be calculated to be about 76 nm (for ZnO with values of V_s and N_d of 3V and $5 \cdot 10^{17} cm^{-3}$, respectively).

It should be added that under these conditions, the tunneling mechanism starts to be important in the current flow [265]. With this in mind, we evaluated the size contact between the Pt-Si probe and ZnO NW using Hertz's theory [266] to be approximately 5.87 nm (see more details in App. III.3 of Appendix III). By comparing this value with l_c, we can affirm that the Schottky

barriers formed within air and N_2 ambient conditions are affected by the contact size. So, the I-V characteristic should not be approached only with a simple thermionic emission theory [253]. In this regard, the analysis of all I-V characteristics measured from AFM equipment is investigated employing Cheung's method, where the n factor and R_s can be extracted for each junction contact, as will be shown later.

It is certainly possible that a layer with H and O over the Zn-polar surface of ZnO NW (i.e., the top surface) can be formed and evolved in time, changing its top layer stoichiometry as well as the electric properties (as the work function and the Fermi level position) for n-type conductivity [247,248]. Assuming this interfacial layer, the Schottky mechanism will be locally structured as a metal-insulator-semiconductor (as was discussed in IV.2.3.1), allowing the introduction of the surface trap charge. As was demonstrated by changing the ambient conditions, this surface trap charge is strongly affected, thus modifying the electrical characteristics of the ZnO NW/Pt-Si junctions.

IV.2.4.1 Initial I-V measurements under air and N_2

A single NW was selected for electrical measurements under both atmospheric air and N2 conditions (see Figure IV-10(a)). The adhesion images, that are shown in Figure IV-10(b) and IV-10(c), demonstrate that both measurements correspond to the same ZnO NW. They also show the shape of the top surface of the NW (blue color in the same Figure). Figure IV-10(d) exhibits the current distribution of the chosen single ZnO NW under atmospheric air. The measurements in N_2 conditions (see Figure IV-10(e)) were carried out under a constant flux of N_2 and a minimum value of chamber humidity of 8%.

The current distribution on the top NW surface corresponds to the maximum value of the forward bias (i.e., at 3V) and it is related to the reverse current of the tip/NW contact junction. According to these results, no electric current is evidenced on the top surface of NW for atmospheric air, as shown in Figure IV-10(d). In contrast, the current values of about 300 nA are measured at the top surface of NW for N_2 conditions (see Figure IV-10(e)).

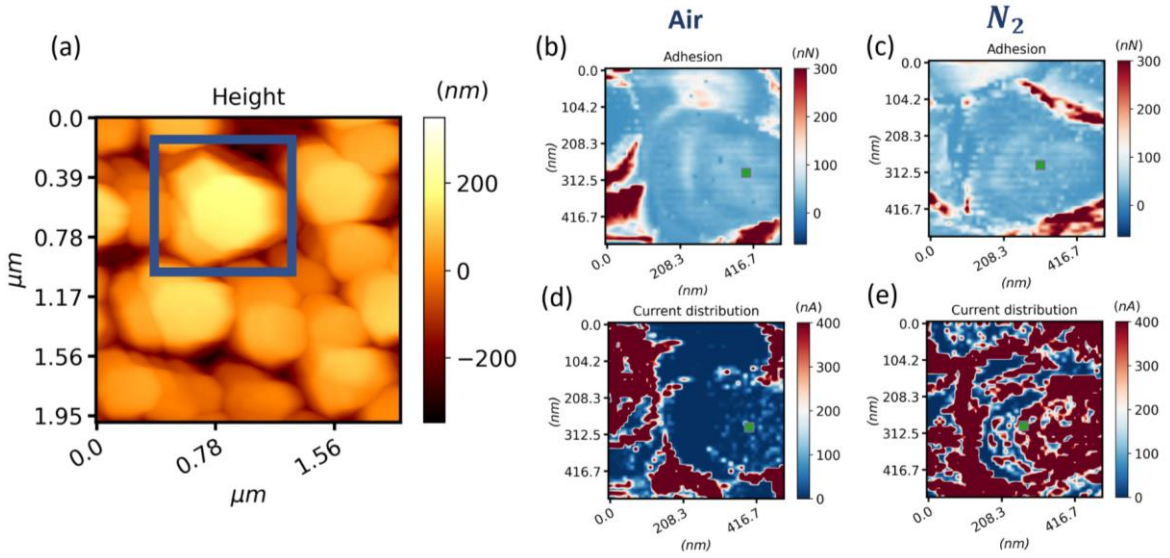

Figure IV-10 AFM topography (a) of a large area showing the selected NW (within the blue square) for the electrical characterization. Adhesion, and current distribution of the single ZnO NW under (b, d) atmospheric air and (c, e) N_2 gas. The current distribution was taken at 3 V of DC bias.

Some reports in the literature have demonstrated that ambient humidity impacts the electric properties of ZnO NW, leading to the adsorption and desorption process of oxygen (O_2) molecules, water, and other chemical species on the NW surface [203,267–269]. This means that the surface charge depletion layer plays an important role in modifying the barrier height of the contact between NW and the AFM tip in our experiments, as explained in section IV.2.3.1 and illustrated in Figure IV-8.

Until now, we have demonstrated that the values of current are negligible for the reverse current of NW/Pt junction at the top NW surface into air ambient, keeping the same input parameters, as the contact force, DC bias and probe. It can be associated with a higher value of barrier height created in this junction. Once the N_2 gas is inserted in the AFM chamber, the conduction starts to appear at the surface of NWs, evidencing an effect of the gas which could be associated with a modification of the N_{it} parameters as well as its barrier height. For instance, ϕ_B for NW with totally clean surfaces and no piezo effect can be calculated to be 0.6 eV approximately, assuming $\gamma = 1$ (see section IV-2.3.1) and knowing ϕ_m (5.1 eV according to KPFM) and χ (4.5 eV according to the literature). A more deep experimental study of the barrier height will be presented in the next section.

IV.2.4.2 Full I-V measurements under N_2

The contact junction between ZnO NW/Pt-Si tip demonstrated low conductivity under an external bias under air ambient. On the contrary, a current could be measured under N_2 gas (see Figure IV-9(a)) thanks to a reduction of the barrier height because of the influence of the surface trap charge. Hence, all electrical parameters (as n, R_s, and ϕ_B) were extracted from the measurements under N_2 gas. The measurements were carried out for ZnO NW growth on PET-ITO substrate using Pt-Si tips. A DC bias voltage was applied between the tip and the sample during a dwell time of 300 ms with a constant cantilever deflection of 30 nm. We varied the DC voltage between -1.5 V and 1.5 V and made a separate analysis of the I-V curves obtained for positive and negative values in order to extract information about the limited diode. To ensure that electric parameters were accurate and reproducible, I-V measurements were made in three different places for three other NWs, as shown in Figure IV-11(a-c). We used Cheung's method (see section VI.2.3.3) for extracting the electrical parameters n, R_s, and ϕ_B of the junctions ITO/ZnO and ZnO/Pt-Si tip.

For ITO/ZnO junction, I-V curves stored from a scanning area of a single ZnO NW were statistically analysed (see Figure IV-11(d-f)). A Python programming code was developed to extract all appropriate electrical parameters for all I-V curves, maintaining the linearity condition on the $\frac{dV}{d(Ln(I))}$ vs. I and H vs. I functions. Figure IV-11(g-i) shows that the average value of n for each NW is between 1 and 5. These n values are higher than unity (the value for an ideal diode). They could be associated with a high trap density [270]. However, these values are lower than those reported for ZnO nanorods ($n \sim 7-9$) [264].

As for series resistance R_s, their values were between 5MΩ to 15MΩ, as illustrated in Figure IV-11(j-l). As can be seen in Figure IV-11(m-o), the average of ϕ_B is between 0.44 eV and 0.47 eV for the three experiments that are associated with the large-scale ZnO layer coated ITO contact at the bottom side of the sample. As this junction contact is not exposed to the environment, ϕ_B does not change as the environmental conditions are modified. This was demonstrated experimentally for the same ZnO NW under air and N_2, obtaining a value ϕ_B of 0.45 eV (see more detail in App. III.4 from Appendix III).

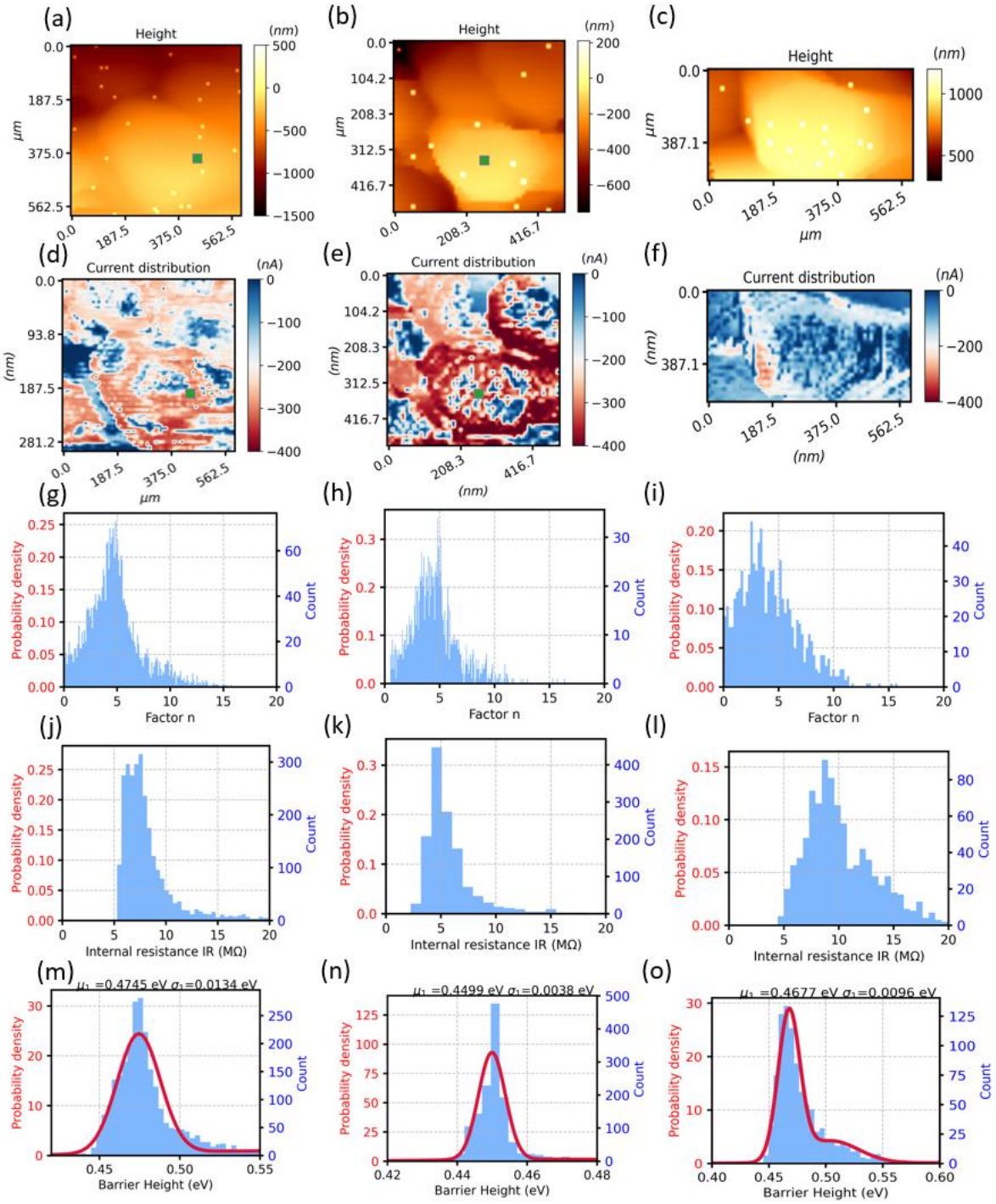

Figure IV-11 (a-c) This figure gathers the results obtained on the top surface of 3 different nanowires. The results corresponding to a given nanowire are shown in the same column. AFM topography images and (d-f) current distribution for a single ZnO NW. (g-i) Ideality factor n, (j-l) series resistance Rs, and (m-o) the Schottky barrier ϕ_B distributions obtained from at least 1000 I-V curves related to the ITO/ZnO NW junction analyzed from the scanned area. All measurements were carried out under N_2 gas at -1.5V of DC signal.

As for the contact junction formed by the ZnO NW/Pt-Si tip, it is openly exposed to environmental conditions, altering the conductivity as was discussed above. Figure IV-12(a-c) shows the current distribution at 1.5 V under N_2 gas, revealing current values at the top surface

of ZnO NW. Their n and R_s values of at least 1000 analysed I-V curves vary from 1 to 4 and 1MΩ to 20MΩ (see Figure IV-12(d-f) and 11(g-i)), respectively. Using these electrical parameters (n and R_s), the mean value of ϕ_B for NW/Pt junction is between 0.55 eV and 0.63 eV, which is greater than the ϕ_B for the contact junction at the bottom (ITO/ZnO junction).

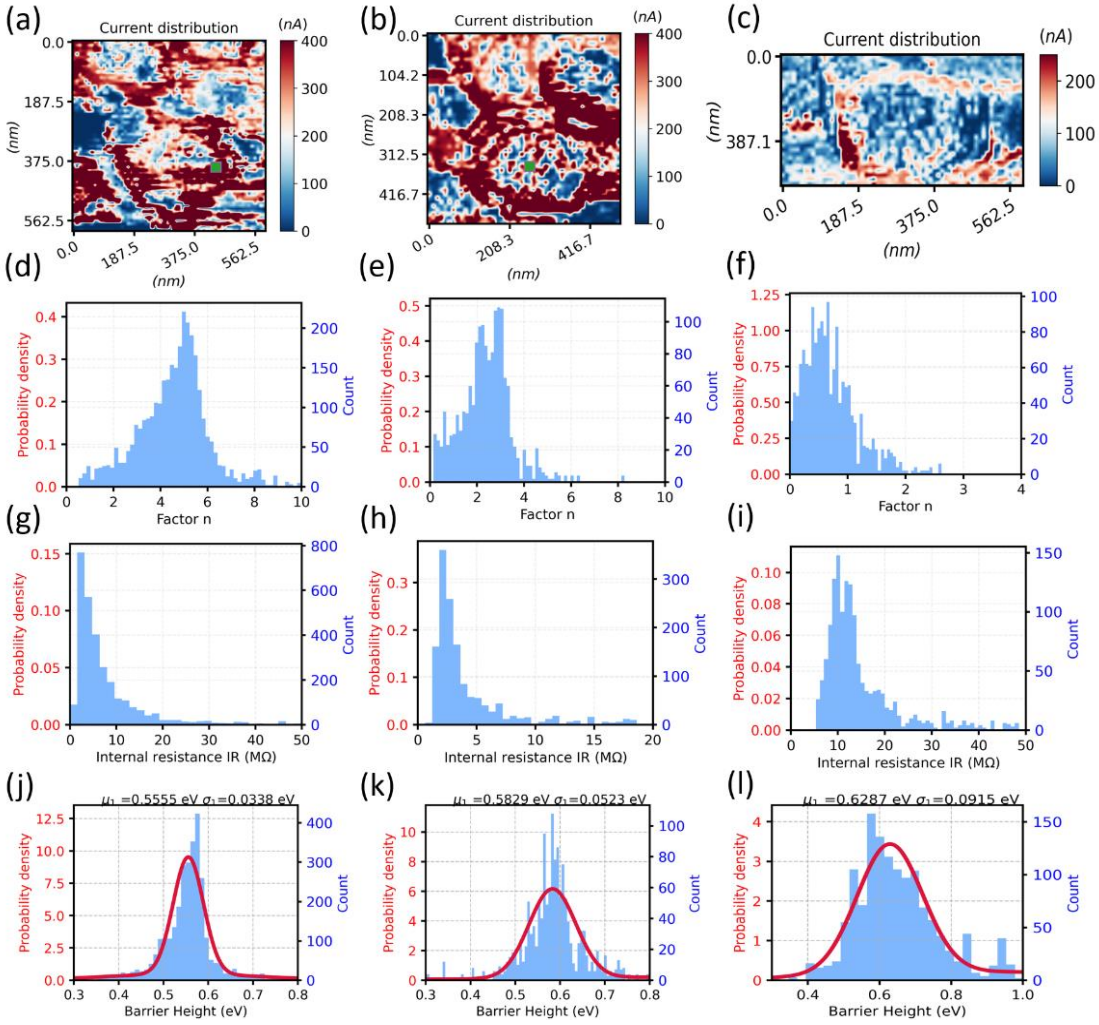

Figure IV-12 (a-c) Current distribution for a single ZnO NW. (d-f) Ideality factor n, (g-i) series resistance R_s, and (j-l) the Schottky barrier ϕ_B distributions from at least 1000 I-V curves related to ZnO NW/Pt-Si analyzed from the scanned area. All measurements were carried out under N_2 gas at 1.5V of DC signal

IV.2.5 Experiments vs. the theoretical model

In this section, the theoretical values of the NW/Tip Schottky barrier height (ϕ'_B) are calculated using Eq. IV- 5 and compared to the experimental values obtained in the precedent section. The yellow shadowed region of Figure IV-13 corresponds to the theoretical prediction of ϕ'_B for N_d and N_{it} values expected with the CBD growth of ZnO NWs. This figure shows that ϕ'_B decreases by 15 % as N_d increases from $5{\cdot}10^{17}$ cm^{-3} to 10^{19} cm^{-3}, thus exposing a doping level

dependency for ZnO NWs grown by CBD technique. We also observe the ϕ'_B has a significant increase of 23 % as N_{it} increases from $10^{12} eV^{-1} cm^{-2}$ to $10^{13} eV^{-1} cm^{-2}$. This trend was observed for both doping concentrations. Moreover, the Schottky barrier values measured experimentally using current-voltage measurements were compared to the theoretical predictions by putting them randomly (scattered points in Figure IV-13) inside the theoretical range corresponding to CBD (yellow region). Although we don't have experimental values of N_d and N_{it}, the theoretical and experimental values are in fair agreement in this range. This validates the proposed values of N_d and N_{it} found in the literature for NW grown in CBD. More experiments are required to confirm the exact values of N_d and N_{it} for own ZnO NWs.

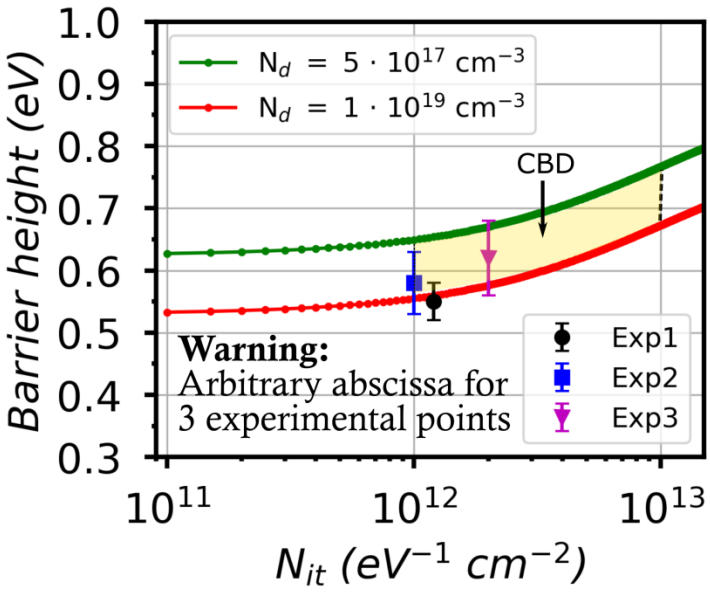

Figure IV-13 Barrier height values (ϕ'_B) calculated from Eq. IV- 5 as a function of N_{it} for two extreme values of N_d according to the growth of ZnO NW using CBD. The scattered points are the three average values of barrier height calculated experimentally in this work. The values are placed into the shaded region corresponding to N_{it}, and N_d values for the CBD growth technique found in the literature.

Assuming that the surface trap density N_{it} on the NW in atmospheric air (around of $10^{13} eV^{-1} cm^{-2}$) is larger than in N_2 gas, ϕ'_B would be significantly larger than 0.8 eV, preventing the electrons to flow through the ZnO NW/Pt junction. In the present case, it was impossible to measure any current values in this contact junction under this environmental condition, thus we will not have sufficient information about the Schottky barrier. Finally, these complementary characterizations can be used to estimate the N_d and N_{it} parameters of piezoelectric semiconducting NWs. We would require in future studies the measurement of at least one of these two parameters to extract the second one. In this work, the atmospheric

ambient can effectively tune the Schottky barrier height to improve its electric current sensitivity, as it has been previously reported for flexible humidity and oxygen sensors based on an individual ZnO NW [203,271]. Moreover, these studies confirm that a higher surface trap density might be present in atmospheric air conditions, which in turn produced a larger depletion region inside the NWs, improving their piezoelectric performance, as was demonstrated by PFM measurements in these ambient conditions.

IV.3 Conclusions

In this chapter, we used the modification of the ambient atmosphere to evaluate experimentally the potential role of surface trap density on the piezoelectric response of individual ZnO NW grown on flexible substrates (PET/ITO). Piezoelectric force microscopy (PFM) was used to measure the piezoelectric response of a single NW into atmospheric air and N_2 gas. A larger effective piezoelectric coefficient $\boldsymbol{d_{33}^{eff}}$ was found at the edges of NWs into atmospheric air. In contrast, $\boldsymbol{d_{33}^{eff}}$ values into atmospheric N_2 were strongly reduced. This was attributed to the role of oxygen molecules. This influence of oxygen molecule has not been taken into account yet in PFM measurements, although their effect on the piezoelectric output potential of VING devices has been observed recently with sensing applications in view. The increase of $\boldsymbol{d_{33}}$ was consistent with an increase in surface trap density (N_{it}) at the surface of ZnO NW in atmospheric air, resulting in increased electron trapping at the surface and formation of a depletion region along NW edges. These results are in good agreement with the simulations of Chapter 2, which accounted for the coupling of semiconducting and piezoelectric, and found that the $\boldsymbol{d_{33}^{eff}}$ of individual NW increases as N_{it} increases.

Kelvin probe force microscopy (KPFM) and current-voltage measurements were also carried out under different environmental conditions for several individual ZnO NWs grown on a flexible substrate (PET/ITO). Using KPFM, we extracted the work function of the Pt-Si tip and of the top surface of ZnO NWs. The values obtained for ZnO NWs in N_2 gas were smaller than in atmospheric air, showing a modification of the position of the energy band levels. Moreover, the work function of ZnO was lower than that of the Pt-Si probe, showing that the Pt-Si probed formed a Schottky contact on ZnO, with an upward band bending at the surface.

When measuring the current-voltage characteristics of the ZnO NWs with the AFM, the system to be considered consisted thus of an ITO-substrate/ZnO-NW/Pt-tip stack, which can be viewed as a pair of back-to-back Schottky junctions in series. The current in such a system is limited by the current through the diode which is reverse biased, so it is possible to characterize the two

junctions using the same experimental configurations, by simply varying the sign of the potential difference across the system. Current-voltage characteristics showed non-linear curves, consistent with this electrical model. They were also non-symmetrical, indicating that the barrier height of the two Schottky junctions was not the same. A programing code was developed to extract at least 1000 values of Schottky barrier ϕ_B from a complete scanning area over the top surface of ZnO NWs. Statistical analysis was used to determine the average value of ϕ_B both for ITO/ZnO NW and ZnO NW/Pt junctions. The Schottky barrier height was smaller at ITO/ZnO than at ZnO/Pt interface. As could be expected, ϕ_B values at the interface between ITO and the ZnO seed layer were independent of atmospheric variation, which is an important result in terms of validation of the measurement. In contrast, the Pt/ZnO NW barrier height exhibited a strong dependence on the ambient atmosphere, with a current being measurable only in N_2 gas.

Finally, a complete theoretical model was used to investigate the dependence of ϕ_B with ZnO doping level (N_d) and surface trap density (N_{it}), with account for the piezoelectric effect. For N_d and N_{it}, we used the reduced range of values expected for ZnO NWs grown by CBD. The measured ϕ_B values fit quite fairly within the range of values expected with this theoretical model. This study opens very promising avenues for the understanding of surface effects in ZnO nanowire-based devices. It provides some clues about the origin of the improvement in electromechanical transduction that can be expected from ZnO nanowires, with high-performance and sensitive harvesters and sensors in perspective.

Conclusions and Outlooks

ZnO NWs have been studied quite extensively, showing outstanding electromechanical properties at nanoscale in comparison to bulk and thin-film forms. Nevertheless, the theoretical study of the coupling between their piezoelectric and semiconducting properties needs further attention, both at the level of individual nanowires and for nanowires integrated in nanocomposites. Moreover, the dependence of their electromechanical properties with ZnO growth method or with NWs surrounding environment has not been completely tackled so far.

Most theoretical works developed in the past have considered ZnO NWs as insulating, with no account for their semiconducting properties, such as doping level N_d and surface trap density N_{it}. A first attempt to take into account N_d and N_{it} in the simulation of nanocomposites based on ZnO NWs has been recently reported by our group. It has been shown that decent piezoelectric potential values could be generated under mechanical compression, provided the NWs were fully depleted. With 100 nm radius NWs, this condition was achieved for instance with values of N_{it} and N_d of $5\times10^{11}cm^{-2}eV^{-1}$ and $10^{17}cm^{-3}$, respectively. However, this study considered the case of ultra-slow traps only. In this thesis, we have proposed a complete nanocomposite model considering also the opposite case of ultra-fast traps as a first step towards the study of trap dynamics. The simulated structure represented a typical unit cell of a VING and consisted of a single vertical ZnO NW, grown on a ZnO seed layer and integrated into a polymer matrix (PMMA), with contacts placed at the bottom and on the top of the cell. It was evaluated under an axial compressive load. Reference ZnO thin films, as well as composite structures, where ZnO was considered as an insulator, were also simulated for comparison. The introduction of traps into the numerical simulations provided explanations to several poorly addressed problems:

i) A better electromechanical response would be achieved with higher values of N_{it}, thanks to free carriers depletion and suppression of screening effects. The scattering of the values of electric potential and piezoelectric coefficients $\boldsymbol{d_{33}}$ reported in the literature may result from differences in doping level, NW diameter, and even more, surface trap density;

ii) The electromechanical response strongly depends on traps dynamics;

iii) The non-symmetric output voltage of the nanocomposite, reported in some experiments, may be explained by the presence of a certain amount of ultra-slow surface traps;

iv) An alternative explanation of the saturation of the electromechanical response of long semiconducting nanowires was proposed. Until now, it had been stated that such a

saturation should be observed, based on the consideration that the piezoelectric response of a semiconducting NW should be limited to a very thin region, depleted of free carriers by the pressure applied on top of NW. However, such a mechanism was not consistent with experimental results, which found much larger piezoelectric responses, with an impact of length up to much longer NWs. This was without taking into account the role of surface traps. In contrast, we found that the piezoelectric response was dominated by the bottom of the NW, and that saturation occurred when the NW was so long that the potential variation resulting from piezoelectric polarization was bending the conduction band towards the Fermi level, allowing the presence of free carriers and polarization screening in the upper part of the NW.

v) The nanocomposite performance strongly depends on the NWs growth method, through the afforded range of doping level and trap density.

Finally, optimization guidelines were provided as a function of a connected resistive load. One important result of this PhD thesis is the explanation of the variability of the experimental performance values found in the literature, which could only be retrieved by self-consistent numerical simulations, coupling piezoelectric and semiconducting properties of ZnO NWs.

The analytical and computational investigations provided some insight into the physical principle operation of devices, thus guiding experimental research. Theoretical models show that the effective piezoelectric coefficient d_{33}^{eff} was closely linked to the electromechanical response and efficiency of piezoelectric materials. We have shown that it was affected by the semiconducting properties inherent to ZnO. However, this coefficient has been rarely measured at nanoscale, while its value would be needed to evaluate correctly the performance of energy transducers based on ZnO NWs. Among the different methods that have been employed until now, PFM can measure the effective piezoelectric coefficient $\boldsymbol{d_{33}^{eff}}$ employing the converse piezoelectric effect. However, the electrostatic effect induced by surface potential or surface charges can amplify the piezoelectric amplitude signal, resulting in misinterpretations or parasitic piezoelectric amplitude magnification. In this PhD thesis, we proposed a sophisticated statistical method to analyse the piezoelectric response and to extract $\boldsymbol{d_{33}}$ on ZnO NWs. We used an automated, well-controlled and non-destructive method known as DataCube mode applied to PFM. For this study, innovative samples were fabricated in our group in collaboration with some partners of the European project PULSE-COM. ZnO NWs were grown over a flexible gravure-printed ZnO nanoparticle seed layer. We directly measured $\boldsymbol{d_{33}}$ on vertically aligned ZnO NWs grown on these flexible substrates. The measured $\boldsymbol{d_{33}}$ values were found in the range of 4 pm/V to 5 pm/V, which are close to those obtained from ZnO NWs grown on

rigid substrates. In addition, a single polarity was measured for these NWs. Besides, we noticed that the $\boldsymbol{d_{33}}$ value was not homogeneous throughout the top surface of the NWs and that its magnitude depended on NW radius. Based on numerical simulations performed with COMSOL software, the non-homogeneity of $\boldsymbol{d_{33}}$ could be explained by semiconducting properties. The proposed method allows investigating, in a careful and direct manner, the piezoelectric parameters of aligned arrays of ZnO NWs, avoiding extra manufacturing processes and artifacts induced by electrostatic forces.

We used complementary AFM techniques to further investigate the role of surface trap density. To do so, we performed piezoelectric force microscopy (PFM), Kelvin probe force microscopy (KPFM), and conducting atomic force microscopy (C-AFM), using different controlled environmental conditions with the aim of modifying ZnO surface properties. We found that the environmental conditions do play a key role and modify surface potential, piezoelectric response and local electric current. These results confirm once more the role of the semiconducting properties of ZnO NWs in their performance. The values of piezoelectric coefficient ($\boldsymbol{d_{33}}$), ZnO work function (ϕ_{ZnO}) and Schottky barrier at the contact between AFM tip and ZnO NWs (ϕ_B), were measured in either air or N2 ambient. Consequently, the correlation between the surface traps and atmospheric conditions was investigated, showing the variability of the $\boldsymbol{d_{33}}$ values at the top surface of ZnO NWs. The current transport values of the ZnO/Pt (AFM tip) Schottky contact were deeply studied by comparing the experimental results with a theoretical model of the Schottky barrier, which included the additional semiconducting properties for ZnO (N_d and N_{it}) as well as the piezoelectric properties of ZnO.

At the end of this thesis, we built a complete simulation model that includes linear piezoelectricity and semiconducting properties in ZnO material. Both static and transient simulations are possible with this model.

Of course, there remain several issues which could not be addressed within the time limit of a PhD thesis but could be interestingly addressed in the future. For instance, many parameters of ZnO NWs are crucial for the optimization of nanocomposites, in particular the doping level. Do our NWs have the same doping value of those reported in the literature [168,169,272,273]?. Further complementary electrical characterizations are needed to address this issue, for instance scanning capacitance microscopy (SCM) [169,272]. What would be effect of non-linear piezoelectricity on the nanocomposite? Indeed, according to theoretical reports in the literature, this affects the current transport processes for single ZnO NWs [274]. What would be the importance of flexoelectric effects, which bring into play the role of strain gradients in the electromechanical response? Indeed, some theoretical models about piezoelectric nano beams

[275] have demonstrated a significant effect on the bending rigidity and deflection of NWs. A wide field of research is also concerned with the practical use of NW-based composites for the realization of innovative energy harvesters, self-powered devices or sensors. All these points would be extremely interesting to explore, remembering that, as demonstrated throughout this Ph.D. thesis, semiconducting properties should be considered for the correct analysis and design of electromechanical transducers based in ZnO NWs.

Résumé en Français

Contribution à l'étude des propriétés piézoélectriques de nanofils de ZnO et de nanocomposites associés en vue d'une application à la conversion d'énergie mécanique à électrique

Le marché des réseaux sans fil de capteurs de faible puissance destinés à l'Internet des objets (IoT) s'est développé rapidement au cours de la dernière décennie. Il cible des applications telles que la surveillance de l'état des structures, ou la surveillance médicale et environnementale, en fournissant des observations continues sur certains paramètres. Certaines de ces applications nécessitent un nombre considérable de capteurs, potentiellement localisés dans des lieux difficiles d'accès. Pour cette raison, les capteurs qui utilisent une batterie comme source d'alimentation sont peu pratiques et très coûteux. A l'inverse, des capteurs collectant dans l'environnement l'énergie nécessaire à leur fonctionnement constituent une solution intelligente pour mettre en œuvre un réseau de capteurs sans fils auto-alimentés.

L'énergie mécanique est l'une des sources d'énergie que l'on trouve en abondance dans l'environnement et il est possible d'imaginer des applications récupérant l'énergie de vibration des structures, de mouvements humains, de flux d'air, de vagues dans le milieu aquatique, etc. Les technologies piézoélectriques sont l'une des alternatives pour collecter l'énergie mécanique et la convertir en électricité, sous une charge mécanique par compression ou flexion. Elles sont développées et commercialisées depuis de nombreuses années à l'échelle macroscopique mais la piézo-conversion générée par des nanofils (NFs) piézoélectriques est un axe de recherche scientifique relativement récent. Les premières démonstrations de piézo-conversion à partir de NFs ont été publiées en 2006 par le Professeur Zhong Lin Wang en utilisant des NFs de ZnO. De nombreuses avancées ont été réalisées depuis comme, au niveau fondamental, l'étude du rôle de la charge mécanique, de la matrice diélectrique ou la densité de surface de NFs à l'intérieur d'un nanocomposite (voir la partie bleue de la Figure 1). Cependant, il reste encore beaucoup à faire en ce qui concerne la prise en compte des propriétés semi-conductrices de ces NFs de ZnO et leur couplage aux propriétés piézoélectriques. Cette thèse vise à approfondir la compréhension des phénomènes électromécaniques à l'échelle nanométrique par rapport à l'état de l'art, de façon à identifier les conditions permettant d'optimiser les performances d'un dispositif de conversion d'énergie basé sur ce type de composite. Nous nous concentrerons sur des NFs de ZnO individuels obtenus par croissance verticale à partir d'un substrat et sur des

nanocomposites constitués d'un réseau dense de NFs verticaux, noyés dans un matériau différent jouant le rôle de matrice. Nous nous intéresserons notamment à l'influence de la taille des NFs sur leurs propriétés piézoélectriques, en tenant compte des effets d'écrantage par les dopants ionisés, les porteurs libres et les pièges d'interface. Pour atteindre cet objectif, plusieurs paramètres ont été étudiés, notamment le niveau de dopage, la densité des pièges d'interface et les dimensions des NFs, comme indiqué dans la partie jaune de la Figure 1 ci-dessous.

Figure 1: Diagramme des paramètres qui jouent un rôle très important dans la performance des nanocomposites basés sur les NFs de ZnO.

Au cours de ma première année de thèse et sur la base de l'expertise développée ou sein de l'équipe, j'ai d'abord réalisé des simulations multi-physiques (modèles analytiques et simulations numériques basées sur la méthode des éléments finis) pour acquérir une compréhension du fonctionnement des nanocomposites à base de NFs de ZnO, lorsqu'ils sont soumis à une force axiale compressive, en tenant compte des couplages entre propriétés mécaniques, piézoélectriques et semi-conductrices. Cela a été utile pour l'un de mes objectifs, qui était d'identifier des pistes d'optimisation et de réaliser des démonstrateurs de recherche sur la base des expériences récentes développées à l'IMEP-LaHC. En parallèle, je me suis formé à différentes techniques, comme le dépôt par couches atomiques (ALD) et le dépôt en bain chimique (CBD), pour la croissance de NFs de ZnO sur des substrats rigides comme le silicium (Si) ou sur des substrats flexibles comme le poly téréphtalate d'éthylène (PET). Les échantillons sur substrats de Si ont été utilisés comme référence, en particulier pour la caractérisation de la réponse piézoélectrique des NFs individuels, , telles que le coefficient piézoélectrique d_{33}^{eff}, à

l'aide de techniques de microscopie à force atomique (AFM). Par exemple, la technique de la microscopie à force piézoélectrique (PFM) a été employée pour étudier le coefficient d_{33}^{eff}, en utilisant l'effet piézoélectrique inverse, c'est-à-dire, un potentiel électrique est appliqué localement sur la nanostructure produisant une déformation mécanique. En analysant cette déformation par rapport à la tension appliquée, le coefficient d_{33}^{eff} peut-être calculé. Au cours des deux années suivantes, la caractérisation AFM a été importante pour la mesure électrique des NFs de ZnO obtenus par CBD sur des substrats flexibles (dans le cadre du projet européen PULSE-COM), avec la mise en œuvre PFM, de la microscopie par sonde Kelvin (KPFM) et de mesures courant-tension locales (TUNA ou C-AFM). Toutes ces mesures ont été corrélées entre elles pour mettre en lumière les phénomènes électromécaniques à l'échelle nanométrique, et les propriétés semi-conductrices et piézoélectriques, grâce au développement de méthodologies de mesure originales.

Le manuscrit est organisé en quatre chapitres:

I) Chapitre I: État de l'art des céramiques et nanocomposites piézoélectriques.

De nos jours, les transducteurs électromécaniques – électromagnétiques, électrostatiques et piézoélectriques – constituent une piste prometteuse pour la récupération d'énergie. Parmi les différentes solutions possibles, nous nous sommes focalisés sur la piézoélectricité qui est la capacité d'un matériau dont la structure cristalline est non centrosymétrique à se polariser en réponse à une déformation mécanique (effet piézoélectrique direct) ou à se déformer en réponse à un champ électrique (effet piézoélectrique inverse).

Dans ce chapitre, nous avons exploré l'efficacité et la performance des matériaux piézoélectriques synthétiques sur la base de paramètres comme les coefficients piézoélectriques (d_{33}) et les constantes diélectriques (ε_r) publiés dans la littérature. Quelques matériaux contenant du plomb (comme le titanate de zirconium de plomb, PZT) et sans plomb (comme le titanate de baryum, $BaTiO_3$, et des céramiques ferroélectriques) présentent des coefficients piézoélectriques très élevés. Toutefois, ces matériaux nécessitent un traitement à haute température (> 300 °C) et doivent être polarisés par l'application d'un champ électrique élevé avant d'être utilisés (étape de *poling* en anglais). Or, notre objectif est d'utiliser des matériaux piézoélectriques qui seraient faciles à fabriquer, produits à basse température et exempts d'éléments toxiques ou rares. Avec ces contraintes à l'esprit, nous avons comparé différents types de matériaux, piézoélectriques inorganiques, piézoélectriques organiques et piézoélectriques composites, qui sont les plus couramment étudiés dans les applications de récupération d'énergie. Les récupérateurs d'énergie piézoélectriques traditionnels à base de

céramique ont quelques obstacles associés à leur fragilité dans les applications avec de grandes déformations, limitant ainsi leur fonctionnalité. Par conséquent, la fabrication de nouvelles technologies comme les microrésonateurs (voir Figure 2 (a)) et les nanocomposites (voir Figure2 (b)) ont récemment gagné en popularité en raison de certaines de leurs caractéristiques lors de l'utilisation de matériaux à l'échelle micro et nanométrique.

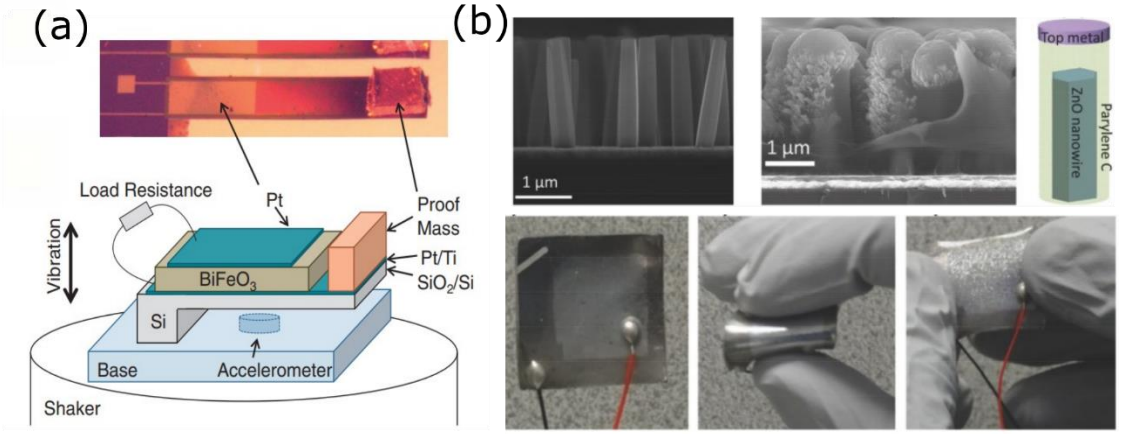

Figure 2: Schéma d'un (a) micro résonateur (images tirées de [276]) et (b) nanocomposite (images tirées de [97]) pour la récupération de l'énergie mécanique.

En ce qui concerne le type de matériau et le type de technologie qui ont été utilisés dans ces travaux, nous avons porté une attention particulière au matériau ZnO et aux composites à base de NFs de ZnO noyés dans une matrice organique (comme le PMMA) qui permet d'améliorer la conversion électromécanique. D'autre part, des recherches récentes ont montré que l'anisotropie des propriétés élastiques et piézoélectriques jouent un rôle important dans l'efficacité piézoélectrique de NFs de ZnO liés à la polarité. De plus, des propriétés électroniques de ZnO comme le dopage (N_d), éventuellement non intentionnel, pendant le processus de croissance des NFs, et la densité des pièges de surface (N_{it}) ont été définis selon les valeurs trouvées dans la littérature. En ce qui concerne les nanocomposites pour la récupération d'énergie, nous faisons le point sur l'état de l'art en termes de résultats expérimentaux et de simulations. Il permet de constater qu'il existe dans la littérature une très grande variabilité dans les valeurs du potentiel piézoélectrique produit par des dispositifs intégrant des NFs verticaux de ZnO (structures dites VING) sous compression mécanique. Cette variabilité n'est pour l'heure pas expliquée et sa compréhension constituera une des motivations de notre travail.

Dans ce chapitre, nous pourrons conclure que les charges de surface ou la densité des pièges de surface ne sont pas bien connues pour les NFs de ZnO, ainsi que leurs effets sur les dispositifs VING pour la récupération d'énergie mécanique sont mal compris et probablement non

contrôlés. Par ailleurs, les paramètres comme N_d et N_{it} dépendent fortement de la méthode de croissance des NFs de ZnO. Une étude par simulation numérique pourrait être un point clé pour corréler les données expérimentales et les modèles théoriques. Tout cela pourrait être possible en explorant l'influence de la géométrie des NFs de ZnO (comme le rayon et la longueur). Afin de pousser le raisonnement un peu plus loin, l'étude de la dynamique de la densité des pièges de surface – en commençant par les deux cas extrêmes de pièges ultra-lents ou ultra-rapides – pourrait mettre en évidence certains impacts significatifs sur les performances de VING. D'autres paramètres comme la densité de puissance et le coefficient piézoélectrique (d_{33}^{eff}), qui jouent un rôle important pour l'optimisation de dispositifs VING devraient être aussi étudiés pour comprendre comment améliorer la conception des dispositifs à base de NF de ZnO en tenant compte des paramètres comme N_d et N_{it}. Ces différents aspects sont explorés dans les chapitres suivants.

II) Chapitre II: Simulation numérique de dispositifs à base réseaux de NFs verticaux (VING).

Dans ce chapitre, nous développons une étude numérique de la réponse électrique à l'aide de simulations par éléments finis (FEM) de dispositifs VING sous compression axiale. La simulation peut être limitée à une cellule élémentaire du nanocomposite, composée d'un NF vertical immergé dans un polymère isolant souple (une matrice de PMMA et une couche isolante supérieure). La cellule simulée intègre également le substrat et les contacts inférieur et supérieur.

Il est important de noter que la plupart des travaux de simulation numérique basés sur la méthode FEM ont considéré ZnO comme un isolant ou comme un semi-conducteur non dopé, situation dans laquelle un NF donné fournit sa performance maximale. Or cette hypothèse peut ne pas être valable pour certaines dimensions de NF. À l'inverse, d'autres simulations numériques, dans lesquelles le niveau de dopage N_d a été pris en compte (cas plus réaliste), ont fourni des valeurs de potentiel de sortie extrêmement faibles, de quelques millivolts au maximum, en raison de l'écrantage de la polarisation piézoélectrique par les porteurs libres à l'intérieur des NFs. Ces résultats n'expliquent donc pas les valeurs parfois élevées obtenues expérimentalement dans des NFs pourtant dopés. Nous avons émis l'hypothèse que la présence de pièges d'interface à la surface de ZnO – et le piégeage du niveau de Fermi en surface (SFL, pour Surface Fermi Level) qui peut en résulter – pourrait expliquer qu'il soit possible d'obtenir une réponse importante malgré le dopage. Nous avons développé un modèle complet couplant

les propriétés semi-conductrices et piézoélectriques de ZnO en tenant compte des valeurs expérimentales du niveau de dopage N_d et en incorporant la densité de piège N_{it} dans les conditions aux limites aux interfaces entre ZnO et les matériaux environnants. Ce nouveau modèle génère de fait des valeurs de potentiel de sortie de l'ordre de grandeur de celles publiées dans les rapports expérimentaux. Ces effets avaient été abordés dans une thèse antérieure en supposant que les pièges étaient ultra-lents. Dans ce chapitre, nous reprenons cette hypothèse en l'étendant à des densités de pièges variables et nous la comparons à l'hypothèse opposée de pièges ultra-rapides pour évaluer leur influence respective sur les performances d'un VING.

Le coefficient piézoélectrique effectif d_{33}^{eff} est aussi très important pour qualifier les propriétés piézoélectriques d'un matériau. Nous avons donc utilisé également les simulations pour évaluer la valeur de d_{33}^{eff} en tenant compte du couplage complet entre les propriétés piézoélectriques et semi-conductrices pour les dispositifs VING basés sur NFs de ZnO. Notons que ce coefficient effectif est alors celui de la structure composite dans son ensemble.

Expérimentalement, les dimensions des NFs, le niveau de dopage N_d et la densité de piège N_{it} peuvent varier dans des gammes de valeurs spécifiques, bien qu'assez larges, en fonction de la méthode de croissance des NF de ZnO. Nous avons donc étudié les performances théoriques qui pouvaient être attendues d'un VING pour ces gammes de valeurs de N_d et N_{it}, pour les principales méthodes de croissance. Dans tous les cas, les performances sont améliorées par une réduction du diamètre et par un allongement des NFs, conformément à certaines conclusions expérimentales, mais nos résultats permettent de comparer les gammes de diamètres exploitables pour les différentes techniques de croissance.

Finalement, l'évaluation de l'énergie récoltée par des nanocomposites à base de NFs de ZnO dans une application pratique nécessite l'ajout d'une charge résistive externe (entre 100 Ω et 10 MΩ) afin d'extraire la puissance maximale générée par l'adaptation d'impédance. Par conséquent, nous avons réalisé une étude numérique complète sur tous les paramètres électriques permettant de quantifier les performances du VING en tant que composant, tels que la densité de puissance, la densité de courant, la densité de charge et l'énergie électrique, en tenant compte des paramètres comme N_d et N_{it} par NFs de ZnO.

Dans ce chapitre, nous pouvons conclure que le champ de polarisation généré par un VING est considérablement affecté par les porteurs libres pour les faibles densités de pièges de surface (N_{it}), tandis que pour les grandes densités, le nanofil peut être déserté et l'écrantage supprimé, ce qui permet d'atteindre de bien meilleures performances. Nous avons défini la piézoréponse du NF comme la différence entre les potentiels de sortie calculés avec la charge mécanique

(concernant à l'état finale) et sans la charge mécanique (concernant à l'état initiale). Une asymétrie entre les piézoréponses obtenues après les actions de compression et de libération a été détectée pour certaines valeurs de N_{it} dans le cas où les pièges sont considérés comme ultra-lents. Elle a été expliquée par un effet d'écrantage partiel de la polarisation électrique près du sommet du NF lors de l'action de libération. Nous avons observé un impact significatif de la dynamique des pièges sur la piézoréponse et sur d_{33}^{eff}, avec une réponse piézoélectrique beaucoup plus importante pour les pièges ultra-lents que pour les pièges ultra-rapides. Les différences de densité des pièges, mais également de dynamique des pièges, pourraient donc expliquer la dispersion des valeurs expérimentales trouvées dans la littérature en termes de piézoréponse.

En ce qui concerne l'effet de la technique de croissance des NFs de ZnO et de leurs dimensions, nos résultats ont explicitement montré que la réponse piézoélectrique dépend du rayon et de la longueur de NF, conformément à ce qui a été montré dans certains rapports expérimentaux. Les NFs plus longs et plus étroits, qui sont totalement désertés de leurs porteurs libres, fournissent une bien meilleure réponse piézoélectrique. Cependant, le rayon critique en dessous duquel le NF est déserté sur toute sa longueur varie selon la méthode de croissance

Nous avons inclus dans cette analyse, la méthode CBD utilisée pour la fabrication de dispositifs VING dans notre groupe. Nous avons constaté que l'orientation de croissance (Zn-polaire ou O-polaire) a une influence notable sur la performance du VING.

D'ailleurs, nous avons démontré qu'il n'y a aucun avantage à augmenter la longueur du NF au-delà de 3µm avec la méthode CBD (O-polaire). Nos résultats de simulations montrent une saturation du potentiel piézoélectrique généré au-delà de cette longueur. Cette tendance est obtenue en tenant compte du N_d et N_{it} dans le modèle. Ceci a été comparé avec les tendances obtenues avec des modèles sans N_{it} et en considérant le NF comme isolant.

Concernant les simulations du fonctionnement du VING connecté à une résistance de charge, ce qui correspond à une situation expérimentale réaliste, nous pouvons conclure que les résultats numériques obtenus pour la piézoréponse, extrapolés pour les valeurs optimales de la résistance de charge, sont en bon accord avec les études précédentes publiés par la communauté scientifique ainsi qu'avec les résultats expérimentaux de notre groupe. Il en est de même pour la capacité du VING. Nos simulations prédisent une dépendance des caractéristiques électriques du VING sous compression avec le rayon des NFs, avec de meilleures performances pour les NFs fins. En utilisant un niveau de dopage de $5 \cdot 10^{17} cm^{-3}$ et une densité de piège de 10^{13} eV^{-}

$^{1}cm^{-2}$, qui se situent dans la plage de valeurs attendues pour la méthode CBD selon la littérature, la valeur du rayon de NF doit rester inférieure à 70 nm.

III) Chapitre III : Évaluation locale de la piézoélectricité des NFs de ZnO.

Comme nous l'avons vu aux chapitres I et II, les performances d'un matériau piézoélectrique peuvent être évaluées au moyen du coefficient piézoélectrique d_{33}^{eff}. D'après nos simulations, des valeurs optimales de potentiel de sortie et de densité de puissance peuvent être obtenues pour les NFs de ZnO ayant un rayon inférieur à 70 nm avec la méthode CBD, ce qui fournissait également des valeurs optimales pour d_{33}^{eff}. De plus, la littérature a montré que deux polarités cristallines (Zn-polaire ou O-polaire) ont déjà été observées sur des NFs de ZnO obtenus par CBD, ce qui peut donc affecter les propriétés piézoélectriques telles que le coefficient piézoélectrique d_{33}^{eff}. Dans ce chapitre nous avons donc étudié expérimentalement la réponse piézoélectrique (c'est-à-dire le coefficient d_{33}^{eff} global), en utilisant la technique de microscopie à force piézoélectrique (PFM), qui avait déjà été employée par d'autres chercheurs pour étudier le coefficient d_{33}^{eff} et la polarité de couches minces et de nanostructures.

Nous avons donc proposé une nouvelle méthode de mesure, associant la méthode d'acquisition DataCube à une stratégie d'analyse statistique, pour extraire d_{33}^{eff} et la polarité seulement sur la surface des NFs de ZnO à l'exclusion des espaces entre NFs. Nous avons fait ces mesures pour 3 types d'échantillons, avec des NFs obtenus par CBD sur des substrats rigides (Si/oxyde d'indium-étain ou ITO) ou flexibles (PET/ITO et PET/oxyde de zinc dopé à l'aluminium ou AZO). L'un des principaux objectifs est d'analyser les effets du dopage, du diamètre et de la charge de surface des NFs sur le coefficient d_{33}^{eff}.

D'après nos résultats expérimentaux, nous pouvons conclure que la méthode DataCube est une technique AFM puissante pour mesurer directement les propriétés piézoélectriques des NFs de ZnO. Elle permet d'éviter un traitement supplémentaire, comme l'encapsulation de tous les NFs dans un polymère isolant souple proposé dans la littérature. Les NFs obtenus sur les substrats souples ont fourni le même coefficient piézoélectrique effectif d_{33}^{eff} (environ 4-5 pm/V) que les échantillons de référence sur Si (le substrat rigide). En outre, tous les échantillons analysés ont révélé une polarité unique (Zn-polaire) sur la surface supérieure du NF de ZnO, ce qui serait un bon signal pour renforcer la piézoélectricité à grande échelle.

Un autre aspect important que nous devons souligner est lié à la dépendance de ce coefficient d_{33}^{eff} avec le rayon des NFs, qui a été détectée sur les NFs de ZnO obtenus sur les substrats rigides et flexibles, avec des valeurs plus élevées pour les NFs plus fins et des valeurs plus faibles pour les NFs plus larges. Ceci est cohérent avec la tendance déduite de la simulation du chapitre II lorsque l'on considère les niveaux de dopage et les pièges de surface dans les NFs de ZnO.

Enfin, il a été remarqué que l'amplitude piézoélectrique n'était pas homogène sur la surface supérieure des NFs, avec les valeurs d'amplitude les plus faibles pour quelques NFs et les valeurs d'amplitude les plus élevées sur les bords de la plupart des NFs. Cet effet est soutenu par des simulations numériques en incluant à la fois les propriétés piézoélectriques et semi-conductrices dans les nanostructures. Des simulations plus complexes (tenant compte de la géométrie 3D et des pièges sur la surface des NFs) seraient nécessaires pour bien comprendre cet effet.

IV) Chapitre IV : Mesures électriques complémentaires sur les NFs de ZnO dans des conditions ambiantes contrôlées.

Afin de pousser plus en avant les travaux concernant le rôle de la densité de pièges en surface sur les propriétés des NFs de ZnO, nous avons effectué des mesures électriques locales sur des NFs individuels en présence d'atmosphères différentes, dans notre cas l'air et l'azote (N_2). L'objectif principal est de modifier les propriétés de surface du NF de ZnO. En effet, selon la littérature, les conditions environnementales peuvent jouer un rôle-clé en modifiant le potentiel de surface, la réponse piézoélectrique et le courant électrique local, via notamment des modifications des états de surface. Nous avons utilisé les NFs sur substrat flexible (PET/ITO) et nous avons utilisé les techniques KPFM, PFM ainsi que des mesures locales de courant électrique en fonction de la tension (I-V). Le coefficient piézoélectrique d_{33}^{eff} du NF, les travaux de sortie et la hauteur de barrière Schottky à l'interface AFM pointe/NF ont été mesurés dans les deux conditions environnementales. Enfin, nous avons développé une méthodologie pour extraire le niveau de dopage et/ou la densité de piège d'interface à partir d'une étude approfondie de la hauteur de barrière Schottky aux deux interfaces métal / semi-conducteur.

En ce que concerne le coefficient piézoélectrique, nous pouvons dire que les valeurs d_{33}^{eff} mesurées sont plus élevées au bord des NFs dans l'air. En revanche, les valeurs de d_{33}^{eff} sont fortement réduites sous azote. Au vu de la littérature, cette tendance peut être attribuée au rôle

des molécules d'oxygène qui augmentent la densité de piège de surface (N_{it}) à la surface du NF de ZnO dans l'air, entraînant un piégeage accru des porteurs libres à la surface et désertant la périphérie du NF. Ces résultats sont en bon accord avec les simulations du chapitre II, qui prenaient en compte le couplage entre les propriétés semi-conductrices et piézoélectriques et nous constatons aussi que le coefficient d_{33}^{eff} des NF individuels augmente à mesure que N_{it} augmente.

D'autre part, nous avons extrait le travail de sortie de la pointe AFM (Pt-Si) et de la surface supérieure des NFs de ZnO. Les valeurs obtenues pour les NF de ZnO étaient plus faibles sous N_2 que dans l'air, montrant une modification de la position des niveaux de la bande d'énergie. De plus, le travail de sortie de ZnO était inférieur à celui de la sonde Pt-Si, montrant que la sonde Pt-Si formait un contact Schottky sur ZnO, avec une courbure des bandes d'énergie vers le haut (désertion en surface pour un matériau de type n comme ZnO).

Des cartographies de mesures courant-tension locales ont été effectuées dans les deux conditions (sous air et sous azote). Les caractéristiques I-V relevées en chaque point ont montré des courbes non linéaires, conformes à un modèle électrique formé de 2 contacts Schottky tête-bêche. Les caractéristiques étaient également non symétriques, ce qui indique que la hauteur de barrière des deux jonctions Schottky (aux interfaces ITO/ZnO NF et ZnO NF/Pt) n'était pas la même, ce qui est cohérent avec le fait que les matériaux qui sont en contact avec le NF de ZnO ont un travail de sortie différent comme il a été démontré par KPFM. La zone de polarisation intéressante pour l'étude de l'influence des états d'interface est celle où le courant est limité par la jonction Schottky ZnO/Pt. Les valeurs de courant électrique dans cette zone n'ont pu être mesurées que sous N_2, les valeurs dans l'air étant trop faibles. Les paramètres électriques comme le facteur d'idéalité de la jonction Schottky (n), la résistance série (R_s) et la hauteur de la barrière de potentiel (ϕ_B) ont été extraits en analysant statistiquement toutes les courbes I-V sous gaz N_2.

Dans ce chapitre, nous pouvons conclure que la hauteur de barrière Schottky était plus faible à l'interface ITO/ZnO qu'à l'interface ZnO/Pt. Comme on pouvait s'y attendre, les valeurs ϕ_B à l'interface entre ITO/ZnO étaient indépendantes du type d'atmosphère, ce qui est un résultat important en termes de validation de la mesure. En revanche, la hauteur de la barrière à l'interface Pt/ZnO NF présentait une forte dépendance à l'atmosphère ambiante. De plus, un modèle théorique complet a été utilisé pour analyser la dépendance des valeurs ϕ_B avec le niveau de dopage de ZnO (N_d) et la densité de piège de surface (N_{it}), en tenant compte de l'effet piézoélectrique. Pour N_d et N_{it}, nous avons utilisé la plage réduite de valeurs attendues pour les NF de ZnO obtenus par CBD. Les valeurs mesurées ϕ_B s'inscrivent alors assez bien dans la

plage de valeurs attendue avec ce modèle théorique. Cette étude ouvre des voies très prometteuses pour la compréhension des effets de surface dans les dispositifs à base de nanofils de ZnO.

Appendix I. Numerical simulation results

App. I.1 Power values using the R_L term and I_0 term

Upon evaluating the current value, which flows through the external circuit corresponding to the piezo-semiconducting ZnO NW, we found that their values are in good agreement with those current values calculated in the model with insulating ZnO NW, as shown in Figure App. I- 1. In addition, we assessed the power values using two different ways to extract them. One option is using the load resistance (R_L) term (circle shape in Figure App. I- 1), and the other option is using the electric current (I_0) term (triangular shape in Figure App. I- 1). Figure App. I- 1 (a) and (b) show that both power densities are consistent whatever the definition of power, achieving a maximum value of power density of around 450 pW cm^{-2} at an R_L of 3MΩ.

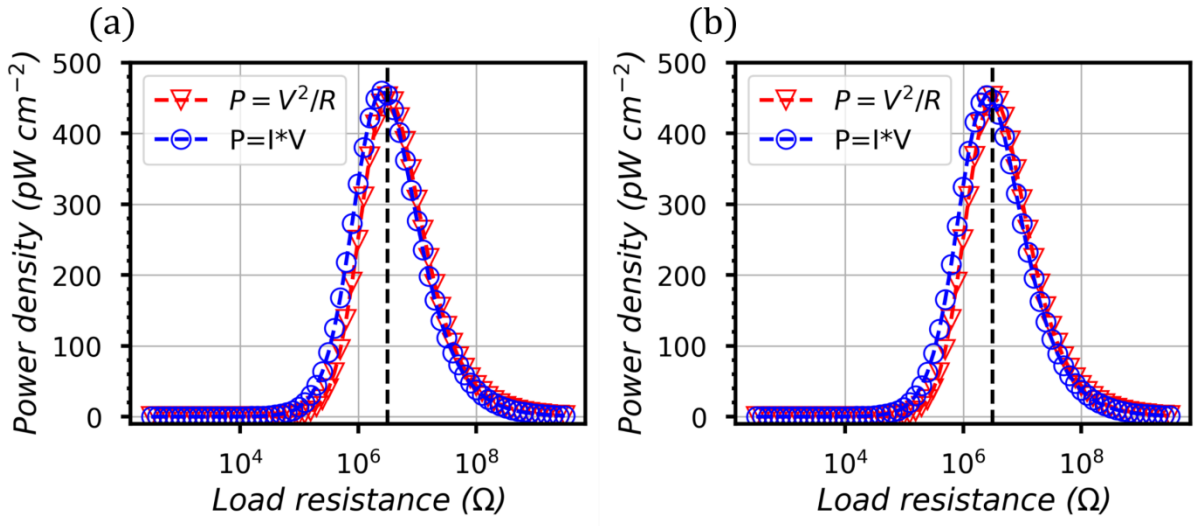

Figure App. I- 1 Generated power values as a function of load resistance for the VING device with (a) the insulating and (b) piezo-semiconducting ZnO NW. Everything was made for ZnO NW with 50nm wide and 3µm long after applying a force of about 3.14nN.

App. I.2 Optimal resistance and capacitance values for a unit cell of VING device

In order to optimize the values of load resistance (R_{opt}) and capacitance (C_{NG}) of the VING, we have calculated these quantities as a function of the ZnO radius. The determination of R_{opt} and C_{NG} requires two different steps for each radius. Firstly, a sweep of the load resistance R_L in a static study allows to compute of the output power as a function of R_L from which R_{opt} is extracted as the load resistance leading to the maximum power (see Figure II-16 (d)). Then, a time-dependent study is carried out for a value of R_L equal to R_{opt}. The resulting voltage pulse obtained after applying the mechanical input at t=0 allows extracting C_{NG} (see section II.2.5 in the main text). Figure App. I- 2 (a,b) presents the R_{opt} and C_{NG} as a function of ZnO radius.

These values for ZnO NW at 50 nm wide are in agreement with the values obtained by harmonic FEM simulations [209] and analytical calculations [204] both with the same R_{opt}~10^{16} Ω and C_{NG}~10^{-19} F for a 50 nm width ZnO NW. As expected, R_{opt} increases as the ZnO radius decrease (see Figure App. I- 2(a)). Indeed, when the radius increases, the internal impedance of the NW decreases, while an opposite relation between capacitance and area, the capacitance C_{NG} increases together with the NW radius (see Figure App. I- 2(b)).

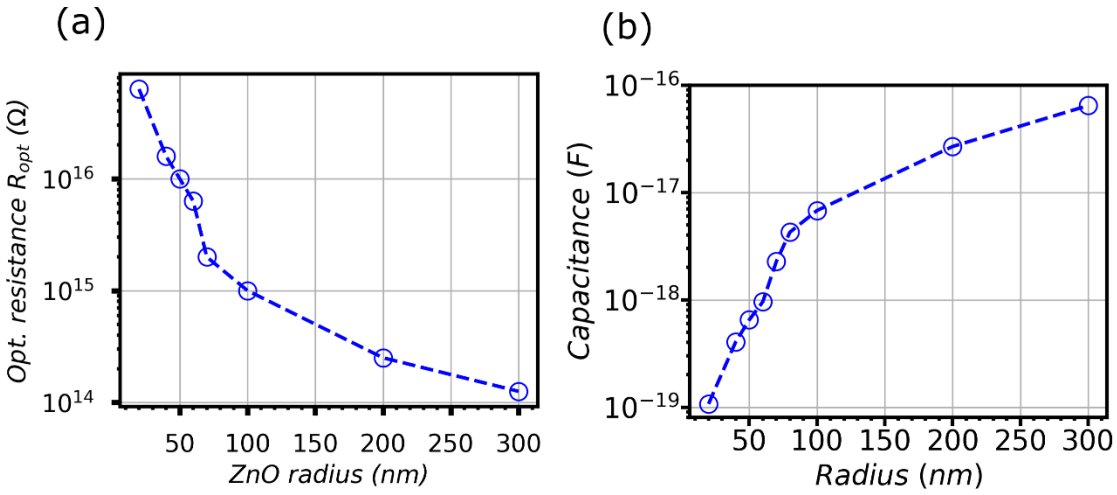

Figure App. I- 2 (a) Optimal value of load resistance (R_{opt}) and capacitance value (C_{NG}) as a function of ZnO radius after applying a constant mechanical pressure of 100 kPa for a single unit cell of one ZnO NW with 3μm long.

App. I.3 Electrical characterization using Impedance Spectroscopy (IS)

Electrical Impedance Spectroscopy (EIS) is a powerful technique to probe the resistance, capacitance, and also inductance variations of any electrical device. This technique has been used on ZnO NWs to evaluate the effect of surface modification using copper thiocyanate (CuSCN) [197] and Au nanoparticles [152]. In addition, it has been employed to study the piezotronics effect under certain strains [277] as well as the structural effect by changing the dielectric matrix in a VING device based on ZnO NWs [230]. We fabricated several VING devices by growing ZnO NWs on flexible substrates such as AZO-PET and ITO-PET (find more details of these samples in Chapter III, section III-1.5). The area of NWs in these VING devices was fixed at around 3 cm x 1.5 cm; the NWs were then covered by a PMMA matrix of 1 μm thickness. According to the structural characterization results (more details in the following Chapter), the samples exhibit slight variations in the mean NW radius (see Table App. I- 1).

Table App. I- 1 Results of electrical impedance spectroscopy for five different VING devices.

Sample N°	Sample name	Mean value of ZnO radius (nm)	Internal capacitance C_{int} (nF)
1	AZO/ZnO NWs 0h	84	7.9
2	AZO/ZnO NWs 1h	86	7.5
3	AZO/ZnO NWs 1h30	94	11.0
4	ITO/ZnO NWs 1h	110	22.2
5	ITO/ZnO NWs 1h30	100	14.0

Each VING device's EIS measurement was carried out in the frequency range from 20 kHz to 1 MHz at room temperature upon application of a 40 mV AC voltage. The real part Z_{real} and the imaginary part Z_{imag} of the impedance were measured as shown in Figure App. I- 3(a). Once the imaginary part Z_{imag} is plotted on the y-axis, and the real part Z_{real} is plotted on the x-axis, a characteristic semi-circular shape, also well-known as Nyquist plot, is formed as shown in Figure App. I- 3(b). This arc-shaped curve is common for an RC circuit, while the negative imaginary impedance represents a capacitive behavior [197,230]. Consequently, the internal resistance can be extracted from the diameter of the arc of this Nyquist plot, whose values can be extracted. Finally, the internal capacitance (C_{int}) is obtained when the absolute value of Z_{imag} reaches its maximum value (see Table App. I- 1), namely at the resonance or critical frequency f_c:

$$RC = \frac{1}{2\pi \cdot f_c} \qquad \text{App. 1}$$

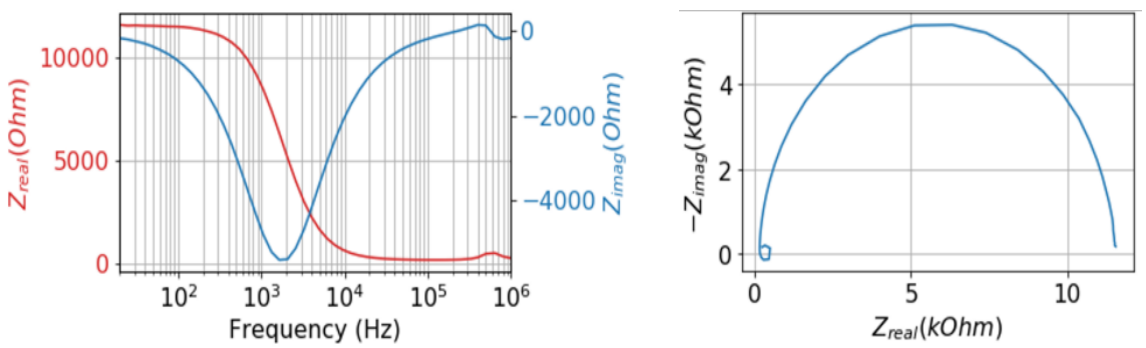

(a) (b)

Figure App. I- 3 (a) Real and imaginary impedance values measured between 20Hz to 1MHz of frequency. (b) Nyquist plot for a VING device based on ZnO NWs.

Appendix II. PFM characterization

App. II.1 Gravure printing for ZnO seed layer deposition

Gravure printing techniques are often used to print large-area flexible organic electronics. A low-viscosity ink (1-100mPas) is transferred from carved microcavities to a flexible substrate using engraved and pressure cylinders. The substrate was pressed with a force of 500 N at a speed of 60 m/min by rolling both cylinders in opposite directions, as shown in Figure App.II- 1(a). Once the ZnO ink has been spread along all the surface of the substrate (see Figure App.II- 1(b)), these samples were dried at 100°C for one hour (Figure App.II- 1(c)) for obtaining the thin film of crystalline ZnO nanoparticles (NPs), as shown in Figure App.II- 1(d).

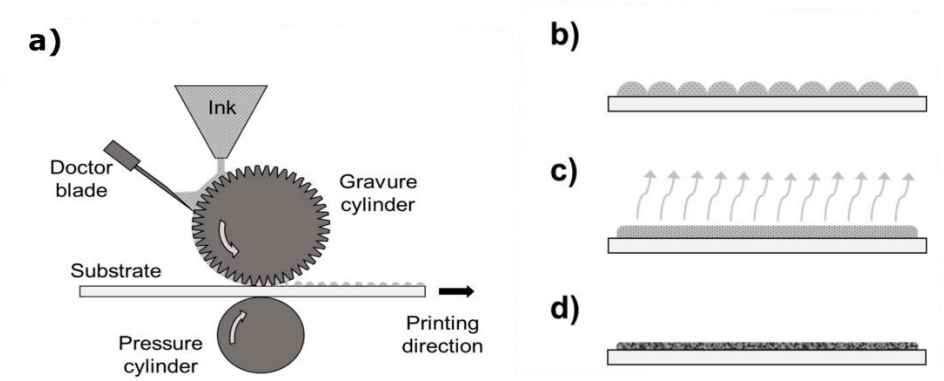

Figure App.II- 1 Schematic of the deposition process of ZnO seed layers by a gravure printing method. The gravure printing process consists in the following steps: (a) inking, doctoring, and transfer; (b) spreading; (c) drying; (d) production of the final solid thin film. Figure is taken from [278].

App. II.2 Length values of the ZnO NWs grown on rigid and flexible substrates

SEM images were taken from a side view in order to measure the value of length of ZnO NW grown on ZnO (ALD)/ITO/Si and as-printed (not sintered) ZnO seed layer/ITO/PET substrates. As can be seen in the side view images in Figure App.II- 2 (a, b), a similar length value of 3.5 µm is observed in both samples.

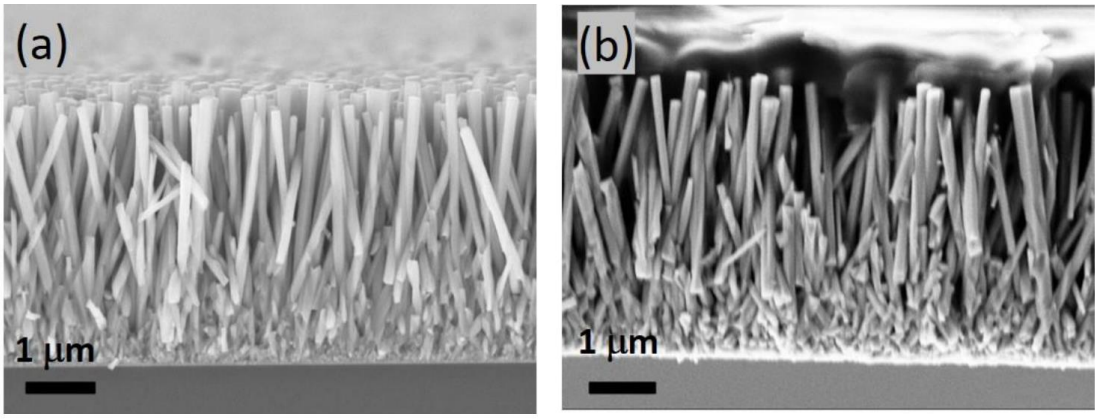

Figure App.II- 2 Cross-sectional SEM images of ZnO NWs grown on the (a) ZnO (ALD)/ITO/Si and as-printed (not sintered) ZnO seed layer/ITO/PET substrates.

App. II.3 Radius distribution values for ZnO grown on flexible substrates

The histograms of the radius distribution were taken from the SEM images using ImageJ software for the ZnO NWs grown on PET/ITO (see Figure App.II- 3Histograms of the radius distributions extracted from the SEM images of the top view of ZnO NWs grown on (a) PET-ITO and (b) PET-AZO substrates by CBD technique for different sintering treatment times in ZnO seed layer as 0h, 1h, 1.5h and 2.5h.Figure App.II- 3 (a)) and PET/AZO (see Figure App.II- 3Histograms of the radius distributions extracted from the SEM images of the top view of ZnO NWs grown on (a) PET-ITO and (b) PET-AZO substrates by CBD technique for different sintering treatment times in ZnO seed layer as 0h, 1h, 1.5h and 2.5h.Figure App.II- 3 (b)) at different sintering treatment times in the seed layer. To extract the mean value of ZnO NWs radius, each frequency distribution was fitted using a single Gaussian curve. These fits curves were used to build the plots of section III.1.5.

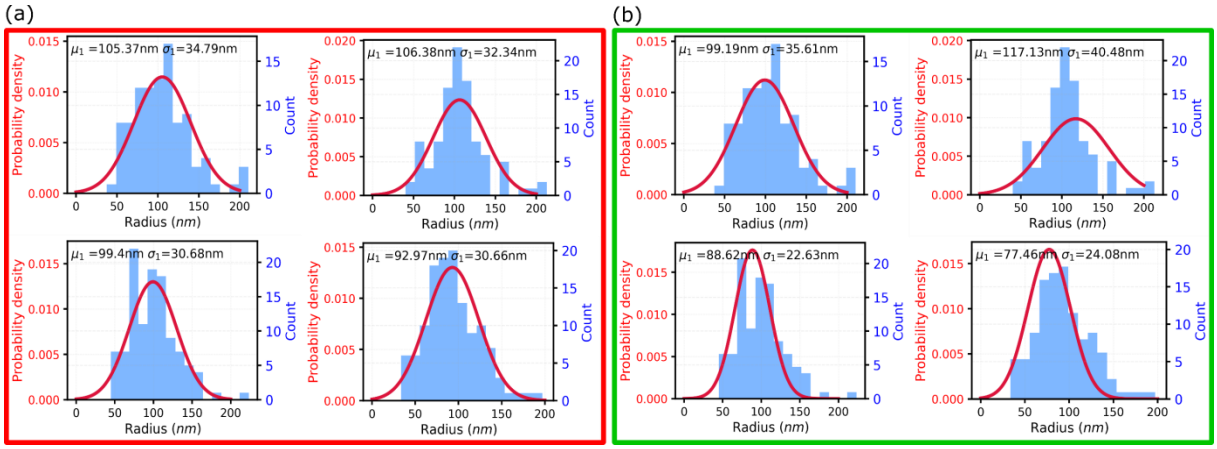

Figure App.II- 3 Histograms of the radius distributions extracted from the SEM images of the top view of ZnO NWs grown on (a) PET-ITO and (b) PET-AZO substrates by CBD technique for different sintering treatment times in ZnO seed layer as 0h, 1h, 1.5h and 2.5h.

App. II.4 Assessment of the drive frequency in the AC signal for ZnO NWs

Before each PFM measurement, the amplitude and phase were evaluated by sweeping the drive frequency parameter in order to locate the resonance frequency in contact mode between the Pt-Si probe and ZnO NWs. It can be seen in Figure App.II- 4(a), that the amplitude is rather stable and without amplification at low frequency (below 50 kHz). However, the amplitude is significantly increased at high drive frequency. Simultaneously, the phase is also affected by the drive frequency, exhibiting positive and stable phase values below 20 kHz (see Figure App.II- 4(b)). Therefore, an optimal frequency of about 14kHz was chosen when employing the Pt-Si probe on ZnO NWs.

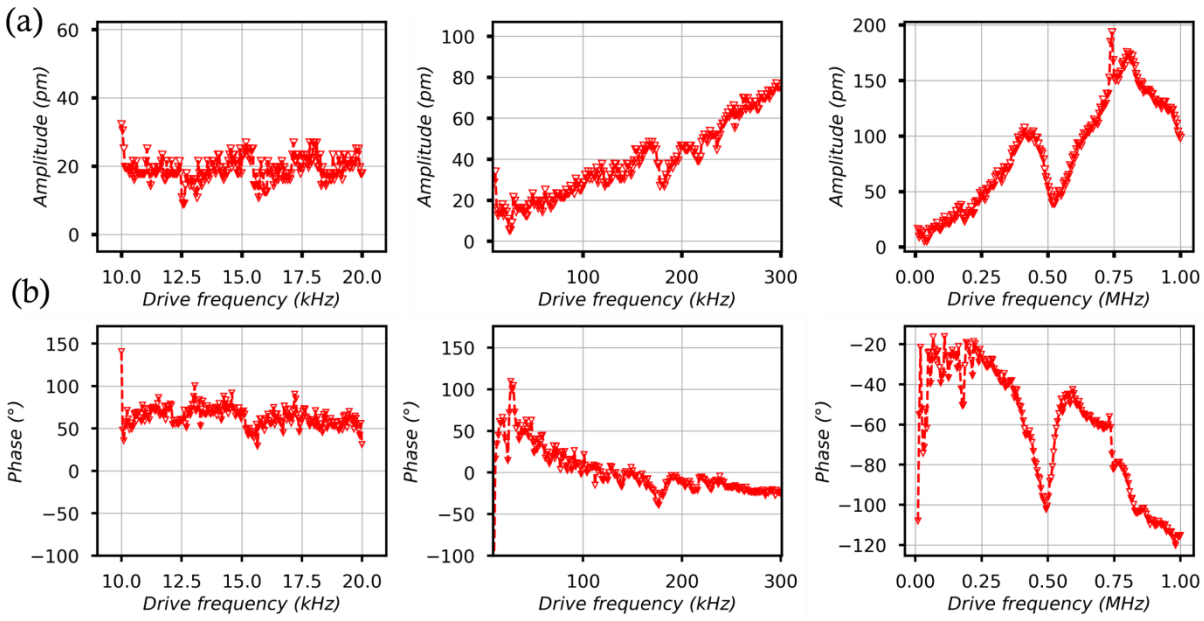

Figure App.II- 4 (a) PFM amplitude and (b) phase response as a function of drive frequency (different ranges) generated by ZnO NWs and using a Pt-Si probe at $V_{AC} = 5\ V$.

App. II.5 Filtering the PFM values using the mechanical properties

"DataCube mode" allows obtaining the mechanical and electrical properties utilizing the force-volume method. Among these mechanical properties, the adhesion force distribution is successfully extracted throughout the scanning surface (see Figure App.II- 5(a)). As it can be

seen, the top surface of NWs (red color) is clearly distinguished from the rest (blue color). The adhesion force corresponds to the minimum force required to disengage the probe from the surface. For instance, Figure App.II- 5(b) shows that a smaller force is required to detach the tip from the NWs top (red curve) surface than from the other regions (blue curve). Thus, the piezoelectric response on the top surface of NWs can be extracted by filtering the PFM amplitude values upon comparing them with the adhesion values. The result of the PFM amplitude histogram extracted from the scanning surface in Figure App.II- 5(a) is displayed without any filtering process, as depicted in Figure App.II- 5(c). When carrying out the mechanical and electrical correlation (i.e., the filtering process), it is possible to extract the PFM response which corresponds solely to the top surface of ZnO NWs (see Figure App.II- 5(d)). As a result of this, some piezoelectric artifacts are removed from the final distribution.

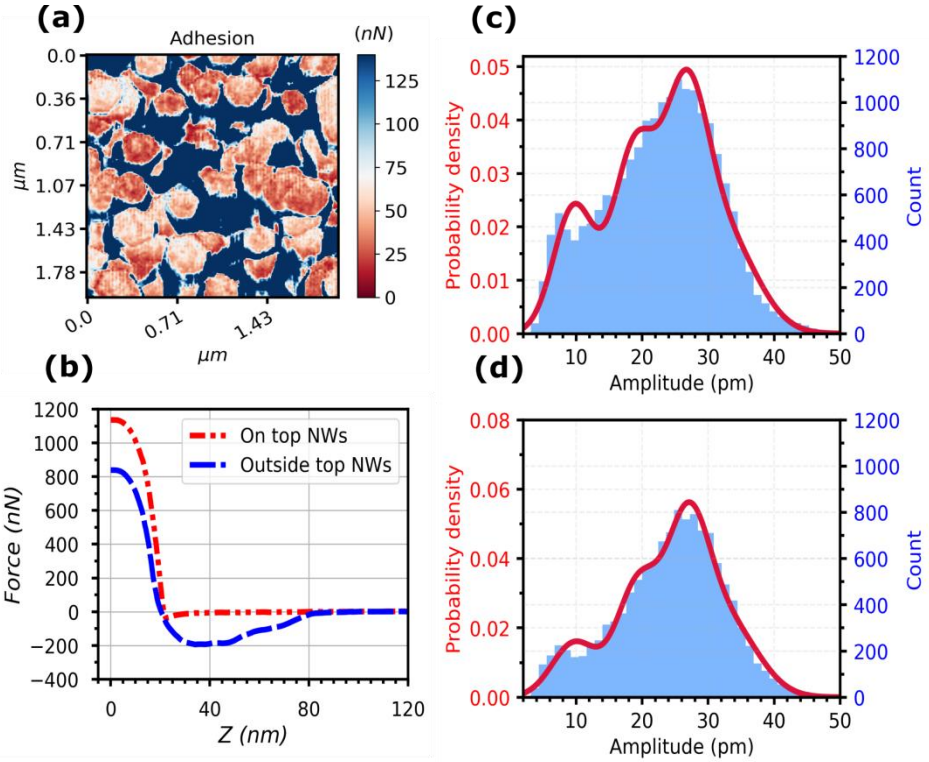

Figure App.II- 5 (a) Adhesion force distribution of ZnO NWs grown on ITO/PET substrate with a sintering treatment time of 1h (sample #5). (b) AFM force-distance curve during retracting action between the Pt-Si tip and the top surface of ZnO NWs (red curve) and spaces among NWs (blue curve). Piezoelectric amplitude histograms with (c) all contributions (without filtering process) and (d) only the top surface of ZnO NWs contribution (with filtering process).

App. II.6 Reproducibility of PFM measurement in a single sample

In order to test the reproducibility and to sum up the PFM results, three PFM measurements were performed at three different positions of each sample with different substrates and sintering treatment times (Figure App.II- 6(a)). Each measurement provides an amplitude histogram that is fitted using multiple Gaussian curves. As discussed in the main text, these Gaussian curves are related to four piezoelectric contributions, such as NW radius and border effect. By extracting the mean value of these contributions and when compared against other measurements, it can be seen that the mean amplitude does not change for different spots, as shown in Figure App.II- 6(b). Consequently, the piezoresponse amplitude histograms from the different spots are collected in a single histogram reflecting the piezoelectric properties of the sample (see the bottom histogram in Figure App.II- 6(c)).

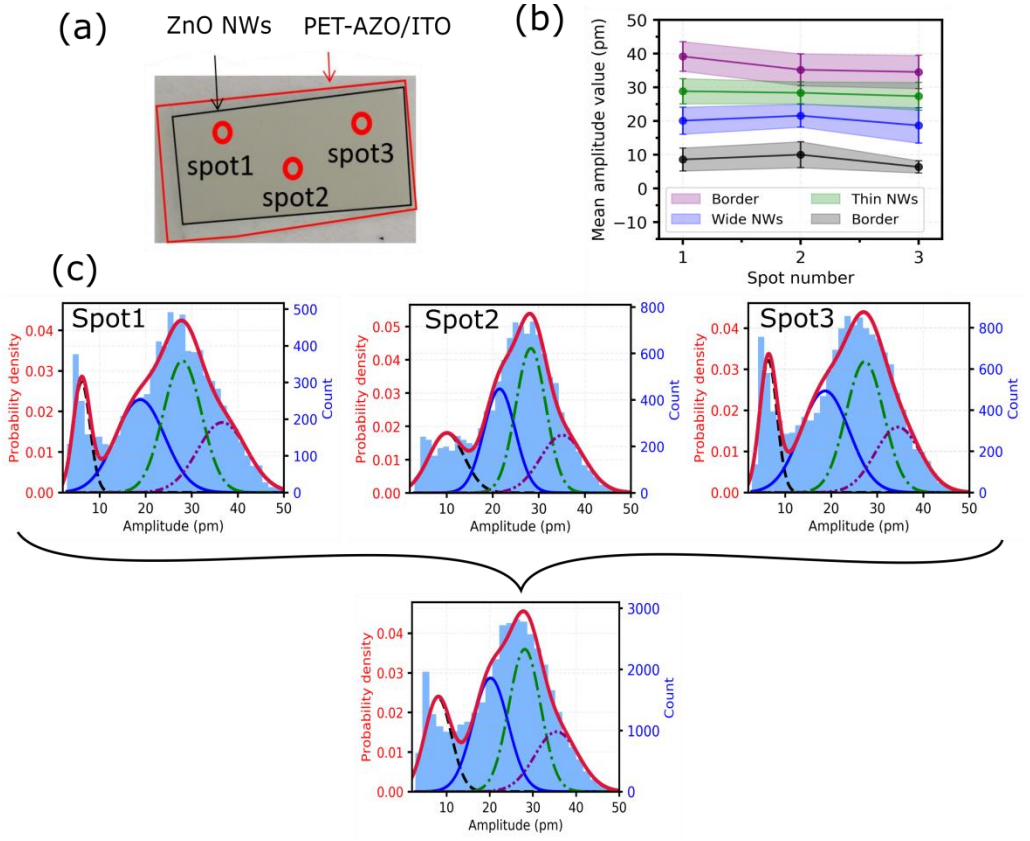

Figure App.II- 6 (a) Position of the three random spots where PFM measurements were performed for a single sample. (b) The values of mean piezoelectric amplitude were extracted from the multiple Gaussian curves for each measuring spot. (c) Piezoresponse amplitude histogram of these three spots and final amplitude histogram when adding the contributions of all spots. The sample was constituted of ZnO NWs grown on PET-AZO with a sintering treatment time of 2.5 h (sample #10). Measurements were recorded applying 5 V in AC drive voltage at 13 kHz. The same technique was applied to the other samples.

App. II.7 ZnO NWs with the lowest values of piezoelectric amplitude

The lowest piezoelectric signals corresponding to the black Gaussian curves on the piezoelectric amplitude histograms come from the top surface of some ZnO NWs. Figure App.II- 7(a-c) displays the piezoelectric amplitude distribution for PET/ITO and PET/AZO samples with black lines across the top of ZnO NW with the lowest piezoelectric signals. The values of piezoelectric amplitude were extracted along these lines and plotted in an individual figure (see Figure App.II- 7(d-f)), demonstrating that the amplitude values were between 8 pm and 12 pm. It is likely that the piezoresponse of these NWs is limited by free carriers (see more details in the main text).

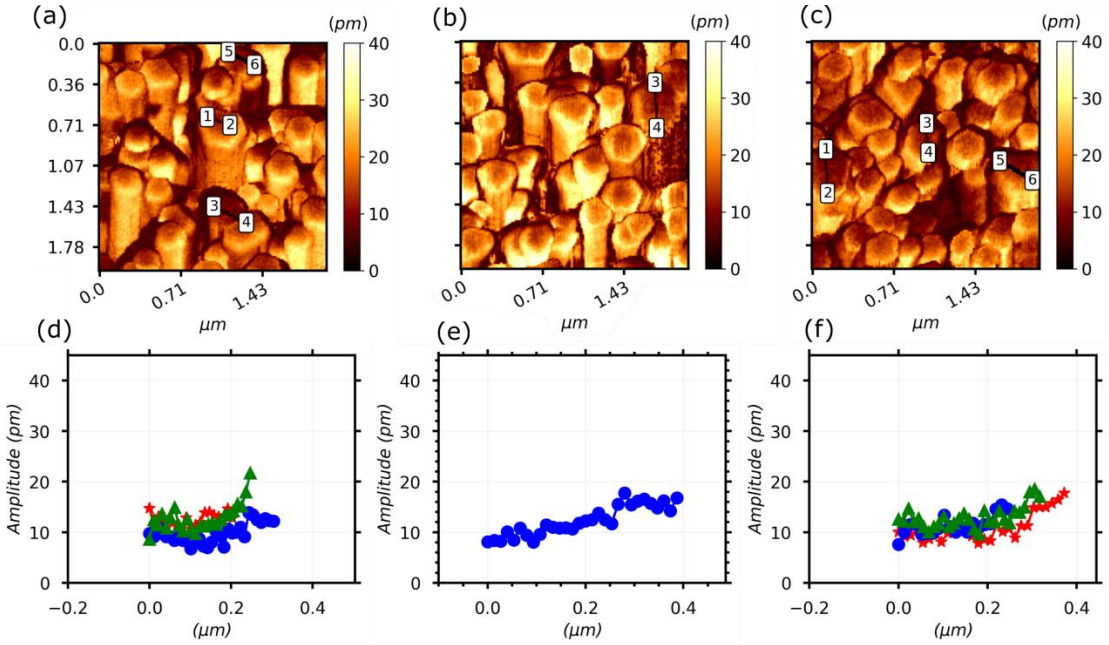

Figure App.II- 7 Distribution of piezoelectric amplitude response for ZnO NWs grown on flexible substrates as (a) PET/ITO substrate at 1h 30 minutes (1h5) and (b, c) PET/AZO substrate at 1h and 1h5 in sintering times. Trace of amplitude value on the top surface of ZnO NW along the black line between the initial and final points.

App. II.8 PFM measurement for wide and thin ZnO NWs

To obtain a clearer statistical interpretation of the amplitude values for wide and thin ZnO NWs, some PFM measurements were carried out on smaller scanning areas and with higher resolution for two, wide and thin, ZnO NWs. The piezoresponse amplitude maps of a wide NW (with a radius around 200 nm) and a thin NW (with a radius around 100 nm) are depicted in Figure App.II- 8(a) and II-8(b), respectively. As can be seen, the thin NW reveals a larger brighter domain compared to the wide NW, indicating that almost the whole top surface has higher values of piezoelectric amplitude (around 28 pm) than the wide NW (around 20 pm). When

plotting the amplitude histograms (see Figure App.II- 8(c) and II-8(d)), the wide NW has a mean value of 21 pm, whereas the thin NW reached a value of 26 pm, thus demonstrating the dependence of the piezoelectric amplitude on ZnO NW radius and associating it to the blue and green Gaussian curves obtained using a larger scanning length.

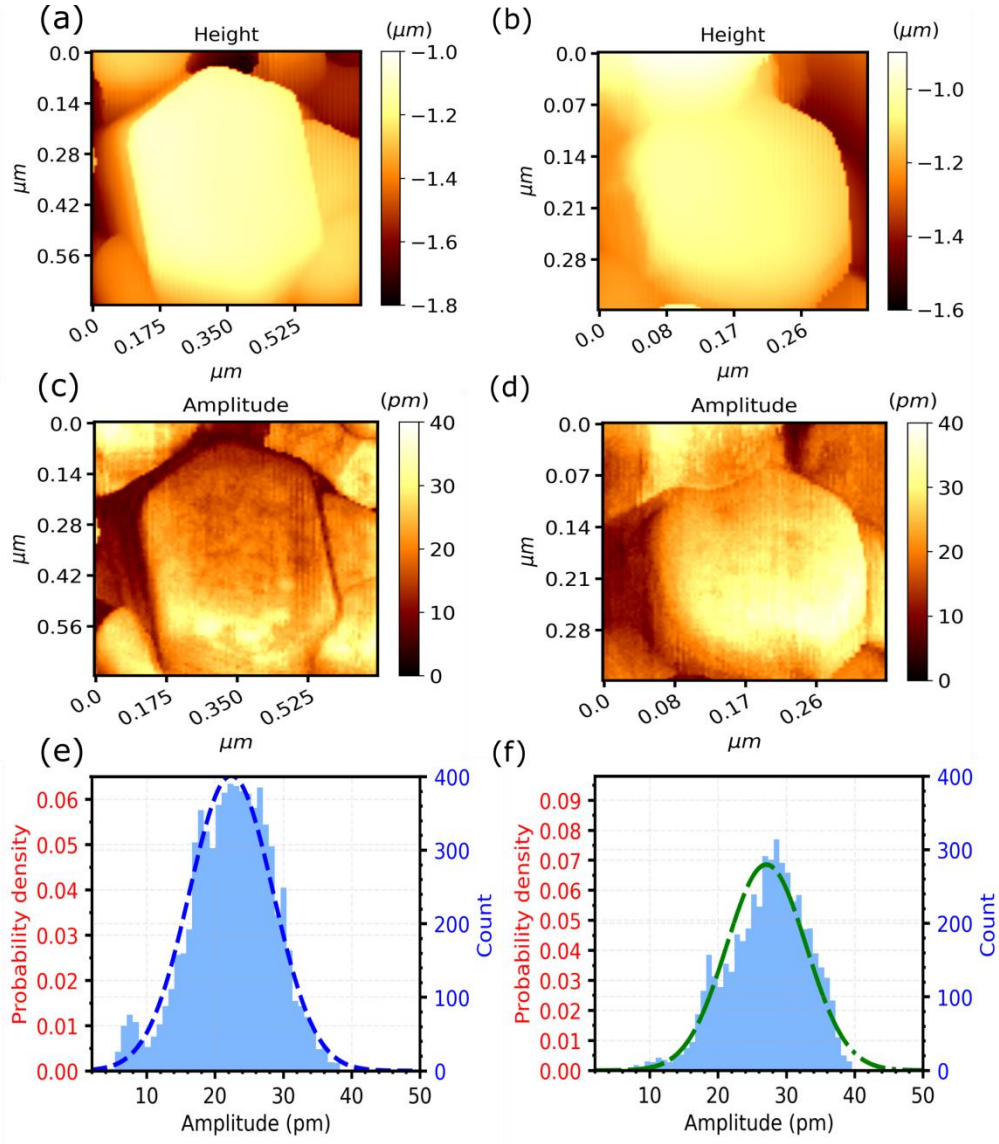

Figure App.II- 8 Maps of topography, piezoelectric amplitude values and their histograms at the top surface of (a), (c), (e) a wide (approximately 200 nm diameter) and (b), (d), (f) a thin (approximately 100 nm diameter) ZnO NW grown on PET-ITO substrate with a sintering treatment time of 1h (sample #5).

App. II.9 Histograms of PFM measurements for flexibles samples

In order to analyse statistically all the results of PFM measurements, we have extracted the radius histogram in each measured spot from the topography data for ZnO NWs grown on

PET/ITO and PET/AZO substrates at different sintering times in the ZnO seed layer (see images of the first column in Figure App.II- 9 and Figure App.II- 10). Similarly, the piezoelectric amplitude and phase histograms were extracted after grouping the results of three measured spots, as revealed in the images of the second and third columns in Figure App.II- 9 and Figure App.II- 10.

The amplitude histogram curves were fitted by using four Gaussian curves, which was attributed to different families of piezoelectric contribution originating from NWs of different range of diameter (and thus different amounts of screening) or to NW edge, as discussed in the main text.

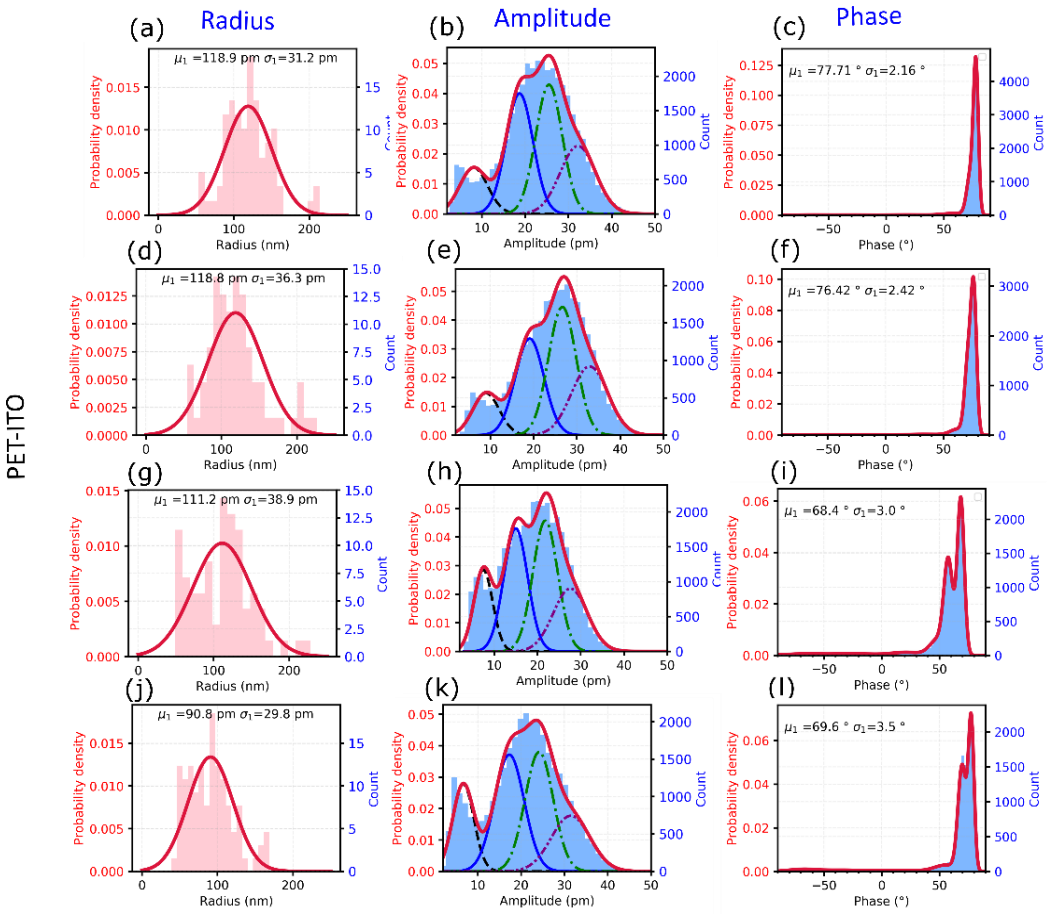

Figure App.II- 9 Histograms of ZnO NWs radius, piezoelectric amplitude and piezoelectric phase values for samples over PET-ITO substrates with sintering treatment times of (a-c) 0h, (d-f) 1h, (g-i) 1.5h and (j-l) 2.5h. In amplitude graphs, from left to right, black, blue, green and purple Gaussian fits correspond to different NW sizes and border effects.

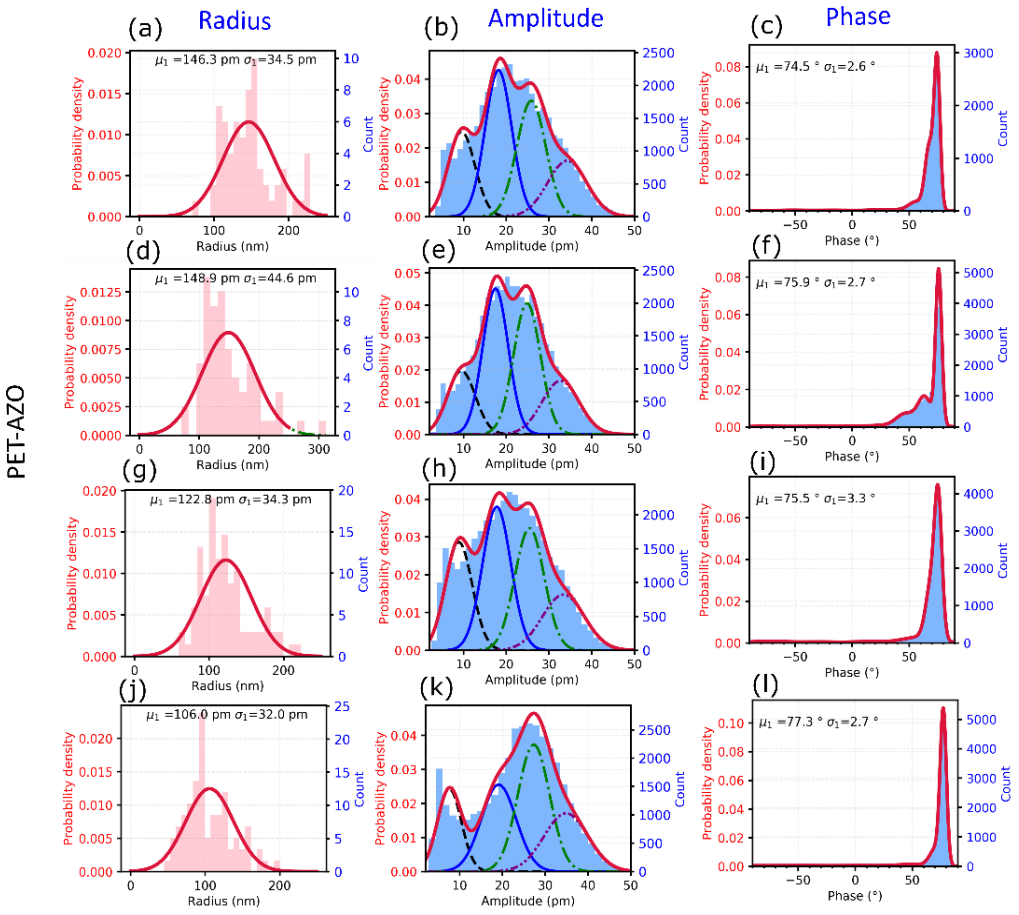

Figure App.II- 10 Histograms of ZnO NWs radius, piezoelectric amplitude and piezoelectric phase values for samples over PET-AZO substrates with sintering treatment times of (a-c) 0h, (d-f) 1h, (g-i) 1.5h and (j-l) 2.5h. In amplitude graphs, from left to right, black, blue, green and purple Gaussian fits correspond to different NW sizes and border effects.

App. II.10 Boundary conditions used in COMSOL PFM simulations

The simulated structure consisted of a ZnO seed layer substrate and a ZnO nanostructure with respective thicknesses of 40 nm and 3 μm and widths of 200 nm and 100 nm, corresponding to the dimensions of our ZnO NWs. The AFM tip was modeled by a 25 nm wide and 25 nm thick square on top of the ZnO NW, as shown in Figure App.II- 11(a). The simulations solved the same coupled equations as in section II.1.1 in Chapter II.

As for the electrical boundary conditions, a static voltage of 5 V was applied between the bottom contact area and the top surface of ZnO as illustrated in Figure App.II- 11(b). The ground potential was imposed on the bottom substrate. For the mechanical boundary conditions, the bottom side was fully clamped while the rest of the sidewalls remained free (see Figure App.II- 11(b)).

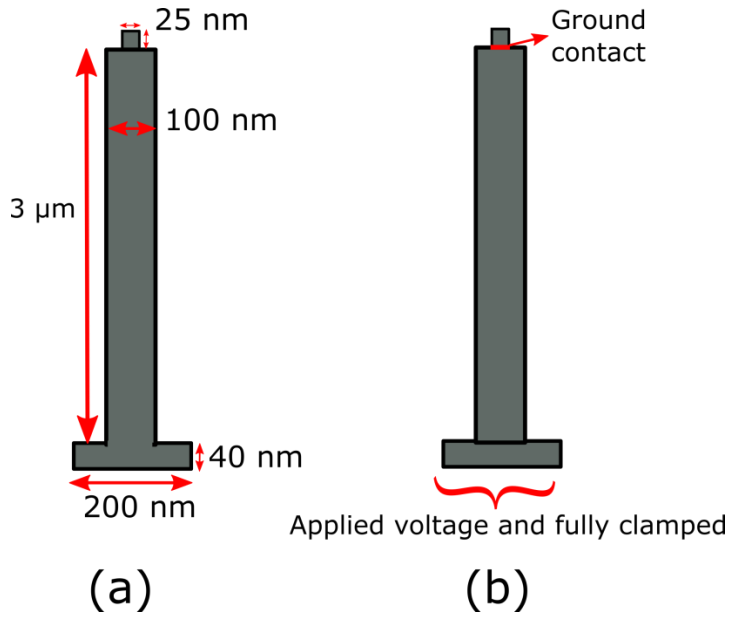

Figure App.II- 11 Schematics of a 2D numerical simulation of a single ZnO nanostructure in COMSOL environment with specific (a) dimension, (b) electrical and boundary conditions.

App. II.11 COMSOL simulation of PFM displacement for a single ZnO nanostructure

In the simulation, the nanowire was considered undoped. As can be seen, although the ground contact was applied locally, it resulted globally in a homogenous vertical field in the undoped NW and the NW deformation was thus independent of the exact position of the tip.

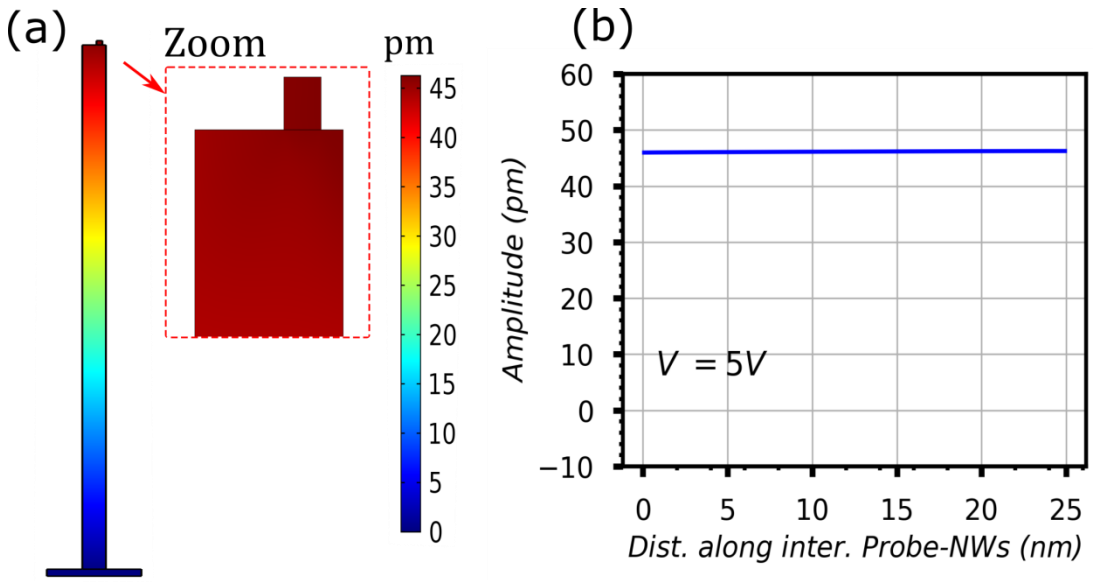

Figure App.II- 12 Numerical simulation of (a) electric field-induced displacement distribution and (b) the amplitude value along the interface of the tip and NW for a simple model without semiconductor properties (i.e., without N_d).

Appendix III. Complementary electrical measurements

App. III.1 Kelvin probe force microscopy (KPFM)

Kelvin probe force microscopy (KPFM) is one of the techniques used to characterise the electrical properties of semiconducting surfaces. The two main KPFM techniques are the amplitude modulation KPFM (AM-KPFM) which is the most common and frequency modulation KPFM (FM-KPFM) [279]. AM- and FM-KPFM techniques have different advantages related to spatial resolution and accuracy. For instance, FM-KPFM requires short tip-sample distances to get accurate values, and it also needs high AC voltages due to its low sensitivity. In contrast, AM-KPFM uses low AC voltages with a moderately high energy resolution, although the effect of tip geometry decreases the contrast of the contact potential difference [280]. In the present PhD, several KPFM measurements were performed using the FM-KPFM technique.

App. III.1.1 Principle of FM-KPFM

FM-KPFM microscopy's working principle relies on measuring the contact potential difference (V_{CPD}) generated between the tip and sample after putting them at an average distance 'z', as depicted in Figure App. III- 1(a). The conductive tip (e.g., Pt-Si) and the sample form a capacitor component whose capacitance value can be evaluated by applying an AC voltage to the tip. From a mechanical point of view, the tip cantilever starts to oscillate in amplitude at ω due to the electrostatic forces given by:

$$F_{el} = -\frac{1}{2}\frac{\partial C(z)}{\partial z}(\Delta V)^2 \qquad \textit{App. 2}$$

Where F_{el}, $C(z)$ and ΔV are the electric force, the capacitance value and the potential difference between the probe and the sample.

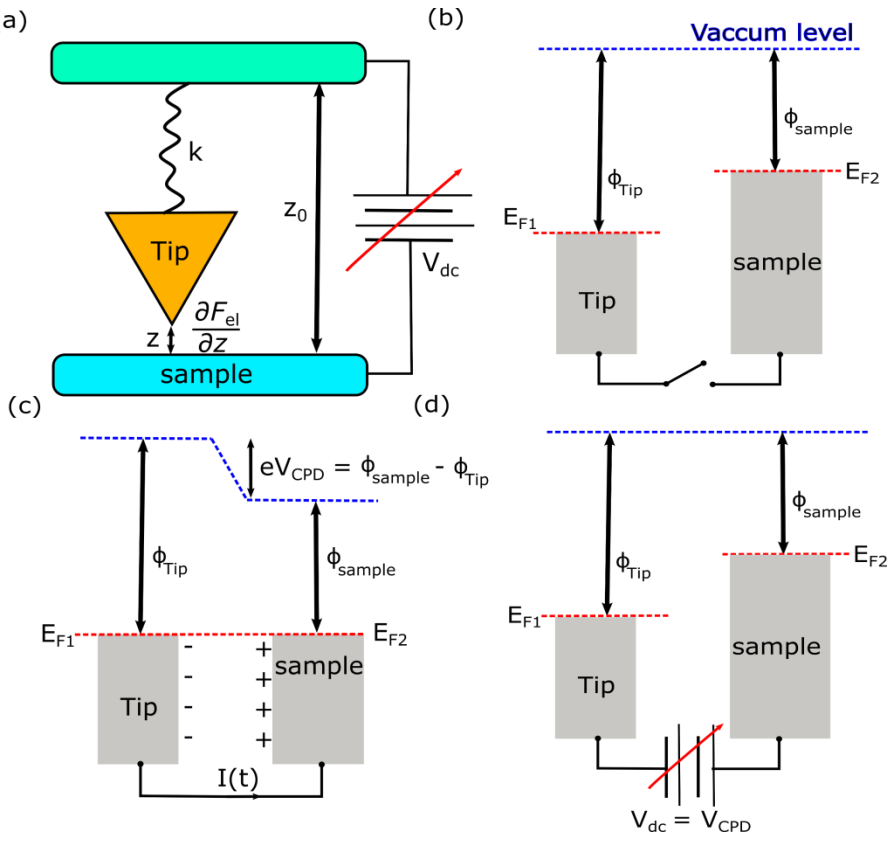

Figure App. III- 1 Schematic of the (a) FM-KPFM mechanism and energy band levels (b) before, (c) after thermodynamic equilibrium, and (d) under contact potential compensation for Metal-sample structure with $V_{dc} = V_{CPD}$.

Generally, two metals or metal/semiconductor materials of different work functions are brought into close proximity between each other (see Figure App. III- 1(b)), an electronic equilibrium is established aligning the Fermi levels, as depicted in Figure App. III- 1(c). It means that a spontaneous transient current is generated in the external circuit, transferring electrons from the material with the smaller work function to the material with the larger work function. This transfer occurs naturally until both systems reach thermodynamic equilibrium. Consequently, V_{CPD} appears between both materials after thermodynamic equilibrium that corresponds to the difference in the work functions.

In this regard, FM-KPFM technique takes into account the intrinsic V_{CPD}, DC offset voltage V_{dc} and ac voltage V_{AC} on ΔV.

$$\Delta V = V_{dc} - V_{CPD} + V_{AC}\sin(\omega t) \qquad \textit{App. 3}$$

The resulting electrostatic force (Eq. App. 2) is therefore defined by three spectral components [281]:

$$F_{DC} = -\frac{\partial C(z)}{\partial z}\left(\frac{1}{2}(V_{dc} - V_{CPD})^2 + \frac{1}{4}{V_{AC}}^2\right) \quad \textit{App. 4}$$

$$F_{\omega}(t) = -\frac{\partial C(z)}{\partial z}(V_{dc} - V_{CPD})\, V_{AC}\sin(\omega t) \quad \textit{App. 5}$$

$$F_{2\omega}(t) = \frac{1}{4}\frac{\partial C(z)}{\partial z}{V_{AC}}^2 \cos(2\omega t) \quad \textit{App. 6}$$

The first equation represents static force, while the second and third equations symbolize the cantilever oscillation at ω and 2ω. Upon applying the AC signal on the tip, the variation of a non-uniform electric field causes the mechanical force gradient between the tip and sample. In addition, a shift ($\Delta\omega$) of the peak amplitude signal at the resonance frequency (ω) occurs due to the repulsive and attractive forces. For instance, the attractive force gradient moves the peak towards the lower frequency value, while the repulsive force gradient moves the peak to the opposite side. $\Delta\omega$ can be extracted by considering the cantilever connected to two springs in parallel under small oscillations (see [282] for more details)

$$\Delta\omega \approx -\frac{\omega}{4\pi\, k}\left(\frac{\partial F_{\omega}}{\partial z}\Big|_{z=z_o}\right) \approx \frac{\omega}{4\pi\, k}\frac{\partial^2 C(z)}{\partial z^2}(V_{dc} - V_{CPD})\, V_{AC}\sin(\omega t) \quad \textit{App. 7}$$

Where the amplitude $A_{\Delta\omega} = \frac{\omega}{4\pi\, k}\frac{\partial^2 C(z)}{\partial z^2}\, V_{AC}\,(V_{dc} - V_{CPD})$ depends linearly on the V_{dc}. In FM-KPFM mode, the variation of the oscillation frequency delivers information concerning the tip-sample interactions and depends on distance variation, as illustrated schematically in Figure App. III- 2(a). The changes in the cantilever oscillation frequency in the time domain are represented by the top schematic of Figure App. III- 2(a), while its representation in the frequency domain is represented by the middle of Figure App. III- 2(a). The modulation of the resonant frequency conduces to one pair of sidebands at $\omega \pm \omega_m$. Putting $V_{dc} = V_{CPD}$, $A_{\Delta\omega}$ will be zero, while the sidebands at $\omega \pm \omega_m$ will disappear. A topography measurement is performed at the first scan using tapping mode in trace and retrace moments. Then, the cantilever ascends until a lift scan height to measure the KPFM parameters, following the stored surface topography (see the bottom schematic in Figure App. III- 2(a)).

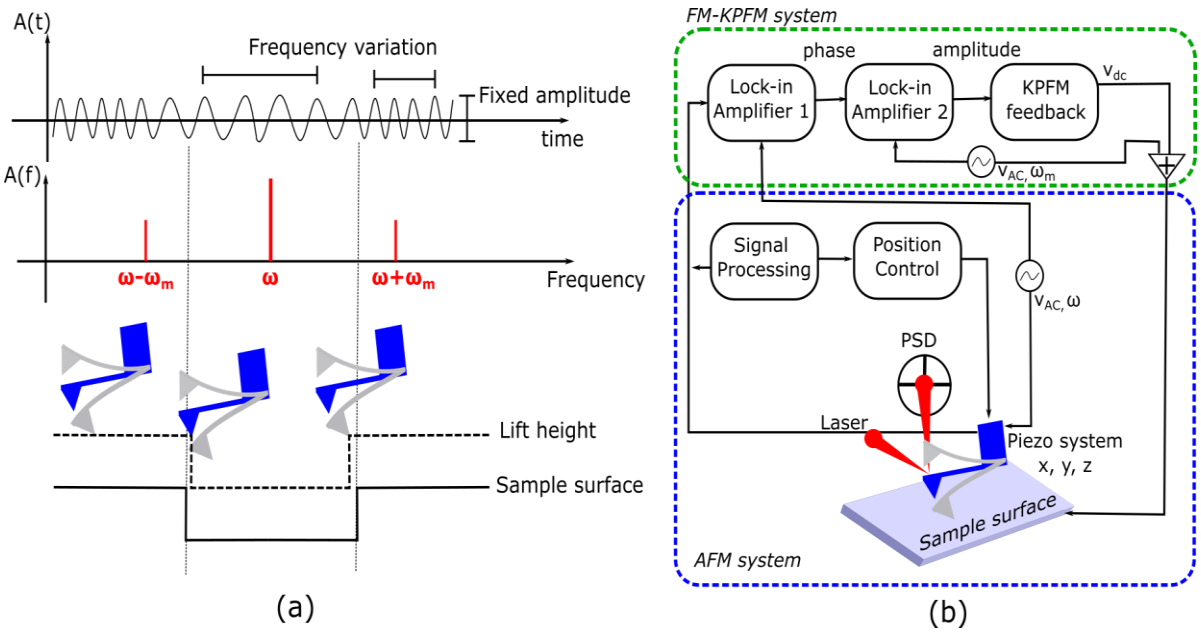

Figure App. III- 2(a) Schematic representation of non-contact AFM operation mode for frequency modulation mode. Tip-sample separation remains constant and FM mode uses frequency variation as a feedback signal. The figure was adapted from [283]. *(b) Schematic diagram of FM-KPFM technique mode. The bottom part of the diagram is an AFM system for topography scanning and the top part is an FM-KPFM system for CPD measurement. This figure was adapted from* [284].

An AFM system is typically composed of the AFM system and the feedback system, as shown by the squares with dashed lines in Figure App. III- 2(b). The lock-in amplifier 1 is used to send the AC signal on the tip at the resonance frequency ω, as a reference signal. The tip oscillation is supervised by the position-sensitive detector (PSD). The frequency modulation signal ($\Delta\omega$) captured from the cantilever oscillation is used in the position control system for topography imaging and is sent to the lock-in amplifier 1. The lock-in amplifier extracts the phase signal with the same frequency as V_{AC} to feed the lock-in amplifier 2. The signal is fed into the KPFM controller maintaining the nullity condition in the amplitude signal ($A_{\Delta\omega}$~0) by applying V_{dc} to the sample. Once $A_{\Delta\omega}$ is minimized at $\omega \pm \omega_m$, the AFM system measures V_{CPD} that corresponds to the differential contact potential between the tip and sample. As mentioned before, this is proportional to the difference in work functions of tip and sample.

App. III.1.2 KPFM in reference sample

In KPFM technique, the measured contact potential difference (V_{CPD}) is useful to calculate the work function of semiconductor material as well as the AFM tip. This work function (ϕ) is not

commonly found in the literature due to the unique electrical characteristics of each sample and the coating material of AFM tip. Therefore, a reference sample consisting of three different materials, as aluminum (Al), silicon (Si), and gold (Au) is used by measuring the surface potential of each material (see Figure App. III- 3(a) and App.III-3(b)). Figure App. III- 3(c) and App.III-3(d) show that V_{CPD} are 0.1 V, -0.4 V and -1.55 V for Au, Si and Al, respectively. This values were obtained using a Pt-Si AFM tip under N_2.

Assuming that the work function of Au on the sample is well-known (around 5.1 eV), the work function of the AFM tip can be determined with the following expression

$$qV_{CPD}^{measured} = \phi_{tip} - \phi_{sample} \qquad \textit{App. 8}$$

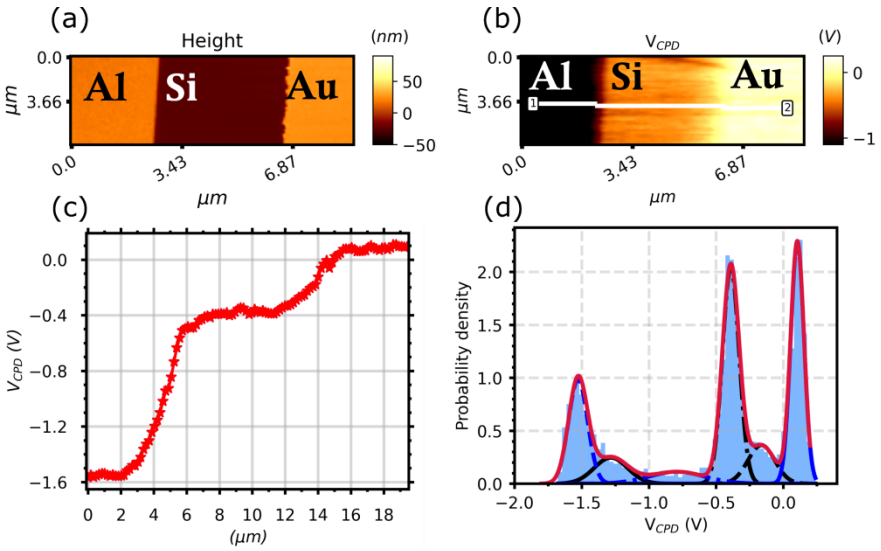

Figure App. III- 3 (a) Topography and (b) surface potential difference images of reference sample with aluminum (Al), silicon (Si) and gold (Au) materials for Pt-Si AFM tip under N_2 gas. (c) Profile surface potential curve of the line between points 1 and 2. (d) Histogram of the surface potential for the whole scanned surface.

App. III.2 Cheung method for extracting Φ_B from ITO/ZnO/Pt diode

Each AFM measurement contains at least 2300 pixels that are equivalent to the number of times the AFM tip contacts the surface of the sample for ITO/ZnO and ZnO NW/Pt-Si junctions (see Figure App. III- 4(a) and III-4(e)). Not all pixels have perfect I-V characteristics for extracting the electrical parameters in each junction contact. So, we analyzed the current data as a function of voltage, extrapolating the best fit curve for each pixel in both junctions, as shown in Figure App. III- 4(b) and III-4(f). Subsequently, the dV/dln(I) function is plotted as a function of I by

employing the Eq. IV-9 from the main text (see Figure App. III- 4(c) and III-4(g)). The R_s and ideal factor are extracted from the slope and y-axis interception, respectively. Using Eq. App. 9 and the extracted parameters (n and R_s) from Eq. IV- 9, $H(I,V)$ is calculated and plotted as a function of I, where its y-axis interception corresponds to the Schottky barrier (see Figure App. III- 4(d) and III-4(h)). For instance, ITO/ZnO and ZnO/Pt-Si junctions have barrier values of 0.426 eV and 0.517 eV, respectively.

$$H(I,V,n) = V - (nKT/q)\ln\left(I/(A_{eff}A^{**}T^2)\right) \qquad \textit{App. 9}$$

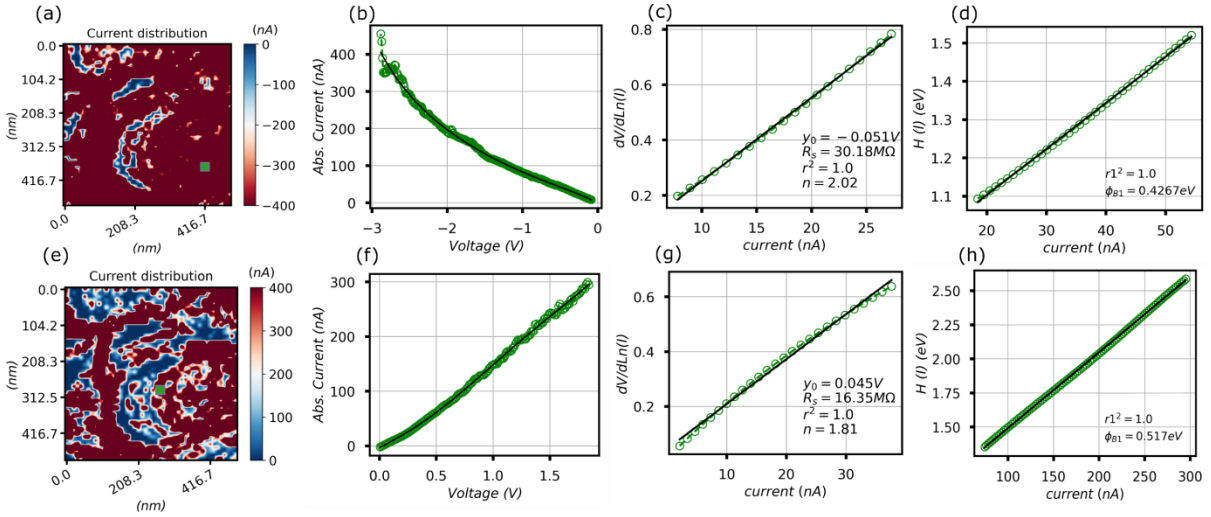

Figure App. III- 4 Current distribution on the top surface of ZnO NW, the curve of the absolute value of current versus the forwards and reverse bias, the dV/d(ln I), and H(I) functions versus I for (a-d) ITO/ZnO and (e-h) ZnO NW/Pt-Si diodes. All the electrical measurements were made under N_2 gas and using a Pt-Si tip in the AFM equipment. The I-V data corresponds to the same ZnO NWs measured in Figure IV-10 from the main text.

App. III.3 Calculation of the ZnO NW/Pt-Si probe surface contact using Hertz' theory

Hertz's theory predicts the contact pressure and contact area between two elastic bodies for simple geometries [266], as a half-sphere (for the AFM probe) and a plane (for the top surface of ZnO NW). According to this theory, the contact area can be represented by a disk of radius a and expressed as:

$$a = \left(\frac{3}{4}\frac{F\ R}{E^*}\right)^{\frac{1}{3}} \qquad \textit{App. 10}$$

where R, F, and E^* are the AFM probe radius, the force applied by the AFM probe over the sample and the contact Young's modulus of the two materials (ZnO and Pt-Si). This contact modulus is given by

$$\frac{1}{E^*} = \left(\frac{1-\nu_1^2}{E_1}\right) + \left(\frac{1-\nu_2^2}{E_2}\right) \qquad \textit{App. 11}$$

where the E_1, E_2 and ν_1, ν_2 are respectively Young's modulus and Poisson's ratio of two materials. Table App. III- 2 summarises the mechanical parameters used to calculate the contact radius of ZnO NW/Pt-Si probe.

Table App. III- 2 Mechanical parameters used for calculating the contact radius.

	ZnO NW	Pt-Si
Young's modulus (GPa)	140 [285]	238 [286]
Poisson's ratio	0.31 [285]	0.32 [286]
AFM probe radius (nm)	NA	25
Force (nN)	NA	1050
Contact radius (nm)	5.84	

App. III.4 Barrier height values of ITO/ZnO junctions under different ambient conditions

I-V curves were measured on the same spot by modifying the environmental conditions. The I-V data corresponds to the same NW of Figure IV-10 from the main text. Figure App. III- 5(a, b) shows the current distributions generated for a bias of -3V for a single ZnO NW exposed to the atmospheric air and N_2 gas, respectively. In order to demonstrate that there is no effect of the ambient condition in the ϕ_B of the junction (i.e., ITO/ZnO NW contact), we have extracted ϕ_B from the I-V curves using Cheung's method.

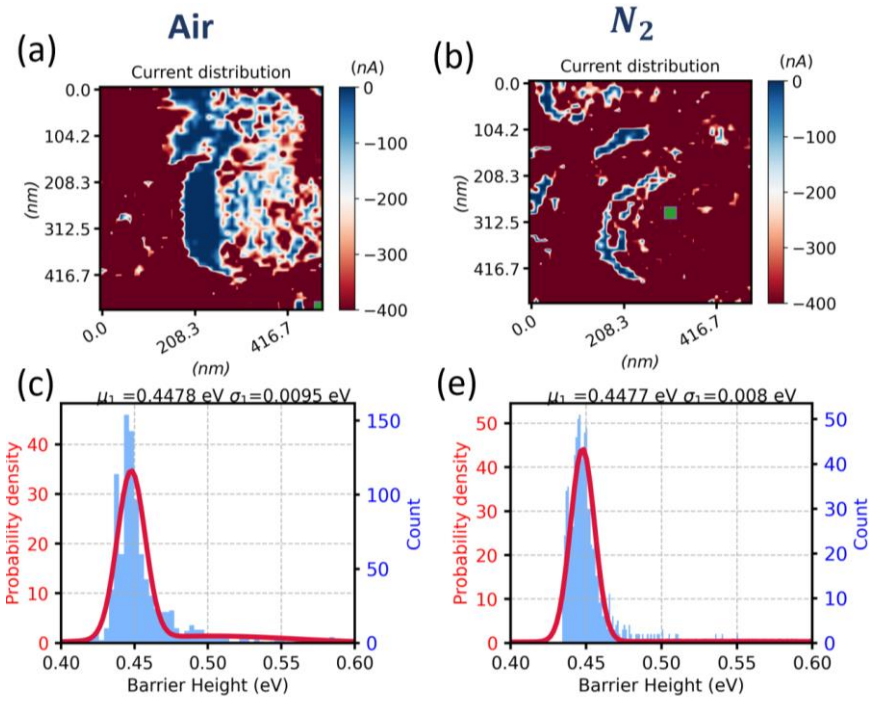

Figure App. III- 5 (a, b) Current distribution for a single ZnO NW at -3 V into air ambient and N_2 gas. (c, d) Schottky barrier ϕ_B distributions were taken from at least 1000 I-V curves related to the ITO/ZnO junction analyzed from the scanning area.

Figure App. III- 5(c, d) shows the ϕ_B distribution taken from at least 1000 curves analyzed from the top surface of ZnO NW into the air and N_2 ambient. These results reveal that the average value of ϕ_B is the same (0.44 eV), suggesting the environmental conditions do not play any role in the electron transport on that junction contact since it is formed internally without exposure to the environment.

References

[1] N. Sezer, M. Koç, A comprehensive review on the state-of-the-art of piezoelectric energy harvesting, Nano Energy. 80 (2021) 105567. https://doi.org/10.1016/j.nanoen.2020.105567.

[2] A. Roy, J. Mead, S. Wang, H. Huang, Effects of surface defects on the mechanical properties of ZnO nanowires, Sci. Rep. 7 (2017) 9547. https://doi.org/10.1038/s41598-017-09843-5.

[3] Y. Yang, W. Guo, X. Wang, Z. Wang, J. Qi, Y. Zhang, Size Dependence of Dielectric Constant in a Single Pencil-Like ZnO Nanowire, Nano Lett. 12 (2012) 1919–1922. https://doi.org/10.1021/nl204353t.

[4] R. Agrawal, H.D. Espinosa, Giant Piezoelectric Size Effects in Zinc Oxide and Gallium Nitride Nanowires. A First Principles Investigation, Nano Lett. 11 (2011) 786–790. https://doi.org/10.1021/nl104004d.

[5] R. Tao, G. Ardila, L. Montès, M. Mouis, Modeling of semiconducting piezoelectric nanowires for mechanical energy harvesting and mechanical sensing, Nano Energy. 14 (2015) 62–76. https://doi.org/10.1016/j.nanoen.2014.11.035.

[6] R. Tao, M. Mouis, G. Ardila, Unveiling the Influence of Surface Fermi Level Pinning on the Piezoelectric Response of Semiconducting Nanowires, Adv. Electron. Mater. 4 (2018) 1–9. https://doi.org/10.1002/aelm.201700299.

[7] S. Das, E. Mao, The global energy footprint of information and communication technology electronics in connected Internet-of-Things devices, Sustain. Energy, Grids Networks. 24 (2020) 100408. https://doi.org/10.1016/j.segan.2020.100408.

[8] E.M. Yeatman, Energy scavenging for wireless sensor nodes, in: 2007 2nd Int. Work. Adv. Sensors Interface, IEEE, 2007: pp. 1–4. https://doi.org/10.1109/IWASI.2007.4420014.

[9] K.L. Lueth, State of the IoT 2020: 12 billion IoT connections, surpassing non-IoT for the first time, (2020).

[10] C. Arcadius Tokognon, B. Gao, G.Y. Tian, Y. Yan, Structural Health Monitoring Framework Based on Internet of Things: A Survey, IEEE Internet Things J. 4 (2017) 619–635. https://doi.org/10.1109/JIOT.2017.2664072.

[11] Y.-W. Chong, W. Ismail, K. Ko, C.-Y. Lee, Energy Harvesting For Wearable Devices:

A Review, IEEE Sens. J. 19 (2019) 9047–9062. https://doi.org/10.1109/JSEN.2019.2925638.

[12] C.H. Ng, H.N. Lim, S. Hayase, Z. Zainal, N.M. Huang, Photovoltaic performances of mono- and mixed-halide structures for perovskite solar cell: A review, Renew. Sustain. Energy Rev. 90 (2018) 248–274. https://doi.org/10.1016/j.rser.2018.03.030.

[13] A.A.F. Husain, W.Z.W. Hasan, S. Shafie, M.N. Hamidon, S.S. Pandey, A review of transparent solar photovoltaic technologies, Renew. Sustain. Energy Rev. 94 (2018) 779–791. https://doi.org/10.1016/j.rser.2018.06.031.

[14] J.L. Blackburn, A.J. Ferguson, C. Cho, J.C. Grunlan, Thermoelectric Materials: Carbon-Nanotube-Based Thermoelectric Materials and Devices (Adv. Mater. 11/2018), Adv. Mater. 30 (2018) 1870072. https://doi.org/10.1002/adma.201870072.

[15] R. Tian, C. Wan, N. Hayashi, T. Aoai, K. Koumoto, Wearable and flexible thermoelectrics for energy harvesting, MRS Bull. 43 (2018) 193–198.

[16] R.L. Harne, K.W. Wang, A review of the recent research on vibration energy harvesting via bistable systems, Smart Mater. Struct. 22 (2013) 023001. https://doi.org/10.1088/0964-1726/22/2/023001.

[17] F. Narita, M. Fox, A Review on Piezoelectric, Magnetostrictive, and Magnetoelectric Materials and Device Technologies for Energy Harvesting Applications, Adv. Eng. Mater. 20 (2018) 1700743. https://doi.org/10.1002/adem.201700743.

[18] N.G. Stephen, On energy harvesting from ambient vibration, J. Sound Vib. 293 (2006) 409–425. https://doi.org/10.1016/j.jsv.2005.10.003.

[19] H. Liu, J. Zhong, C. Lee, S.-W. Lee, L. Lin, A comprehensive review on piezoelectric energy harvesting technology: Materials, mechanisms, and applications, Appl. Phys. Rev. 5 (2018) 041306. https://doi.org/10.1063/1.5074184.

[20] R. Vullers, R. Schaijk, H. Visser, J. Penders, C. Hoof, Energy Harvesting for Autonomous Wireless Sensor Networks, IEEE Solid-State Circuits Mag. 2 (2010) 29–38. https://doi.org/10.1109/MSSC.2010.936667.

[21] Y. Wu, J. Qiu, F. Kojima, H. Ji, W. Xie, S. Zhou, Design methodology of a frequency up-converting energy harvester based on dual-cantilever and pendulum structures, AIP Adv. 9 (2019) 045312. https://doi.org/10.1063/1.5093361.

[22] H. Fu, E.M. Yeatman, Rotational energy harvesting using bi-stability and frequency up-conversion for low-power sensing applications: Theoretical modelling and experimental

validation, Mech. Syst. Signal Process. 125 (2019) 229–244. https://doi.org/10.1016/j.ymssp.2018.04.043.

[23] H. Kulah, K. Najafi, Energy Scavenging From Low-Frequency Vibrations by Using Frequency Up-Conversion for Wireless Sensor Applications, IEEE Sens. J. 8 (2008) 261–268. https://doi.org/10.1109/JSEN.2008.917125.

[24] C. Dagdeviren, P. Joe, O.L. Tuzman, K.-I. Park, K.J. Lee, Y. Shi, Y. Huang, J.A. Rogers, Recent progress in flexible and stretchable piezoelectric devices for mechanical energy harvesting, sensing and actuation, Extrem. Mech. Lett. 9 (2016) 269–281. https://doi.org/10.1016/j.eml.2016.05.015.

[25] X.-J. Zhang, G.-S. Wang, Y.-Z. Wei, L. Guo, M.-S. Cao, Polymer-composite with high dielectric constant and enhanced absorption properties based on graphene–CuS nanocomposites and polyvinylidene fluoride, J. Mater. Chem. A. 1 (2013) 12115. https://doi.org/10.1039/c3ta12451g.

[26] S. Sripadmanabhan Indira, C. Aravind Vaithilingam, K.S.P. Oruganti, F. Mohd, S. Rahman, Nanogenerators as a Sustainable Power Source: State of Art, Applications, and Challenges, Nanomaterials. 9 (2019) 773. https://doi.org/10.3390/nano9050773.

[27] D. Dinulovic, M. Brooks, M. Haug, T. Petrovic, Rotational Electromagnetic Energy Harvesting System, Phys. Procedia. 75 (2015) 1244–1251. https://doi.org/10.1016/j.phpro.2015.12.137.

[28] H. Liu, C. Hou, J. Lin, Y. Li, Q. Shi, T. Chen, L. Sun, C. Lee, A non-resonant rotational electromagnetic energy harvester for low-frequency and irregular human motion, Appl. Phys. Lett. 113 (2018) 203901. https://doi.org/10.1063/1.5053945.

[29] C.H. Lu, Y.J. Wang, C.K. Sung, P.C.P. Chao, A Hula-Hoop Energy-Harvesting System, IEEE Trans. Magn. 47 (2011) 2395–2398. https://doi.org/10.1109/TMAG.2011.2155636.

[30] Y. Tan, Y. Dong, X. Wang, Review of MEMS Electromagnetic Vibration Energy Harvester, J. Microelectromechanical Syst. 26 (2017) 1–16. https://doi.org/10.1109/JMEMS.2016.2611677.

[31] W. Manthey, N. Kroemer, V. Magori, Ultrasonic transducers and transducer arrays for applications in air, Meas. Sci. Technol. 3 (1992) 249–261. https://doi.org/10.1088/0957-0233/3/3/001.

[32] S. Meninger, J.O. Mur-Miranda, R. Amirtharajah, A. Chandrakasan, J.H. Lang,

Vibration-to-electric energy conversion, IEEE Trans. Very Large Scale Integr. Syst. 9 (2001) 64–76. https://doi.org/10.1109/92.920820.

[33] R. TASHIRO, N. KABEI, K. KATAYAMA, Y. ISHIZUKA, F. TSUBOI, K. TSUCHIYA, Development of an Electrostatic Generator that Harnesses the Motion of a Living Body. Use of a Resonant Phenomenon., JSME Int. J. Ser. C. 43 (2000) 916–922. https://doi.org/10.1299/jsmec.43.916.

[34] J. Lowell, A.C. Rose-Innes, Contact electrification, Adv. Phys. 29 (1980) 947–1023. https://doi.org/10.1080/00018738000101466.

[35] L.S. McCarty, G.M. Whitesides, Electrostatic Charging Due to Separation of Ions at Interfaces: Contact Electrification of Ionic Electrets, Angew. Chemie Int. Ed. 47 (2008) 2188–2207. https://doi.org/10.1002/anie.200701812.

[36] H.T. Baytekin, A.Z. Patashinski, M. Branicki, B. Baytekin, S. Soh, B.A. Grzybowski, The Mosaic of Surface Charge in Contact Electrification, Science (80-.). 333 (2011) 308–312. https://doi.org/10.1126/science.1201512.

[37] Y. Liu, W. Liu, Z. Wang, W. He, Q. Tang, Y. Xi, X. Wang, H. Guo, C. Hu, Quantifying contact status and the air-breakdown model of charge-excitation triboelectric nanogenerators to maximize charge density, Nat. Commun. 11 (2020) 1599. https://doi.org/10.1038/s41467-020-15368-9.

[38] S. Khalid, I. Raouf, A. Khan, N. Kim, H.S. Kim, A Review of Human-Powered Energy Harvesting for Smart Electronics: Recent Progress and Challenges, Int. J. Precis. Eng. Manuf. Technol. 6 (2019) 821–851. https://doi.org/10.1007/s40684-019-00144-y.

[39] N. Wu, B. Bao, Q. Wang, Review on engineering structural designs for efficient piezoelectric energy harvesting to obtain high power output, Eng. Struct. 235 (2021) 112068. https://doi.org/10.1016/j.engstruct.2021.112068.

[40] C. Chen, A. Sharafi, J.-Q. Sun, A high density piezoelectric energy harvesting device from highway traffic – Design analysis and laboratory validation, Appl. Energy. 269 (2020) 115073. https://doi.org/10.1016/j.apenergy.2020.115073.

[41] H. Liang, G. Hao, O.Z. Olszewski, A review on vibration-based piezoelectric energy harvesting from the aspect of compliant mechanisms, Sensors Actuators A Phys. 331 (2021) 112743. https://doi.org/10.1016/j.sna.2021.112743.

[42] V.U. Somkuwar, A. Pragya, B. Kumar, Structurally engineered textile-based triboelectric nanogenerator for energy harvesting application, J. Mater. Sci. 55 (2020)

5177–5189. https://doi.org/10.1007/s10853-020-04359-2.

[43] S. Boisseau, G. Despesse, B.A. Seddik, Electrostatic conversion for vibration energy harvesting, Small-Scale Energy Harvest. 5 (2012).

[44] F. Khan, F. Sassani, B. Stoeber, Nonlinear behaviour of membrane type electromagnetic energy harvester under harmonic and random vibrations, Microsyst. Technol. 20 (2014) 1323–1335. https://doi.org/10.1007/s00542-013-1938-1.

[45] P. Miao, P.D. Mitcheson, A.S. Holmes, E.M. Yeatman, T.C. Green, B.H. Stark, Mems inertial power generators for biomedical applications, Microsyst. Technol. 12 (2006) 1079–1083. https://doi.org/10.1007/s00542-006-0152-9.

[46] K. Ylli, D. Hoffmann, A. Willmann, P. Becker, B. Folkmer, Y. Manoli, Energy harvesting from human motion: exploiting swing and shock excitations, Smart Mater. Struct. 24 (2015) 025029. https://doi.org/10.1088/0964-1726/24/2/025029.

[47] J.L. Atwood, Comprehensive supramolecular chemistry II, Elsevier, 2017.

[48] H. Huang, J.F. Scott, Ferroelectric materials for energy applications, John Wiley & Sons, 2018.

[49] Y. Yang, W. Guo, K.C. Pradel, G. Zhu, Y. Zhou, Y. Zhang, Y. Hu, L. Lin, Z.L. Wang, Pyroelectric Nanogenerators for Harvesting Thermoelectric Energy, Nano Lett. 12 (2012) 2833–2838. https://doi.org/10.1021/nl3003039.

[50] M. Zhang, Q. Hu, K. Ma, Y. Ding, C. Li, Pyroelectric effect in CdS nanorods decorated with a molecular Co-catalyst for hydrogen evolution, Nano Energy. 73 (2020) 104810. https://doi.org/10.1016/j.nanoen.2020.104810.

[51] S.C. Abrahams, J.M. Reddy, J.L. Bernstein, Ferroelectric lithium niobate. 3. Single crystal X-ray diffraction study at 24°C, J. Phys. Chem. Solids. 27 (1966) 997–1012. https://doi.org/10.1016/0022-3697(66)90072-2.

[52] H. Ghayour, M. Abdellahi, A brief review of the effect of grain size variation on the electrical properties of BaTiO3-based ceramics, Powder Technol. 292 (2016) 84–93. https://doi.org/10.1016/j.powtec.2016.01.030.

[53] C.R. Bowen, H.A. Kim, P.M. Weaver, S. Dunn, Piezoelectric and ferroelectric materials and structures for energy harvesting applications, Energy Environ. Sci. 7 (2014) 25–44. https://doi.org/10.1039/C3EE42454E.

[54] R.A. Kishore, Harvesting thermal energy with ferroelectric materials, in: Ferroelectr. Mater. Energy Harvest. Storage, Elsevier, 2021: pp. 85–106.

https://doi.org/10.1016/B978-0-08-102802-5.00003-0.

[55] J.I. Roscow, R.W.C. Lewis, J. Taylor, C.R. Bowen, Modelling and fabrication of porous sandwich layer barium titanate with improved piezoelectric energy harvesting figures of merit, Acta Mater. 128 (2017) 207–217. https://doi.org/10.1016/j.actamat.2017.02.029.

[56] T.R. Shrout, S.J. Zhang, Lead-free piezoelectric ceramics: Alternatives for PZT?, J. Electroceramics. 19 (2007) 113–126. https://doi.org/10.1007/s10832-007-9047-0.

[57] T. Kimura, Q. Dong, S. Yin, T. Hashimoto, A. Sasaki, T. Sato, Synthesis and piezoelectric properties of Li-doped BaTiO3 by a solvothermal approach, J. Eur. Ceram. Soc. 33 (2013) 1009–1015. https://doi.org/10.1016/j.jeurceramsoc.2012.11.007.

[58] L.-F. Zhu, B.-P. Zhang, W.-G. Yang, Enhancing piezoelectric coefficient d33 in LiF-doped BaTiO3 ceramics by optimizing excess Ba content, Mater. Res. Bull. 52 (2014) 158–161. https://doi.org/10.1016/j.materresbull.2014.01.018.

[59] W.-G. Yang, B.-P. Zhang, N. Ma, L. Zhao, High piezoelectric properties of BaTiO3–xLiF ceramics sintered at low temperatures, J. Eur. Ceram. Soc. 32 (2012) 899–904. https://doi.org/10.1016/j.jeurceramsoc.2011.10.054.

[60] L.-F. Zhu, B.-P. Zhang, W.-G. Yang, N. Ma, X.-K. Zhao, L. Zhao, High piezoelectric properties of (Ba,Ca)TiO3-0.04LiF ceramics sintered at a low temperature, J. Electroceramics. 30 (2013) 24–29. https://doi.org/10.1007/s10832-012-9701-z.

[61] M. Chen, Z. Xu, R. Chu, Z. Wang, S. Gao, G. Yu, W. Li, S. Gong, G. Li, Y 2 O 3 -modified Ba(Ti 0.96 Sn 0.04)O 3 ceramics with improved piezoelectricity and raised Curie temperature, Mater. Res. Bull. 59 (2014) 305–310. https://doi.org/10.1016/j.materresbull.2014.07.040.

[62] D. Maurya, A. Kumar, V. Petkov, J.E. Mahaney, R.S. Katiyar, S. Priya, Local structure and piezoelectric instability in lead-free (1 − x)BaTiO 3 -xA(Cu 1/3 Nb 2/3)O 3 (A = Sr, Ca, Ba) solid solutions, RSC Adv. 4 (2014) 1283–1292. https://doi.org/10.1039/C3RA44886J.

[63] Z. Yi, B. Yang, G. Li, J. Liu, X. Chen, X. Wang, C. Yang, High performance bimorph piezoelectric MEMS harvester via bulk PZT thick films on thin beryllium-bronze substrate, Appl. Phys. Lett. 111 (2017) 013902. https://doi.org/10.1063/1.4991368.

[64] H. Takahashi, Y. Numamoto, J. Tani, K. Matsuta, J. Qiu, S. Tsurekawa, Lead-Free Barium Titanate Ceramics with Large Piezoelectric Constant Fabricated by Microwave Sintering, Jpn. J. Appl. Phys. 45 (2006) L30–L32. https://doi.org/10.1143/JJAP.45.L30.

[65] R. Mbarki, N. Baccam, K. Dayal, P. Sharma, Piezoelectricity above the Curie temperature? Combining flexoelectricity and functional grading to enable high-temperature electromechanical coupling, Appl. Phys. Lett. 104 (2014) 122904. https://doi.org/10.1063/1.4869478.

[66] Y. Saito, H. Takao, T. Tani, T. Nonoyama, K. Takatori, T. Homma, T. Nagaya, M. Nakamura, Lead-free piezoceramics, Nature. 432 (2004) 84–87. https://doi.org/10.1038/nature03028.

[67] S.S. Won, J. Lee, V. Venugopal, D.-J. Kim, J. Lee, I.W. Kim, A.I. Kingon, S.-H. Kim, Lead-free Mn-doped (K 0.5 ,Na 0.5)NbO 3 piezoelectric thin films for MEMS-based vibrational energy harvester applications, Appl. Phys. Lett. 108 (2016) 232908. https://doi.org/10.1063/1.4953623.

[68] A. Herabut, A. Safari, Processing and Electromechanical Properties of (Bi 0.5 Na 0.5) (1?1.5x) La x TiO 3 Ceramics, J. Am. Ceram. Soc. 80 (1997) 2954–2958. https://doi.org/10.1111/j.1151-2916.1997.tb03219.x.

[69] M. Rawat, K.L. Yadav, Structural, dielectric and ferroelectric properties of Ba1−x(Bi0.5Na0.5)xTiO3 ceramics, Ceram. Int. 39 (2013) 3627–3633. https://doi.org/10.1016/j.ceramint.2012.10.191.

[70] W.-S. Kang, J.-H. Koh, (1−x)Bi0.5Na0.5TiO3–xBaTiO3 lead-free piezoelectric ceramics for energy-harvesting applications, J. Eur. Ceram. Soc. 35 (2015) 2057–2064. https://doi.org/10.1016/j.jeurceramsoc.2014.12.036.

[71] A. Cho, D. Bin Kim, Y.S. Cho, Electric-Field-Dependent Surface Potentials and Vibrational Energy-Harvesting Characteristics of Bi(Na 0.5 Ti 0.5)O 3 -Based Pb-Free Piezoelectric Thin Films, ACS Appl. Mater. Interfaces. 11 (2019) 13244–13250. https://doi.org/10.1021/acsami.9b00367.

[72] C. Fei, X. Liu, B. Zhu, D. Li, X. Yang, Y. Yang, Q. Zhou, AlN piezoelectric thin films for energy harvesting and acoustic devices, Nano Energy. 51 (2018) 146–161. https://doi.org/10.1016/j.nanoen.2018.06.062.

[73] A. Khan, Z. Abas, H. Soo Kim, I.-K. Oh, Piezoelectric thin films: an integrated review of transducers and energy harvesting, Smart Mater. Struct. 25 (2016) 053002. https://doi.org/10.1088/0964-1726/25/5/053002.

[74] M.-H. Zhao, Z.-L. Wang, S.X. Mao, Piezoelectric Characterization of Individual Zinc Oxide Nanobelt Probed by Piezoresponse Force Microscope, Nano Lett. 4 (2004) 587–

590. https://doi.org/10.1021/nl035198a.

[75] N. Novak, P. Keil, T. Frömling, F.H. Schader, A. Martin, K.G. Webber, J. Rödel, Influence of metal/semiconductor interface on attainable piezoelectric and energy harvesting properties of ZnO, Acta Mater. 162 (2019) 277–283. https://doi.org/10.1016/j.actamat.2018.10.008.

[76] Q.C. Bui, B. Salem, H. Roussel, X. Mescot, Y. Guerfi, C. Jiménez, V. Consonni, G. Ardila, Effects of thermal annealing on the structural and electrical properties of ZnO thin films for boosting their piezoelectric response, J. Alloys Compd. 870 (2021) 159512. https://doi.org/10.1016/j.jallcom.2021.159512.

[77] X. He, Q. Wen, Z. Lu, Z. Shang, Z. Wen, A micro-electromechanical systems based vibration energy harvester with aluminum nitride piezoelectric thin film deposited by pulsed direct-current magnetron sputtering, Appl. Energy. 228 (2018) 881–890. https://doi.org/10.1016/j.apenergy.2018.07.001.

[78] P. Wang, H. Du, ZnO thin film piezoelectric MEMS vibration energy harvesters with two piezoelectric elements for higher output performance, Rev. Sci. Instrum. 86 (2015) 075002. https://doi.org/10.1063/1.4923456.

[79] R. Gregorio, Determination of the α, β, and γ crystalline phases of poly(vinylidene fluoride) films prepared at different conditions, J. Appl. Polym. Sci. 100 (2006) 3272–3279. https://doi.org/10.1002/app.23137.

[80] B.B. Tian, X.F. Bai, Y. Liu, P. Gemeiner, X.L. Zhao, B.L. Liu, Y.H. Zou, X.D. Wang, H. Huang, J.L. Wang, S. Sun, J.L. Sun, B. Dkhil, X.J. Meng, J.H. Chu, β phase instability in poly(vinylidene fluoride/trifluoroethylene) thin films near β relaxation temperature, Appl. Phys. Lett. 106 (2015) 092902. https://doi.org/10.1063/1.4913968.

[81] A.G. Holmes-Siedle, P.D. Wilson, A.P. Verrall, PVdF: An electronically-active polymer for industry, Mater. Des. 4 (1983) 910–918. https://doi.org/10.1016/0261-3069(84)90003-7.

[82] A.J. Lovinger, Ferroelectric Polymers, Science (80-.). 220 (1983) 1115–1121. https://doi.org/10.1126/science.220.4602.1115.

[83] A.N. Arshad, M.H.M. Wahid, M. Rusop, W.H.A. Majid, R.H.Y. Subban, M.D. Rozana, Dielectric and Structural Properties of Poly(vinylidene fluoride) (PVDF) and Poly(vinylidene fluoride-trifluoroethylene) (PVDF-TrFE) Filled with Magnesium Oxide Nanofillers, J. Nanomater. 2019 (2019) 1–12. https://doi.org/10.1155/2019/5961563.

[84] H. Xu, Dielectric properties and ferroelectric behavior of poly(vinylidene fluoride-trifluoroethylene) 50/50 copolymer ultrathin films, J. Appl. Polym. Sci. 80 (2001) 2259–2266. https://doi.org/10.1002/app.1330.

[85] S. Khadtare, E.J. Ko, Y.H. Kim, H.S. Lee, D.K. Moon, A flexible piezoelectric nanogenerator using conducting polymer and silver nanowire hybrid electrodes for its application in real-time muscular monitoring system, Sensors Actuators A Phys. 299 (2019) 111575. https://doi.org/10.1016/j.sna.2019.111575.

[86] W.-S. Jung, M.-J. Lee, M.-G. Kang, H.G. Moon, S.-J. Yoon, S.-H. Baek, C.-Y. Kang, Powerful curved piezoelectric generator for wearable applications, Nano Energy. 13 (2015) 174–181. https://doi.org/10.1016/j.nanoen.2015.01.051.

[87] Z. Pi, J. Zhang, C. Wen, Z. Zhang, D. Wu, Flexible piezoelectric nanogenerator made of poly(vinylidenefluoride-co-trifluoroethylene) (PVDF-TrFE) thin film, Nano Energy. 7 (2014) 33–41. https://doi.org/10.1016/j.nanoen.2014.04.016.

[88] X. Yuan, X. Gao, J. Yang, X. Shen, Z. Li, S. You, Z. Wang, S. Dong, The large piezoelectricity and high power density of a 3D-printed multilayer copolymer in a rugby ball-structured mechanical energy harvester, Energy Environ. Sci. 13 (2020) 152–161. https://doi.org/10.1039/C9EE01785B.

[89] M.M. Abolhasani, M. Naebe, K. Shirvanimoghaddam, H. Fashandi, H. Khayyam, M. Joordens, A. Pipertzis, S. Anwar, R. Berger, G. Floudas, J. Michels, K. Asadi, Thermodynamic approach to tailor porosity in piezoelectric polymer fibers for application in nanogenerators, Nano Energy. 62 (2019) 594–600. https://doi.org/10.1016/j.nanoen.2019.05.044.

[90] F. Mokhtari, B. Azimi, M. Salehi, S. Hashemikia, S. Danti, Recent advances of polymer-based piezoelectric composites for biomedical applications, J. Mech. Behav. Biomed. Mater. 122 (2021) 104669. https://doi.org/10.1016/j.jmbbm.2021.104669.

[91] K.-I. Park, C.K. Jeong, N.K. Kim, K.J. Lee, Stretchable piezoelectric nanocomposite generator, Nano Converg. 3 (2016) 12. https://doi.org/10.1186/s40580-016-0072-z.

[92] J. Briscoe, S. Dunn, Piezoelectric nanogenerators – a review of nanostructured piezoelectric energy harvesters, Nano Energy. 14 (2015) 15–29. https://doi.org/10.1016/j.nanoen.2014.11.059.

[93] Y. Sun, Y. Liu, Y. Zheng, Z. Li, J. Fan, L. Wang, X. Liu, J. Liu, W. Shou, Enhanced Energy Harvesting Ability of ZnO/PAN Hybrid Piezoelectric Nanogenerators, ACS

Appl. Mater. Interfaces. 12 (2020) 54936–54945. https://doi.org/10.1021/acsami.0c14490.

[94] C.K. Jeong, K. Park, J. Ryu, G. Hwang, K.J. Lee, Large-Area and Flexible Lead-Free Nanocomposite Generator Using Alkaline Niobate Particles and Metal Nanorod Filler, Adv. Funct. Mater. 24 (2014) 2620–2629. https://doi.org/10.1002/adfm.201303484.

[95] K. Park, C.K. Jeong, J. Ryu, G. Hwang, K.J. Lee, Nanocomposites: Flexible and Large-Area Nanocomposite Generators Based on Lead Zirconate Titanate Particles and Carbon Nanotubes (Adv. Energy Mater. 12/2013), Adv. Energy Mater. 3 (2013) 1530–1530. https://doi.org/10.1002/aenm.201370050.

[96] N.R. Alluri, A. Chandrasekhar, V. Vivekananthan, Y. Purusothaman, S. Selvarajan, J.H. Jeong, S.-J. Kim, Scavenging Biomechanical Energy Using High-Performance, Flexible BaTiO 3 Nanocube/PDMS Composite Films, ACS Sustain. Chem. Eng. 5 (2017) 4730–4738. https://doi.org/10.1021/acssuschemeng.7b00117.

[97] A.S. Dahiya, F. Morini, S. Boubenia, K. Nadaud, D. Alquier, G. Poulin-Vittrant, Organic/Inorganic Hybrid Stretchable Piezoelectric Nanogenerators for Self-Powered Wearable Electronics, Adv. Mater. Technol. 3 (2018) 1700249. https://doi.org/10.1002/admt.201700249.

[98] H. Lee, H. Kim, D.Y. Kim, Y. Seo, Pure Piezoelectricity Generation by a Flexible Nanogenerator Based on Lead Zirconate Titanate Nanofibers, ACS Omega. 4 (2019) 2610–2617. https://doi.org/10.1021/acsomega.8b03325.

[99] K. Park, M. Lee, Y. Liu, S. Moon, G. Hwang, G. Zhu, J.E. Kim, S.O. Kim, D.K. Kim, Z.L. Wang, K.J. Lee, Flexible Nanocomposite Generator Made of BaTiO3 Nanoparticles and Graphitic Carbons, Adv. Mater. 24 (2012) 2999–3004. https://doi.org/10.1002/adma.201200105.

[100] L. Lin, C.-H. Lai, Y. Hu, Y. Zhang, X. Wang, C. Xu, R.L. Snyder, L.-J. Chen, Z.L. Wang, High output nanogenerator based on assembly of GaN nanowires, Nanotechnology. 22 (2011) 475401. https://doi.org/10.1088/0957-4484/22/47/475401.

[101] N. Jamond, P. Chrétien, F. Houzé, L. Lu, L. Largeau, O. Maugain, L. Travers, J.C. Harmand, F. Glas, E. Lefeuvre, M. Tchernycheva, N. Gogneau, Piezo-generator integrating a vertical array of GaN nanowires, Nanotechnology. 27 (2016) 325403. https://doi.org/10.1088/0957-4484/27/32/325403.

[102] A. El Kacimi, E. Pauliac-Vaujour, J. Eymery, Flexible Capacitive Piezoelectric Sensor

with Vertically Aligned Ultralong GaN Wires, ACS Appl. Mater. Interfaces. 10 (2018) 4794–4800. https://doi.org/10.1021/acsami.7b15649.

[103] J. Eymery, X. Chen, C. Durand, M. Kolb, G. Richter, Self-organized and self-catalyst growth of semiconductor and metal wires by vapour phase epitaxy: GaN rods versus Cu whiskers, Comptes Rendus Phys. 14 (2013) 221–227. https://doi.org/10.1016/j.crhy.2012.10.009.

[104] A.T. Le, M. Ahmadipour, S.-Y. Pung, A review on ZnO-based piezoelectric nanogenerators: Synthesis, characterization techniques, performance enhancement and applications, J. Alloys Compd. 844 (2020) 156172. https://doi.org/10.1016/j.jallcom.2020.156172.

[105] M.-Y. Choi, D. Choi, M. Jin, I. Kim, S.-H. Kim, J. Choi, S.Y. Lee, J.M. Kim, S. Kim, Mechanically Powered Transparent Flexible Charge-Generating Nanodevices with Piezoelectric ZnO Nanorods, Adv. Mater. 21 (2009) 2185–2189. https://doi.org/10.1002/adma.200803605.

[106] Y. Hu, Y. Zhang, C. Xu, L. Lin, R.L. Snyder, Z.L. Wang, Self-Powered System with Wireless Data Transmission, Nano Lett. 11 (2011) 2572–2577. https://doi.org/10.1021/nl201505c.

[107] Q. Wang, D. Yang, Y. Qiu, X. Zhang, W. Song, L. Hu, Two-dimensional ZnO nanosheets grown on flexible ITO-PET substrate for self-powered energy-harvesting nanodevices, Appl. Phys. Lett. 112 (2018) 063906. https://doi.org/10.1063/1.5012950.

[108] M. Choi, G. Murillo, S. Hwang, J.W. Kim, J.H. Jung, C.-Y. Chen, M. Lee, Mechanical and electrical characterization of PVDF-ZnO hybrid structure for application to nanogenerator, Nano Energy. 33 (2017) 462–468. https://doi.org/10.1016/j.nanoen.2017.01.062.

[109] W. Wang, Y. Zheng, X. Jin, Y. Sun, B. Lu, H. Wang, J. Fang, H. Shao, T. Lin, Unexpectedly high piezoelectricity of electrospun polyacrylonitrile nanofiber membranes, Nano Energy. 56 (2019) 588–594. https://doi.org/10.1016/j.nanoen.2018.11.082.

[110] B. Sen, M. Stroscio, M. Dutta, Piezoelectricity in wurtzite polar semiconductor nanowires: A theoretical study, J. Appl. Phys. 110 (2011) 024506. https://doi.org/10.1063/1.3603036.

[111] M.E. Levinshtein, S.L. Rumyantsev, M.S. Shur, Properties of Advanced Semiconductor

Materials: GaN, AIN, InN, BN, SiC, SiGe, John Wiley & Sons, 2001.

[112] K. Tsubouchi, K. Sugai, N. Mikoshiba, AlN Material Constants Evaluation and SAW Properties on AlN/Al2 O3 and AlN/Si, in: 1981 Ultrason. Symp., IEEE, 1981: pp. 375–380. https://doi.org/10.1109/ULTSYM.1981.197646.

[113] F. Bernardini, V. Fiorentini, D. Vanderbilt, Spontaneous polarization and piezoelectric constants of III-V nitrides, Phys. Rev. B. 56 (1997) R10024–R10027. https://doi.org/10.1103/PhysRevB.56.R10024.

[114] T. Inushima, T. Shiraishi, V.Y. Davydov, Phonon structure of InN grown by atomic layer epitaxy, Solid State Commun. 110 (1999) 491–495. https://doi.org/10.1016/S0038-1098(99)00108-8.

[115] V.W.L. Chin, T.L. Tansley, T. Osotchan, Electron mobilities in gallium, indium, and aluminum nitrides, J. Appl. Phys. 75 (1994) 7365–7372. https://doi.org/10.1063/1.356650.

[116] G. Carlotti, G. Socino, A. Petri, E. Verona, Acoustic investigation of the elastic properties of ZnO films, Appl. Phys. Lett. 51 (1987) 1889–1891. https://doi.org/10.1063/1.98502.

[117] N. Ashkenov, B.N. Mbenkum, C. Bundesmann, V. Riede, M. Lorenz, D. Spemann, E.M. Kaidashev, A. Kasic, M. Schubert, M. Grundmann, G. Wagner, H. Neumann, V. Darakchieva, H. Arwin, B. Monemar, Infrared dielectric functions and phonon modes of high-quality ZnO films, J. Appl. Phys. 93 (2003) 126–133. https://doi.org/10.1063/1.1526935.

[118] Lucia PETTI, PULSE-COM project, PULSE-COM. (2019). https://www.pulsecom-h2020.eu/.

[119] P.J.P. Espitia, N. de F.F. Soares, J.S. dos R. Coimbra, N.J. de Andrade, R.S. Cruz, E.A.A. Medeiros, Zinc Oxide Nanoparticles: Synthesis, Antimicrobial Activity and Food Packaging Applications, Food Bioprocess Technol. 5 (2012) 1447–1464. https://doi.org/10.1007/s11947-012-0797-6.

[120] S. Verma, S.A. Younis, K.-H. Kim, F. Dong, Anisotropic ZnO nanostructures and their nanocomposites as an advanced platform for photocatalytic remediation, J. Hazard. Mater. 415 (2021) 125651. https://doi.org/10.1016/j.jhazmat.2021.125651.

[121] Ü. Özgür, Y.I. Alivov, C. Liu, A. Teke, M.A. Reshchikov, S. Doğan, V. Avrutin, S.-J. Cho, H. Morkoç, A comprehensive review of ZnO materials and devices, J. Appl. Phys.

98 (2005) 041301. https://doi.org/10.1063/1.1992666.

[122] C.-Q. Luo, F.C.-C. Ling, M.A. Rahman, M. Phillips, C. Ton-That, C. Liao, K. Shih, J. Lin, H.W. Tam, A.B. Djurišić, S.-P. Wang, Surface polarity control in ZnO films deposited by pulsed laser deposition, Appl. Surf. Sci. 483 (2019) 1129–1135. https://doi.org/10.1016/j.apsusc.2019.03.228.

[123] T. Cossuet, E. Appert, J.-L. Thomassin, V. Consonni, Polarity-Dependent Growth Rates of Selective Area Grown ZnO Nanorods by Chemical Bath Deposition, Langmuir. 33 (2017) 6269–6279. https://doi.org/10.1021/acs.langmuir.7b00935.

[124] M.W. Allen, P. Miller, R.J. Reeves, S.M. Durbin, Influence of spontaneous polarization on the electrical and optical properties of bulk, single crystal ZnO, Appl. Phys. Lett. 90 (2007) 062104. https://doi.org/10.1063/1.2450642.

[125] M.W. Allen, R.J. Mendelsberg, R.J. Reeves, S.M. Durbin, Oxidized noble metal Schottky contacts to n-type ZnO, Appl. Phys. Lett. 94 (2009) 103508. https://doi.org/10.1063/1.3089871.

[126] C. Li, W. Dai, S. Xu, X. Li, C. Gao, X. Chen, B. Yang, Local Piezoelectric Properties and Polarity Distribution of ZnO Films Deposited at Different Substrate Temperatures, J. Electron. Mater. 44 (2015) 1095–1099. https://doi.org/10.1007/s11664-015-3659-y.

[127] Q.C. Bui, G. Ardila, E. Sarigiannidou, H. Roussel, C. Jiménez, O. Chaix-Pluchery, Y. Guerfi, F. Bassani, F. Donatini, X. Mescot, B. Salem, V. Consonni, Morphology Transition of ZnO from Thin Film to Nanowires on Silicon and its Correlated Enhanced Zinc Polarity Uniformity and Piezoelectric Responses, ACS Appl. Mater. Interfaces. 12 (2020) 29583–29593. https://doi.org/10.1021/acsami.0c04112.

[128] O. Dulub, U. Diebold, G. Kresse, Novel Stabilization Mechanism on Polar Surfaces: ZnO(0001)-Zn, Phys. Rev. Lett. 90 (2003) 016102. https://doi.org/10.1103/PhysRevLett.90.016102.

[129] O. Dulub, L.A. Boatner, U. Diebold, STM study of the geometric and electronic structure of ZnO()-Zn, ()-O, (), and () surfaces, Surf. Sci. 519 (2002) 201–217. https://doi.org/10.1016/S0039-6028(02)02211-2.

[130] H. Noei, L. Jin, H. Qiu, M. Xu, Y. Gao, J. Zhao, M. Kauer, C. Wöll, M. Muhler, Y. Wang, Vibrational spectroscopic studies on pure and metal-covered metal oxide surfaces, Phys. Status Solidi. 250 (2013) 1204–1221. https://doi.org/10.1002/pssb.201248534.

[131] V. Consonni, E. Sarigiannidou, E. Appert, A. Bocheux, S. Guillemin, F. Donatini, I.-C. Robin, J. Kioseoglou, F. Robaut, Selective Area Growth of Well-Ordered ZnO Nanowire Arrays with Controllable Polarity, ACS Nano. 8 (2014) 4761–4770. https://doi.org/10.1021/nn500620t.

[132] W.L. Hughes, Z.L. Wang, Controlled synthesis and manipulation of ZnO nanorings and nanobows, Appl. Phys. Lett. 86 (2005) 043106. https://doi.org/10.1063/1.1853514.

[133] H.D. Espinosa, R.A. Bernal, M. Minary-Jolandan, A Review of Mechanical and Electromechanical Properties of Piezoelectric Nanowires, Adv. Mater. 24 (2012) 4656–4675. https://doi.org/10.1002/adma.201104810.

[134] G. Jing, X. Zhang, D. Yu, Effect of surface morphology on the mechanical properties of ZnO nanowires, Appl. Phys. A. 100 (2010) 473–478. https://doi.org/10.1007/s00339-010-5736-7.

[135] C.Q. Chen, Y. Shi, Y.S. Zhang, J. Zhu, Y.J. Yan, Size Dependence of Young's Modulus in ZnO Nanowires, Phys. Rev. Lett. 96 (2006) 075505. https://doi.org/10.1103/PhysRevLett.96.075505.

[136] M.Y. Soomro, I. Hussain, N. Bano, E. Broitman, O. Nur, M. Willander, Nanoscale elastic modulus of single horizontal ZnO nanorod using nanoindentation experiment, Nanoscale Res. Lett. 7 (2012) 146. https://doi.org/10.1186/1556-276X-7-146.

[137] A.J.L. Garcia, M. Mouis, V. Consonni, G. Ardila, Dimensional Roadmap for Maximizing the Piezoelectrical Response of ZnO Nanowire-Based Transducers: Impact of Growth Method, Nanomaterials. 11 (2021) 941. https://doi.org/https://doi.org/10.3390/nano11040941.

[138] F.R. Fan, W. Tang, Z.L. Wang, Flexible Nanogenerators for Energy Harvesting and Self-Powered Electronics, Adv. Mater. 28 (2016) 4283–4305. https://doi.org/10.1002/adma.201504299.

[139] A. Dal Corso, M. Posternak, R. Resta, A. Baldereschi, Ab initio study of piezoelectricity and spontaneous polarization in ZnO, Phys. Rev. B. 50 (1994) 10715–10721. https://doi.org/10.1103/PhysRevB.50.10715.

[140] L. Jaloustre, Piezoelectricity in single III-Nitride nanowires for nanopiezotronics: a scanning force microscopy investigation, (2019).

[141] M.-H. Zhao, Z.-L. Wang, S.X. Mao, Piezoelectric Characterization of Individual Zinc Oxide Nanobelt Probed by Piezoresponse Force Microscope, Nano Lett. 4 (2004) 587–

590. https://doi.org/10.1021/nl035198a.

[142] H.J. Fan, W. Lee, R. Hauschild, M. Alexe, G. Le Rhun, R. Scholz, A. Dadgar, K. Nielsch, H. Kalt, A. Krost, M. Zacharias, U. Gösele, Template-Assisted Large-Scale Ordered Arrays of ZnO Pillars for Optical and Piezoelectric Applications, Small. 2 (2006) 561–568. https://doi.org/10.1002/smll.200500331.

[143] D.A. Scrymgeour, T.L. Sounart, N.C. Simmons, J.W.P. Hsu, Polarity and piezoelectric response of solution grown zinc oxide nanocrystals on silver, J. Appl. Phys. 101 (2007) 014316. https://doi.org/10.1063/1.2405014.

[144] D. Tamvakos, S. Lepadatu, V.-A. Antohe, A. Tamvakos, P.M. Weaver, L. Piraux, M.G. Cain, D. Pullini, Piezoelectric properties of template-free electrochemically grown ZnO nanorod arrays, Appl. Surf. Sci. 356 (2015) 1214–1220. https://doi.org/10.1016/j.apsusc.2015.08.187.

[145] D. Cavallini, M. Fortunato, G.D. Bellis, M.S. Sarto, PFM Characterization of Piezoelectric PVDF/ZnONanorod thin films, in: 2018 IEEE 18th Int. Conf. Nanotechnol., IEEE, 2018: pp. 1–3. https://doi.org/10.1109/NANO.2018.8626362.

[146] E. Broitman, M.Y. Soomro, J. Lu, M. Willander, L. Hultman, Nanoscale piezoelectric response of ZnO nanowires measured using a nanoindentation technique, Phys. Chem. Chem. Phys. 15 (2013) 11113. https://doi.org/10.1039/c3cp50915j.

[147] M. Chelu, H. Stroescu, M. Anastasescu, J.M. Calderon-Moreno, S. Preda, M. Stoica, Z. Fogarassy, P. Petrik, M. Gheorghe, C. Parvulescu, C. Brasoveanu, A. Dinescu, C. Moldovan, M. Gartner, High-quality PMMA/ZnO NWs piezoelectric coating on rigid and flexible metallic substrates, Appl. Surf. Sci. 529 (2020) 147135. https://doi.org/10.1016/j.apsusc.2020.147135.

[148] D. Seol, B. Kim, Y. Kim, Non-piezoelectric effects in piezoresponse force microscopy, Curr. Appl. Phys. 17 (2017) 661–674. https://doi.org/10.1016/j.cap.2016.12.012.

[149] A. Janotti, C.G. Van de Walle, Fundamentals of zinc oxide as a semiconductor, Reports Prog. Phys. 72 (2009) 126501. https://doi.org/10.1088/0034-4885/72/12/126501.

[150] P. Kofstad, Defects and transport properties of metal oxides, Oxid. Met. 44 (1995) 3–27. https://doi.org/10.1007/BF01046721.

[151] R. Zhang, W. Pang, Z. Feng, X. Chen, Y. Chen, Q. Zhang, H. Zhang, C. Sun, J.J. Yang, D. Zhang, Enabling selectivity and fast recovery of ZnO nanowire gas sensors through resistive switching, Sensors Actuators B Chem. 238 (2017) 357–363.

https://doi.org/10.1016/j.snb.2016.07.068.

[152] S. Lu, Q. Liao, J. Qi, S. Liu, Y. Liu, Q. Liang, G. Zhang, Y. Zhang, The enhanced performance of piezoelectric nanogenerator via suppressing screening effect with Au particles/ZnO nanoarrays Schottky junction, Nano Res. 9 (2016) 372–379. https://doi.org/10.1007/s12274-015-0916-6.

[153] W.-K. Hong, J. Yoon, T. Lee, Hydrogen plasma-mediated modification of the electrical transport properties of ZnO nanowire field effect transistors, Nanotechnology. 26 (2015) 125202. https://doi.org/10.1088/0957-4484/26/12/125202.

[154] C. Opoku, A.S. Dahiya, F. Cayrel, G. Poulin-Vittrant, D. Alquier, N. Camara, Fabrication of field-effect transistors and functional nanogenerators using hydrothermally grown ZnO nanowires, RSC Adv. 5 (2015) 69925–69931. https://doi.org/10.1039/C5RA11450K.

[155] B. Mallampati, A. Singh, A. Shik, H.E. Ruda, U. Philipose, Electro-physical characterization of individual and arrays of ZnO nanowires, J. Appl. Phys. 118 (2015) 034302. https://doi.org/10.1063/1.4926793.

[156] P.-C. Chang, C.-J. Chien, D. Stichtenoth, C. Ronning, J.G. Lu, Finite size effect in ZnO nanowires, Appl. Phys. Lett. 90 (2007) 113101. https://doi.org/10.1063/1.2712507.

[157] J. Goldberger, D.J. Sirbuly, M. Law, P. Yang, ZnO Nanowire Transistors, J. Phys. Chem. B. 109 (2005) 9–14. https://doi.org/10.1021/jp0452599.

[158] S. Song, W.-K. Hong, S.-S. Kwon, T. Lee, Passivation effects on ZnO nanowire field effect transistors under oxygen, ambient, and vacuum environments, Appl. Phys. Lett. 92 (2008) 263109. https://doi.org/10.1063/1.2955512.

[159] W.-K. Hong, J.I. Sohn, D.-K. Hwang, S.-S. Kwon, G. Jo, S. Song, S.-M. Kim, H.-J. Ko, S.-J. Park, M.E. Welland, T. Lee, Tunable Electronic Transport Characteristics of Surface-Architecture-Controlled ZnO Nanowire Field Effect Transistors, Nano Lett. 8 (2008) 950–956. https://doi.org/10.1021/nl0731116.

[160] A.M. Lord, T.G. Maffeis, A.S. Walton, D.M. Kepaptsoglou, Q.M. Ramasse, M.B. Ward, J. Köble, S.P. Wilks, Factors that determine and limit the resistivity of high-quality individual ZnO nanowires, Nanotechnology. 24 (2013) 435706. https://doi.org/10.1088/0957-4484/24/43/435706.

[161] S.-P. Chiu, H.-F. Chung, Y.-H. Lin, J.-J. Kai, F.-R. Chen, J.-J. Lin, Four-probe electrical-transport measurements on single indium tin oxide nanowires between 1.5 and 300 K,

Nanotechnology. 20 (2009) 105203. https://doi.org/10.1088/0957-4484/20/10/105203.

[162] A.D.L. Bugallo, F. Donatini, C. Sartel, V. Sallet, J. Pernot, Metallic core conduction in unintentionally doped ZnO nanowire, Appl. Phys. Express. 8 (2015) 025001. https://doi.org/10.7567/APEX.8.025001.

[163] T. Cossuet, F. Donatini, A.M. Lord, E. Appert, J. Pernot, V. Consonni, Polarity-Dependent High Electrical Conductivity of ZnO Nanorods and Its Relation to Hydrogen, J. Phys. Chem. C. 122 (2018) 22767–22775. https://doi.org/10.1021/acs.jpcc.8b07388.

[164] J. Villafuerte, F. Donatini, J. Kioseoglou, E. Sarigiannidou, O. Chaix-Pluchery, J. Pernot, V. Consonni, Zinc Vacancy–Hydrogen Complexes as Major Defects in ZnO Nanowires Grown by Chemical Bath Deposition, J. Phys. Chem. C. 124 (2020) 16652–16662. https://doi.org/10.1021/acs.jpcc.0c04264.

[165] L.-T. Tsai, S.-P. Chiu, J.G. Lu, J.-J. Lin, Electrical conduction mechanisms in natively doped ZnO nanowires (II), Nanotechnology. 21 (2010) 145202. https://doi.org/10.1088/0957-4484/21/14/145202.

[166] J.B. Baxter, C.A. Schmuttenmaer, Conductivity of ZnO Nanowires, Nanoparticles, and Thin Films Using Time-Resolved Terahertz Spectroscopy †, J. Phys. Chem. B. 110 (2006) 25229–25239. https://doi.org/10.1021/jp064399a.

[167] L. Wang, J.M. Chauveau, R. Brenier, V. Sallet, F. Jomard, C. Sartel, G. Brémond, Access to residual carrier concentration in ZnO nanowires by calibrated scanning spreading resistance microscopy, Appl. Phys. Lett. 108 (2016) 132103. https://doi.org/10.1063/1.4945100.

[168] L. Wang, S. Guillemin, J. Chauveau, V. Sallet, F. Jomard, R. Brenier, V. Consonni, G. Brémond, Characterization of carrier concentration in ZnO nanowires by scanning capacitance microscopy, Phys. Status Solidi. 13 (2016) 576–580. https://doi.org/10.1002/pssc.201510268.

[169] O. Synhaivskyi, D. Albertini, P. Gaffuri, J.-M. Chauveau, V. Consonni, B. Gautier, G. Bremond, Evidence of Piezoelectric Potential and Screening Effect in Single Highly Doped ZnO: Ga and ZnO: Al Nanowires by Advanced Scanning Probe Microscopy, J. Phys. Chem. C. 125 (2021) 15373–15383. https://doi.org/https://doi.org/10.1021/acs.jpcc.1c00926.

[170] A. Janotti, C.G. Van de Walle, Native point defects in ZnO, Phys. Rev. B. 76 (2007) 165202. https://doi.org/10.1103/PhysRevB.76.165202.

[171] R.M. Sheetz, I. Ponomareva, E. Richter, A.N. Andriotis, M. Menon, Defect-induced optical absorption in the visible range in ZnO nanowires, Phys. Rev. B. 80 (2009) 195314. https://doi.org/10.1103/PhysRevB.80.195314.

[172] T. Nguyen, N.T. Tuan, V.D. Nguyen, N.D. Cuong, N.D.T. Kien, P.T. Huy, V.H. Nguyen, D.H. Nguyen, Near-infrared emission from ZnO nanorods grown by thermal evaporation, J. Lumin. 156 (2014) 199–204. https://doi.org/10.1016/j.jlumin.2014.08.018.

[173] M. Wang, Y. Zhou, Y. Zhang, E. Jung Kim, S. Hong Hahn, S. Gie Seong, Near-infrared photoluminescence from ZnO, Appl. Phys. Lett. 100 (2012) 101906. https://doi.org/10.1063/1.3692584.

[174] Y.W. Heo, D.P. Norton, S.J. Pearton, Origin of green luminescence in ZnO thin film grown by molecular-beam epitaxy, J. Appl. Phys. 98 (2005) 073502. https://doi.org/10.1063/1.2064308.

[175] L. Ke, S.C. Lai, J.D. Ye, V.L. Kaixin, S.J. Chua, Point defects analysis of zinc oxide thin films annealed at different temperatures with photoluminescence, Hall mobility, and low frequency noise, J. Appl. Phys. 108 (2010) 084502. https://doi.org/10.1063/1.3494046.

[176] L. Lin, J. Liu, J. Lv, S. Shen, X. Wu, D. Wu, Y. Qu, W. Zheng, F. Lai, Correlation between native defects and morphological, structural and optical properties of ZnO nanostructures, J. Alloys Compd. 695 (2017) 1523–1527. https://doi.org/10.1016/j.jallcom.2016.10.292.

[177] K.H. Tam, C.K. Cheung, Y.H. Leung, A.B. Djurišić, C.C. Ling, C.D. Beling, S. Fung, W.M. Kwok, W.K. Chan, D.L. Phillips, L. Ding, W.K. Ge, Defects in ZnO Nanorods Prepared by a Hydrothermal Method, J. Phys. Chem. B. 110 (2006) 20865–20871. https://doi.org/10.1021/jp063239w.

[178] A. Soudi, C.-H. Hsu, Y. Gu, Diameter-Dependent Surface Photovoltage and Surface State Density in Single Semiconductor Nanowires, Nano Lett. 12 (2012) 5111–5116. https://doi.org/10.1021/nl301863e.

[179] F. Donatini, A. de Luna Bugallo, P. Tchoulfian, G. Chicot, C. Sartel, V. Sallet, J. Pernot, Comparison of Three E-Beam Techniques for Electric Field Imaging and Carrier Diffusion Length Measurement on the Same Nanowires, Nano Lett. 16 (2016) 2938–2944. https://doi.org/10.1021/acs.nanolett.5b04710.

[180] Q.X. Zhao, L.L. Yang, M. Willander, B.E. Sernelius, P.O. Holtz, Surface recombination

in ZnO nanorods grown by chemical bath deposition, J. Appl. Phys. 104 (2008) 073526. https://doi.org/10.1063/1.2991151.

[181] S. Xu, Y. Wei, J. Liu, R. Yang, Z.L. Wang, Integrated Multilayer Nanogenerator Fabricated Using Paired Nanotip-to-Nanowire Brushes, Nano Lett. 8 (2008) 4027–4032. https://doi.org/10.1021/nl8027813.

[182] E. Gerstner, Rubbed the right way, Nat. Phys. 4 (2008) 166–166. https://doi.org/10.1038/nphys906.

[183] T.B. Bateman, Elastic Moduli of Single-Crystal Zinc Oxide, J. Appl. Phys. 33 (1962) 3309–3312. https://doi.org/10.1063/1.1931160.

[184] Z.L. Wang, Piezoelectric Nanogenerators Based on Zinc Oxide Nanowire Arrays, Science (80-.). 312 (2006) 242–246. https://doi.org/10.1126/science.1124005.

[185] Y. Qin, X. Wang, Z.L. Wang, Microfibre–nanowire hybrid structure for energy scavenging, Nature. 451 (2008) 809–813. https://doi.org/10.1038/nature06601.

[186] S. Xu, Y. Qin, C. Xu, Y. Wei, R. Yang, Z.L. Wang, Self-powered nanowire devices, Nat. Nanotechnol. 5 (2010) 366–373. https://doi.org/10.1038/nnano.2010.46.

[187] W. Deng, L. Jin, B. Zhang, Y. Chen, L. Mao, H. Zhang, W. Yang, A flexible field-limited ordered ZnO nanorod-based self-powered tactile sensor array for electronic skin, Nanoscale. 8 (2016) 16302–16306. https://doi.org/10.1039/c6nr04057h.

[188] G. Zhu, A.C. Wang, Y. Liu, Y. Zhou, Z.L. Wang, Functional electrical stimulation by nanogenerator with 58 v output voltage, Nano Lett. 12 (2012) 3086–3090. https://doi.org/10.1021/nl300972f.

[189] A. Yu, H. Li, H. Tang, T. Liu, P. Jiang, Z.L. Wang, Vertically integrated nanogenerator based on ZnO nanowire arrays, Phys. Status Solidi - Rapid Res. Lett. 5 (2011) 162–164. https://doi.org/10.1002/pssr.201105120.

[190] V. Gaddam, S. Joshi, M. Parmar, K. Rajanna, M.M. Nayak, A novel piezoelectric ZnO nanogenerator on flexible metal alloy substrate, in: 2012 IEEE Sensors, IEEE, 2012: pp. 1–4. https://doi.org/10.1109/ICSENS.2012.6411535.

[191] Y. Hu, L. Lin, Y. Zhang, Z.L. Wang, Replacing a Battery by a Nanogenerator with 20 V Output, Adv. Mater. 24 (2012) 110–114. https://doi.org/10.1002/adma.201103727.

[192] R. Tao, M. Parmar, G. Ardila, P. Oliveira, D. Marques, L. Montès, M. Mouis, Performance of ZnO based piezo-generators under controlled compression, Semicond. Sci. Technol. 32 (2017) 064003. https://doi.org/10.1088/1361-6641/aa691f.

[193] L. Lin, Y. Hu, C. Xu, Y. Zhang, R. Zhang, X. Wen, Z. Lin Wang, Transparent flexible nanogenerator as self-powered sensor for transportation monitoring, Nano Energy. 2 (2013) 75–81. https://doi.org/10.1016/j.nanoen.2012.07.019.

[194] C. Opoku, A.S. Dahiya, C. Oshman, F. Cayrel, G. Poulin-Vittrant, D. Alquier, N. Camara, Fabrication of ZnO Nanowire Based Piezoelectric Generators and Related Structures, Phys. Procedia. 70 (2015) 858–862. https://doi.org/10.1016/j.phpro.2015.08.176.

[195] T. Slimani Tlemcani, C. Justeau, K. Nadaud, D. Alquier, G. Poulin-Vittrant, Fabrication of Piezoelectric ZnO Nanowires Energy Harvester on Flexible Substrate Coated with Various Seed Layer Structures, Nanomaterials. 11 (2021) 1433. https://doi.org/10.3390/nano11061433.

[196] Q. He, X. Li, J. Zhang, H. Zhang, J. Briscoe, P–N junction-based ZnO wearable textile nanogenerator for biomechanical energy harvesting, Nano Energy. 85 (2021) 105938. https://doi.org/10.1016/j.nanoen.2021.105938.

[197] N. Jalali, P. Woolliams, M. Stewart, P.M. Weaver, M.G. Cain, S. Dunn, J. Briscoe, Improved performance of p–n junction-based ZnO nanogenerators through CuSCN-passivation of ZnO nanorods, J. Mater. Chem. A. 2 (2014) 10945. https://doi.org/10.1039/c4ta01714e.

[198] S. Lee, R. Hinchet, Y. Lee, Y. Yang, Z. Lin, G. Ardila, L. Montès, M. Mouis, Z.L. Wang, Ultrathin Nanogenerators as Self-Powered/Active Skin Sensors for Tracking Eye Ball Motion, Adv. Funct. Mater. 24 (2014) 1163–1168. https://doi.org/10.1002/adfm.201301971.

[199] Z.L. Wang, Nanopiezotronics, Adv. Mater. 19 (2007) 889–892. https://doi.org/10.1002/adma.200602918.

[200] X. Wang, J. Zhou, J. Song, J. Liu, N. Xu, Z.L. Wang, Piezoelectric Field Effect Transistor and Nanoforce Sensor Based on a Single ZnO Nanowire, Nano Lett. 6 (2006) 2768–2772. https://doi.org/10.1021/nl061802g.

[201] J. Zhou, Y. Gu, P. Fei, W. Mai, Y. Gao, R. Yang, G. Bao, Z.L. Wang, Flexible Piezotronic Strain Sensor, Nano Lett. 8 (2008) 3035–3040. https://doi.org/10.1021/nl802367t.

[202] C. Pan, L. Dong, G. Zhu, S. Niu, R. Yu, Q. Yang, Y. Liu, Z.L. Wang, High-resolution electroluminescent imaging of pressure distribution using a piezoelectric nanowire LED

array, Nat. Photonics. 7 (2013) 752–758. https://doi.org/10.1038/nphoton.2013.191.

[203] G. Hu, R. Zhou, R. Yu, L. Dong, C. Pan, Z.L. Wang, Piezotronic effect enhanced Schottky-contact ZnO micro/nanowire humidity sensors, Nano Res. 7 (2014) 1083–1091. https://doi.org/10.1007/s12274-014-0471-6.

[204] N. Doumit, G. Poulin-Vittrant, Effect of the Dielectric and Mechanical Properties of the Polymer Matrix on ZnO-Nanowire-Based Composite Nanogenerators Performance, Adv. Theory Simulations. 3 (2020) 2000128. https://doi.org/10.1002/adts.202000128.

[205] X. Zhang, J. Villafuerte, V. Consonni, J.-F. Capsal, P.-J. Cottinet, L. Petit, M.-Q. Le, Characterizing and Optimizing Piezoelectric Response of ZnO Nanowire/PMMA Composite-Based Sensor, Nanomaterials. 11 (2021) 1712. https://doi.org/10.3390/nano11071712.

[206] S.M. Kim, J.I. Sohn, H.J. Kim, J. Ku, Y.J. Park, S.N. Cha, J.M. Kim, Radially dependent effective piezoelectric coefficient and enhanced piezoelectric potential due to geometrical stress confinement in ZnO nanowires/nanotubes, Appl. Phys. Lett. 101 (2012) 013104. https://doi.org/10.1063/1.4731779.

[207] O. Graton, G. Poulin-Vittrant, A.S. Dahiya, N. Camara, L.T.H. Hue, M. Lethiecq, Equivalent circuit model of a nanogenerator based on a piezoelectric nanowire-polymer composite, Phys. Status Solidi - Rapid Res. Lett. 7 (2013) 915–918. https://doi.org/10.1002/pssr.201308017.

[208] L. Serairi, D. Yu, Y. Leprince-Wang, Numerical modeling and simulation of ZnO nanowire devices for energy harvesting, Phys. Status Solidi. 13 (2016) 683–687. https://doi.org/10.1002/pssc.201510270.

[209] N. Doumit, G. Poulin-Vittrant, A New Simulation Approach for Performance Prediction of Vertically Integrated Nanogenerators, Adv. Theory Simulations. 1 (2018) 1800033. https://doi.org/10.1002/adts.201800033.

[210] C. Falconi, G. Mantini, A. D'Amico, Z.L. Wang, Studying piezoelectric nanowires and nanowalls for energy harvesting, Sensors Actuators B Chem. 139 (2009) 511–519. https://doi.org/10.1016/j.snb.2009.02.071.

[211] R. Hinchet, S. Lee, G. Ardila, L. Montès, M. Mouis, Z.L. Wang, Performance Optimization of Vertical Nanowire-based Piezoelectric Nanogenerators, Adv. Funct. Mater. 24 (2014) 971–977. https://doi.org/10.1002/adfm.201302157.

[212] Y. Gao, Z.L. Wang, Equilibrium potential of free charge carriers in a bent piezoelectric

semiconductive nanowire, Nano Lett. 9 (2009) 1103–1110. https://doi.org/10.1021/nl803547f.

[213] S. Fathi, T.F. Sheikholeslami, Investigation of external charges effects on piezoelectric ZnO nanogenerator, J. Nano- Electron. Phys. 8 (2016) 6–11. https://doi.org/10.21272/jnep.8(2).02047.

[214] G. Romano, G. Mantini, A. Di Carlo, A. D'Amico, C. Falconi, Z.L. Wang, Piezoelectric potential in vertically aligned nanowires for high output nanogenerators, Nanotechnology. 22 (2011) 465401. https://doi.org/10.1088/0957-4484/22/46/465401.

[215] Y. Gao, Z.L. Wang, Electrostatic potential in a bent piezoelectric nanowire. The fundamental theory of nanogenerator and nanopiezotronics, Nano Lett. 7 (2007) 2499–2505. https://doi.org/10.1021/nl071310j.

[216] S. Min Kim, H. Kim, Y. Nam, S. Kim, Effects of external surface charges on the enhanced piezoelectric potential of ZnO and AlN nanowires and nanotubes, AIP Adv. 2 (2012) 042174. https://doi.org/10.1063/1.4770314.

[217] Y.S. Zhou, R. Hinchet, Y. Yang, G. Ardila, R. Songmuang, F. Zhang, Y. Zhang, W. Han, K. Pradel, L. Montès, M. Mouis, Z.L. Wang, Nano-Newton Transverse Force Sensor Using a Vertical GaN Nanowire based on the Piezotronic Effect, Adv. Mater. 25 (2013) 883–888. https://doi.org/10.1002/adma.201203263.

[218] A.J. Lopez Garcia, R. Tao, M. Mouis, G. Ardila, A New Approach to Calculate the Piezoelectric Coefficient of Piezo-Semiconductor Nanowires Integrated in Nanocomposites: Experiment and Simulation, in: 2021 21st Int. Conf. Solid-State Sensors, Actuators Microsystems, IEEE, 2021: pp. 1056–1059. https://doi.org/10.1109/Transducers50396.2021.9495621.

[219] G. Carlotti, D. Fioretto, G. Socino, E. Verona, Brillouin scattering determination of the whole set of elastic constants of a single transparent film of hexagonal symmetry, J. Phys. Condens. Matter. 7 (1995) 9147–9153. https://doi.org/10.1088/0953-8984/7/48/006.

[220] M. Laurenti, S. Stassi, M. Lorenzoni, M. Fontana, G. Canavese, V. Cauda, C.F. Pirri, Evaluation of the piezoelectric properties and voltage generation of flexible zinc oxide thin films, Nanotechnology. 26 (2015) 215704. https://doi.org/10.1088/0957-4484/26/21/215704.

[221] K. Zhang, Y. Zhao, F. He, D. Liu, Piezoelectricity of ZnO Films Prepared by Sol-Gel Method, Chinese J. Chem. Phys. 20 (2007) 721–726. https://doi.org/10.1088/1674-

0068/20/06/721-726.

[222] P. Sharma, Z. Guler, N. Jackson, Development and characterization of confocal sputtered piezoelectric zinc oxide thin film, Vacuum. 184 (2021) 109930. https://doi.org/10.1016/j.vacuum.2020.109930.

[223] R.S. Kammel, R.S. Sabry, Effects of the aspect ratio of ZnO nanorods on the performance of piezoelectric nanogenerators, J. Sci. Adv. Mater. Devices. 4 (2019) 420–424. https://doi.org/10.1016/j.jsamd.2019.08.002.

[224] B.D. Yao, Y.F. Chan, N. Wang, Formation of ZnO nanostructures by a simple way of thermal evaporation, Appl. Phys. Lett. 81 (2002) 757–759. https://doi.org/https://doi.org/10.1063/1.1495878.

[225] T. Nobis, E.M. Kaidashev, A. Rahm, M. Lorenz, J. Lenzner, M. Grundmann, Spatially Inhomogeneous Impurity Distribution in ZnO Micropillars, Nano Lett. 4 (2004) 797–800. https://doi.org/10.1021/nl049889y.

[226] S. Peulon, D. Lincot, Cathodic electrodeposition from aqueous solution of dense or open-structured zinc oxide films, Adv. Mater. 8 (1996) 166–170. https://doi.org/10.1002/adma.19960080216.

[227] L. Vayssieres, K. Keis, S.-E. Lindquist, A. Hagfeldt, Purpose-Built Anisotropic Metal Oxide Material: 3D Highly Oriented Microrod Array of ZnO, J. Phys. Chem. B. 105 (2001) 3350–3352. https://doi.org/10.1021/jp010026s.

[228] M.-T. Hoang, J. Yvonnet, A. Mitrushchenkov, G. Chambaud, First-principles based multiscale model of piezoelectric nanowires with surface effects, J. Appl. Phys. 113 (2013) 014309. https://doi.org/10.1063/1.4773333.

[229] V.F. Rivera, F. Auras, P. Motto, S. Stassi, G. Canavese, E. Celasco, T. Bein, B. Onida, V. Cauda, Length-dependent charge generation from vertical arrays of high-aspect-ratio ZnO nanowires, Chem. - A Eur. J. 19 (2013) 14665–14674. https://doi.org/10.1002/chem.201204429.

[230] J. Briscoe, N. Jalali, P. Woolliams, M. Stewart, P.M. Weaver, M. Cain, S. Dunn, Measurement techniques for piezoelectric nanogenerators, Energy Environ. Sci. 6 (2013) 3035. https://doi.org/10.1039/c3ee41889h.

[231] K. Nadaud, G. Poulin-Vittrant, D. Alquier, Effect of the excitation waveform on the average power and peak power delivered by a piezoelectric generator, Mech. Syst. Signal Process. 133 (2019) 106278.

[232] R. Tao, Piezoelectric generators based on semiconducting nanowires: simulation and experiments, (2017).

[233] G. Nagaraju, Y.H. Ko, J.S. Yu, Effect of diameter and height of electrochemically-deposited ZnO nanorod arrays on the performance of piezoelectric nanogenerators, Mater. Chem. Phys. 149–150 (2015) 393–399. https://doi.org/10.1016/j.matchemphys.2014.10.034.

[234] M. Ahmad, M.A. Iqbal, J. Kiely, R. Luxton, M. Jabeen, Enhanced output voltage generation via ZnO nanowires (50 nm): Effect of diameter thinning on voltage enhancement, J. Phys. Chem. Solids. 104 (2017) 281–285. https://doi.org/10.1016/j.jpcs.2017.01.006.

[235] Z. Guan, H. Hu, X. Shen, P. Xiang, N. Zhong, J. Chu, C. Duan, Recent Progress in Two-Dimensional Ferroelectric Materials, Adv. Electron. Mater. 6 (2020) 1900818. https://doi.org/10.1002/aelm.201900818.

[236] L. Jaloustre, S. Le Denmat, T. Auzelle, M. Azadmand, L. Geelhaar, F. Dahlem, R. Songmuang, Toward Quantitative Measurements of Piezoelectricity in III-N Semiconductor Nanowires, ACS Appl. Nano Mater. 4 (2021) 43–52. https://doi.org/10.1021/acsanm.0c02078.

[237] A.L. Kholkin, V. V Shvartsman, D.A. Kiselev, I.K. Bdikin, Nanoscale Characterization of Ferroelectric Materials for Piezoelectric Applications, Ferroelectrics. 341 (2006) 3–19. https://doi.org/10.1080/00150190600889304.

[238] Q. Zhu, E.N. Esfahani, S. Xie, J. Li, Minimizing electrostatic interactions from piezoresponse force microscopy via capacitive excitation, Theor. Appl. Mech. Lett. 10 (2020) 23–26.

[239] S. Kim, D. Seol, X. Lu, M. Alexe, Y. Kim, Electrostatic-free piezoresponse force microscopy, Sci. Rep. 7 (2017) 41657. https://doi.org/10.1038/srep41657.

[240] T. Jungk, Á. Hoffmann, E. Soergel, Quantitative analysis of ferroelectric domain imaging with piezoresponse force microscopy, Appl. Phys. Lett. 89 (2006) 163507. https://doi.org/10.1063/1.2362984.

[241] T. Jungk, A. Hoffmann, E. Soergel, Consequences of the background in piezoresponse force microscopy on the imaging of ferroelectric domain structures, J. Microsc. 227 (2007) 72–78.

[242] S. Jesse, B. Mirman, S. V Kalinin, Resonance enhancement in piezoresponse force

microscopy: Mapping electromechanical activity, contact stiffness, and Q factor, Appl. Phys. Lett. 89 (2006) 022906. https://doi.org/10.1063/1.2221496.

[243] A. Labuda, R. Proksch, Quantitative measurements of electromechanical response with a combined optical beam and interferometric atomic force microscope, Appl. Phys. Lett. 106 (2015) 253103. https://doi.org/10.1063/1.4922210.

[244] M. Jazbinšek, M. Zgonik, Material tensor parameters of LiNbO 3 relevant for electro- and elasto-optics, Appl. Phys. B Lasers Opt. 74 (2002) 407–414. https://doi.org/10.1007/s003400200818.

[245] G. Tian, D. Xiong, Y. Su, T. Yang, Y. Gao, C. Yan, W. Deng, L. Jin, H. Zhang, X. Fan, C. Wang, W. Deng, W. Yang, Understanding the Potential Screening Effect through the Discretely Structured ZnO Nanorods Piezo Array, Nano Lett. 20 (2020) 4270–4277. https://doi.org/10.1021/acs.nanolett.0c00793.

[246] K. Jacobi, G. Zwicker, A. Gutmann, Work function, electron affinity and band bending of zinc oxide surfaces, Surf. Sci. 141 (1984) 109–125. https://doi.org/10.1016/0039-6028(84)90199-7.

[247] L. Qiao, Y. Zeng, C.Q. Qu, H.Z. Zhang, X.Y. Hu, L.J. Song, D.M. Bi, S.J. Liu, Adsorption of oxygen atom on Zn-terminated (0001) surface of wurtzite ZnO: A density-functional theory investigation, Phys. E Low-Dimensional Syst. Nanostructures. 48 (2013) 7–12. https://doi.org/10.1016/j.physe.2012.11.020.

[248] A.M. Lucero Manzano, J.D. Fuhr, E.D. Cantero, M. Famá, E.A. Sánchez, V.E. Esaulov, O. Grizzi, Hydroxylation of the Zn terminated ZnO(0 0 0 1) surface under vacuum conditions, Appl. Surf. Sci. 572 (2022) 151271. https://doi.org/10.1016/j.apsusc.2021.151271.

[249] S. Rackauskas, N. Barbero, C. Barolo, G. Viscardi, ZnO Nanowire Application in Chemoresistive Sensing: A Review, Nanomaterials. 7 (2017) 381. https://doi.org/10.3390/nano7110381.

[250] M. Ahmad, M.K. Ahmad, N. Nafarizal, C.F. Soon, A.B. Suriani, A. Mohamed, M.H. Mamat, Adsorption effect of oxygen on ZnO Nanowires (100 nm) leading towards pronounced edge effects and voltage enhancement, Mater. Res. Express. 7 (2020) 095004. https://doi.org/10.1088/2053-1591/ab9d51.

[251] J.I. Sohn, S.N. Cha, B.G. Song, S. Lee, S.M. Kim, J. Ku, H.J. Kim, Y.J. Park, B.L. Choi, Z.L. Wang, J.M. Kim, K. Kim, Engineering of efficiency limiting free carriers and an

interfacial energy barrier for an enhancing piezoelectric generation, Energy Environ. Sci. 6 (2013) 97–104. https://doi.org/10.1039/C2EE23404A.

[252] J. Liu, P. Fei, J. Song, X. Wang, C. Lao, R. Tummala, Z.L. Wang, Carrier Density and Schottky Barrier on the Performance of DC Nanogenerator, Nano Lett. 8 (2008) 328–332. https://doi.org/10.1021/nl0728470.

[253] N. Jamond, P. Chrétien, L. Gatilova, E. Galopin, L. Travers, J.-C. Harmand, F. Glas, F. Houzé, N. Gogneau, Energy harvesting efficiency in GaN nanowire-based nanogenerators: the critical influence of the Schottky nanocontact, Nanoscale. 9 (2017) 4610–4619. https://doi.org/10.1039/C7NR00647K.

[254] A.M. Cowley, S.M. Sze, Surface States and Barrier Height of Metal-Semiconductor Systems, J. Appl. Phys. 36 (1965) 3212–3220. https://doi.org/10.1063/1.1702952.

[255] J. Bardeen, Surface States and Rectification at a Metal Semi-Conductor Contact, Phys. Rev. 71 (1947) 717–727. https://doi.org/10.1103/PhysRev.71.717.

[256] S.K. Cheung, N.W. Cheung, Extraction of Schottky diode parameters from forward current-voltage characteristics, Appl. Phys. Lett. 49 (1986) 85–87. https://doi.org/10.1063/1.97359.

[257] H. Oh, S.A. Dayeh, Physics-Based Device Models and Progress Review for Active Piezoelectric Semiconductor Devices, Sensors. 20 (2020) 3872. https://doi.org/10.3390/s20143872.

[258] O.T. Hofmann, J.-C. Deinert, Y. Xu, P. Rinke, J. Stähler, M. Wolf, M. Scheffler, Large work function reduction by adsorption of a molecule with a negative electron affinity: Pyridine on ZnO($10\bar{1}0$), J. Chem. Phys. 139 (2013) 174701. https://doi.org/10.1063/1.4827017.

[259] Z.L. Wang, Zinc oxide nanostructures: growth, properties and applications, J. Phys. Condens. Matter. 16 (2004) R829.

[260] A.A. Sokol, S.A. French, S.T. Bromley, C.R.A. Catlow, H.J.J. van Dam, P. Sherwood, Point defects in ZnO, Faraday Discuss. 134 (2007) 267–282.

[261] E. Miranda, G. Milano, C. Ricciardi, Compact Modeling of the I-V Characteristics of ZnO Nanowires Including Nonlinear Series Resistance Effects, IEEE Trans. Nanotechnol. 19 (2020) 297–300. https://doi.org/10.1109/TNANO.2020.2981214.

[262] R. Labar, T.K. Kundu, Fabrication and Characterization of Back-to-Back Schottky Diode in Ni/ZnO/Ag Nanojunction, J. Electron. Mater. 51 (2022) 223–231.

https://doi.org/10.1007/s11664-021-09280-1.

[263] A.M. Lord, V. Consonni, T. Cossuet, F. Donatini, S.P. Wilks, Schottky Contacts on Polarity-Controlled Vertical ZnO Nanorods, ACS Appl. Mater. Interfaces. 12 (2020) 13217–13228. https://doi.org/10.1021/acsami.9b23260.

[264] W.I. Park, G.-C. Yi, J.-W. Kim, S.-M. Park, Schottky nanocontacts on ZnO nanorod arrays, Appl. Phys. Lett. 82 (2003) 4358–4360. https://doi.org/10.1063/1.1584089.

[265] G.D.J. Smit, S. Rogge, T.M. Klapwijk, Scaling of nano-Schottky-diodes, Appl. Phys. Lett. 81 (2002) 3852–3854. https://doi.org/10.1063/1.1521251.

[266] J.A. Greenwood, K.L. Johnson, E. Matsubara, A surface roughness parameter in Hertz contact, Wear. 100 (1984) 47–57. https://doi.org/10.1016/0043-1648(84)90005-X.

[267] Y. Li, F. Della Valle, M. Simonnet, I. Yamada, J.-J. Delaunay, Competitive surface effects of oxygen and water on UV photoresponse of ZnO nanowires, Appl. Phys. Lett. 94 (2009) 23110.

[268] T. Belagodu, E.A. Azhar, H. Yu, Modulation of charge conduction in ZnO nanowires through selective surface molecular functionalization, Nanoscale. 4 (2012) 7330–7333.

[269] C. Lai, X. Wang, Y. Zhao, H. Fong, Z. Zhu, Effects of humidity on the ultraviolet nanosensors of aligned electrospun ZnO nanofibers, RSC Adv. 3 (2013) 6640–6645.

[270] H.C. Card, E.H. Rhoderick, Studies of tunnel MOS diodes I. Interface effects in silicon Schottky diodes, J. Phys. D. Appl. Phys. 4 (1971) 319. https://doi.org/10.1088/0022-3727/4/10/319.

[271] S. Niu, Y. Hu, X. Wen, Y. Zhou, F. Zhang, L. Lin, S. Wang, Z.L. Wang, Enhanced Performance of Flexible ZnO Nanowire Based Room-Temperature Oxygen Sensors by Piezotronic Effect, Adv. Mater. 25 (2013) 3701–3706. https://doi.org/10.1002/adma.201301262.

[272] M. Bah, T.S. Tlemcani, S. Boubenia, C. Justeau, N. Vivet, J.-M. Chauveau, F. Jomard, K. Nadaud, G. Poulin-Vittrant, D. Alquier, Assessing the electrical activity of individual ZnO nanowires thermally annealed in air, Nanoscale Adv. 4 (2022) 1125–1135. https://doi.org/10.1039/D1NA00860A.

[273] E. Muchuweni, T.S. Sathiaraj, H. Nyakotyo, Effect of annealing on the microstructural, optical and electrical properties of ZnO nanowires by hydrothermal synthesis for transparent electrode fabrication, Mater. Sci. Eng. B. 227 (2018) 68–73. https://doi.org/https://doi.org/10.1016/j.mseb.2017.10.006.

[274] R. Araneo, F. Bini, M. Pea, A. Notargiacomo, A. Rinaldi, S. Celozzi, Impact of non-linear piezoelectricity on the piezotronic effect of ZnO nanowires, IEEE Trans. Nanotechnol. 15 (2016) 512–520. https://doi.org/10.1109/TNANO.2016.2538798.

[275] X. Liang, S. Hu, S. Shen, Effects of surface and flexoelectricity on a piezoelectric nanobeam, Smart Mater. Struct. 23 (2014) 35020. https://doi.org/https://doi-org.gaelnomade-1.grenet.fr/10.1088/0964-1726/23/3/035020.

[276] T. Yoshimura, S. Murakami, K. Wakazono, K. Kariya, N. Fujimura, Piezoelectric Vibrational Energy Harvester Using Lead-Free Ferroelectric BiFeO 3 Films, Appl. Phys. Express. 6 (2013) 051501. https://doi.org/10.7567/APEX.6.051501.

[277] Y. Li, Z. Zhang, W. Han, C. Jiang, E. Xie, Analysis on the piezotronic effect in a strained piezo-Schottky junction with AC impedance spectroscopy, Nano Energy. 36 (2017) 118–125. https://doi.org/10.1016/j.nanoen.2017.04.021.

[278] A.J.L. Garcia, G. Sico, M. Montanino, V. Defoor, M. Pusty, X. Mescot, F. Loffredo, F. Villani, G. Nenna, G. Ardila, Low-Temperature Growth of ZnO Nanowires from Gravure-Printed ZnO Nanoparticle Seed Layers for Flexible Piezoelectric Devices, Nanomaterials. 11 (2021) 1430. https://doi.org/10.3390/nano11061430.

[279] J. Colchero, A. Gil, A.M. Baró, Resolution enhancement and improved data interpretation in electrostatic force microscopy, Phys. Rev. B. 64 (2001) 245403. https://doi.org/10.1103/PhysRevB.64.245403.

[280] T. Glatzel, S. Sadewasser, M.C. Lux-Steiner, Amplitude or frequency modulation-detection in Kelvin probe force microscopy, Appl. Surf. Sci. 210 (2003) 84–89. https://doi.org/10.1016/S0169-4332(02)01484-8.

[281] S. Hudlet, M. Saint Jean, B. Roulet, J. Berger, C. Guthmann, Electrostatic forces between metallic tip and semiconductor surfaces, J. Appl. Phys. 77 (1995) 3308–3314. https://doi.org/10.1063/1.358616.

[282] H. Hölscher, U.D. Schwarz, R. Wiesendanger, Calculation of the frequency shift in dynamic force microscopy, Appl. Surf. Sci. 140 (1999) 344–351. https://doi.org/10.1016/S0169-4332(98)00552-2.

[283] W. Melitz, J. Shen, A.C. Kummel, S. Lee, Kelvin probe force microscopy and its application, Surf. Sci. Rep. 66 (2011) 1–27. https://doi.org/10.1016/j.surfrep.2010.10.001.

[284] C. Li, S. Minne, Y. Hu, J. Ma, J. He, H. Mittel, V. Kelly, N. Erina, S. Guo, T. Mueller,

PeakForce Kelvin probe force microscopy, Bruker Appl. Note. 140 (2013) 1–14.

[285] S. Tripathi, R. Agarwal, D. Singh, Size Dependent Elastic and Thermophysical Properties of Zinc Oxide Nanowires, Johnson Matthey Technol. Rev. 63 (2019) 166–176. https://doi.org/10.1595/205651319X15514400132039.

[286] H. Koc, E. Deligöz, A.M. Mamedov, The elastic, electronic, and optical properties of PtSi and PtGe compounds, Philos. Mag. 91 (2011) 3093–3107. https://doi.org/10.1080/14786435.2011.566229.